THÈSE

En vue de l'obtention du

DOCTORAT DE L'UNIVERSITÉ DE TOULOUSE

Délivré par : *l'Université Toulouse 3 Paul Sabatier (UT3 Paul Sabatier)*

Présentée et soutenue le *28/09/2016* **par :**

Philippe PEILLE

Développement d'un simulateur pour le X-ray Integral Field Unit : du signal astrophysique à la performance instrumentale

---

JURY

Pr. Pierre Jean	Professeur des universités	Président du jury
Dr. Caroline Kilbourne	NASA Staff Scientist	Rapporteur
Pr. Mariano Mendez	Professor	Rapporteur
Dr. Richard Kelley	NASA Staff Scientist	Examinateur
Pr. Jörn Wilms	Professor	Examinateur
Dr. Edward Cackett	Associate Professor	Examinateur
Dr. Didier Barret	Directeur de recherche	Examinateur
Mr. Thien Lam-Trong	Ingénieur	Invité

École doctorale et spécialité :
SDU2E : Astrophysique, Sciences de l'Espace, Planétologie
Unité de Recherche :
Institut de Recherche en Astrophysique et Planétologie
Directeur de Thèse :
Didier BARRET
Rapporteurs :
Dr. Caroline Kilbourne et *Prof. Dr. Mariano Mendez*

Remerciements

Je tiens tout d'abord à remercier mes deux rapporteurs Caroline Kilbourne et Mariano Mendez pour avoir relu avec attention mon manuscrit et pour leur avis précieux. Un grand merci également à Richard Kelley, Joern Wilms, Edward Cackett, Pierre Jean et Thien Lam-Trong, pour avoir accepté de former mon jury.

Ma plus grande gratitude s'adresse bien évidemment à Didier Barret, mon directeur de thèse, sans qui je n'aurais probablement jamais décidé de faire une thèse et qui a toujours été un encadrant passionné, motivant, mais aussi à l'écoute et disponible quand il le fallait. C'est toujours avec plaisir que je le voyais arriver en trombe dans mon bureau pour discuter de mes derniers résultats. J'ai particulièrement apprécié la confiance qu'il a su me donner très rapidement et j'aime à penser que nous avons fini plus en tant que collègues que directeur et étudiant.

Ces trois années n'auraient également pas été les mêmes sans la fameuse X-IFU tiger team de l'IRAP au sein de laquelle j'ai eu le plaisir de travailler pendant la majeure partie de ma thèse : merci à Etienne et Laurent, le bureau de choc qui a eu la joie (ou pas) de me voir arriver de temps en temps avec une question existentielle de statistique ou sur la science d'Athena, à François, notre transfuge des grandes longueurs d'onde que l'on va finir par pervertir pour de bon, à Edoardo avec qui la relève est assurée, mais aussi Natalie, Olivier, et Michael, et tous les autres membres du projet, notamment Antoine et Bernard avec qui j'ai pu le plus échanger sur les tenants et aboutissants du DRE. En dehors du cadre X-IFU, j'ai vraiment apprécié mon passage à l'IRAP et souhaite remercier l'ensemble des membres de ce laboratoire. Je pense malgré tout plus particulièrement à Jean-François pour son encadrement lors de mes débuts dans l'astrophysique X, Pierrick pour avoir refait le monde régulièrement avec Camille et moi (et aussi pour avoir accepté de se faire casser les oreilles à la toute fin), Peter pour sa bienveillance, Pierre qui au-delà d'avoir été mon président de jury a été un très bon tuteur pour ma période d'enseignement à l'Université, sans oublier Martin en qui j'ai trouvé un directeur de laboratoire toujours à l'écoute des doctorants.

Je souhaite tout autant remercier les membres CNES du projet X-IFU avec lesquels il a toujours été très agréable de travailler. Je pense tout particulièrement à Thien, Jean-Michel, Françoise et Hervé avec qui j'ai eu le plus l'occasion d'échanger, mais c'est avec grand plaisir que je rejoins aujourd'hui l'équipe au grand complet. Même si il a maintenant quitté le projet, je remercie également Rodolphe pour nos discussions et ses conseils dès le début de ma thèse.

De manière plus large, je tiens à souligner la chance que j'ai eue de travailler dans un contexte aussi stimulant que le consortium X-IFU qui rassemble de si nombreux scientifiques auprès desquels il y a tellement à apprendre. Dans ce grand ensemble, un merci très spécial à l'équipe End-to-End avec qui j'ai vraiment apprécié travailler: Joern, Thomas, Thorsten, Roland, Jelle, Maite, Bea, Steeve et Simon.

Au-delà du travail, une chose est sûre, mon passage à l'IRAP n'aurait jamais été aussi plaisant sans la fine équipe du tarot. Un grand merci à vous tous : Cyril (super colloc qui n'a pas 36 ans, mais qui vient de Bordeaux), Camille (le meilleur des co-bureaux toujours prêt à écouter mes questions absurdes), Damien (le meilleur d'entre nous, un roi, un bout ;)), David (c'est quand tu veux pour "ça me vénère"), William (le martien et ses fameux randoms), Jessie, Delphine et Giovanni, mais aussi à ceux qui nous ont rejoint, Nicolas, Thomas, Armelle, Logithan, Edoardo et Emmy. Une toute aussi grande pensée pour les membres d'UniverSCiel avec qui j'ai passé des moments mémorables au cours de

ces trois années pour organiser le festival Astrojeunes, des plus anciens aux nouveaux, en commençant par notre guide à tous Nicolas L. (Clermont a perdu ce week-end non ?), puis Laurianne, Aurélia, Nicolas V., Simon, Arnaud, Claire, Vincent, Bernard, David et William (team ballon forever), Ilane, Gab (tu seras toujours en princesse dans mon esprit), Jason (I have just one question for you...), Fabien, Marina (malgré les licornes), Wilhem (avec un seul h), Damien (toujours prêt à déflater), Lucile, Anne, Annick, Thomas, Emmy, et Morgane.

Pour finir, je souhaite adresser un merci tout particulier à ma famille : à mes parents pour m'avoir soutenu, encouragé et éveillé ma curiosité dès mon plus jeune âge, à ma grande soeur Carole pour avoir toujours été là pour moi y compris jusque dans le money time, et à son mari François qui a accepté de découvrir les détails des QPOs et du X-IFU dans le texte. Enfin, cette thèse n'aurait peut-être jamais vu le jour sans la présence à mes côtés de Marie-Hélène, qui fait tous les jours mon plus grand bonheur. Je ne sais encore comment je vais pouvoir te rendre tout ce que tu as fait pour moi au cours de ces trois années.

Résumé

Cette thèse est consacrée au développement d'un modèle End-to-End pour le spectrocalorimètre X-IFU qui observera à partir de 2028 l'Univers en rayons X avec une précision jamais atteinte auparavant. Ce travail s'est essentiellement organisé en deux parties.

J'ai dans un premier temps étudié la dynamique des parties les plus internes des binaires X de faible masse à l'aide de deux sondes particulières que sont les sursauts X et les oscillations quasi-périodiques au kHz (kHz QPOs). En me basant sur les données d'archive du satellite Rossi X-ray Timing Explorer et sur des méthodes d'analyse spécifiquement développées dans ce but, j'ai notamment pu mettre en évidence pour la première fois une réaction du premier sur le second, confirmant le lien très étroit entre ces oscillations et les parties les plus internes du système. Le temps de rétablissement du système suite aux sursauts entre également en conflit dans la plupart des cas avec l'augmentation supposée du taux d'accrétion suite à ces explosions. Au travers d'une analyse spectro-temporelle complète des deux kHz QPOs de 4U 1728-34, j'ai également pu confirmer l'incompatibilité des spectres de retard des deux QPOs qui suggère une origine différente de ces deux oscillations. L'étude de leurs spectres de covariance, obtenus pour la première fois dans cette thèse, a quant à elle mis en évidence le rôle central de la couche de Comptonisation et potentiellement celui d'une zone particulièrement compacte de la couche limite pour l'émission des QPOs.

Dans le second volet de ma thèse, j'ai développé un simulateur End-to-End pour l'instrument X-IFU permettant de représenter l'ensemble du processus menant à une observation scientifique en rayons X, de l'émission des photons par une source jusqu'à leur mesure finale à bord du satellite. J'ai notamment mis en place des outils permettant la comparaison précise de plusieurs matrices de détecteurs en prenant en compte les effets de la reconstruction du signal brut issu des électroniques de lecture. Cette étude a mis en évidence l'intérêt de configurations hybrides, contenant une sous-matrice de petits pixels capables d'améliorer par un ordre de grandeur la capacité de comptage de l'instrument. Une solution alternative consisterait à défocaliser le miroir lors de l'observation de sources ponctuelles brillantes.

Situées au coeur de la performance du X-IFU, j'ai également comparé de manière exhaustive différentes méthodes de reconstruction des signaux bruts issus des détecteurs X-IFU. Ceci a permis de montrer qu'à faible coût en termes de puissance de calcul embarquée, une amélioration significative de la résolution en énergie finale de l'instrument pouvait être obtenue à l'aide d'algorithmes plus sophistiqués. En tenant compte des contraintes de calibration, le candidat le plus prometteur apparaît aujourd'hui être l'analyse dans l'espace de résistance.

En me servant de la caractérisation des performances des différents types de pixels, j'ai également mis en place une méthode de simulation rapide et modulable de l'ensemble de l'instrument permettant d'obtenir des observations synthétiques à long temps d'exposition de sources X très complexes, représentatives des futures capacités du X-IFU. Cet outil m'a notamment permis d'étudier la sensibilité de cet instrument aux effets de temps mort et de confusion, mais également d'estimer sa future capacité à distinguer différents régimes de turbulence dans les amas de galaxies et de mesurer leur profil d'abondance et de température. A plus long terme ce simulateur pourra servir à l'étude d'autres cas scientifiques, ainsi qu'à l'analyse d'effets à l'échelle de l'ensemble du plan de détection tels que la diaphonie entre pixels.

Abstract

This thesis is dedicated to the development of an End-to-End model for the X-IFU spectrocalorimeter scheduled for launch in 2028 on board the *Athena* mission and which will observe the X-ray universe with unprecedented precision. This work has been mainly organized in two parts.

I studied first the dynamics of the innermost parts of low mass X-ray binaries using two specific probes of the accretion flow: type I X-ray bursts and kHz quasi-periodic oscillations (kHz QPOs). Starting from the archival data of the *Rossi X-ray Timing Explorer* mission and using specific data analysis techniques, I notably highlighted for the first time a reaction of the latter to the former, confirming the tight link between this oscillation and the inner parts of the system. The measured recovery time was also found in conflict with recent claims of an enhancement of the accretion rate following these thermonuclear explosions. From the exhaustive spectral timing analysis of both kHz QPOs in 4U 1728-34, I further confirmed the inconsistancy of their lag energy spectra, pointing towards a different origin for these two oscillations. The study of their covariance spectra, obtained here for the first time, has revealed the key role of the Comptonization layer, and potentially of a more compact part of it, in the emission of the QPOs.

In the second part of my thesis, I focused on the development of an End-to-End simulator for the X-IFU capable of depicting the full process leading to an X-ray observation, from the photon emission by the astrophysical source to their on-board detection. I notably implemented tools allowing the precise comparison of different potential pixel array configurations taking into account the effects of the event reconstruction from the raw data coming from the readout electronics. This study highlighted the advantage of using hybrid arrays containing a small pixel sub-array capable of improving by an order of magnitude the count rate capability of the instrument. An alternative solution would consist in defocusing the mirror during the observation of bright point sources.

Being a key component of the overall X-IFU performance, I also thoroughly compared different reconstruction methods of the pixel raw signal. This showed that with a minimal impact on the required on-board processing power, a significant improvement of the final energy resolution could be obtained from more sophisticated reconstruction methods. Taking into account the calibration constraints, the most promising candidate currently appears to be the so-called "resistance space analysis".

Taking advantage of the obtained performance characterization of the different foreseen pixel types, I also developed a fast and modular simulation method of the complete instrument providing representative synthetic observations with long exposure times of complex astrophysical sources sufficiently detailed for evaluating the future capabilities of the X-IFU. I notably used this tool to study the X-IFU sensitivity to dead time and confusion effects, but also to estimate its capability to distinguish different turbulence regimes in galaxy clusters and to measure abundance and temperature profiles. In the longer run, this simulator will be useful for the study of other scientific cases as well as the analysis of instrumental effects at the full detection plane level such as pixel crosstalk.

Table of Contents

Avant-propos

Ce manuscrit présente le résumé des travaux que j'ai effectués durant mes trois années de doctorat de l'Université Toulouse III, au sein de l'Institut de Recherche en Astrophysique et Planétologie. Cette thèse a été consacrée au développement d'un simulateur End-to-End pour l'instrument *X-ray Integral Field Unit* (X-IFU) de la mission *Athena* de l'ESA. Elle s'est essentiellement déroulée en deux temps: une première partie a été dédiée à l'étude de la dynamique des disques d'accrétion autour des étoiles à neutrons afin de me familiariser avec les techniques de traitement des données X, alors qu'une deuxième s'est focalisée sur l'étude des performances haut niveau du X-IFU via la mise en place et le perfectionnement d'un simulateur End-to-End.

Les phénomènes d'accrétion sont présents dans l'univers à diverses échelles très différentes, allant des disques proto-planétaires jusqu'aux noyaux actifs de galaxie. En astronomie X, l'accrétion est un phénomène incontournable puisqu'elle est la source d'énergie de l'écrasante majorité des sources détectées jusqu'à aujourd'hui. Les traces de celle-ci sont observables en rayons X lorsqu'elle se déroule autour de trous noirs ou d'étoiles à neutrons dont la densité dépasse celle de la matière nucléaire. Les disques d'accrétion se formant autour de ces objets atteignent des température de plusieurs millions de degré. L'émission X qui en résulte provient des parties les plus internes de ces systèmes dont la dynamique est décrite par la relativité générale en champ fort. Ceci en fait des de véritables laboratoires pour l'étude de questions clés de la physique et de l'astrophysique moderne telles que: *quel est l'état stable de la matière à des densités supra-nucléaires ? La relativité générale doit-elle être modifiée pour décrire la mécanique en champs forts ? Comment se produisent les supernovae donnant naissance à ces objets ? Et enfin, quel est leur rôle et leur évolution lors de la formation des très grandes structures de l'univers ?*

Depuis la détection historique du premier trou noir Cygnus X-1 en 1965, de nombreuses observations confirment le caractère universel de la géométrie des systèmes accrétants qu'ils aient en leur centre une étoile à neutrons ou un trou noir supermassif. En étudiant la dynamique des disques d'accrétion autour des étoiles à neutrons, c'est donc à une question beaucoup plus générale que la physique de ces systèmes que nous souhaitons nous adresser. Malgré de nombreuses similarités avec les systèmes à trou noir, il est indéniable que la présence d'une surface physique dans le cas des étoiles à neutrons va venir modifier le flot de matière dans les parties les plus internes du disque. Si cela peut-être vu comme un complication par rapport au cas plus "pur" des trous noirs, cette particularité offre également la possibilité de regarder le problème de la physique de l'accrétion avec un angle différent. Dans cette thèse, nous avons donc décidé d'utiliser deux sondes spécifiques des systèmes binaires à étoile à neutrons que sont les sursauts X de type I et les oscillations quasi-périodiques au kHz (kHz QPOs).

Les sursauts X sont le résultat de l'accumulation de matière à la surface de l'étoile à neutrons donnant naissance à une soudaine explosion thermonucléaire libérant en quelques secondes une grande luminosité, ainsi qu'une quantité d'énergie supérieure à l'énergie de liaison des parties internes d'un disque d'accrétion. Les kHz QPOs quant à eux sont des oscillations très cohérentes de la luminosité de la binaire X à des fréquences commensurables à la fréquence orbitale au niveau du bord interne du disque, et il est communément accepté qu'elles sont produites au coeur même du système. Il apparaît donc intéressant de combiner ces deux signaux et d'étudier la réaction des QPOs aux sursauts X, ce que je présenterai dans une première étude. Les QPOs en eux-mêmes sont une sonde unique de la géométrie

des binaires X car ils mettent en jeu non seulement le disque d'accrétion, mais également la couche d'électrons chauds responsable de l'émission à haute énergie. Comprendre leur origine permettrait donc de fortement contraindre la physique de ces systèmes. C'est dans ce but que j'ai appliqué ensuite à ces signaux des techniques d'analyse novatrices en utilisant simultanément l'information spectrale et temporelle. Ces techniques ont permis récemment de grandes avancées, notamment dans l'étude des noyaux actifs de galaxie. La détection et caractérisation des QPOs nécessite une instrumentation particulière permettant d'observer avec une grande résolution temporelle des sources très brillantes. J'ai donc utilisé pour ces deux études les données d'archive de l'instrument *Proportional Counter Array* (PCA) du satellite *Rossi X-ray Timing Explorer* (RXTE).

Alors que de nombreux auteurs continuent d'utiliser des données d'anciennes missions telles que RXTE pour étudier la physique de l'accrétion, celle-ci est également au coeur de l'astronomie X de la prochaine décennie, et la mission *Athena* ne sera pas une exception. Il permettra notamment d'étudier en détail les vents puissants émis par les objets compacts accrétants ainsi que leur influence sur leur galaxie/amas environnant. Bien sûr, en tant que véritable observatoire, *Athena* s'adresse à un plus large panel de problématiques scientifiques et tentera de répondre aux deux questions fondamentales que sont: *Comment la matière ordinaire s'est elle assemblée pour former les grandes structures que l'on observe aujourd'hui ? Comment les trous noirs grandissent-ils et façonnent-ils l'Univers ?* Pour cela, cette mission embarquera notamment à son bord l'instrument X-IFU.

Le X-IFU est un spectromètre d'intégrale de champ qui fournira sur un champ de vue de 5 arcminutes une résolution spectrals révolutionnaire de 2.5 eV et une résolution spatiale de 5 arcsecondes. Pour cela, cet instrument cryogénique reposera sur une matrice de près de 4000 pixels opérés en deçà de 100 mK. Ceux-ci seront constitués d'absorbeurs bi-couche lus par des thermomètres de très haute précision de type "Transition Edge Sensors" (TESs). Concrètement, suite à la thermalisation d'un photon X dans un des absorbeurs, l'augmentation de température en résultant sera mesurée par le TES qui, polarisé dans sa transition fine entre les états supraconducteur et normal, verra sa résistance et donc le courant le traversant être modifié. Ce changement de courant sera alors analysé par une chaîne de lecture complexe incluant un multiplexage fréquentiel ainsi qu'une boucle de rétroaction active et se terminant par un calculateur embarqué responsable de l'extraction de l'énergie de chaque photon à partir des signaux bruts.

Afin d'analyser les performances haut niveau de cet instrument complexe, il convient de prendre en compte de façon réaliste l'ensemble de ses différentes composantes. C'est le but du simulateur End-to-End SIXTE (Simulation of X-ray Telescopes) au développement duquel j'ai largement participé au cours de la deuxième partie de ma thèse. SIXTE se veut être une représentation complète du processus menant à une observation scientifique en rayons X: en partant d'un catalogue de sources caractérisées par leur position, spectre, extension spatiale, et variabilité temporelle, différents modules viennent simuler les étapes d'émission de photons par les sources, d'imagerie par le télescope et de détection des événements par l'instrument. C'est sur cette dernière étape spécifique au X-IFU que l'essentiel de mon travail se focalisera, en particulier sur la prise en compte de matrices de détecteurs hybrides avec des petits pixels dédiés aux hauts taux de comptage et des pixels plus larges consacrés à l'observation de sources étendues moins brillantes. Ces pixels auront des propriétés très différentes en termes de composition, de rapidité et de caractéristiques de leur transition supraconductrice. L'évaluation comparée des performances de ces détecteurs passera donc par l'utilisation d'un simulateur de TESs représentatif, traitant de manière satisfaisante le caractère non-linéaire de ce type de détecteurs, ainsi que par l'étude précise de la reconstruction de l'énergie des photons à partir du signal brut pour pouvoir estimer la résolution finale des différents pixels, notamment en fonction de l'énergie et du taux de comptage.

Pour ce dernier étage de la chaîne de mesure, différents algorithmes aux performances et complexités variables existent dans la littérature et il conviendra d'en faire une étude comparative poussée afin, non seulement, d'avoir un regard plus juste sur les performances atteignables par certains pixels, mais également de prévoir en amont le niveau de raffinement nécessaire à la bonne tenue des spécifications scientifiques. Cela pourrait en effet avoir un impact lourd notamment sur les besoins de calibration de l'instrument ainsi que sur la puissance de calcul du calculateur embarqué.

Une fois le comportement individuel de chaque type de pixels caractérisé, ces résultats seront utilisés pour la mise en place d'un simulateur scientifique de plus haut niveau capable d'obtenir des observations synthétiques de longue durée de sources complexes représentatives du niveau de détail que pourront caractériser les cubes de données X-IFU. Je m'attarderai notamment sur l'étude d'amas de galaxies dont l'observation est des plus contraignantes et la caractérisation de la turbulence qui a lieu en leur sein, ainsi que sur la reconstruction de profils de température et d'abondance. Ce simulateur sera également utilisé pour analyser des aspects plus techniques de la performance scientifique de cet instrument tels que sa sensibilité aux effets de temps mort et de confusion de sources.

Dans ce manuscrit, je présenterai tout d'abord le contexte scientifique de cette thèse en montrant l'importance de la physique de l'accrétion et notamment autour des étoiles à neutrons pour répondre à certaines des grandes questions de la physique et de l'astrophysique moderne. Je m'attarderai en particulier sur notre connaissance actuelle des deux sondes de l'accrétion que j'ai utilisées au cours de cette thèse que sont les sursauts X et les kHz QPOs. Le chapitre 2 sera consacré à l'analyse des données d'archive de l'instrument PCA que j'ai utilisées pour l'étude de la dynamique des disques d'accrétion autour des étoiles. J'y décrirai les différentes méthodes que j'ai mises en place ainsi que mes principaux résultats. Dans un troisième chapitre, je détaillerai ensuite le fonctionnement de l'instrument X-IFU qui a été au coeur de la plus grande partie de ma thèse, en présentant les différentes composantes déterminant sa performance. Le chapitre 4 présentera la caractérisation de différents types de pixels dans le cadre d'un exercice d'optimisation de la matrice de détecteurs X-IFU, et le chapitre 5 l'étude comparée de différentes techniques de reconstruction des signaux émis par ces pixels. Enfin, je montrerai dans une dernière partie les simulations scientifiques que j'ai menées à l'aide du simulateur End-to-End avant de conclure sur la portée de mes résultats et les perspectives qu'ils ouvrent pour l'étude future de la physique de l'accrétion et la suite du développement du X-IFU.

Foreword

This manuscript presents the summary of the studies I conducted during the three years I spent preparing my PhD at the *Institut de Recherche en Astrophysique et Planétologie* of the *Université Toulouse III*. This thesis has been dedicated to the development of the End-to-End simulator for the *X-ray Integral Field Unit Instrument* (X-IFU) of the European Space Agency mission *Athena*. My work has been mostly organized into two steps: the first part concerned the study of the dynamics of accretion disks around neutron stars which allowed me to familiarize myself with X-ray data analysis techniques, whereas the second focused on the analysis of the high level performance of the X-IFU through the implementation and perfecting of an End-to-End simulator.

Accretion phenomena are present in the Universe at very different scales, from protoplanetary disks to active galactic nuclei. In X-ray astronomy, accretion is a major subject as it is the power source of the large majority of the sources detected at this date. Its traces can be observed in X-rays when it occurs around black holes or neutron stars, whose density is larger than nuclear matter. The accretion disks forming around these objects reach temperatures of several million degrees. The resulting X-ray emission originates from the innermost parts of these systems whose dynamics must be described by strong field general relativity. This makes them laboratories of choice for the study of key questions of modern physics and astrophysics such as: *What is the stable state of matter at supra-nuclear densities? Must general relativity be modified to describe mechanics under strong field? What drives the mechanisms of the supernovae giving birth to these objects? And finally, what is their role and evolution in the formation of the large scale structures of the Universe?*

Since the historical detection of the first black hole in Cygnus X-A in 1965, numerous observations have confirmed the universal character of the geometry of accreting systems, regardless of them having in their centre a neutron star or a supermassive black hole. By studying the dynamics of accretion disks around neutron stars, it is therefore a much larger question that we wish to address. Despite the strong similarities with black hole systems, it cannot be denied that the presence of a physical surface in the case of neutron stars will modify the flow of matter in the innermost parts of the disk. If this can be viewed as a complexification with respect to the "purer" black hole case, this particularity also offers to use a different angle to look at the question of accretion physics. In this thesis, I thus decided to focus on two probes, specific to neutron star binaries, which are X-ray bursts and kHz quasiperiodic oscillations (kHz QPOs).

X-ray bursts are the result of the accumulation of matter at the surface of the neutron star giving birth to a sudden and bright thermonuclear explosion releasing a large amount of energy, larger than the binding energy of the innermost parts of the accretion disk. kHz QPOs are very coherent oscillations of the binary X-ray emission at frequencies commensurable with the orbital frequency at the inner edge of the disk and it is commonly accepted that they are produced at the heart of these systems. It thus seems interesting to combine these two signals and study the reaction of the QPOs to X-ray bursts, which I will present in a first study. kHz QPOs in themselves are a unique probe of the geometry of neutron star X-ray binaries as they bring into play not only the accretion disk, but also the hot electron layer responsible for the high energy radiation. Understanding the mechanism at the origin of their emission could therefore allow to strongly constrain the physics of these systems. It was in that perspective that I then applied to these signals innovative data analysis techniques which use simultaneously the spectral and timing information inherently contained in X-ray data. The detection

and characterization of QPOs require a dedicated instrumentation capable of observing very bright sources with a fine timing resolution. I thus used for these two studies the archives of the *Proportional Counter Array* instrument (PCA) of the *Rossi X-ray Timing Explorer* satellite (RXTE). Whereas numerous authors continue to analyze datasets from previous missions like RXTE to study accretion physics, this topic will also be central for the X-ray astronomy of the next decade, and *Athena* will not be an exception. This mission will notably allow to study in detail the fast outflows emitted by accreting compact objects as well as their influence on their host galaxy/cluster. Of course, as a true observatory, *Athena* will address a larger panel of scientific problematics and will try to answer to two fondamental questions: *How does ordinary matter assemble into the large-scale structures we see today? How do black holes grow and shape the Universe?* To do so, this mission will have as one of its payload instruments the X-IFU.

The X-IFU is an X-ray microcalorimeter that will provide spectro-imaging capability across a five arcminutes field of view with a revolutionary 2.5 eV energy resolution. This cryogenic instrument will rely on a matrix of nearly 4000 pixels operated below 100 mK, consisting in bilayer absorbers read out by very sensitive "Transition Edge Sensor" thermometers (TES). Following the thermalization of an X-ray photon in one of the absorbers, the resulting temperature rise will be measured by a TES voltage biased in its transition between the superconducting and normal states whose resistance and current will thus be modified. This current change will then be analyzed by a sophisticated readout chain featuring a frequency domain multiplexing scheme, an active feedback loop and at its end an onboard Event Processor (EP) responsible for the extraction of the time and energy of each photon from the raw signals. In order to analyze the high level performance of this complex instrument, it is necessary to take into account in a representative fashion all of these various components. This is the aim of the End-to-End simulator SIXTE (Simulation of X-ray Telescopes) to which development I strongly participated during the second part of my thesis.

SIXTE is thought as a complete representation of the process leading to an X-ray scientific observation: from a catalog of sources defined by their position, spectrum, spatial extent, etc., various modules will simulate the photon emission from the sources, the imaging by the telescope and the detection in the instrument. It is on this last stage, specific to the X-IFU, that most of my work will be focused and notably on the implementation of hybrid detection planes featuring a small pixel array dedicated to high count rate observations and a large pixel array for fainter extended sources. These pixels have different properties in terms of composition, rapidity and characteristics of their superconducting transition. The comparative evaluation of the performance of these detectors will thus require the use of representative TES simulations taking into account their non-linearity as well as the precise study of the energy reconstruction step to evaluate the final energy resolution of the different pixels, notably as a function of energy and count rate.

For this last stage of the detection chain, several algorithms exist in the literature with varying complexity. In order to have an accurate estimate of the performance achievable by certain pixels, but also to predict the level of refinement necessary to reach the scientific requirements, a thorough comparative study of these methods should be conducted. This could indeed have a significant impact on the computational power to install in the EP.

Once the behavior of individual pixels characterized, these results will be used to implement a higher level scientific simulator capable of producing long exposure observations of complex astrophysical sources. I will notably have a look at the study of galaxy clusters, which is one of the most constraining science cases, in particular at the observation of turbulence and at the reconstruction of abundance and temperature profiles. This simulator will also be used to analyze more technical aspects of the X-IFU scientific performance such as its sensibility to dead time effects and source

confusion.

In this manuscript, I will first present the astrophysical context of my thesis by showing the importance of accretion physics and notably around neutron stars in the modern scientific landscape. I will describe in particular our current knowledge of the two probes of accretion I used, which are X-ray bursts and kHz QPOs. Chapter 2 will be dedicated to the data analyses I performed with the archival data of the PCA, showing the different methods I implemented as well as the main results I obtained. In a third part, I will then detail the functioning of the X-IFU instrument which has been the focus of the majority of my thesis, with the main components driving its performance. Chapter 4 will present the characterization of different pixel types I performed in the frame of a TES array optimization exercise and chapter 5 the comparative study of various reconstruction techniques of the raw signal generated by these detectors. Finally, I will show the scientific simulations I conducted with the End-to-End simulator before concluding on the impact of my results and the prospects they open for the future study of accretion physics and the ongoing development of the X-IFU.

Chapter 1: Astrophysical context: accreting compact objects

1.1 Why do we study accreting compact objects?

The existence of neutron stars and black holes was first postulated at the beginning of the last century and, for many years, these objects mainly stayed of theoretical interest. It was not until the first radio pulsar was detected by Hewish et al. (1968) that the existence of neutron stars was confirmed. For black holes, if the hypothesis that the radiation of active galactic nuclei (AGNs) was powered by supermassive black holes was made around the same years (Lynden-Bell, 1969; Salpeter, 1964), it was only with the detection of Cyg X-1 that the consensus gradually shifted from the possibility of existence of these objects to an accepted fact. The situation has now largely changed and more than 2500 neutron stars have been cataloged[1] whereas several tens of thousand AGNs and thus supermassive black holes have been identified (Kauffmann et al., 2003). In our own galaxy, we count more than 100 stellar mass black holes (Corral-Santana et al., 2016).

Compact objects are known to be the end point of the evolution of massive stars: over the course of its lifetime, a star will accumulate in its central layers heavier and heavier elements through fusion and release energy to sustain the gravitational contraction. This process will continue until the formation of an iron core, ^{55}Fe being the most stable element in the sense that the fusion of heavier atomic nuclei requires energy. For massive stars ($M \gtrsim 8M_\odot$), this core will eventually exceed the Chandrasekhar limit and collapse into a neutron star or a stellar mass black hole ($M \gtrsim 20M_\odot$) after a type II supernova (Woosley et al., 2002). Alternatively, type Ia supernovae are thought to originate from accreting white dwarfs going over the same limit to turn into a neutron star (see e.g. van den Heuvel et al., 1992).

If the majority of the neutron stars have been identified from pulsars, a significant part of them and many black holes (in fact all of them until the recent detection of gravitational waves Abbott et al., 2016b), are actually being detected from the accretion of matter. The large energy release coming with it leads to the heating of the falling gas to millions of degrees and creates proficient X-ray emission (Frank et al., 2002). As I will present in the next sections, this makes them perfect laboratories to study core physics questions such as the behavior of matter under strong gravity conditions (Sect. 1.1.2) or the interiors of the densest objects of the Universe (Sect. 1.1.1), but also for astrophysics in general (Sect. 1.1.3).

[1] http://www.atnf.csiro.au/research/pulsar/psrcat/

1.1.1 Cold dense matter

Very high instantaneous densities are reached at high temperatures by ground-based particle accelerators like the *Large Hadron Collider*. In turn, neutron stars are stable objects of macroscopic size featuring in their center densities higher than nuclear material by several amounts. This makes them targets of choice for the study of matter in these extreme conditions and their composition has been a matter of debate for the past four decades. Several models have been proposed ranging from a mix of mostly neutrons and protons to strange quark matter, corresponding to different equations of state for cold dense matter (see Lattimer, 2012, for a review). Conveniently, these can be folded to give large scale observational constraints in the form of a mass versus radius relation (see Fig. 1.1) to be tested against the distribution of the measured parameters from astrophysical sources.

Whereas the obtention of a neutron star mass is relatively straightforward when it is located in a binary system using the orbital properties of the system[2], any measurement of its radius currently relies on indirect methods subject to large systematic uncertainties and offers less constraints on the neutron star equation of state (see e.g. Miller, 2013). For many years, the distribution of neutron star masses was clustered around 1–1.4 $M_\odot$ (Lattimer, 2012) and thus consistent with all proposed models. Relatively recent precise mass measurements from two pulsar-white dwarf binaries however confirmed the possibility of masses up to $\sim 2\,M_\odot$(Demorest et al., 2010; Antoniadis et al., 2013)[3] which are already tight constraints for some strange quark matter neutron star models. New neutron star radius and mass measurements, notably at higher masses, are therefore key to our understanding of matter in the cold dense state, but also for our comprehension of the formation of black holes as the maximal neutron star mass represents the limit at which an object evolves either into a neutron star or a black hole. Without relying on the chance detection of a favorable binary system, this could well be done from the study of matter orbiting these objects, notably in accretion disks.

1.1.2 Strong field general relativity

Since the historical solar eclipse expedition, general relativity has been verified in all attempted experiments with stunning precision (the local Lorentz invariance principle has, for instance, been verified down to one part in 10^{20}! See Will (2014) for a recent review on general relativity tests). All of them were however performed under weak field conditions, in the sense that neither the gravitational potential $\epsilon = GM/rc$ nor the space curvature $\xi = GM/r^3c^2$ were large (considering an object at distance r from an object of mass M). Apart from the natural scientific approach of testing a theory in all its aspects, one could question why one would like to verify general relativity particularly in the strong field regime. First, Einstein's theory is not the sole theory that would verify all the observed phenomenons in the weak field regime (see Psaltis, 2008, and references therein). The main reason for this is however that it is actually expected to break down for strong fields: for instance, the gravitational contraction of a very massive object is expected to give birth to a black hole in the shape of a perfect mass and curvature singularity, but it is largely accepted that quantum gravity would prevent the realization of such an unphysical situation (Psaltis, 2008). In this context, neutron stars and stellar mass black holes offer the possibility to test general relativity with a gravitational potential

[2]Direct mass estimates from isolated neutron stars could also be made from micro-lensing (see e.g. Dai et al., 2015).

[3]Previous detections of potentially massive pulsars had already been made (see e.g. Freire et al., 2008a,b) but in these cases, the unknown system inclination did not allow to draw a definite conclusion. These mass measurements indeed rely on orbital Doppler shifts of the pulsar periods which depend not only on the masses of the two objects in the system, but also on its inclination.

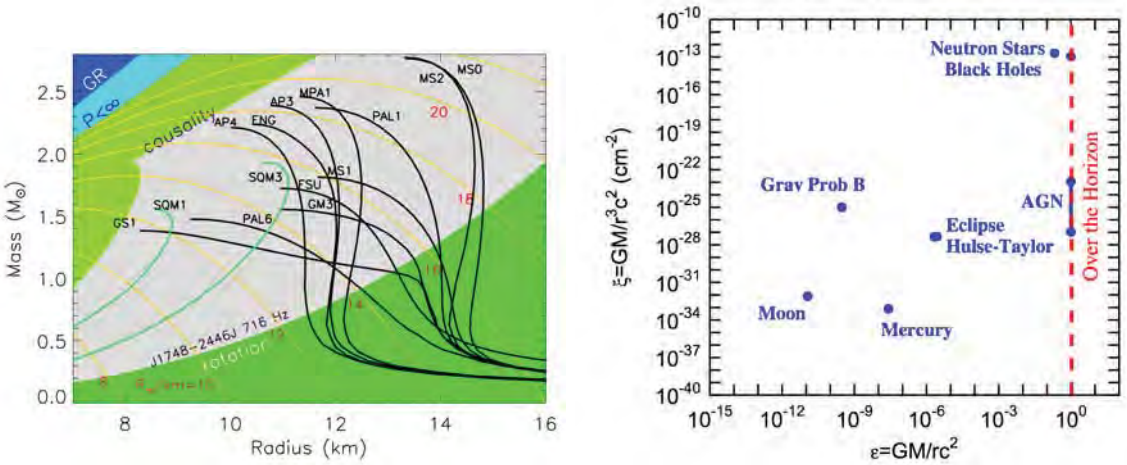

Figure 1.1: Left: Hadronic (black curves) and strange quark (green) mass versus radius relations derived from various possible neutron star equation of states. The different regions depict excluded parts from the requirement of the neutron star not being a black hole (GR), not having infinite pressure at the center of the object, having a sound speed below the speed of light, as well as the constraint from the fastest observed rotating neutron. Figure taken from Lattimer (2012) **Right:** Realized and potential general relativity tests as a function of the probed gravitational potential (x axis) and space curvature (y axis). "Moon" and "Mercury" correspond to the measure of the advance of these object periastron, "Eclipse" to the historical 1919 verification, Hulse-Taylor to the pulsar binary discovered by Hulse & Taylor (1975) which lead to the 1993 Nobel Prize and "Grav Probe B" to the parameter space probed by this NASA mission. Figure taken from (Psaltis, 2008).

and a curvature respectively more than 5 and 10 orders of magnitude higher than any experiment performed in the Solar System (see Fig. 1.1, right, for a comparison).

A very recent and spectacular example of such a verification was made from two direct detections of gravitational waves by the *Laser Interferometer Gravitational-Wave Observatory*: GW150914 (Abbott et al., 2016b) and GW151226 (Abbott et al., 2016a). These consisted in the observation through gravitational waves of the circling down movement of two pairs of black holes which finally merged into single more massive black holes while releasing a large quantity of energy. Apart from being the first observational evidence of the existence of double black hole binaries, the measured signals were found compatible with general relativity and constitute, to date, the most direct verification of Einstein's predictions in the strong field regime.

On top of fundamental physics tests, studying the behavior of matter accreting onto compact objects also offers the possibility to study magneto-hydrodynamics (MHD) and plasma physics under relativistic conditions. This notably includes the understanding of how matter transfers from accretion disks onto the jets observed in a wide range of objects, from protostellar systems up to the supermassive black holes at the center of AGNs.

1.1.3 Astrophysics

Core collapse physics

As the remnants of massive star core collapses, neutron stars and black holes are also essential probes for the collapse and explosion mechanisms that give birth to them in supernovae. Apart from their mass and radius (when defined), their spin and magnetic field can, for instance, give us hints on

off-center kicks (Spruit & Phinney, 1998) or on the dynamo action (Thompson & Duncan, 1993) happening during the collapse. Whereas the spin of neutron stars get largely affected by the accretion of new material in a binary and by magnetic braking when isolated, it is usually believed that thanks to their higher mass, black holes in binaries (BHB) have a spin and mass that have been at most marginally affected by accretion, and are thus representative of birth conditions (King & Kolb, 1999).

The evolution of compact objects

Studying the properties of a large population of black holes and neutron stars inform us on the dynamics and history of the medium in which they evolved. Millisecond pulsars, which are thought to be spun up by the accretion from a companion star, are for instance more frequent in dense stellar systems. This is thought to be due to more frequent encounters with other stars allowing them to acquire companions that will later donate mass. Similarly, the recent detection of stellar-mass black holes in globular clusters led to a revision of the dynamics of these clusters (see e.g. Morscher et al., 2013). In the case of supermassive black holes, the distribution of spins is also a way to constrain the unsolved problem of how these objects arise from their initial stellar mass version, a key element in the understanding of the formation of large scale structures: if this results from mergers, one would expect relatively low spins as the random sum of angular momenta in different directions has no reason to be constructive, whereas if they are created from the steady accretion of surrounding gas, higher spins would be expected due to spin-up mechanisms (see Miller & Miller, 2015, and references therein). The last years have seen the growing success of spin measurements from the disk reflection component observed in both BHBs and AGNs (see Miller & Miller, 2015, for a review). This even lead to the early preference of the sustained accretion scenario which matched the nearly maximal spin values observed from most AGNs (see e.g. Reis et al., 2014). Several authors however suggest caution in such interpretations as there is a significant selection effect from the fact that fast spinning black holes have a high luminosity (Fabian, 2016; Reynolds, 2016).

AGN feedback

Supermassive black holes are thought to play a key role in the formation and evolution of galaxy and galaxy clusters through feedback mechanisms which are though to be divided into two modes depending on the state of the AGN: the radiative and kinetic feedbacks (Fabian, 2012).

The former is thought to happen during the high accretion rate and luminous phase of the supermassive black hole, when high velocity winds are created: the outflows created by the strong radiative pressure will remove gas from the central parts of the host galaxy, delay its growth and quench star formation. Evidence for such large outflows is already clear and Sturm et al. (2011) notably measured up to $1200\,M_\odot$/year depletion in AGN dominated ultraluminous infrared galaxies, enough to remove all the galaxy's gas in only $10^6 - 10^8$ years. This would explain why we observe the peak of the more luminous AGNs before the fainter ones (see e.g. Barger et al., 2005), in a contradicting order to what the usual hierarchical vue of the evolution of the Universe would predict: when the black hole has reached a critical mass, the winds will prevent it from growing further by expelling its fuel, eventually terminating its activity (see e.g. Springel et al., 2005). There is also weak evidence that radiative AGN feedback might actually be responsible for the observed $M_{\rm BH} - \sigma$ relation (Gültekin et al., 2009; Fabian, 2012).

Kinetic feedback is in turn invoked for explaining the delayed cooling of large galaxy clusters. Evolution models incorporating only gravitational heating and radiative cooling would indeed produce

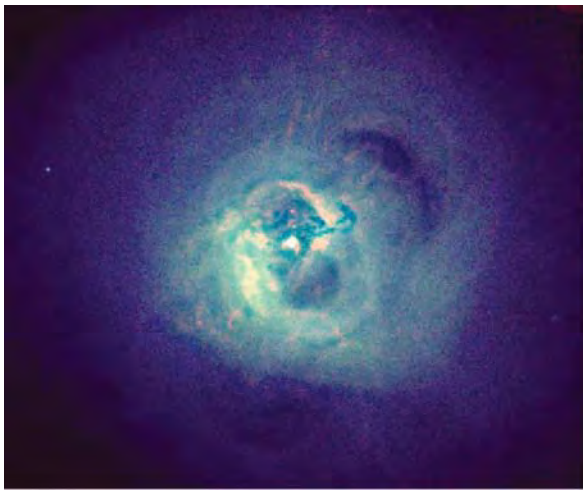

Figure 1.2: *Chandra* image of the Perseus cluster colored is false colors (red: 0.3–1.2 keV, green: 1.2–2 keV, blue: 2–7 keV, Fabian et al., 2006). The shocks and bubbles created by the AGN activity are clearly visible.

too much cold gas and star formation (Balogh et al., 2001), such that another energy source needs to be added to reproduce the observations. The general consensus is now that this is due to the action of AGNs, notably through powerful jets when they are in a low accretion rate regime (see McNamara & Nulsen, 2012, for a review). The idea of such an action actually dates back to the seventies when Gull & Northover (1973) proposed a model for the formation of bubbles in clusters of galaxies, which are now routinely observed thanks to the *Chandra X-ray Observatory* (see Fig. 1.2, for the example of the Perseus cluster). During the birth of each of these bubbles, intense sound waves are created and these will heat the intracluster gas (Fabian et al., 2005).

Understanding how such ejecta and radiation are produced from the study of different accreting compact objects therefore largely overtakes the field of compact objects science.

1.2 A general view of accretion onto compact objects

1.2.1 The most powerful engine: from accretion to X-rays

The extraction of energy from accreting material is known to power a wide range of astrophysical systems, from cataclysmic variables to AGNs. When happening onto compact objects, it is actually the most efficient mechanism known today to obtain energy from a given mass, more for instance than nuclear reactions. If all the potential energy of the falling matter is released in the form of radiation at a distance R of a central object of mass M, it yields to a luminosity of:

$$L_{\rm acc} = \frac{GM\dot{M}}{R} \tag{1.1}$$

which amounts to $\sim 10^{36}$ ergs/s for a standard neutron star ($M \sim 1.4 M_\odot$, $R \sim 15\,$km) accreting a typical $\dot{M} = 10^{16}\,$g/s (Frank et al., 2002). By looking at the corresponding blackbody temperature that would be needed to radiate this from the whole neutron star surface $T \sim 1\,$keV, we quickly see that this will lead to the observed emission in X-rays.

Of course, as a neutron star has a physical surface, there is reason to believe that a significant part of the released energy will indeed be in the form of radiation. For a black hole however, in the

absence of a physical boundary, it is unclear whether the bulk of the energy will actually be released before the matter reaches the event horizon and no luminosity can escape. In astrophysical systems, the overall efficiency of the accretion is usually considered to be $\eta \sim 0.1$ (Frank et al., 2002). This efficiency can however go up to 3 times higher in the case of a maximally spinning black hole (see e.g. Vasudevan et al., 2016).

At very large accretion rates, the radiative pressure generated by the accretion luminosity will eventually overtake the gravitational attraction and prevent the infall of additional matter. This situation is called the Eddington limit. If we consider the steady spherical infall of fully ionized hydrogen, this maximal luminosity amounts to:

$$L_{\mathrm{Edd}} = \frac{4\pi G M m_p c}{\sigma_T} \tag{1.2}$$

where m_p is the proton mass and σ_T is the Thomson cross section. If we take again the example of a $1.4\,M_\odot$ neutron star, $L_{\mathrm{Edd}} \sim 10^{38}$ ergs/s. For the objects whose luminosity is only powered by accretion, one would expect not to detect any source with a luminosity above this limit. In practice, because the accretion is rarely spherical symmetric, a significant part of the luminosity is likely to miss the accretion flow, and this L_{Edd} can be surpassed by some amounts. Even if the Eddington luminosity is not a strong limit in itself, it usually serves as a useful scaling to classify different types of accretion: in the case of disk accretion, authors have thus found evidence that radiative efficiency is achieved above $L/L_{\mathrm{Edd}} \sim 10^{-3}$ (see e.g. Reynolds & Miller, 2013), below which point accretion is expected to occur through radiatively inefficient flows or advection dominated flows (Blandford & Begelman, 1999; Narayan & Yi, 1994). In this picture, growing quasars at the center of clusters are especially interesting targets as they may be transitioning from a radiatively efficient to inefficient AGN, i.e. quasar mode to radio mode (Narayan & McClintock, 2008). At higher rates, the thin disk geometry is expected to break down for $L/L_{\mathrm{Edd}} \gtrsim 0.3$ while at super Eddington rates other mechanisms such as coupling of the disk with the magnetic field would be needed (Basko & Sunyaev, 1976).

1.2.2 The common geometry of accreting compact objects

Whereas mass accretion can take many forms like the transfer of matter through the wind of a massive companion star, or through spherical Bondi accretion (Bondi, 1952), for most objects, the accretion happens through the presence of an accretion disk. This is the case of low mass X-ray binaries (LMXBs) where mass is transferred from a companion donor of mass $M \lesssim M_\odot$ through Roche Lobe overflow (Frank et al., 2002), but also of AGNs. Surprisingly enough, whereas these objects are separated by several orders of magnitude in mass, they actually feature very similar geometries and X-ray emissions. Figure 1.3 shows a generic representation of an accreting compact system with the main components relevant for its X-ray emission which will be described in the following section.

The disk emission

The framework for this unification was first started thanks to the pioneering work of Shakura & Sunyaev (1973). It consists of a model for geometrically thin and optically thick accretion disks inside which angular momentum transfer due to viscosity is parametrized by a dimensionless α parameter, which potentially allows the description of disks in different configurations. This disk is also believed to reach down to an inner radius R_{in} at which there is zero stress. The natural candidate for this is the inner most stable circular orbit (ISCO) below which simple mechanics arguments under general relativity predict that matter will naturally fall towards the hole/neutron star. There is now

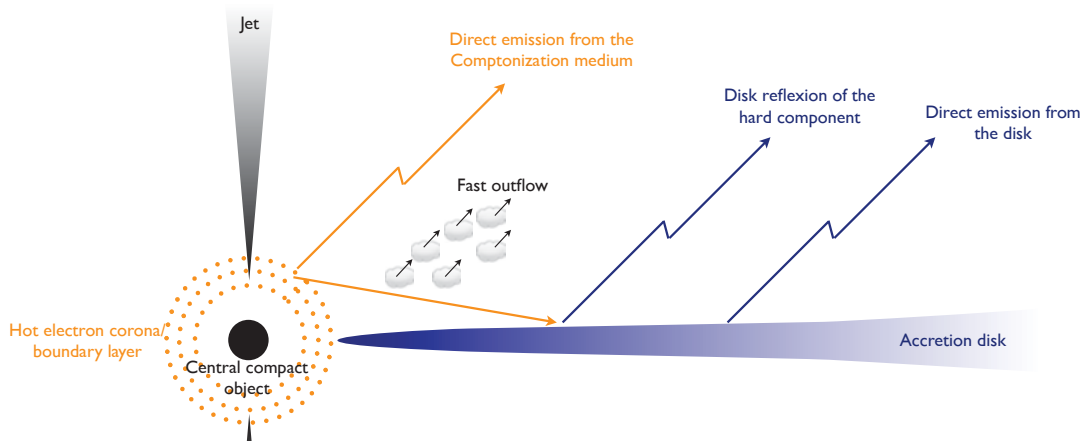

Figure 1.3: Schematic view of the common geometry and emission of accreting compact objects. It features a direct disk emission, a hard component through Comptonization of thermal photons by a plasma of hot electrons, either in a corona or boundary layer, and the reflexion of this component by the disk. On top of these X-ray radiations, evidence of a jet or of fast winds are seen in a number of objects.

observational evidence supporting the idea that this inner radius is indeed stable up to relatively large Eddington ratios ($L/L_{\rm Edd}$, Rykoff et al., 2007; Steiner et al., 2010) and the detection of high frequency oscillations in neutron stars LMXBs do match the frequency and properties of what would be expected from the ISCO (see Section 1.3.2 and Miller et al., 1998; Barret et al., 2005, 2006, 2007) even if it remains a matter of discussion whether the ISCO is responsible for the observed behavior (Méndez, 2006). Recent long term simulations also support the idea of the ISCO limit even though it is not currently possible to simulate at the same time all the details of the accretion flow including small scale turbulence effects (Penna et al., 2010).

For such a disk, the X-ray emission is believed to be a combination of blackbody spectra from the different temperatures of the disk at different radii down to the ISCO, below which the rapidly falling matter becomes optically thin and does not contribute (Reynolds & Begelman, 1997). Because of the scaling of energy release as a function of radius (see Eq. 1.1), this radiation is dominated by the most inner parts of the system. In the case of a maximally spinning black hole, 50 % of the emission indeed originates from the first 5 gravitational radii (Thorne, 1974). Overall, this matches well the thermal emission observed from both AGNs and LMXBs even if some caution is required before interpreting the observed temperatures as the actual temperature of the disk and not as an effective one (Davis et al., 2005). Micro-lensing observations have also shown that there could be minute deviations from the assumed thin geometry in some quasars (see e.g. Rauch & Blandford, 1991; Dai et al., 2010).

Comptonization

These systems also all feature in their central region a hot, compact and optically thin region emitting X-rays from thermal Comptonization of the accretion disk emission. In the case of black holes, this is thought to originate from a corona of hot electrons located some gravitational radii above the black hole (Haardt & Maraschi, 1991). The exact geometry and powering process of this corona is still a matter of dispute and we do not know whether it consists in a slab, a sphere, patches or even the base of relativistic jets. Key observations with NuStar are however being made allowing the routine detection of the high-energy cut-off of this component which confirmed, in the case of black holes, the

compact size of this region (10-100 r_g) as well as the key role of pair production in its physics (Fabian et al., 2015). For the neutron stars, whereas the corona model cannot be excluded, many authors suggest that Comptonization rather happens in the necessary boundary/spreading layer linking the accretion disk to the surface of the compact object (Inogamov & Sunyaev, 2010).

Whereas this Comptonization layer is thought to be present in all neutron star/black hole accreting system, in the case of AGNs, depending on the inclination of the galaxy, it can be buried behind a thick obscuring medium (Seyfert galaxies).

Reflexion component

In X-rays, the last steady component arises from the reprocessing of this hard emission by the accretion disk. Through the competition between photo-electrical absorption and Compton electron scattering, this results in the emission of three major components (see Fig. 1.3, right, and Fabian, 2016). Above a few tens of keV, scattering dominates and this results in the emission of a broad Compton hump, while at lower energies, the cross section of the photoelectrical absorption is higher creating a low energy cutoff. The most striking feature is however a luminous iron K α emission line. Other emission lines are emitted in softer X-rays populating the "soft excess" but through a combination of high abundance and fluorescence yield, iron emission is dominant. As emphasized in Figure 1.4, this whole reflexion emission is then broadened by Doppler shift from the rotating accretion disk and gravitational redshift (Laor, 1991; Fabian et al., 2009). A key element of this broadening is that it depends on the actual geometry of the system, and notably on the spin of the compact object (García et al., 2011, 2013).

The last years have seen a growing success of the study of reflexion in AGNs and BHBs. Using self consistent reflexion models (García et al., 2011, 2013), a large number of black hole spins have notably been measured from broad iron lines (see Miller & Miller, 2015, for a review) and now full reflection spectra with *NuStar*, including the Compton hump (see e.g. Risaliti et al., 2013; Miller et al., 2013; Marinucci et al., 2014). By combining the timing and spectroscopic information, a complete new field has also been unveiled in the form of X-ray reverberation mapping of accretion disks (see Uttley et al., 2014, for a review). The idea is to take advantage of the high frequency variability originating in the corona and that is being propagated to the reflexion spectrum to measure light propagation time lags between these two components which dominate at different energies[4]. The most striking feature that was thus detected are soft time lags over a large frequency range from the broadened iron line complex clearly identifying the delayed reflexion by the disk of the driving corona variation on time scales of a few gravitational radii (Uttley et al., 2014). By carefully modeling the light propagation in the system in the form of an impulse response function incorporating the delayed reaction of different parts of the accretion disk emitting at different energies (Cackett et al., 2014; Chainakun & Young, 2015; Emmanoulopoulos et al., 2014; Reynolds et al., 1999; Wilkins & Fabian, 2013), this technique allows to literally map the geometry of the accretion disk down to its ISCO. This notably allows a complementary assessment in a less degenerated way of the disk structure to the usual spectroscopic methods.

Outflows

Whereas it is not observed directly in X-rays in the majority of the accreting systems, a comprehensive understanding of the accretion process onto compact objects will need to close the link between the

[4]We note that this does require careful modeling of dilution effects from the differential contribution of the components as a function of energy (Uttley et al., 2014).

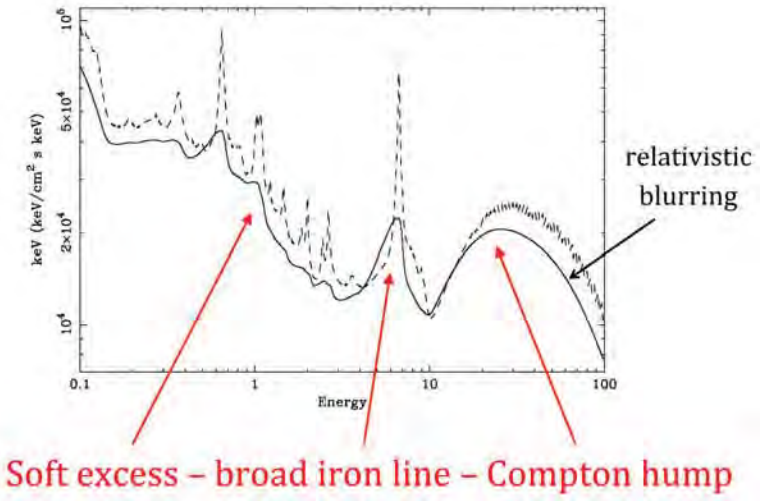

Figure 1.4: The reflection spectrum of an accreting compact object. Usually, three components are identified: a soft excess, a relativistically broadened iron fluorescence line and the Compton hump. The intrinsic emission is represented with a dashed line whereas the solid line presents the observed broadened spectrum. Figure taken from Fabian (2016).

infalling material and the large outflows observed from numerous systems in the form of jets or powerful winds.

In the case of supermassive black holes, large radio jets are for instance thought to be powered far below the Eddington rate through a radiatively inefficient accretion flow in the from a high pressure ionized and geometrically thick disk (see Narayan & McClintock, 2008; Fender, 2016, for reviews). The exact mechanism leading to these large ejections is not yet fully understood and it remains unclear whether the low rate accretion can explain alone the observed released energy in some very powerful AGNs (see e.g. McNamara et al., 2009). Several authors (see McNamara & Nulsen, 2012, and references therein) thus point towards extraction of power from the black hole rotational energy (the rotational energy of a $10^9\,M_\odot$ black hole exceeds 10^{62} ergs). Such a thing would be feasible for instance through the Penrose-Blandford-Znajek effect (Blandford & Znajek, 1977; Hawley & Krolik, 2006).

Jets are common in neutron star systems as well and have been observed from the radio band to X-rays. In most cases, these jets are thought to be rotationally powered in the sense that the outflows are powered by the neutron star spin down (Miller & Miller, 2015). Coherent pulsations have also been observed in accreting systems where the falling matter is channeled by the neutron star magnetic field onto rotating hot spots (Patruno & Watts, 2012). Whereas much fainter than their rotational powered equivalent, evidence is stacking showing that X-ray binaries may also emit jets, which in this case would be accretion powered (see e.g. Russell et al., 2007), reinforcing the idea that outflows are a key component of neutron star systems.

In the recent years, winds in accreting systems have also emerged as being another important aspect for the comprehension of the accretion flow. These are usually observed as blue shifted absorption lines, typically from iron (see e.g. Blustin et al., 2005; McKernan et al., 2007). Whereas most measured velocities range in the hundred to thousand km/s, evidence from ultra fast outflows have been found in AGNs going up to $0.3\,c$ with high mass fluxes (Tombesi et al., 2010), powerful enough to have a potential impact onto the surrounding cluster (Fabian, 2012). The exact scenario leading to these

fast winds is still under debate and several models have been proposed including radiative pressure (see e.g. Proga & Kallman, 2004; Sim et al., 2010), momentum-driven shocks (King, 2010), and magnetohydrodynamic effects (Fukumura et al., 2010). Similar ejections are also being detected in stellar mass black holes, even if at lower velocities (0.01–0.05 c, e.g. King et al., 2012; Miller et al., 2015) and now in neutron star binaries system too (Miller et al., 2016), adding to the long list of mechanisms bringing together the different kinds of accreting objects, from LMXBs to AGNs.

1.3 Neutron star low-mass X-ray binaries as probes for the physics of accretion

As emphasized in Section 1.1, the study of different types of accreting compact objects provides key insights into a large panel of physics problems. In my thesis, I focused on a particular type of accreting system which are neutron star LMXBs. Apart from the simple fact that they are another category of accreting systems, the presence of a neutron star instead of a black hole as the central object enables different conditions to be explored. In the special case of accreting pulsars, the presence of jets for instance allows the direct measurement of the spin and thus of one of the key characteristics of space time in the inner parts of the disks. As will be seen later, this can also be obtained from the oscillations observed in thermonuclear X-ray bursts (see Sect. 1.3.1). With a radius estimated in the 10–15 km range, neutron stars also have an interesting relationship with their ISCO radius which amounts to $\sim$ 12 km for a 1.4 $M_\odot$ star, offering the possibility to observe different disk-neutron star interaction regimes with cases for which the disk is truncated at the ISCO and others for which the accretion flow smoothly merges with the surface. The presence of significant magnetic field likely to channel part of the infalling matter further constitutes an interesting laboratory for MHD and plasma physics in both strong magnetic and gravitational fields. Of course, the neutron star surface and magnetic field in turn make more complex the modeling of such systems compared to black hole ones which could be considered as purer and insights from BHB and AGNs are therefore essential in order to try to disentangle the convoluted effects observed in neutron star LMXBs.

In this thesis, I used two different types of probes to investigate the physics of these accretion disks which I will now present in the following sections.

1.3.1 Type I X-ray bursts

Type I X-ray bursts correspond to the thermo-nuclear runaway burning through the CNO cycle of a helium and/or hydrogen layer accumulated from accretion at the surface of the neutron star. At the first order, the exact composition of the burned material depends on the accretion rate of the system (Galloway et al., 2008): at low accretion rates, it principally consists on the unstable burning of hydrogen, whereas at higher rates, the hydrogen is steadily burned and the burst is triggered by the unstable fusion of helium.

In the X-ray band, they manifest themselves in the form of a very sudden increase of luminosity followed by an exponential decay. A typical burst features a rise time in the 1–10 s range and decays on 10–100 s time scales (see Fig. 1.5, left, for example light curves). The X-ray emission of the bursts is usually well described by a Planck distribution with a blackbody temperature of a few keV (Galloway et al., 2008). Some deviations from the simple thermal model may have however been identified even if other authors claim that they are due to a local increase of the accretion rate through the Poynting-Robertson effect (Worpel et al., 2013, 2015). In total, type I X-ray bursts release in the system an

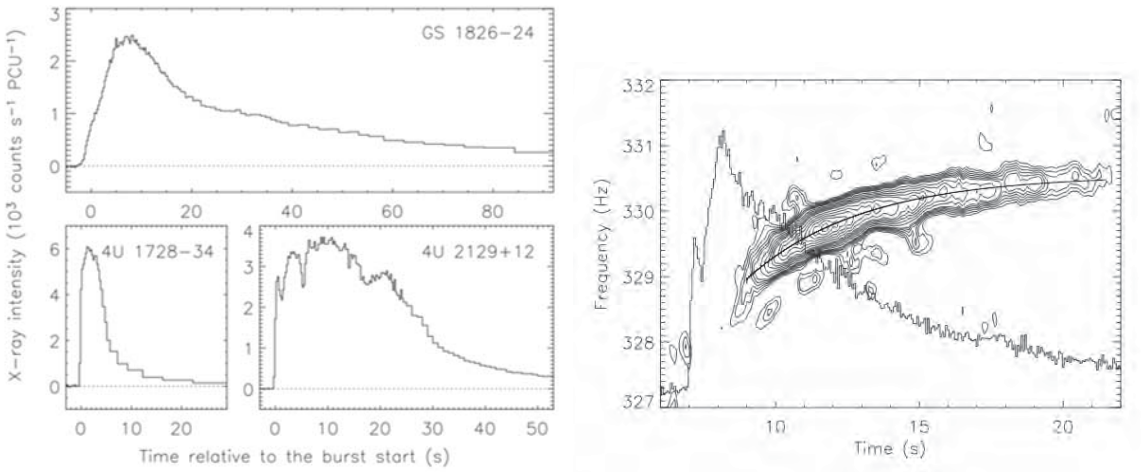

Figure 1.5: Left: Sample type I X-ray burst light curves from three different sources (Galloway et al., 2008). **Right:** Example of a burst oscillation increasing in frequency measured by Strohmayer & Markwardt (1999) in 4U 1702-43.

energy around 10^{37}–10^{38} ergs.

The most luminous X-ray bursts can even temporarily exceed the neutron star Eddington limit (see Sect. 1.2.1). As the radiative pressure thus exceeds the local gravity, this results in the lifting of the external layers of the neutron star atmosphere (Galloway et al., 2008). In this case, we speak of photospheric radius expansion (PRE).

Burst oscillations

The first burst oscillation was observed with the RXTE PCA by Strohmayer et al. (1996). It consists in a coherent oscillation which easily stands out in a dynamical Fourier spectrum (see Fig. 1.5, right). During the initial phases of the X-ray burst, the nuclear burning is localized to a limited part of the neutron star surface and the radiation gets modulated by the neutron star spin frequency. With time, the flame propagates to the whole surface and the oscillation dies away. This interpretation was undoubtedly confirmed by the observation of a burst oscillation in an accreting millisecond pulsar at the same frequency as the pulsations (Chakrabarty et al., 2003; Strohmayer et al., 2003). Usually, a slight increase and settling of the frequency is observed (see Fig. 1.5, right) due to the initial lifting of the emitting region through radiative pressure which initially orbits slower than the star itself. We note that the modeling of these oscillations may offer a proxy to the measurement of the neutron star mass and radius (Artigue et al., 2013; Lo et al., 2013).

Superbursts

Whereas the bulk of type I X-ray bursts are only limited to a few tens of seconds, some particular events called *superbursts* last for several hours. First detected by Cornelisse et al. (2000), these particularly long bursts can emit up to 10^{41}–10^{42} ergs. Unlike the normal type I events, *superbursts* are emitted from the burning of a deeper layer of carbon material (Cumming & Bildsten, 2001; Strohmayer & Brown, 2002) originating either from the ashes of previous explosions or directly from the accreted material (in't Zand, 2011). These *superbursts* are of great interest as they notably give the opportunity to study more precisely the disk reaction to the sudden increase of the central luminosity (see e.g.

Ballantyne & Strohmayer, 2004; Ballantyne & Everett, 2005). In a recent reanalysis of *superburst* from 4U1636-536 observed by RXTE, Keek et al. (2014b) thus found evidence of the mapping of the accretion disk at different radii and ionization states by the burst emission.

1.3.2 kHz quasiperiodic oscillations

A quasiperiodic oscillation (QPO) is a time oscillation of the source luminosity. In a power spectrum, it appears as a broad peak and is characterized by its centroid frequency, width and amplitude, which is often expressed as the RMS fraction of the count rate that is modulated at the QPO frequency. A key parameter of a QPO is also its so-called quality factor, which is defined as the ratio between its frequency and width and corresponds to the number of coherent cycles the QPO can maintain. QPOs are being detected in X-ray binaries in a large variety of states in both neutron star and black hole binaries (see van der Klis, 2006, for a review), but also in AGNs (Gierliński et al., 2008; Alston et al., 2016) even if some caution is required for those last systems (Vaughan et al., 2016). In this thesis, I focused my work on a particular type of QPOs which are kHz QPOs.

Regularly observed in pairs, kHz QPOs are observed in the $\sim$ 400–1200 Hz frequency range in LMXBs whose compact object is a neutron star. From their first detection in Scorpius X-1 by RXTE (see Fig. 1.6, left and van der Klis et al., 1996, for the historical detection), kHz QPOs have triggered a vast interest, mostly owning to the commensurability of their frequency with the orbital frequency in the most inner parts of the binary were strong field general relativity applies (see Sect. 1.1.2). Since then, several models have been put forward to try to explain the origin of both kHz QPOs, including the movement of a mass inhomogeneity in the accretion disk around a spinning neutron star (Miller et al., 1998), relativistic precession at a particular orbit (Stella & Vietri, 1998, 1999), oscillation modes of the accretion disk (see e.g. Kluźniak & Abramowicz, 2005), or internal variations of the heating rate in the Comptonization layer (Lee et al., 2001; Kumar & Misra, 2014, 2016). However, a consensus has yet to be found. That being said, in the twenty years of existence of kHz QPOs in astrophysics, a lot has been learned and I will summarize here their main properties before focusing on the latest developments that were made thanks to spectral timing techniques.

The main properties of kHz QPOs

As mentioned before, kHz QPOs are often detected by pairs and are named lower and upper kHz QPO depending on which QPO has the highest frequency. In most sources, the lower kHz QPO is seen between $\sim$ 500 and $\sim$ 950 Hz and the upper kHz QPO can be detected at frequencies as low as $\sim$ 400 Hz, and up to $\sim$ 1200 Hz (see e.g. Barret et al., 2006; Méndez, 2006). The former has a high quality factor that can go up to 200, whereas the latter is much broader and its quality factor rarely exceeds 30 (see e.g. Berger et al., 1996; Méndez et al., 2001; Barret et al., 2005, 2006; Méndez, 2006). This property is actually the most common method to distinguish between the two oscillations when only one can be detected (see Fig. 1.6, right).

One of the most striking feature of kHz QPOs is probably the tight correlation of their frequency with the state of the observed source (Méndez et al., 1999; Di Salvo et al., 2001), as well as, in a weaker sense, with the source count rate (so-called parallel tracks, van der Klis, 2000). This in itself shows how these signals are intimately related to the overall properties of the system in which they are emitted and thus have the potential to be precise probes of the changing geometry of LMXBs. In fact, most of the QPO characteristics are found to strongly depend on their frequency, and thus on the source state: the root mean square (RMS) amplitude of the upper kHz QPO steadily decreases

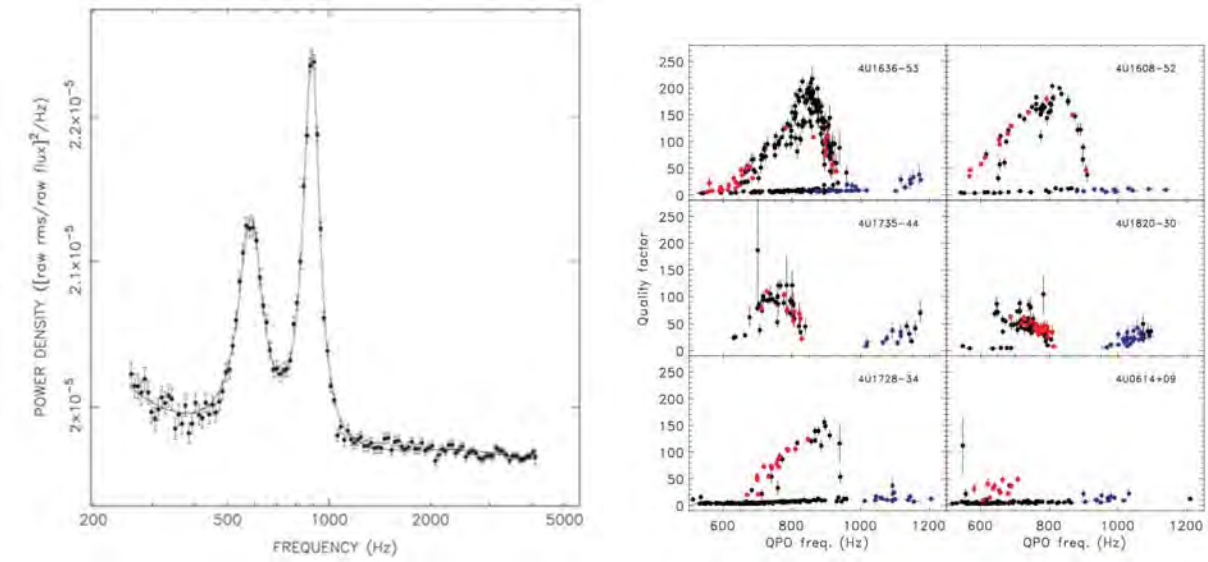

Figure 1.6: Left: Historical detection of the kHz QPO pair by van der Klis et al. (1996) in Scorpius X-1. **Right:** Quality factor versus frequency diagram for a number of kHz QPO sources. Figure taken from Barret et al. (2006).

with frequency, whereas the lower kHz QPO follows a bell-shaped curve (see e.g. Méndez et al., 2001). Similarly, the quality factor of the upper kHz QPO is known to get larger at high frequencies, when for the lower kHz QPO it first smoothly goes up before rapidly falling at large frequencies (see Fig. 1.6, right). This last feature was interpreted by several authors (Miller et al., 1998; Barret et al., 2006, 2007) as being a signature of the ISCO, even if this still remains a matter of dispute (Méndez, 2006).

Finally, the RMS amplitude of both QPOs were found to increase towards high energies (see e.g. Berger et al., 1996; Méndez et al., 2001). This is a very important clue towards the understanding of the origin of these oscillations as this points toward a key role of the Comptonization layer (see Sect. 1.2.2) in the emission process of the QPOs (see e.g. Gilfanov et al., 2003).

Recent developments from spectral timing

The recent success of spectral timing techniques for the study of AGNs (see Sect. 1.2.2) has triggered a renewed interest for the application of these techniques to the study of kHz QPOs. If the first detection of lower kHz QPO soft lags dates back to the early days of RXTE (Kaaret et al., 1999; Vaughan et al., 1998), de Avellar et al. (2013) and Barret (2013) conducted a more thorough analysis using a significant part of this mission archive. They could thus highlight a variation of this soft lag with frequency in 4U1608-522 and 4U1636-536 (see Fig. 1.7, left) and for the upper kHz QPO, de Avellar et al. (2013) reported the detection of a hard lag. The former is possibly due to a changing geometry of the system if these lags were to be interpreted as light travel time and not as a simple consequence of the QPO emission mechanism. A decreasing lag as a function of energy has also been reported by these authors in both sources, with a hint for an iron line reverberation lag in the highest quality data of 4U1608-522 (see Fig. 1.7, right).

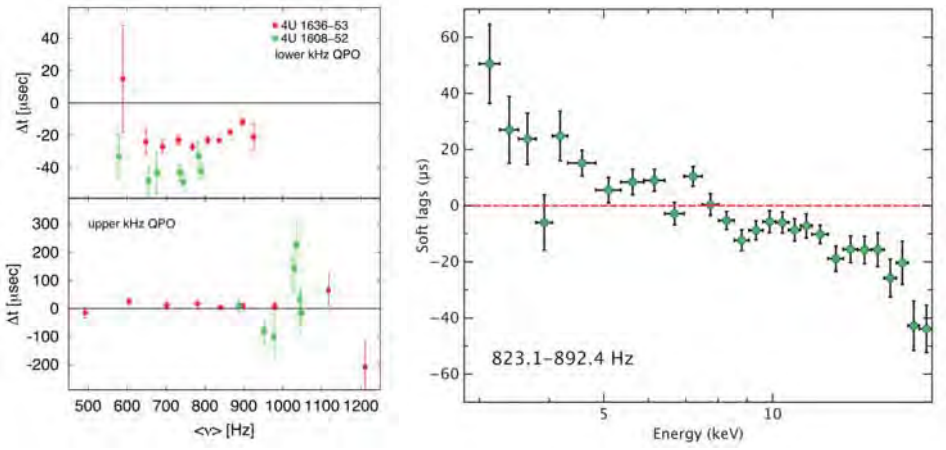

Figure 1.7: Left: Frequency dependent kHz QPO time lags measured by de Avellar et al. (2013) in 4U1608-522 and 4U1636-536. The lower kHz QPO shows a soft lag varying with frequency and the upper kHz QPO a possibly constant hard lag. **Right:** Lag energy spectrum of the best quality lower kHz QPO data set obtained by Barret (2013). We can note a suggestive bump around the iron K-α line energy that may hint towards a reverberation signal.

1.4 From accretion physics to the X-ray Integral Field Unit

The study of accretion onto compact objects can be used to address a large variety of key scientific questions. Present in many objects at very different scales, ranging from LMXBs accreting $\sim 10^{-10} M_{\odot}$/year to AGNs in which several solar masses per year can fall towards the central supermassive black hole, accretion proceeds along a relatively fixed geometry independently of the mass of the compact object. Its mechanisms can thus be studied in many sources, and among them figure neutron star LMXBs which are the main focus of the next chapter.

Without doubt, accretion will be a key aspect for next decade's astrophysics and new instrumentation is expected to bring breakthrough observations in this domain. If a high throughput mission such as the *Large Observatory for X-ray Timing* and its *Large Area Detector* (LOFT LAD; Feroci et al., 2012) could revolutionize timing studies, the future *Athena X-ray observatory* will also bring transformational capabilities by notably allowing the investigation of the geometry of AGNs, and notably the link between the accretion and ejection, up to $z \sim 1$ using spectral timing techniques, as well as spin measurements for objets at $z \sim 2$, but also the detection and characterization of ultra fast outflows in a large variety of objects (Nandra et al., 2013). On the side of the dynamics of galaxy clusters and on the role played by their central accreting AGN, *Hitomi/Soft X-ray Spectrometer* (SXS; Mitsuda et al., 2014) has already shown us a glimpse of what the *X-ray Integral Field Unit* (X-IFU) instrument of this mission should be capable of: from an observation of the Perseus cluster with 230 ksec exposure, the Hitomi Collaboration (2016) has indeed revealed from emission line broadening measurements how little turbulence, contrary to what was expected, is present in the core of the cluster where the AGN inputs a very large amount of energy. The turbulence measurement could even be confirmed from the identification of resonant scattering along the line of sight (Zhuravleva et al., 2013) which shows the exquisite quality of the data they obtained. With its more than one order of magnitude increase in effective area, its doubled energy resolution as well as its spatial resolution of a few arcseconds, there is thus little doubt that the X-IFU will revolutionize the study of galaxy clusters and many other objects as emphasized in Figure 1.8.

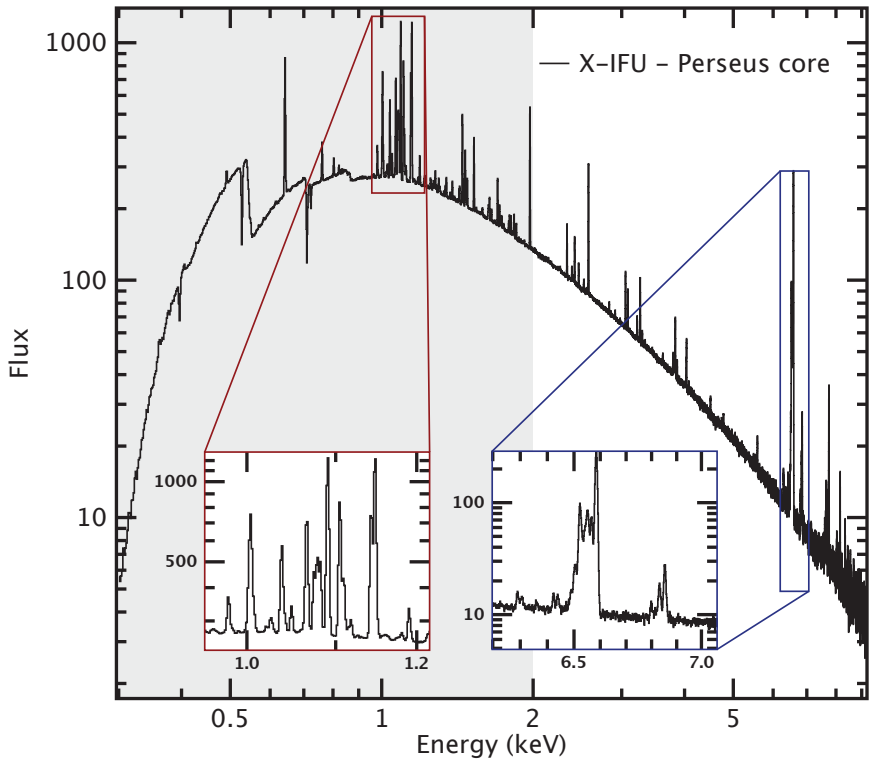

Figure 1.8: Simulation of the spectrum that could be obtained from a 100 ks observation of the core of the Perseus cluster, based on the results of Hitomi Collaboration (2016). The grey area highlights the part of the spectrum not fully explored by *Hitomi/SXS* due to the gate valve being closed during the observation. The wealth of information contained in such a dataset will allow the detailed study of the physics of the hot cluster gas, including the influence by the central accreting AGN. Figure taken from Barret et al. (2016).

Chapter 2: The study of rapid X-ray variability in low-mass X-ray binaries

2.1 The detection and characterization of kHz QPOs in RXTE PCA data

2.1.1 Extracting data from the Proportional Counter Array of the Rossi X-ray Timing Explorer

The Proportional Counter Array of the Rossi X-ray Timing Explorer

Because of their high frequency, only accessible through dedicated timing instruments, most of the kHZ QPO studies have been performed with the *Proportional Counter Array* (PCA, Jahoda et al., 1996) of the *Rossi X-ray Timing Explorer* (RXTE, Bradt et al., 1993) NASA satellite. Launched into low-Earth orbit together with the *High Energy X-ray Timing Experiment* (HEXTE, Gruber et al., 1996) and the *All Sky Monitor* (ASM, Levine et al., 1996) on December 30, 1995, this instrument consisted of five identical Proportional Counter Units (PCUs) working with Xenon gas pressured at 1 atmosphere, adding up to a total effective area of $6500\,\mathrm{cm}^2$. Until its decommissioning on January 5, 2012, it provided X-ray data in the 2–60 keV energy range with an energy resolution better than 18 % at 6 keV and an exquisite time resolution of $\sim 1\,\mu\mathrm{s}$. Due to the high count rate of the observed sources and the instrument timing precision, a high volume of data had to be treated and telemetered, a task which was performed by the *Experiment Data System* (EDS, Bradt et al., 1993).

Throughout the mission lifetime, the number of functioning PCUs varied between observations and due to electric arcs developing in the gas-filled chambers, PCUs were sometimes turned on and off inside a single observation. One of the PCUs was also definitively lost after a few years, such that the best kHz QPO data were obtained during the first observations of the mission. However, in total, the RXTE PCA archive contains several Ms of data of a signal that can be detected on time scales as small as one second.

Extraction of Science Events

The RXTE EDS provided six different data modes during each observation, ranging form a simple low resolution spectrum to time resolved autocorrelation functions. Among those six modes, two were reserved to standard modes constant throughout the mission lifetime (one low resolution mode with 0.1 s time resolution, and one high resolution mode with 16 s time resolution), and the four others could be chosen from a large set by the observer. In this thesis, I restricted my analysis to archive files saved in the so-called *Science Events* mode for which the energy and arrival time of each detected photon were stored. In these files, the energy is coded into discrete channels whose energy ranges vary

with time and with the selected mode.

Before analyzing these datasets, it is necessary to obtain their corresponding instrument response files (RSP). The information in these files is twofold:

- a channel to energy range conversion table
- a so-called response matrix $R(I, E)$ proportional to the probability that an incoming photon of energy E will be detected in channel I, such that for an X-ray source of emission $f(E)$, the count rate in channel I is

$$C(I) = \int_0^\infty f(E)R(I, E)dE \tag{2.1}$$

These files must be computed using the FTOOL `pcarsp` which uses the PCA calibration database as well as the observing conditions to determine the adequate response.

2.1.2 Power spectra and QPO profile reconstruction

The analysis of high frequency variability in X-ray data is usually performed using Fourier techniques and mostly focuses on the study of power spectra (see §2.3 for other more recent techniques).

Computing power spectra

The standard way to compute a power spectrum is to first perform a Discrete Fourier Transform (usually done using the Fast Fourier Transform – FFT – Cooley & Tukey, 1965) on a time binned light curve extracted in a given energy band. From a light curve of duration T with N data points x_k (i.e. with $\delta t = T/N$ time resolution), one thus obtains a discrete Fourier spectrum X_j for N frequencies spaced by $\delta\nu = 1/T$ from 0 up to $(N-1)/T$:

$$X_j = \sum_{k=0}^{N-1} x_k e^{2\pi ijk/N} \text{ for } j = 0, .., N-1 \tag{2.2}$$

The input signal being real, the second half of the spectrum is the conjugate of the first half and the Fourier signal is fully described by the values up to the Nyquist frequency $\nu_{Ny} = \frac{1}{2}N/T$. This frequency represents a limit above which no analysis can be performed. In the case of kHz QPOs, as the upper kHz QPO reaches up to $\sim$1300 Hz and the FFT algorithm has the best performance on data of size equal to a power of two, the adopted time resolution is usually $\delta t = 1/2^{12} \approx 244\,\mu$s or $\delta t = 1/2^{13} \approx 122\,\mu$s (always 244 µs in this work).

The power density spectrum (PDS) is thus defined using the Leahy et al. (1983) normalization:

$$P_j = \frac{2|X_j|^2}{N_\phi} \text{ where } N_\phi \text{ is the total number of photons in the light curve} \tag{2.3}$$

Using Parserval's theorem, the total Leahy power can be related to the fractional root-mean-square (RMS) variance of the signal through:

$$r = \sqrt{\frac{P_{\rm tot}}{N_\phi}} = \sqrt{\frac{\sum_{j=1}^{N/2-1} P_j + 1/2P_{N/2}}{N_\phi}} \tag{2.4}$$

We note that the Leahy et al. (1983) normalization does not have a particular physical meaning but presents several statistical advantages as will be discussed below. Other normalizations are routinely used in the literature, the second most common was introduced by Miyamoto et al. (1992) and gives the power spectrum in units of fractional RMS squared per Hz:

$$P_{\mathrm{rms},j} = \frac{2\delta t}{< x >^2 N} |X_j|^2 \tag{2.5}$$

Finally, one can also express the powers in absolute units squared per Hz, in which case, no scaling by the average count rate is required:

$$P_{\mathrm{abs},j} = \frac{2\delta t}{N} |X_j|^2 \tag{2.6}$$

PDS statistics and QPO detectability

The PDS obtained from the light curve of any astrophysical source not only contains the intrinsic variability of the source but also noise contributions. If one makes the assumption of random and uncorrelated noise, the total observed power spectrum can approximately be separated as $P_j = P_{j,\mathrm{signal}} + P_{j,\mathrm{noise}}$. In the case of X-ray timing, the main noise component is usually Poisson counting noise in which case $P_{j,\mathrm{noise}}$ follows a χ^2 distribution with 2 degrees of freedom (Leahy et al., 1983). The expected signal-free power and standard deviation at all frequencies are therefore:

$$< P_{j,\mathrm{noise}} >= 2 \text{ and } \sigma(P_{j,\mathrm{noise}}) = 2 \tag{2.7}$$

This is true whatever the chosen time resolution and the length of the studied light curve interval. A single PDS is thus extremely noisy and one typically averages a number M of spectra to decrease the standard deviation to $2/\sqrt{M}$ in order to detect a signal. One can also bin the PDS by averaging together W consecutive frequencies and further decrease the fluctuation level by a factor $\sqrt{W}$. When a large number of powers were averaged (in pratice, $MW \geq 64$, Leahy et al., 1983), the χ^2 distribution is close to a Gaussian one and the significance of a given power excess in the averaged spectrum $P_e = P_j - 2$ is:

$$n_\sigma = \frac{P_e \sqrt{MW}}{2} \tag{2.8}$$

The process of detecting an excess in a power spectrum is illustrated in Figure 2.1 (left).

This formula is valid in the case of pure Poisson noise. The PCA however suffers, like all proportional counters, from a so-called dead time process after each detected event during which no subsequent photon can be measured. This phenomenon, dominated at low count rates by the duration of the analogue to digital conversion time, will anti-correlate the signal for all time scales below the dead time value and results in a modification of the power spectrum shape. At high frequencies and for limited dead time fractions such as during typical kHz QPO observations ($\lesssim 3\%$), the Poisson noise level is simply lowered below 2 by a few percents (Zhang et al., 1995). When measuring an excess, it is therefore more accurate to take as reference level the mean value of the power spectrum at very high frequencies ($\sim$1600–2000 Hz) where no significant signal is expected instead of the theoretical value 2.

In practice, to correctly assess whether a certain excess could not have been simply created by noise, it is important to take into account the fact that the QPO signal was looked for in relatively

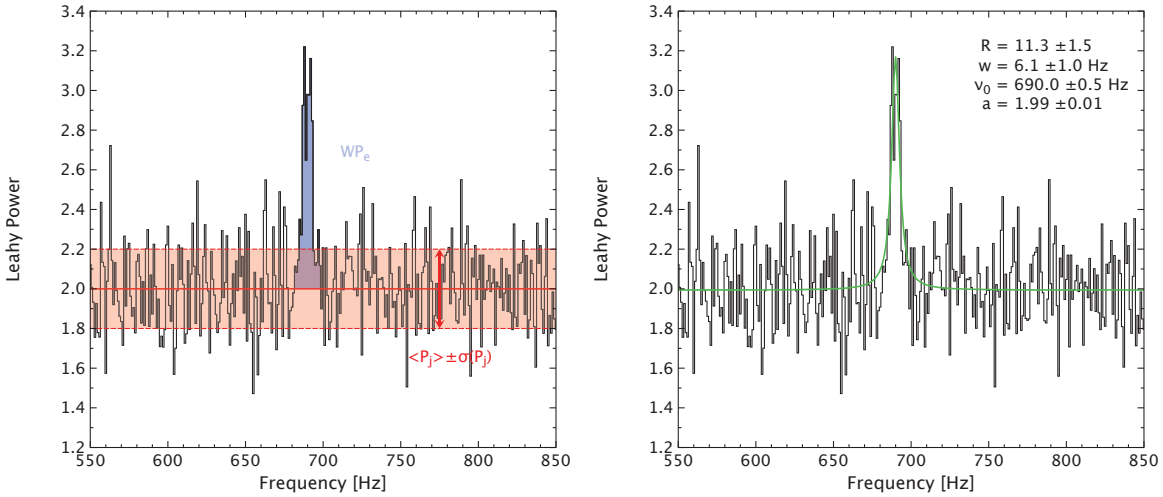

Figure 2.1: Left: Illustration of the detection of an excess in a Leahy normalized PDS resulting for the averaging of 100 elementary 1 s PDS (data extracted from ObsID 30062-02-01-000 between 3 and 30 keV). The red region represents the $\pm 1\sigma$ excursion of single noise powers, while the blue filled region emphasizes the excess due to the QPO. **Right:** Maximum likelihood fit of the same example PDS with a Lorentzian profile.

large frequency band. For a number N_{trials} of tested frequencies, the probability for noise to create at least one excess above a certain significance threshold σ_t (corresponding to a probability P_t) is:

$$P(\text{noise detection}) = 1 - (1 - P_t)^{N_{\text{trials}}} \tag{2.9}$$

When blindly looking for kHz QPOs, it is therefore important to limit the number of trials and take a significance threshold σ_t sufficiently high to have a small enough $P(\text{noise detection})$. In the work presented here, all blind searches were performed with 1 Hz frequency resolution in the 550–1300 Hz band where kHZ QPOs are usually detected and we adopted $\sigma_t = 5.5$ such that $P(\text{noise detection}) < 2 \cdot 10^{-}5$.

Let us now consider the detectability of a QPO signal of fractional RMS r and width w observed during a duration T in a light curve of signal count rate C and background level B. Using equation (2.4), the average expected excess Leahy power over the signal width in a one second power spectrum is:

$$P_e = \left(\frac{C}{C+B} r\right)^2 (C+B) = \frac{C^2}{C+B} r^2 \tag{2.10}$$

Combining this with equation (2.8) thus yields the expected significance of the QPO signal:

$$n_\sigma = \frac{C^2}{C+B} r^2 \sqrt{\frac{T}{w}} \tag{2.11}$$

One sees that the detectability of a QPO scales more or less linearly with the source count rate and quadratically with the RMS value, which is why several next generation timing missions rely on high effective areas at high energies where the RMS value is the biggest (e.g. LOFT, Feroci et al., 2012, ; GRAVITAS, Nandra et al. (2012)). Besides, this formula shows us how the addition of any non-modulated X-ray source will rapidly decrease the expected significance of a signal such as in the case of Type I X-ray bursts as observed in the study presented in §2.2.

Fitting a kHz QPO profile with the maximum likelihood method

Once a kHz QPO signal has been detected in a PDS and deemed significant (see §2.1.2), it is necessary to rely on a fitting procedure in order to extract reliably its characteristics. Usually, the model adopted to do so is the sum of a constant component a to account for Poisson noise (taking into account the dead time modification – see §2.1.2) and a QPO profile modeled by a Lorentzian of widht w, centroid frequency ν_0 and total integrated Leahy power R:

$$S(\nu) = a + \frac{Rw}{2\pi\left[(\nu-\nu_0)^2 + (w/2)^2\right]} \tag{2.12}$$

Whereas in the litterature most authors use a standard χ^2 minimization technique, in this work, we applied the maximum likelihood estimation (MLE) method developed by Barret & Vaughan (2012). Unlike the former, this procedure gives unbiased estimates of the QPO parameters. We note however that for a high number of averaged PDS, both approaches become equivalent.

Let us consider a set of N observed PDS powers P_j. The MLEs QPO parameters $\hat{\theta}_i = [\hat{a}, \hat{w}, \hat{R}, \hat{\nu_0}]$ are obtained by minimizing the logarithm of the inverse squared likelihood

$$\mathcal{S} = -2\ln\mathcal{L} = 2M\sum_{j=1}^{N}\left[\frac{P_j}{S_j} + \ln S_j + (1/M-1)\ln P_j + c(M)\right] \tag{2.13}$$

where M is the number of elementary PDSs averaged to obtain the final spectrum and $c(M)$ is a function independent of the data and model thus irrelevant to the fitting process. This minimization can be performed using a standard minimization algorithm such as POWELL (Powell, 1964) or MINUIT (James & Roos, 1975) as illustrated in Figure 2.1 (right).

To compute the errors on the reconstructed parameters, the easiest is thus to use a Fischer information matrix F:

$$\sigma_i = F_{ii}^{-1} \ , \ F_{ij} = \left\langle -\frac{\partial^2\mathcal{L}}{\partial\theta_i\partial\theta_j} \right\rangle \tag{2.14}$$

As highlighted by Barret & Vaughan (2012) (see also Vaughan, 2005, 2010), a more accurate way to compute confidence intervals for the fitted parameters is to use $\Delta\mathcal{S}$ in a similar fashion as the more common $\Delta\chi^2$ method (Press et al., 1992). Under fairly generic assumptions, $\Delta\mathcal{S}$ indeed follows a χ^2_ν distribution with ν degrees of freedom corresponding to the number of free parameters (Cash, 1979). As a consequence, a 90% confidence interval on a single parameter is for instance given by $\Delta\mathcal{S} = 2.71$. This property can also be used to notably compute an upper limit on the QPO normalization R (related to its RMS amplitude) when no QPO signal is detected: after fitting a Lorentzian profile at the position of the biggest excess in the studied frequency band while fixing the QPO width w to a chosen value (typically either the mean QPO width of the source or the latest measured one), a 90% upper limit on R is obtained by increasing it until $\Delta\mathcal{S}$=1.64.

2.1.3 Frequency variability and shift-and-add technique

The frequency of kHz QPOs is not stable through time and varies in a manner phenomenologically similar to that of a random walk (Belloni et al., 2005). The best way to notice this is to compute a so-called dynamical PDS. It consists in the successive representation as a function of time of PDS computed on small time scales, typically 1 s (see Figure 2.2). As can be seen, the frequency drift through time caused the oscillation power to be spread over a large frequency range. To compensate

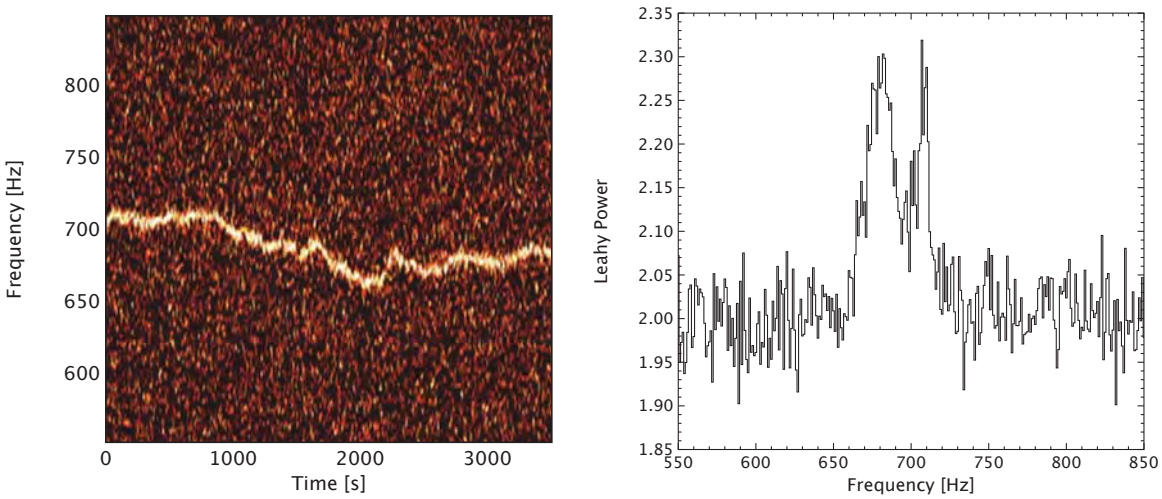

Figure 2.2: Left: Example dynamical PDS (data extracted from ObsID 30062-02-01-000 between 6 and 50 keV). The image corresponds to a series of 1 s PDS plotted as a function of time, convolved with a 4 Hz and 8 s averaging kernel for better visibility. Power is color-coded with a linear scale between 2 (black) and 3 (white). One can clearly see the QPO frequency changing erratically through time. **Right:** Averaged PDS over the whole observation. The frequency drift caused the power to be diluted across a wide frequency range.

for this effect and properly recover the QPO intrinsic parameters, Mendez et al. (1998) introduced the so-called "shift-and-add" technique. It consists in extracting individual PDS regularly, fit them to measure the QPO centroid frequency as a function of time and shift them all to match an arbitrary frequency value. The PDS are then averaged together to obtain a high signal-to-noise spectrum. This technique has now been extensively used to either reconstruct the intrinsic parameters of the QPO without frequency shift, or detect an oscillation which would have a constant frequency separation with a more significant leading QPO, or simply to get a better final signal-to-noise ratio over the QPO profile.

In some cases, it is however necessary to follow the QPO frequency on time scales too small to get a reliable frequency measurement with a fitting procedure like the one presented in Sect. 2.1.2. During my thesis, I therefore developed a QPO frequency tracking algorithm similar to the one used by Barret et al. (2006) to reliably follow the QPO on the smallest time-scale possible.

The global idea of this algorithm is to make use of the relative stability of the QPO frequency on small time scales: starting from a user defined frequency, each second, a Leahy-normalized 1 Hz resolution PDS over 30 s is computed and from there the next frequency is determined by the position in this PDS of the most significant excess over 4 Hz in a 10 Hz frequency band surrounding the previous one. Only excesses (and therefore frequencies) with a probability of not being due to noise over 99% (taking into account the number of trials) are kept. This creates a list of frequency estimates every second (minus the ones rejected due to low significance). To avoid overcorrecting the drift and interpret every positive fluctuation as signal, this list is finally smoothed with a spline function.

To test wether this technique would introduce a bias on the RMS level due to an over-/under-compensation of the frequency drift, 1000 400 s long light curves containing a QPO with a shape similar to the ones studied in Sect. 2.2 ($R = 9.7$, $w = 5.25$ Hz at 600 cts/sec) were simulated: each light curve is obtained by concatenating 1 s QPO light curves simulated using the method presented in Timmer & Koenig (1995) with the frequency drift modeled by a random walk of 0.25 Hz step each

second (Belloni et al., 2005). These 1000 observations were then all shifted-and-added and stacked to create a mean PDS. The resulting R found was 9.73 and the width 5.44 Hz, which correspond to biases of +0.3% and +3.6% for the normalization factor and the width respectively which confirms the reliability of this "shift-and-add" technique.

As we employed this algorithm in the presence of X-ray bursts, we also verified that this tracking method still gave a good frequency monitoring even when a typical X-ray burst would hide the QPO signal for a few tens of seconds. To do so, we computed 1000 new 400 s long QPO light curves like before and added on top of them burst light curves modeled by a simple exponential rise and decay randomized with Poisson noise:

$$C(t) = \begin{cases} C_{\rm pers} + C_{\rm peak} e^{t/\tau_{\rm rise}} & \text{if } t < 0 \\ C_{\rm pers} + C_{\rm peak} e^{-t/\tau_{\rm decay}} & \text{otherwise} \end{cases} \tag{2.15}$$

with C the total count rate, $C_{\rm pers}$ and $C_{\rm peak}$ its persistent and peak values, $\tau_{\rm rise}$ and $\tau_{\rm peak}$ the rise and decay time constants. By comparison with the different 4U 1608-52 burst light curves, representative values of these parameters were chosen: $C_{\rm pers} = 600$ cts/s, $C_{\rm peak} = 10000$ cts/sec, $\tau_{\rm rise} = 2$ s and $\tau_{\rm decay} = 7$ s. In the same way as for the data, the algorithm runs until $t = 200$ s from the start of the observation and backwards for the second part. The true QPO frequencies were given as starting point for the algorithm at the beginning and at the end of the observation. Over the 1000 realizations, the mean error on the frequency was 0.8 Hz, and the mean maximum error over one observation 2.9 Hz. In total, only 3 (0.3%) had a maximum difference between the real frequencies and the ones found by the algorithm superior to 10 Hz. Those are typically cases were the signal is lost at some point by the algorithm which can easily be identified while dealing with data (if one plots the computed frequencies as a function of time against the dynamical PDS, such a big difference is apparent) and were excluded from the statistics. For 951 (95%) simulations, the time spent at more than 4 Hz from the true frequency was inferior to 10 s. In average this time is around 1.2 s.

2.2 The interaction between Type-I X-ray bursts and kHz QPOs

2.2.1 Scientific context

Since their first discovery about 20 years ago by the RXTE satellite, the exact origin of the kHz QPOs still remains a matter of dispute and several models were proposed to explain at least part of the now extensive set of properties of these oscillations (see e.g. van der Klis, 2006). One distinctive character to all the kHz QPO studies performed as of now is that they all used data from LMXBs in a steady state, at least on kilosecond timescales. Most kHz QPO sources however regularly experience thermonuclear X-ray bursts which release in a few tens of seconds $\sim 10^{37-38}$ ergs (Galloway et al., 2008) and therefore have the potential to significantly disrupt the accretion flow. Evidence of such an influence has actually already been reported in some isolated cases (Yu et al., 1999; Kuulkers et al., 2003; Ballantyne & Strohmayer, 2004; Ballantyne & Everett, 2005; Chen et al., 2011; in't Zand et al., 2011; Serino et al., 2012; Degenaar et al., 2013). Worpel et al. (2013) also performed a detailed spectral analysis of photospheric radius expansion bursts and claimed they measured accretion rate enhancements during these events.

As the kHz QPOs are thought to be produced in the inner parts of the accretion disks sensible to the X-ray burst emission, it is worth looking for an interference between the burst and QPO signals. On top of providing a new probe to the X-ray burst – accretion disk interaction problem, studying the QPOs in this context may reveal hints on how they are produced. Of course, this requires observations

during which the kHz QPOs were detectable on tens of seconds timescales. We thus decided to select the two prototypical kHz QPO emitters: 4U1636-536 and 4U1608-522.

2.2.2 Publication 1

A&A 567, A80 (2014)
DOI: 10.1051/0004-6361/201423784

Astronomy & Astrophysics

Probing X-ray burst – accretion disk interaction in low mass X-ray binaries through kilohertz quasiperiodic oscillations

P. Peille, J.-F. Olive, and D. Barret

Université de Toulouse, UPS-OMP, IRAP, Toulouse, France
and CNRS, Institut de Recherche en Astrophysique et Planétologie, 9 Av. colonel Roche, BP 44346, 31028 Toulouse Cedex 4, France
e-mail: ppeille@irap.omp.eu

Received 8 March 2014 / Accepted 24 May 2014

ABSTRACT

The intense radiation flux of Type I X-ray bursts is expected to interact with the accretion flow around neutron stars. High frequency quasiperiodic oscillations (kHz QPOs), observed at frequencies matching orbital frequencies at tens of gravitational radii, offer a unique probe of the innermost disk regions. In this paper, we follow the lower kHz QPOs, in response to Type I X-ray bursts, in two prototypical QPO sources, namely 4U 1636-536 and 4U 1608-522, as observed by the Proportional Counter Array of the *Rossi* X-ray Timing Explorer. We have selected a sample of 15 bursts for which the kHz QPO frequency can be tracked on timescales commensurable with the burst durations (tens of seconds). We find evidence that the QPOs are affected for over ∼200 s during one exceptionally long burst and ∼100 s during two others (although at a less significant level), while the burst emission has already decayed to a level that would enable the pre-burst QPO to be detected. On the other hand, for most of our burst-kHz QPO sample, we show that the QPO is detected as soon as the statistics allow and in the best cases, we are able to set an upper limit of ∼20 s on the recovery time of the QPO. This diversity of behavior cannot be related to differences in burst peak luminosity. We discuss these results in the framework of recent findings that accretion onto the neutron star may be enhanced during Type I X-ray bursts. The subsequent disk depletion could explain the disappearance of the QPO for ∼100 s, as possibly observed in two events. However, alternative scenarios would have to be invoked for explaining the short recovery timescales inferred from most bursts. Heating of the innermost disk regions would be a possibility, although we cannot exclude that the burst does not affect the QPO emission at all. Clearly the combination of fast timing and spectral information of Type I X-ray bursts holds great potential in the study of the dynamics of the inner accretion flow around neutron stars. However, as we show, breakthrough observations will require a timing instrument providing at least ten times the effective area of the RXTE/PCA.

Key words. accretion, accretion disks – X-rays: bursts – stars: individual: 4U 1636-536 – stars: individual: 4U 1608-522 – X-rays: binaries

1. Introduction

Illumination of accreting disks during Type I X-ray bursts gives us the opportunity to study the innermost regions of the accretion flow around neutron stars (Galloway et al. 2008; Strohmayer & Bildsten 2003; Cumming 2004). Evidence of an interaction between the burst emission and the inner disk has been reported in a few individual bursts (Yu et al. 1999; Kuulkers et al. 2003; Chen et al. 2011; in't Zand et al. 2011; Serino et al. 2012; Degenaar et al. 2013). Disk depletion through radiation drag, heating of the inner disk, and even radiatively or thermally powered winds were discussed by Ballantyne & Strohmayer (2004) and Ballantyne & Everett (2005), who attempted to explain the time evolution of the properties of the *superburst* of 4U 1820-303. More recently, Worpel et al. (2013), fitting the spectra of all photospheric radius expansion (PRE) bursts observed with the *Rossi* X-ray Timing Explorer (RXTE) as the sum of a blackbody and a scalable continuum having the shape of the pre-burst persistent emission, reported a systematic increase of the persistent emission during the burst. They interpreted this result as evidence of an accretion rate enhancement due to a rapid increase of the radiation torque on a thin accretion disk, as formalized early on by Walker (1992). A similar finding was reported by in't Zand et al. (2013) for a burst observed simultaneously by *Chandra* and RXTE, although disk reprocessing of the burst emission was preferred as an alternative explanation.

In this paper, we follow a different path and look at kilohertz quasiperiodic oscillations (kHz QPOs) in response to Type I X-ray bursts (see van der Klis 2006 for a review of kHz QPOs). Although there is not yet a consensus on the origin of kHz QPOs, it is generally agreed that they arise from the vicinity of the neutron star (e.g., Barret 2013), most likely in a region to be exposed to the burst emission. It is therefore worth investigating how the QPO properties react to X-ray bursts. For this purpose, we use the RXTE archival data of 4U 1636-536 and 4U 1608-522, known as frequent bursters (Galloway et al. 2008) and whose lower kHz QPOs can be detected and followed on the burst duration timescales of tens of seconds (Méndez et al. 1999; Barret et al. 2005, 2006).

2. Data analysis

We retrieved the archived data of the Proportional Counter Array (PCA) onboard RXTE for all the observations containing an X-ray burst for both 4U 1636-536 and 4U 1608-522, using the catalog provided by Galloway et al. (2008). In total, we obtained 172 bursts for 4U 1636-536 and 31 for 4U 1608-522, respectively. Using the Science Events of the PCA, we computed $1/2^{12}$ s resolution light curves from −200 to +400 s with respect to the burst peak (whenever possible, i.e., when no observation gap restricted this time interval). The date $t = 0$ was fixed for each burst at the peak count rate using 1 s resolution light curves.

A&A 567, A80 (2014)

Table 1. Principal characteristics of the selected X-ray bursts.

Source	Burst ID	Obs ID	Start time (RXTE time)	$L_{peak}{}^a$ (10^{38} erg/s)	$E_{tot}{}^a$ (10^{39} erg)	τ^a (s)	C_{pers} (cts/s)	C_{peak} (cts/s)
4U 1636-536	4	10088-01-08-030	94 671 416	2.68	5.54	20.7	788	9931
	6	30053-02-02-02	146 144 682	2.89	1.78	6.2	679	9740
	9	40028-01-02-00	162 722 852	2.94	1.84	6.3	569	9927
	21	40028-01-18-000	208 401 523	2.79	2.35	7.0	737	9916
	22	40028-01-18-00	208 429 016	2.76	1.85	6.7	574	10 000
	23	40028-01-19-00	208 740 744	2.79	2.13	7.6	541	10 116
	39	60032-01-09-00	242 286 131	1.46	1.33	9.1	417	7089
	40	60032-01-09-01	242 295 310	1.06	1.14	10.9	425	5355
	41	60032-01-10-00	242 708 641	2.00	1.50	7.5	428	9611
	168	91024-01-30-10	374 626 248	2.98	2.06	6.9	473	9604
4U 1608-522	4	30062-02-01-000	133 389 809	1.43	1.35	9.1	643	9004
	5	30062-01-01-00	133 625 123	2.34	2.32	9.9	543	10 339
	21	70059-01-20-00	273 983 179	2.33	1.93	8.3	617	10 562
	23	70059-03-01-000	274 421 898	2.39	3.16	13.2	517	10 549
	24	70059-03-01-000	274 434 678	1.08	1.1	10.2	510	9528

Notes. Burst ID corresponds to the burst number in the Galloway et al. (2008) burst catalog, Obs ID to the identification number of the RXTE observation in which the burst can be found, Start time to the RXTE time of the burst peak used to define the date $t = 0$ in Sect. 2, L_{peak} to the peak luminosity, E_{tot} to the total energy, τ to the decay time constant, C_{pers} to the raw persistent count rate before the burst, and C_{peak} to its value at burst peak. $^{(a)}$ Values taken from Galloway et al. (2008). Distances of 6 and 3.6 kpc were taken to compute the peak luminosity L_{peak} and total energy E_{tot} for 4U 1636-536 and 4U 1608-522, respectively (Pandel et al. 2008; Nakamura et al. 1989).

In order to limit the influence of the nonmodulated burst photons in our analysis, while keeping enough statistics for the QPO detection, we chose to restrict our study to the 6–50 keV band. The burst emission dominates in the soft X-ray band while the QPO modulated photons have a harder spectrum (Berger et al. 1996).

2.1. Data reduction

Dynamical Fourier power density spectra (PDS) containing the time series of Leahy normalized PDS (Leahy et al. 1983) were computed. These spectra were obtained with an integration time of 1 s and a Nyquist frequency of $f_{Ny} = 2048$ Hz. Segments of data containing an X-ray burst and a QPO detectable on short timescales (~20–30 s) were identified. A list of 10 and 5 bursts in 4U 1636-536 and 4U 1608-522, respectively, was so obtained (see Table 1 for a summary of the main properties of these bursts).

2.2. Initial results

The most common pattern observed in the dynamical PDS is illustrated in Fig. 1: the QPO is clearly detected both before and after the X-ray burst at about the same frequency (i.e., at a frequency consistent with the usual drift of the QPO frequency), but in an interval of ~20–30 s after the onset, the QPO is not detected. This nondetection can be explained by the addition of the nonmodulated burst photons[1]. This pattern is, however, not observed in three bursts of 4U 1636-536, for which the QPO remains undetected for up to several hundreds of seconds, while the overall source emission has returned to the level it had before the burst (see Fig. 2).

We then simulated the effect of the burst photons on the QPO detectability. For this purpose, we first estimated the QPO parameters (amplitude, frequency, width) using segments of 100 s duration prior to the bursts between $t = -200$ s and $t = -10$ s, stepped by 10 s (sliding window). The QPO was fitted by a Lorentzian with the maximum likelihood method described in Barret & Vaughan (2012) and was found to be highly significant in each segment. The final parameters were thus obtained by computing the weighted average of the best fit parameters found in each segment (see Table 2). A persistent emission light curve with the same time resolution as the data ($1/2^{12}$ s) containing such a QPO was then randomly simulated following Timmer & Koenig (1995). The burst light curve was itself computed on the same time resolution, starting from the interpolation of the one recorded with one-second time bins. Poisson noise fluctuations were added to the high-time-resolution burst light curve,

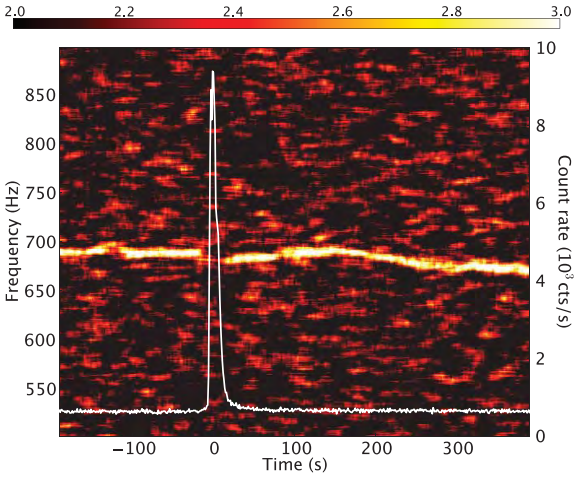

Fig. 1. Dynamical PDS and light curve (white line) around burst 4 of 4U 1608-52. The image corresponds to a series of 1 s PDS plotted as a function of time, convolved with a 6 Hz and 20 s averaging kernel for better visibility. Power is color-coded with a linear scale between 2 (black) and 3 (white).

[1] The significance of excess power is proportional to $\frac{S^2}{S+B}\mathrm{rms}^2$. S, B, and rms correspond to the signal count rate, background count rate, and to the fractional rms amplitude of the QPO emission (van der Klis 1989). A burst corresponds to a large increase of B, causing the significance of the signal to drop abruptly.

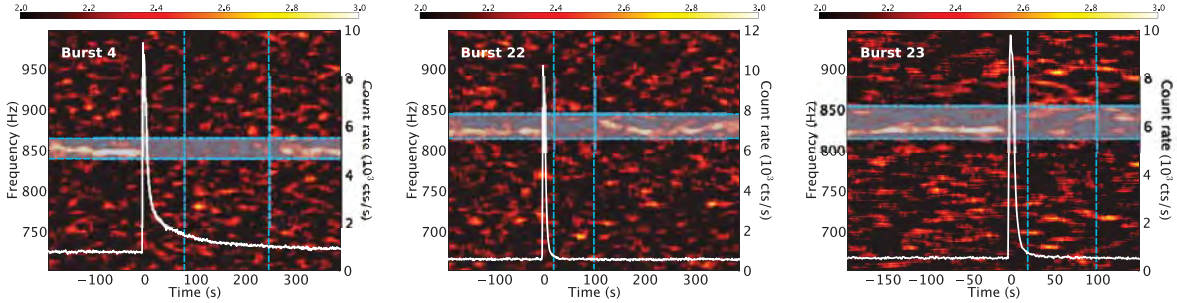

Fig. 2. Dynamical PDS and light curves (white lines) around bursts 4 (*left*), 22 (*middle*), and 23 (*right*) of 4U 1636-536. The image corresponds to a series of 1 s PDS plotted as a function of time, convolved with a 6 Hz and 20 s averaging kernel for better visibility. Power is color-coded with a linear scale between 2 (black) and 3 (white). The blue zones and vertical dashed lines represent the time and frequency intervals used to probe the significance of the QPO nondetection in the simulations, namely 80−248 s and 840−865 Hz for burst 4, 20−100 s and 815−845 Hz for burst 22, and 20−100 s and 815−855 Hz for burst 23. We note that for burst 23 an observation interruption limits the analysis to ∼150 s after the burst.

Table 2. kHz QPO shapes before and after the X-ray bursts.

Source	Burst ID	$\mathrm{Freq_{pers}}$	R_{pers}	$\mathrm{rms_{pers}}$ (%)	w_{pers} (Hz)	$\mathrm{Freq_{burst}}$	R_{burst}	$\mathrm{rms_{burst}}$ (%)	w_{burst} (Hz)
4U 1636-536	4	848	8.5 ± 0.4	10.4 ± 0.2	3.5 ± 0.3	(u.l.)	1.2 (u.l.)	4.9 (u.l.)	(u.l.)
	6	874	6.7 ± 0.4	10.0 ± 0.3	4.3 ± 0.4	876 ± 2.5	7.9 ± 2.8	10.9 ± 1.9	13.8 ± 6.3
	9	862	8.2 ± 0.4	11.9 ± 0.3	5.5 ± 0.4	855 ± 0.6	5.3 ± 1.9	9.8 ± 1.8	4.8 ± 3.0
	21	859	9.5 ± 0.5	11.4 ± 0.3	5.6 ± 0.5	854 ± 0.4	7.2 ± 1.3	10.0 ± 0.9	3.5 ± 0.9
	22	823	5.9 ± 0.4	10.3 ± 0.3	3.9 ± 0.3	(u.l.)	2.6 (u.l.)	6.9 (u.l.)	(u.l.)
	23	825	5.4 ± 0.3	10.0 ± 0.3	2.2 ± 0.2	(u.l.)	2.6 (u.l.)	7.1 (u.l.)	(u.l.)
	39	802	3.2 ± 0.3	8.7 ± 0.4	2.0 ± 0.4	796 ± 2.1	5.1 ± 1.8	11.3 ± 2.0	8.3 ± 3.8
	40	843	5.2 ± 0.4	11.0 ± 0.4	4.2 ± 0.5	839 ± 0.5	5.7 ± 1.3	11.9 ± 1.4	3.7 ± 1.3
	41	820	3.9 ± 0.3	9.5 ± 0.4	2.7 ± 0.3	826 ± 0.7	5.5 ± 1.4	12.0 ± 1.5	5.0 ± 1.7
	168	849	4.9 ± 0.3	10.0 ± 0.3	2.7 ± 0.3	849 ± 0.7	6.7 ± 1.5	12.2 ± 1.4	5.3 ± 1.6
4U 1608-522	4	689	10.9 ± 0.5	12.9 ± 0.3	5.6 ± 0.3	684 ± 0.5	10.9 ± 1.8	13.6 ± 1.1	5.5 ± 1.3
	5	740	8.8 ± 0.4	12.8 ± 0.3	4.7 ± 0.3	722 ± 1.2	11.6 ± 3.0	15.7 ± 2.0	12.1 ± 4.4
	21[a]	703	10.8 ± 0.4	13.2 ± 0.3	4.7 ± 0.3	704 ± 0.8	10.1 ± 2.0	13.4 ± 1.3	7.9 ± 2.1
	23	813	5.8 ± 0.4	10.4 ± 0.3	4.1 ± 0.3	801 ± 2.8	6.0 ± 1.8	12.8 ± 1.9	6.7 ± 2.8
	24	805	8.5 ± 0.5	12.8 ± 0.4	5.7 ± 0.5	790 ± 0.5	9.3 ± 1.8	13.6 ± 1.3	5.3 ± 1.5

Notes. Burst ID corresponds to the burst number in the Galloway et al. (2008) burst catalog, Freq to the centroid frequency of the QPO, R to the Lorentzian normalization factor, rms to the rms amplitude of the QPO, and w to its width. The QPO parameters are given both before (pers index) and after the burst (burst index). The errors here are 1σ errors. For bursts 4, 22, and 23 of 4U 1636-536, the QPO rms amplitude 90% confidence upper limits were computed during the nondetection gap, namely 80−248 s for the first nondetection and 20−100 s for the other two using the pre-burst width as well as a frequency fixed to the position of the most significant excess (denoted u.l. in the table). For all other bursts, the QPO parameters after the burst were computed in the same time interval, 20−100 s, after the burst peak. [(a)] For this burst, not enough data were recorded before the burst and the QPO parameters have been estimated away from the burst (200 s after), and taken as representative of the QPO parameters before the burst.

which was then added to the light curve of the persistent emission containing the QPO. The summed light curve was then processed the same way as the real data to produce one-second PDS. This procedure was repeated 10 000 times. The PDS were averaged within the nondetection gap for both the data and the simulations, and excesses of power were searched over the same frequency interval around the QPO frequency in a 5 Hz window (see Fig. 2). In conditions representative of the three bursts, the simulations systematically reproduced an excess of power larger than the one found in the data, strongly suggesting that the QPO was affected by the burst (see Fig. 3). A more quantitative estimate of the significance of these nondetections can be obtained by comparing the excess of power found in the data with the distributions produced by the simulations. For that particular PDS integration time (1 s), Gaussian fits yield probabilities of observing the gap if the QPO parameters were not affected by the burst of 9.2×10^{-11} for burst 4, 1.3×10^{-4} for burst 22, and 3.3×10^{-4} for burst 23 (see Fig. 3). The nondetection gaps during bursts 22 and 23 can therefore only be considered as marginally significant. Another way to illustrate this is by comparing the rms amplitude of the QPO prior to the burst and the rms upper limit on the QPO during the nondetection gap, considering the QPO width unchanged and the burst photons contributing to the noise. As listed in Table 2, 90% confidence level upper limits are significantly below the QPO rms measured prior to the burst. On the other hand, for all the other bursts of 4U 1636-536 (and 4U 1608-522), the rms amplitude of the QPO measured before and after the burst are consistent with one another, as shown in Fig. 4 (see Table 2 for more detail). We note that in order to take into account the changing count rate during the burst decay and the fact that burst photons are not modulated, the rms amplitude of the QPO was computed from the Lorentzian normalization factor R (Barret & Vaughan 2012) using the relation

$$\mathrm{rms} = \sqrt{\frac{T}{C_{\mathrm{pers}}^2 \sum_t 1/C(t)}} R, \quad (1)$$

A&A 567, A80 (2014)

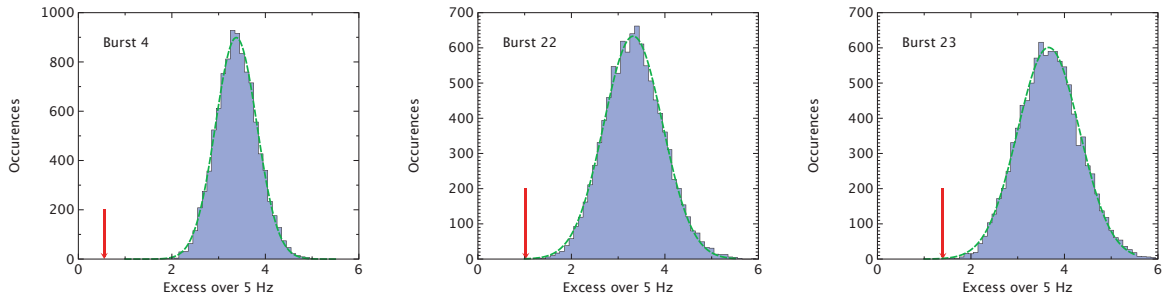

Fig. 3. Results of the PDS simulations for bursts 4 (*left*), 22 (*middle*), and 23 (*right*) of 4U 1636-536. The blue histograms correspond to the distribution of the excesses found in the simulations (see text), the red arrows to the values found in the data, and the dashed green lines to Gaussian fits of the distributions.

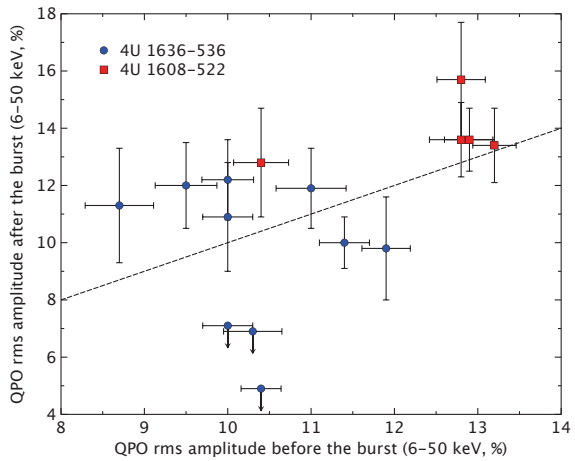

Fig. 4. Distribution of the QPO rms amplitude measured after the burst against the one measured before the burst with 1σ error bars (see Table 2). The upper limits are 90% level. The blue circles correspond to bursts of 4U 1636-536, the red squares to bursts of 4U 1608-522. The dashed line corresponds to equal amplitudes before and after the burst.

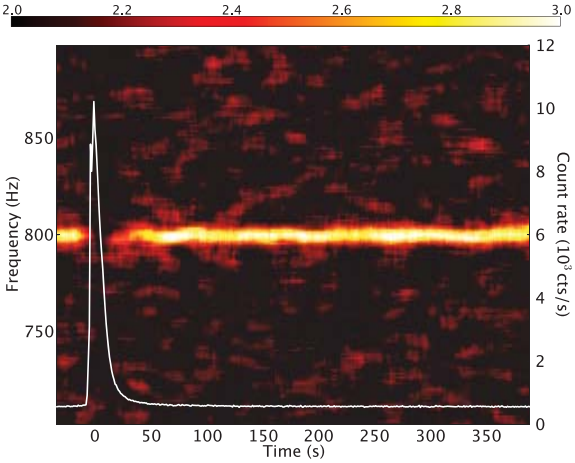

Fig. 5. Dynamical PDS and mean light curve (white line) resulting from the stacking of all the 4U 1608-52 observations. The image corresponds to the succession of 1 s PDS plotted as a function of time, convolved with a 6 Hz and 20 s averaging kernel for better visibility. Power is color-coded with a linear scale between 2 (black) and 3 (white). We note that the plot starts at –43 s because of an observation gap for burst 21.

where $C(t)$ is the one-second resolution count rate in the time interval of duration T and $C_{\rm pers}$ the count rate in the persistent emission.

2.3. Stacking of the bursts

As shown in Fig. 4, all QPOs from 4U 1608-522 show a stable rms amplitude. In addition, for 4U 1608-522, the QPOs are easier to track on short timescales than for 4U 1636-536. As a way to improve our QPO detection sensitivity around the burst, one can combine the PDS from different bursts, after aligning them to a reference frequency. The QPO frequency was tracked before and after the burst using an algorithm similar to the one presented in Barret et al. (2006), which uses the centroid of the excess power as a proxy of the QPO frequency (when the significance of the QPO is not sufficient to obtain a stable fit). We note that because no signal can be detected during the bursts, the frequency is obtained by interpolating between the values before and after the bursts. We have checked through extensive Monte Carlo PDS simulations of QPOs of varying frequency, in the presence of a typical X-ray burst of 4U 1608-522, that such an algorithm did not introduce any systematic biases in the recovered QPO parameters, and is therefore suitable for combining PDS of different bursts. The dynamical PDS produced for 4U 1608-522 after all the PDS were aligned to an 800 Hz reference frequency is shown in Fig. 5. Clearly the nondetection gap is now restricted to an area very close to the burst peak. For example, a 6.6σ excess of power is detected in a 15-second interval, 15 s after the burst peak. We have thus set a conservative upper limit of ~20 s on the QPO reappearance or on its recovery time.

Sliding a 20 s window over the burst (with one-second steps, i.e., steps of one second each), one can track the evolution of the significance of the QPO detection as a function of time, and compare it to the one for which the QPO parameters are unchanged during the bursts and only the burst photons add to the noise to lower the detection significance. This is shown in Fig. 6; the solid curve shows the evolution of the significance of the maximum power excess over 4 Hz (total power exceeding the Poisson level of 2) measured as a function of time in the stacked PDS between 790 Hz and 810 Hz. The dashed line corresponds to the level expected assuming that the QPO parameters measured before the burst do not change during the bursts. It is remarkable

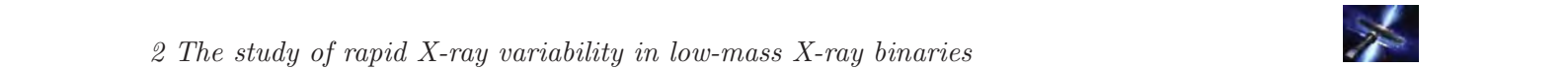

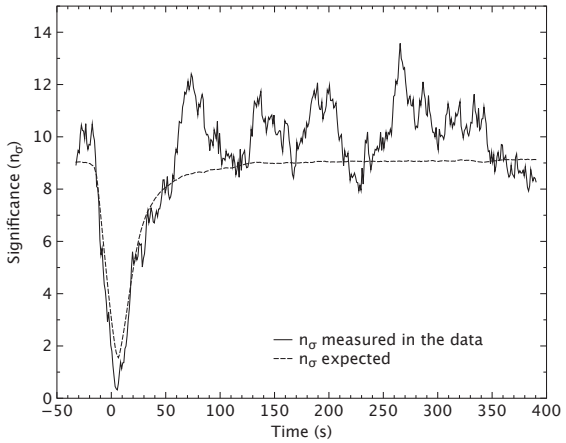

Fig. 6. Significance of the maximum excess over 4 Hz in the 790−810 Hz band as a function of time in the dynamical PDS resulting from the stack of the 4U 1608-52 observations (see text). The solid line corresponds to significance values measured in the data while the dashed line is the level expected from the burst light curves and QPO profiles measured before the burst. We note that the plot starts at −43 s because of an observation gap for burst 21.

how close the observed and predicted profiles are[2], suggesting that for our sample of 4U 1608-522 bursts, the QPOs were unaffected by the presence of the bursts.

3. Comparison with burst parameters

In the above analysis, we have shown that not all QPOs respond the same way to Type I X-ray bursts. Here we wish to investigate whether this can be related to changes in the burst parameters. In Fig. 7 we plot the ratio of the rms amplitude of the QPO after and before the burst (see Table 2 for more detail), against the peak luminosity and burst total energy. As can be seen, no clear trend is observed within the limited sample of the bursts considered in our analysis concerning the peak luminosity. Nonetheless, the burst showing a highly significant disappearance of the QPO (4) – as well as the two bursts where the lack of QPO signal is marginally significant (22 and 23) – has a peak luminosity that lies on the high part of the diagram. It is striking to see that burst 4 has an exceptionally large total energy which is due to its long duration. Unfortunately, extending our analysis to bursts observed after the Galloway et al. (2008) catalog did not provide us with further useful observations and these trends could not be confirmed.

We have also performed a spectral analysis of our burst sample following the recent work of Worpel et al. (2013), where the time resolved burst spectrum is fitted as the sum of an absorbed blackbody and a scalable persistent emission spectrum (with a scaling factor f_a), as fitted before the burst. Fixed hydrogen column densities of $N_{\rm H} = 0.36 \times 10^{21}$ (Pandel et al. 2008) and 1.1×10^{21} cm^{-2} (Güver et al. 2010) were used for 4U 1636-536 and 4U 1608-522, respectively. Spectra were fitted in the 2.5−20 keV band using `xpsec` version 12.8. Burst spectra were extracted with variable time steps matching the burst dynamics. Two different models were used to fit the persistent emission spectrum: `wabs*(nthcomp+diskline)` for 4U 1636-536 and `wabs*(nthcomp+gaussian+bbodyrad)` for 4U 1608-522. As discussed by Worpel et al. (2013), what matters is to have a model that describes accurately the persistent emission before the bursts. Both models provide good and stable fits. Like Worpel et al. (2013), we found that f_a increases during the peak phase (up to 20 or so, with typical values around 5), and remains significantly above 1 over the 20-s interval following the burst. An example of f_a variations for three bursts is shown in Fig. 8. No correlation was found between the ratio of the QPO rms amplitude before and after the burst and f_a, neither its maximum value nor its mean value over the first 20-s interval (as shown in Fig. 7). Yet, it is interesting to note that with the exception of the long burst of 4U 1636-536 (Fig. 2, left panel), f_a has returned to 1 within 20 s. This value is commensurable with the recovery time inferred from the stacking of the 4U 1608-522 data.

[2] The small difference between the two curves in the persistent emission after the burst is due to the measurement of the power excess used here being sensible to positive noise fluctuations around the QPO profile.

4. Discussion

High frequency QPOs are commonly believed to be generated close to the neutron star surface or in the innermost parts of the accretion disk. Similarly, Type I X-ray bursts are produced on the neutron star surface and radiate away enough energy to change the proprieties of the accretion flow. It is therefore natural to investigate the impact of a Type I X-ray burst on kHz QPOs. Our finding that there may be cases where the QPO is affected by the bursts on timescales of hundreds of seconds and cases where the QPO does not suffer from the bursts down to the shortest timescales that can be investigated by current data (∼20 s) is clearly puzzling, especially because these two behaviors cannot be irrefutably connected in our limited sample to different properties of the bursts, such as the burst peak luminosity. We now discuss our results in the framework of the recent work by Worpel et al. (2013), claiming that the accretion rate is enhanced during Type I X-ray bursts.

4.1. A disk recession?

As accretion disks are optically thick in the radial direction, an enhanced accretion rate due to radiation torque can only be attained through disk depletion: $f_a > 1$ implies a receding disk. The Eddington-scaled accretion rate in our data sets is ∼0.12 and 0.04 $\dot{M}_{\rm Edd}$ for 4U 1636-536 and 4U 1608-522, respectively, using a neutron star mass of 1.4 $M_\odot$. If we take conservative values for the mean f_a measured during the 20 s following the burst onset of 1.5 and 2 for the two sources, this gives depleted masses of at least $\sim 3 \times 10^{18}$ and 2×10^{18} g. Using standard accretion disks as described in Shakura & Sunyaev (1973) to model the mass distribution in the inner parts of the disk with an α-parameter of 0.1, these masses correspond approximately to the mass contained between 7–50 R_g for 4U 1636-536, and 7–30 R_g for 4U 1608-522. It is important to note that the disk surface density scales as $1/\alpha$ which is poorly constrained and that these masses are only rough estimates.

An estimate of the timescale at which the disk recovers its former geometry is given by the viscous time (Frank et al. 2002, Eq. (5.69)),

$$t_{\rm visc} \sim 3 \times 10^5 \alpha^{-4/5} \left(\frac{\dot{M}}{10^{16}\ {\rm g/s}}\right)^{-3/10} \left(\frac{M}{M_\odot}\right)^{1/4} \left(\frac{R}{10^{10}\ {\rm cm}}\right)^{5/4} {\rm s}, \quad (2)$$

with R the distance to the neutron star center, $\dot{M}$ the accretion rate, and M the neutron star mass. For $M = 1.4\ M_\odot$, $\alpha = 0.1$, and with the appropriate accretion rates, we find $t_{\rm visc} \sim 130$ s at 50 r_g

A&A 567, A80 (2014)

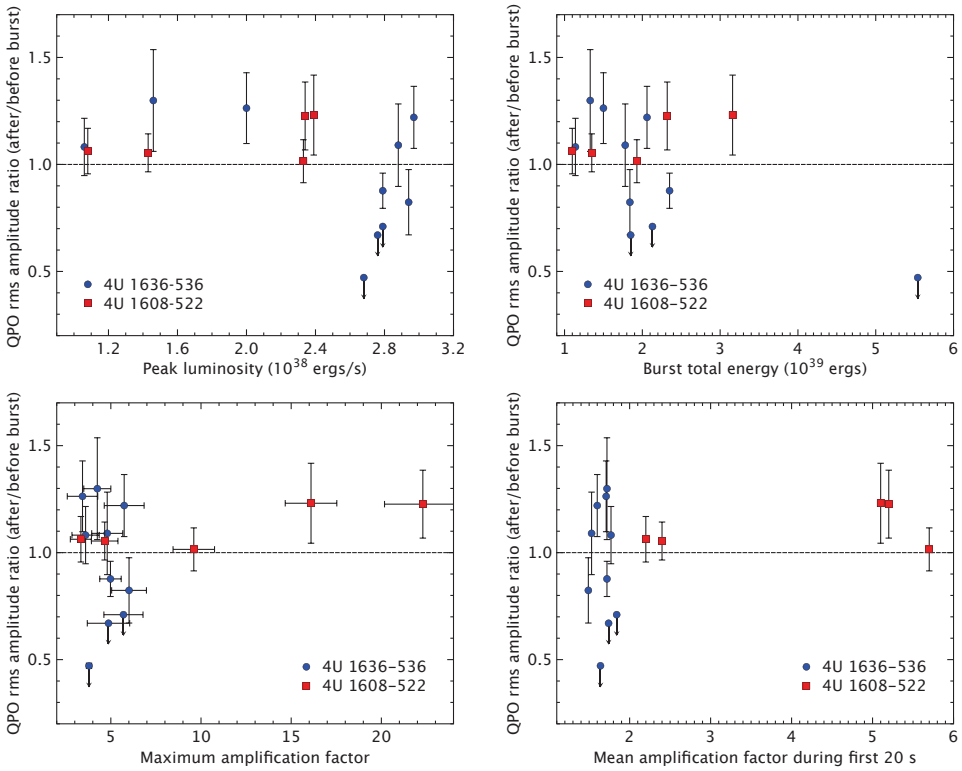

Fig. 7. Ratio of the kHz QPO rms amplitude after the burst over its value before the burst (see Table 2) as a function of the burst peak luminosity (*upper left*), burst total energy (*upper right*), maximum f_a (*lower left*), and mean f_a during the first 20 s (*lower right*) with 1σ error bars. The upper limits are 90% level. The blue circles correspond to bursts of 4U 1636-536, the red squares to bursts of 4U 1608-522. When no significant signal was detected, upper limits were plotted (bursts 4, 22, and 23 of 4U 1636-536).

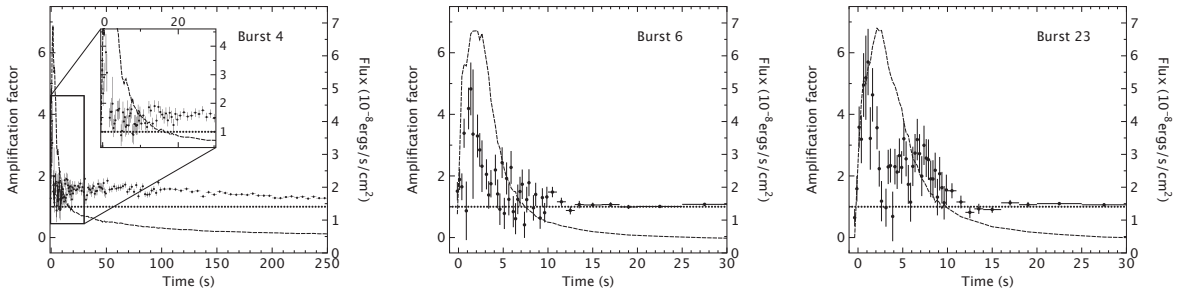

Fig. 8. Amplification factor (f_a) profiles (points with 1σ error bars) obtained from the spectral analysis of bursts 4 (*left*), 6 (*middle*), and 23 (*right*) of 4U 1636-536. For the longer burst 4, the first 30 s of the f_a profile have been magnified for better comparison. The dashed lines correspond to the burst light curves, and the horizontal dotted lines to $f_a = 1$.

for 4U 1636-536 and $t_{\rm visc} \sim 100$ s at 30 r_g for 4U 1608-522. It is worth noting that increasing α gives shorter viscous times, but it also increases the radius matching the loss of mass and similar timescales are found. Within all the caveats of the above assumptions, it is interesting to note that these timescales match the nondetection gap of the two shorter bursts from 4U 1636-536, shown in Fig. 2. We note however that for the longer burst of 4U 1636-536, f_a is still above 1 while the QPO reappears (see Fig. 8), which argues against the idea that the disk is still truncated through depletion. This clearly suggests that caution should be used when using f_a to derive the accretion rate during the burst. Some refinements in the Worpel et al. (2013) model might be necessary such as considering modifications of the spectral shape of the persistent emission during the burst. If such high levels of disk depletion occur, one would expect at least the disk emission to be modified; for example, a change in the disk inner radius from 7 r_g to 50 r_g would decrease its inner temperature by a factor of 4.4, assuming a dependency of $\propto R^{-3/4}$ as in Shakura & Sunyaev (1973). The timescales found are also a factor of 5−10 longer than the recovery time we inferred from 4U 1608-522, thus suggesting that an alternative to disk depletion should be considered.

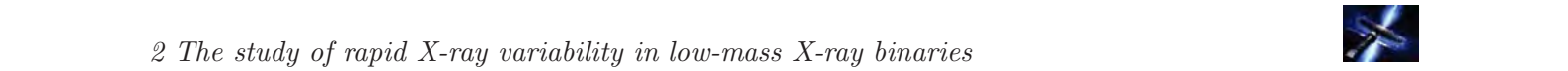

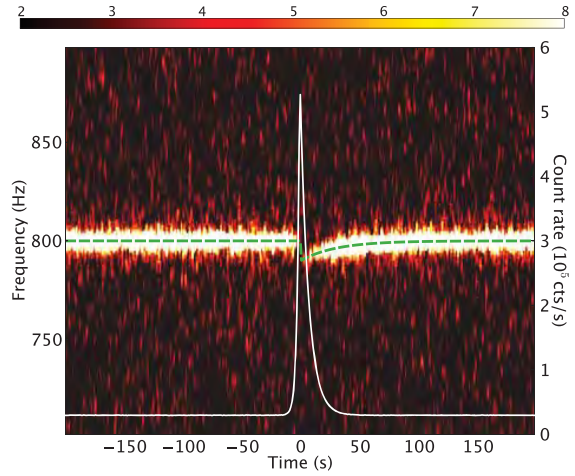

Fig. 9. Simulated dynamical PDS containing a QPO at 800 Hz and a smooth frequency jump of 10 Hz initiated at the burst peak (the dashed green line gives the QPO frequency as a function of time). The QPO rms amplitude is 8% and the QPO width is 3 Hz. The LOFT/LAD 3–30 keV light curve of the Type I X-ray burst (peak at 18 times the persistent emission level, rise time of 2 s, and decay time of 7 s) is overplotted with a white line. The persistent count rate was estimated using 4U 1608-522 as the source. The image corresponds to a series of 1 s PDS plotted as a function of time, convolved with a 6 Hz and 2 s averaging kernel. Power is color-coded. We note that the color scale is different from the one used for RXTE data: it saturates at a power level of 8 instead of 3.

4.2. Heating of the inner region?

To reduce the viscous disk recovery time, only the innermost part of the accretion disk should be affected. At 10 R_g, the viscous time ~18 s for 4U 1636-536 and ~25 s for 4U 1608-522 with an α-parameter of 0.1. One possibility could thus be disk irradiation by the burst photons, which is expected to produce significant heating, and might cause the disk to puff up (Ballantyne & Everett 2005). Leaving aside the two shorter bursts of 4U 1636-536 for which the QPO disappearance is marginally significant, such a mechanism could be consistent with the late reappearance of the QPO in the longer one (while the burst is still ongoing), but also with the short recovery times of the QPOs in 4U 1608-522. This might indicate that the modulated emission reappears only when the level of heating is sufficiently low. Unfortunately, current data cannot tell us what happens to the QPO within the first 20 s in 4U 1608-522, e.g., whether its amplitude drops or its coherence decreases. Hence, although that seems unlikely, we also cannot exclude that there is no effect of the burst on the QPO in this source.

Existing data are therefore insufficient to access timescales shorter than 20 s, while we would like to measure the QPO parameters as close as possible to the burst peak. Assuming that the QPO amplitude and width remain constant within the burst and only the QPO frequency varies, in Fig. 9 we show that a new generation timing instrument like the LOFT/LAD (Feroci et al. 2012) would allow us to track the QPO frequency, even at the burst peak. Tracking the QPO frequency along the frequency drift assumed in the simulation requires an increase in effective area by at least one order of magnitude (15 in the case considered here[3]). This simulation illustrates how such a large area timing instrument could deliver breakthrough observations on the burst-QPO interaction, providing at the same time insights on the location of the QPO modulated emission.

[3] LOFT/LAD response files were downloaded from http://www.isdc.unige.ch/loft for the simulation. We have assumed the goal effective area of 12 m^2 at 8 keV for the LAD.

4.3. Conclusions

The interaction between the kHz QPO signals and Type-I X-ray bursts has been studied in two LMXBs: 4U 1636-536 and 4U 1608-522. Two types of behaviors of different timescales have been identified. We have found clear evidence of an interaction of the burst with the QPO emission during an exceptionally long burst (and a possible indication for two others) while for most of them, within the current data, the QPO does not seem to be affected by the burst. We have set an upper limit of 20 s for the recovery time of the QPO in 4U 1608-522. We have shown that a next generation timing mission providing an increase in effective area of at least an order of magnitude, such as LOFT, would be able to detect the QPO throughout the bursts and hence provide better constraints on the physics of the interaction of the burst emission and its surroundings. This would need to be complemented by theoretical work aimed at a better modeling of the burst-disk interaction.

Acknowledgements. This research has made use of data obtained through the High Energy Astrophysics Science Archive Research Center On-line Service, provided by the NASA/Goddard Space Flight Center. We thank Duncan K. Galloway and Hauke Worpel for helpful conversations and suggestions. We also thank Mariano Mendez for a careful review of the paper, and comments which helped to improve its quality.

References

Ballantyne, D. R., & Everett, J. E. 2005, ApJ, 626, 364
Ballantyne, D. R., & Strohmayer, T. E. 2004, ApJ, 602, L105
Barret, D. 2013, ApJ, 770, 9
Barret, D., & Vaughan, S. 2012, ApJ, 746, 131
Barret, D., Kluźniak, W., Olive, J. F., Paltani, S., & Skinner, G. K. 2005, MNRAS, 357, 1288
Barret, D., Olive, J.-F., & Miller, M. C. 2006, MNRAS, 370, 1140
Berger, M., van der Klis, M., van Paradijs, J., et al. 1996, ApJ, 469, L13
Chen, Y.-P., Zhang, S., Torres, D. F., et al. 2011, A&A, 534, A101
Cumming, A. 2004, Nucl. Phys. B Proc. Suppl., 132, 435
Degenaar, N., Miller, J. M., Wijnands, R., Altamirano, D., & Fabian, A. C. 2013, ApJ, 767, L37
Feroci, M., Stella, L., van der Klis, M., et al. 2012, Exp. Astron., 34, 415
Frank, J., King, A., & Raine, D. J. 2002, Accretion Power in Astrophysics: 3rd edn. (Cambridge, UK: Cambridge Uni. Press)
Galloway, D. K., Muno, M. P., Hartman, J. M., Psaltis, D., & Chakrabarty, D. 2008, ApJS, 179, 360
Güver, T., Özel, F., Cabrera-Lavers, A., & Wroblewski, P. 2010, ApJ, 712, 964
in't Zand, J. J. M., Galloway, D. K., & Ballantyne, D. R. 2011, A&A, 525, A111
in't Zand, J. J. M., Galloway, D. K., Marshall, H. L., et al. 2013, A&A, 553, A83
Kuulkers, E., den Hartog, P. R., in't Zand, J. J. M., et al. 2003, A&A, 399, 663
Leahy, D. A., Darbro, W., Elsner, R. F., et al. 1983, ApJ, 266, 160
Méndez, M., van der Klis, M., Ford, E. C., Wijnands, R., & van Paradijs, J. 1999, ApJ, 511, L49
Nakamura, N., Dotani, T., Inoue, H., et al. 1989, PASJ, 41, 617
Pandel, D., Kaaret, P., & Corbel, S. 2008, ApJ, 688, 1288
Serino, M., Mihara, T., Matsuoka, M., et al. 2012, PASJ, 64, 91
Shakura, N. I., & Sunyaev, R. A. 1973, A&A, 24, 337
Strohmayer, T., & Bildsten, L. 2003 [arXiv:astro-ph/0301544]
Timmer, J., & Koenig, M. 1995, A&A, 300, 707
van der Klis, M. 1989, in Timing Neutron Stars, eds. H. Ögelman, & E. P. J. van den Heuvel, 27
van der Klis, M. 2006, Compact stellar X-ray sources, eds. W. Lewin, & M. van der Klis, Cambridge Astrophys. Ser., 39, 39
Walker, M. A. 1992, ApJ, 385, 642
Worpel, H., Galloway, D. K., & Price, D. J. 2013, ApJ, 772, 94
Yu, W., Li, T. P., Zhang, W., & Zhang, S. N. 1999, ApJ, 512, L35

2.2.3 Conclusions and perspectives

In this study, we have found for the first time evidence for an interaction between type I X-ray bursts and the lower kHz QPO signal. Even if no complete physical model could be put forward to explain the full variety of observed behaviors, these results are encouraging for the future use of kHz QPOs to probe the interaction between the X-ray bursts and the accretion flow. From a simple modeling of the disk depletion scenario proposed by Worpel et al. (2013), we also found that in most cases the recovery time of the kHz QPO signal strongly conflicted with the expected return time of the inner accretion disk obtained from the supposedly measured accretion rate enhancement.

Since the publication of this article, Worpel et al. (2015) confirmed the presence of an enhanced persistent emission during non PRE bursts, and Keek et al. (2014a) also detected one during the *superburst* of 4U1636-536. It however still remains unclear wether this increase is due to higher mass accretion rates due to Poynting Robertson drag or disk reprocessing of the burst emission as suggested by in't Zand et al. (2013), but all observations indicate that some burst/disk interaction is at work. As pointed out by Keek et al. (2014a), the absence of such a feature during the more luminous *superburst* of 4U 1820-30 (Ballantyne & Strohmayer, 2004; Strohmayer & Markwardt, 2002) is however puzzling as we would expect a bigger effect, especially in the Poynting Robertson scenario.

Clearly, the need for new data is pressing and Keek et al. (2016) already showed how new facilities could revolutionize the use of X-ray bursts to study accretion disks with spectral analysis. On the timing side, the *Large Area X-ray Proportional Counter* (LAXPC) instrument on *ASTROSAT* (Agrawal, 2006) could bring in a shorter time frame new constraints on the kHz QPO reaction to X-ray bursts: the regular observation of X-ray bursts and QPO emitters could notably increase the statistics presented in this paper and maybe allow to identify what is governing the ambivalent behavior we reported. With its higher effective area at high energies than the PCA, where the fractional RMS of the QPOs is the highest, this instrument could even allow the significant detection of kHz QPOs on short time scales at energies where the burst does no contribute. It might thus be possible to confirm whether there are really cases for which the bursts do not have any influence on the oscillations. Of course, transformational missions like LOFT (Feroci et al., 2012) would bring even stronger constrains and offer the capability to follow the evolution of the QPO signal during the burst.

2.3 Spectral timing tools for the study of kHZ QPOs

In this section, we will present the relevant tools to perform the spectral timing analysis of kHz QPO data. While most of the derivations are inspired by Uttley et al. (2014) we will also insist on particular aspects relevant to this work.

2.3.1 Cross spectrum: definition and uncertainties

The cross spectrum is defined as the DFT of the cross-correlation function between two light curves $x(t)$ and $y(t)$ (typically extracted in two different energy bands) and characterizes how the variability at frequency ν_n in $x(t)$ correlates linearly with the one in $y(t)$. Following the same notation as in Sect. 2.1.2, the cross spectrum can be computed as:

$$C_{XY} = X_n^* Y_n \tag{2.16}$$

Depending on the application, the cross spectrum is typically normalized in two different manners. The most common one is to transpose Equation 2.5 and express the cross spectrum in units of fractional

RMS per Hz:

$$C_{\mathrm{rms},XY} = \frac{2\delta t}{< x >< y > N} X_n^* Y_n \tag{2.17}$$

Alternatively, the scaling by the average count rates can be removed and the cross spectrum computed in absolute units squared per Hz:

$$C_{\mathrm{abs},XY} = \frac{2\delta t}{N} X_n^* Y_n \tag{2.18}$$

In order to ease the reading, in the following derivations we will drop the nature of the chosen normalization and simply use C_{XY}. We nonetheless emphasize on the fact that whatever choice is made, the same scaling needs to be adopted for the power spectra to retain consistency. As pointed out by Alston et al. (2013) and Uttley et al. (2014), in real applications, time lags (see Sect. 2.3.3) can be slightly different depending on the chosen normalization. We note however that in the case of this study, no significant difference was observed after thoroughly comparing both choices.

In a real application, similarly to power spectra, a single cross spectrum is usually very noisy. Consequently, to obtain reliable estimates, the cross spectra computed from numerous subsequent segments are often averaged together and binned in frequency following the exact same procedure as for power spectra (see Sect. 2.1.2). We note that in the case of kHz QPOs, when studying long observations with significant frequency variation, one can use "shift-and-add" techniques on the cross spectrum to avoid signal dilution (cf. Sect. 2.1.3). If M individual spectra were combined and the final spectrum binned over W frequencies, the $1\,\sigma$ uncertainty levels on both the real and imaginary parts of the final cross spectrum is:

$$\Delta C_{XY} = \sqrt{\frac{1}{2MW}\left[|S_X|^2|N_Y|^2 + |S_Y|^2|N_X|^2 + |N_X|^2|N_Y|^2\right]} = \sqrt{\frac{n^2}{2}} \tag{2.19}$$

with $|N_X|^2$ and $|N_Y|^2$ the noise power levels, and $|S_X|^2 = P_X - |N_X|^2$ and $|S_X|^2 = P_X - |N_X|^2$ the measured excess powers in both light curves. This equation, derived in Vaughan & Nowak (1997) is formally valid under the assumption that the noise processes in the two light curves are uncorrelated with both the source intrinsic signal powers and between each other. This hypothesis is however standardly made.

2.3.2 Coherence: raw measurement and intrinsic value

The raw coherence function between two light curves is defined by (Bendat & Piersol, 1986)[1]:

$$\gamma^2(f) = \frac{| < X(f)^* Y(f) > |^2}{< |X(f)|^2 >< |Y(f)|^2 >} = \frac{| < C_{XY}(f) > |^2}{< P_X(f) >< P_Y(f) >} \tag{2.20}$$

where $<>$ denotes the ensemble averaging over several segments/observations. The $1\,\sigma$ uncertainty on the coherence while averaging over MW values is given by:

$$\Delta\gamma^2(f) = \frac{\sqrt{2}\gamma^2(f)[1-\gamma^2(f)]}{|\gamma(f)|\sqrt{MW}} \tag{2.21}$$

[1]Some authors (e.g. Uttley et al., 2014) use a slightly different formula for the raw coherence, removing the Poisson noise contribution n^2 to the cross spectrum in the denominator. This notably slightly changes the errors obtained for lag measurements (see Sect. 2.3.3). In this work, we followed the prescription of Bendat & Piersol (1986) and Nowak et al. (1999). We nonetheless checked that this change had a negligible influence on the results presented below.

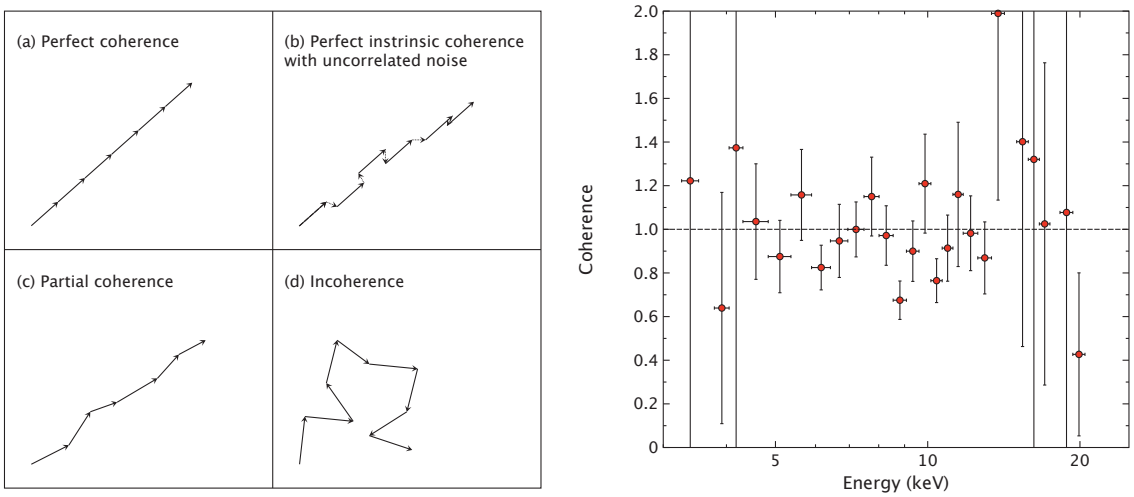

Figure 2.3: Left: Geometrical representation of the coherence function. Each vector corresponds to a single measurement of C_{XY} at a given frequency f. In the case of two perfect coherent signals (a), the cross spectrum will always be the same, the vectors will be perfectly aligned and $|\sum C_{XY}|$ will equal $\sum |C_{XY}|$ thus yielding $\gamma^2 = 1$. When adding uncorrelated noise on top of coherent signals (b), small vectors of random phases will be added on top of the original signal breaking the perfect alignment. As illustrated in (c), without knowledge about the expected amount of noise in the data, this cannot be distinguished for an intrinsically partially coherent process. If the signals are incoherent (d), the phases of the cross spectra will be uniformly distributed in $[-\pi; \pi]$ and for an infinite number of measurements, $\gamma^2 \to 0$. This figure was adapted from Nowak et al. (1999). **Right:** Example of the measured intrinsic coherence as a function of energy for the lower kHz QPO during the first RXTE observation of 4U1608-522 (10072-05-01-00). The QPO was detected and characterized with 1 Hz resolution PDS shifted and added on 1024 s time scale. The coherence measure was performed using the corresponding shifted and added cross spectrum on one QPO Lorentzian width. Each bin shows the intrinsic coherence between the light curve in the energy bin and a reference light curve obtained between 3 and 30 keV.

It is important to note that this function only has meaning with the ensemble average as it would systematically give 1 when computed on a single spectrum. Concretely, the coherence measures the amount of variability in the light curve $y(t)$ that can be predicted from $x(t)$ with a linear transformation (Bendat & Piersol, 1986): when $y(t)$ and $x(t)$ are linearly related, there exists a transfer function $H(f)$ giving $Y(f) = H(f)X(f)$ and $\gamma^2(f) = 1$. Otherwise, the Cauchy-Schwartz inequality ensures that $\gamma^2(f) < 1$. One can get a better feeling of the coherence function with a simple geometry representation of the cross spectrum as a vector in the complex plane (see Fig. 2.3 (left)).

In practice, because of the presence of noise in the data (typically Poisson counting noise), the *raw* coherence given by equation 2.20 does not measure the intrinsic coherence of the signal but the observed one including the loss of coherence introduced by uncorrelated noise. As derived by Vaughan & Nowak (1997), this formula needs to be modified in order to give a proper estimate of the real coherence of the signal:

$$\gamma_I^2(f) = \frac{| < C_{XY}(f) > |^2 - n^2}{(< |S_X|^2 >)(< |S_Y|^2 >)} \tag{2.22}$$

Similarly, Equation 2.21 can be modified to account for the presence of noise (Vaughan & Nowak,

1997). We give here the formula in the case of strong signals and high measured coherence:

$$\Delta\gamma_I^2(f) = \frac{\gamma_I^2(f)}{\sqrt{MW}}\sqrt{\frac{2n^4MW}{(|<C_{XY}(f)>|^2-n^2)^2}+\frac{|N_X|^4}{<|S_X|^2>^2}+\frac{|N_Y|^4}{<|S_Y|^2>^2}+\frac{MW\Delta\gamma^2(f)^2}{\gamma_I^4(f)}} \tag{2.23}$$

Figure 2.3 (right) shows an example of intrinsic coherence measurements as a function of energy for the lower kHz QPO. As can be seen, the coherence is compatible with unity throughout the whole RXTE energy range (as previously observed by de Avellar et al., 2013).

2.3.3 Frequency and energy dependent time lags

Using a polar representation for the DFTs $X(f) = A_X e^{i\psi_X}$ and $Y(f) = A_Y e^{i\psi_Y}$, equation 2.16 can be expanded as:

$$C_{XY}(f) = A_X A_Y e^{i\phi_{XY}} \ , \ \phi_{XY}(f) = \arg(C_{XY}(f)) = \psi_Y - \psi_X \tag{2.24}$$

This highlights $\phi_{XY}(f)$, the phase lag between the two light curves at frequency f. Usually, in order to ease the physical interpretation, the phase lag is then transformed into a time lag by dividing by the corresponding frequency:

$$\tau_{XY}(f) = \frac{\phi_{XY}(f)}{2\pi f} \tag{2.25}$$

As emphasized by Uttley et al. (2014), when a broad-band emission is considered, the choice of the denominator frequency can be problematic. In the case of narrow features like kHz QPOs however, it appears only natural to use the centroid frequency of the QPO. That being said, it is important to remember that a phase lag is only sensitive to variations inside $[-\pi;\pi]$ and that there is no way to distinguish between phenomena producing the same lags but separated by a multiple of $1/f$.

To compute error values for time lag measurements, the standard procedure is to use the raw coherence function which quantifies the scatter of the cross-spectrum vectors due to non-coherent contributions like Poisson counting noise (see Fig. 2.3 as well as Bendat & Piersol, 1986; Nowak et al., 1999):

$$\Delta\phi_{XY}(f) = \sqrt{\frac{1-\gamma^2(f)}{2\gamma^2(f)MW}} \tag{2.26}$$

It is important to note that the *raw* coherence should be used to estimate the lag error and not the intrinsic one in order to properly take into account the actual scatter of the cross spectrum.

Influence of dead time on time lag measurements

As mentioned in Section 2.1.2, the RXTE PCA is subject to dead time due to the instrument readout process. This induces anti-correlation between light curves extracted using the same PCUs, e.g. between two light curves in different energy ranges: if an event is detected in the energy range corresponding to the first one, the impacted PCU will be "dead" for a short amount of time, which will reduce the probability to simultaneously detect an event in the other energy range. We thus talk about dead time induced channel crosstalk (van der Klis et al., 1987). In a cross spectrum, this translates in a negative offset of the real part of the spectrum at all frequencies. To illustrate this and show the effect in an exaggerated manner, we shifted and added all the cross spectra between the 3–8 keV and 8–30 keV light curves corresponding to lower kHz QPO observations of 4U1636-536,

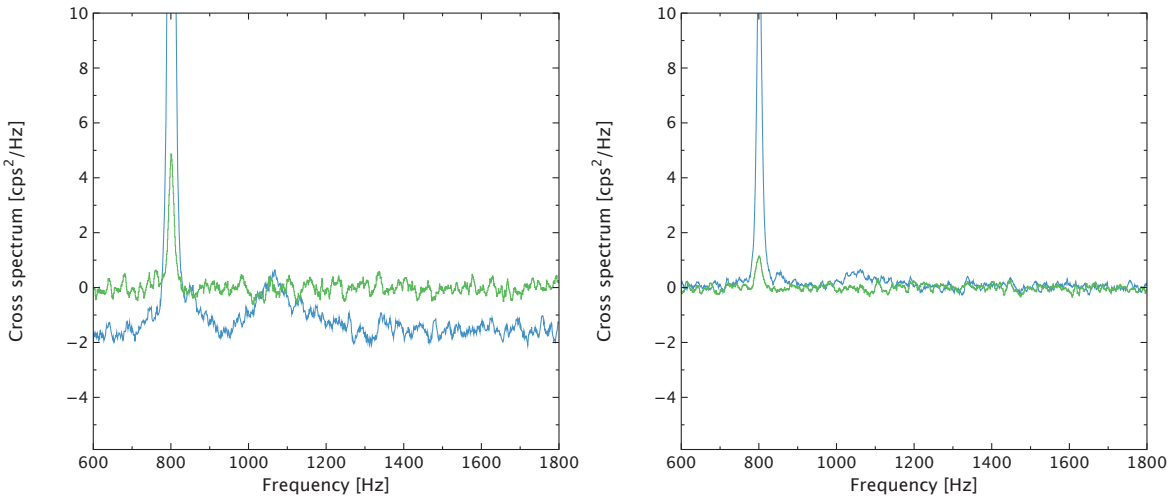

Figure 2.4: Illustration of the dead time influence on a cross spectrum. **Left:** Real (blue) and imaginary (green) parts of the cross spectrum obtained from the "shift-and-add" of all the cross spectra between the 3–8 keV and 8–30 keV light curves corresponding to all lower kHz QPO observations of 4U1636-536 using all PCUs for both energy bands. The individual spectra were computed from 1024 s intervals with 1 s integration time and $1/2^{12}$ s time resolution. The final cross spectrum was convolved with a 10 Hz averaging kernel for better visibility. One clearly sees the negative offset on the real part due to dead time induced channel crosstalk. If not correct, this would lead to an incorrect lag measurement. **Right:** Same figure but using independent PCUs for the two energy bands. As the counting noise is now uncorrelated, no dead time offset is visible. This is done at the expense of statistics and in practice, it is more interesting to correct the dead time bias by measuring it at high frequencies (see text).

and compared two cases: Figure 2.4 (left) shows the resulting cross spectrum when all the available PCUs are used to extract both light curves, while Figure 2.4 (right) was obtained with independent PCUs. One clearly sees that the first one is affected by dead time induced channel crosstalk and has a negative offset on the real part of the cross spectrum whereas the second one is unaffected.

If one does not take this effect into account, this creates a bias on the lag measurement and in the case of a too low signal power, this will make the lags tend towards $\pm\pi$. There exist several solutions to correct for this bias (Vaughan et al., 1999) but the most common one, proposed by van der Klis et al. (1987), is to subtract to the whole cross spectrum the Fourier amplitude measured at high frequencies where only the Poisson counting noise contributes to the variability (see e.g. Dieters et al., 2000; Wijnands & van der Klis, 2000; Wijnands et al., 2001; Altamirano & Méndez, 2015; Méndez et al., 2013). In the case of kHz QPOs, a suitable frequency range to perform this correction is typically 1350–1700 Hz. We note that one can verify the viability of the correction by checking that in the chosen frequency interval, no significant cross power can be found in the imaginary part.

Frequency dependent energy time lags of kHz QPOs

The most direct application of spectral timing tools for kHz QPOs is to look for time lags between the soft and hard X-ray emission at the kHz QPO frequency. Once the kHz QPO has been detected and characterized using a broad band PDS as described in Sect. 2.1, the first step is to extract two light curves, one in the soft X-rays and one in hard X-rays (3–8 keV and 8–30 keV in this work, see also Barret, 2013) and compute the corresponding cross spectrum (see Sect. 2.3.1). If the light curves were obtained using common PCUs, the bias introduced by dead time needs to be corrected following

the procedure explained in the previous section. The time lag between the soft and hard emission can then be computed using Equations 2.24 and 2.25. The corresponding $1\,\sigma$ error is finally obtained by measuring the *raw* coherence at the QPO frequency and applying Equation 2.26. In this work, we used the convention that a positive lag corresponds to the soft emission laging the hard emission and a negative lag to the soft emission being in advance.

As one can see from Equation 2.26, the easiest way to diminish the uncertainties on a lag measurement is to either average together more realizations (M) or bin up the cross spectrum in frequency (W). In the case of a single observation (see e.g. Vaughan et al., 1998; Kaaret et al., 1999), the number of available realizations is simply limited by the total observing time. One could however in principle average the cross spectrum over a very large frequency band as is done for AGNs and obtain a high W. In the case of kHz QPOs however, there is significant variability only in a narrow frequency range and the cross spectrum can typically be binned over one or two Lorentzian widths of the QPO profile (e.g. Barret, 2013; de Avellar et al., 2013). In this work, we chose to make all our measurements while binning on one Lorentzian width as a trade-off between better cross spectrum statistics and only using clean parts of the QPO profile. We nonetheless tested that our results were mostly not affected by a different choice.

In the case of systematic studies like the ones presented here, one can also make use of the known correlation of the source properties with the kHz QPO frequency (see e.g. van der Klis, 2006) and combine together observations with QPOs of similar frequencies. There are two equivalent manners to do so: the first one, adopted by Barret (2013) is to compute individual lags with their errors per QPO detection and fit a constant value to the distribution inside a frequency interval. The second one, adopted in this work, is to simply shift-and-add all the cross spectra and directly measure an overall time lag with its error (de Avellar et al., 2013). In both cases, there is a trade-off to be made to choose the size of the frequency intervals to consider: the larger the frequency interval, the better the statistics will be, but a too large frequency binning will hide potentially real time lag variations with frequency. We further note that for both methods, taking very large frequency intervals will not necessarily lead to the smallest error bars if there is lag variation in the interval: for the former, the scatter of the different measurements will increase, diminishing the constraint on the fit, and for the latter, the mixing of cross spectra with different lags will decrease the overall measured coherence and increase the error on the lag (see Sect. 2.3.2). For most kHz QPO sources, 100 Hz bins are typically a good choice, but for sources with a very large number of observations like 4U1608-522 or 4U1636-536, bins as small as 50 Hz can be adopted. An example of kHz QPO time lags variations with frequency is shown in Figure 2.5 (left).

Whereas both methods were found to be equivalent, the latter has the advantage of being applicable for all spectral timing products, but also to allow the extension of the frequency band over which a reliable estimate of a kHz QPO lag can be obtained. It is indeed well known that the detectability of the lower and upper kHz QPO decreases at low and high frequency respectively (Barret et al., 2006). As the frequency separation between both QPOs is roughly constant over a limited frequency range (Méndez & Belloni, 2007), it is possible to shift-and-add multiple power spectra using one QPO to obtain a significant detection of the other. The lag measurement for the second QPO is then simply obtained from the corresponding shifted-and-added cross spectrum.

Lag energy spectra of kHz QPOs

Although a simple lag measurement between the overall soft and hard emissions can already give valuable insights, when the statistics permit, it is often more useful to look at the dependence of

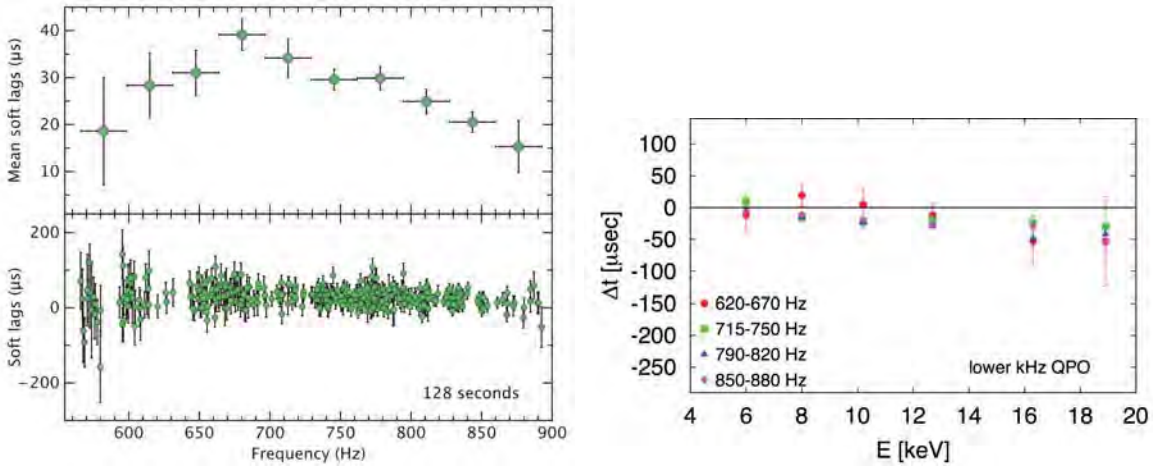

Figure 2.5: Left: Mean lower kHz QPO soft lags measured in 4U1608-522 by Barret (2013) between the 3–8 keV and 8–30 keV time series, binned in 10 adjacent QPO frequency intervals (top). The bottom panel shows the distribution of the individual lags measured on 128 s timescales. The lags show a clear dependency with frequency, with the most significant trend being the smooth decrease at frequencies above $\sim$ 650 Hz. **Right:** Lag energy spectra of the lower kHz QPO in 4U1636-536 computed in different QPO frequency ranges (taken from de Avellar et al., 2013).

the lag on energy at higher spectral resolution. This indeed allows the identification of the spectral components contributing to the lags, and the investigation of the causal relationship between the different emission components. In order to do that, instead of measuring the lag between two large energy bands, one can measure the time lag of each energy channel light curve with respect to a constant reference light curve. Provided that the signal is intrinsically coherent with the reference band at all energies (which is verified for kHz QPOs, see Sect. 2.4.3), by transitivity one can then observe the time lag between the variations in two individual channels.

During this procedure, the reference light curve can correspond to a specific energy channel of the instrument but it is usually preferable to use a broad-band one to maximize the sensitivity. If one does so, it is however necessary to subtract the light curve of the channel of interest from the reference one (if the channel is contained in the reference band) to avoid contamination from the Poisson noise component in the current channel which is correlated with itself in the reference light curve (Uttley et al., 2014). This means that each light curve is formally compared to a different reference (i.e. a different average energy), but provided that each channel does not individually contribute significantly to the reference, the subsequent effect on the lag energy spectrum remains small (Zoghbi & Fabian, 2011).

Similarly to the previous simple lag measurements, a lag energy spectrum can either be obtained from a single observation or, when studying overall trends in a source, by averaging cross-spectra measured during several observations featuring a kHz QPO in a given frequency range. We note that a systematic study is only valid under the assumption that the overall spectral shape of the source is the same for all the combined observations such that the reference band used always corresponds to roughly the same average energy. As previously mentioned, this is verified if one stacks kHz QPO observations from a limited QPO frequency range as the LMXBs spectra are known to strongly correlate with the QPO frequency (see e.g. Di Salvo et al., 2001). Another important aspect to keep in mind when combining observations from different epochs in the lifetime of the RXTE PCA is also

that the instrument response shifted through time. As a consequence, the available energy channels are not always exactly the same and it is necessary to use large energy bins. This way, minor changes in energy channel boundaries over the course of the observations considered in the average are small compared to the width of the energy bin.

Figure 2.5 (right) shows an example of such a lag energy spectrum obtained for the lower kHz QPO in 4U1636-536. One important aspect to keep in mind while looking at lag spectra is that the null value does not contain a particular meaning as it depends on the chosen reference band. The lags should therefore only be considered in relative units.

2.3.4 Covariance spectrum: definition and interpretation

Computing a covariance spectrum

The covariance spectrum was first introduced in X-ray astronomy by Wilkinson & Uttley (2009). Whereas the lag spectrum uses the phase of the cross spectrum of light curves at different energies (X_i) with respect to a reference (Y), the covariance spectrum can be seen as its equivalent for the amplitude and measures at each energy the amount of variability that is coherent with the reference band. It is defined as:

$$Cov_{X_iY}(f) = \sqrt{\frac{\Delta f(|\overline{C}_{X_iY}(f)| - n^2)}{\overline{P}_Y(f) - P_{Y,noise}}} \tag{2.27}$$

where the over line denotes an averaging over the frequency band of interest Δf (in this work, the QPO Lorentzian width). As for the lag spectrum, if the individual light curves X_i are included in the reference Y, they need to be individually subtracted to avoid contamination. The covariance is usually expressed either in fractional RMS or in absolute values. Depending on the choice, the cross spectrum and powers need to be normalized accordingly (see Sect. 2.1.2 and 2.3.1).

Using Equation 2.22, the covariance definition can be modified so as to isolate the intrinsic coherence between the two light curves:

$$Cov_{X_iY}(f) = \sqrt{\Delta f \gamma_I^2(f)(\overline{P}_{X_i}(f) - P_{X_i,noise})} \tag{2.28}$$

In case of perfect coherence, one then sees that the covariance spectrum is equivalent to the more widely used RMS spectrum $\sigma_{X_i}(f) = \sqrt{\Delta f(\overline{P}_{X_i}(f) - P_{X_i,noise})}$ (see e.g. Gilfanov et al., 2003). The main difference is that the covariance spectrum benefits from much better statistics than the RMS spectrum (see Wilkinson & Uttley, 2009; Uttley et al., 2011, 2014, for details). The ultimate reason for this is that whereas the rms spectrum considers the variability in each each energy channel independently, the covariance spectrum uses the coherence with the reference band to act as a matched filter. Of course, this is valid at the expense of assuming perfect intrinsic coherence of the signal of interest throughout the whole spectrum, which is the case for kHz QPOs (see Sect. 2.4.3). Under this assumption, the $1\,\sigma$ error on the covariance is:

$$\Delta Cov_{X_iY}(f) = \sqrt{\frac{Cov_{X_iY}(f)^2\sigma^2_{Y,noise} + \sigma^2_Y(f)\sigma^2_{X_i,noise} + \sigma^2_{X_i,noise}\sigma^2_{Y,noise}}{2MW\sigma^2_Y(f)}} \tag{2.29}$$

where $\sigma^2_{Z,noise} = P_{Z,noise}\Delta f$ is the integrated noise power.

Similarly to the lag spectrum, a covariance spectrum can either be obtained from an individual observation or averaged across several similar observations to obtain an overall spectral shape of the

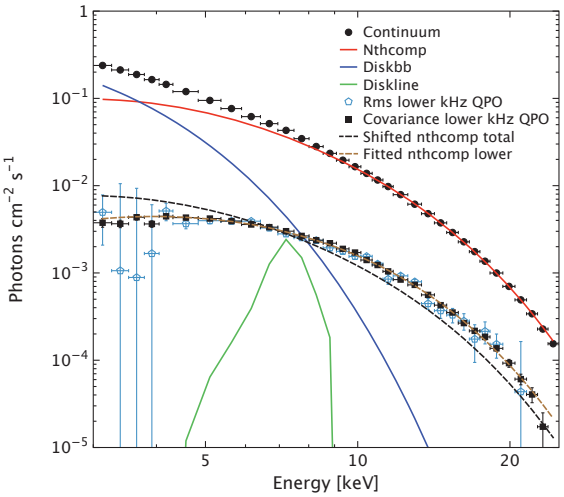

Figure 2.6: Left: Comparison of the decomposition of the continuum spectrum (black circles) obtained from the first ObsID of 4U1608-522 (10072-05-01-00) with the covariance (black squares) and rms spectra (open blue points) of the lower kHz QPO detected in the same data segment (figure taken from Peille et al., 2015).

variability of interest using exactly the same method. A very interesting case is when the covariance spectrum is measured under a single instrument configuration and computed in absolute units. It can indeed be seen as the emission spectrum of the studied variability and fitted like a normal X-ray spectrum. It is then possible to compare it for instance with the shape of the continuum emission. An example of such a comparison is shown in Figure 2.6 (left).

2.4 The spectral-timing properties of the kHz QPOs

2.4.1 Scientific context

While X-ray data is intrinsically the combination of two pieces of information, each detected X-ray photon being attributed an arrival time and energy, those two aspects of a source emission have often been treated separately. kHz QPOs have not been an exception to this rule and most authors focused on their timing properties (frequency, quality factor and rms amplitude) and tried to independently study correlations with the spectral properties of LMXBs (see e.g. Méndez et al., 1999; Méndez & van der Klis, 1999; van der Klis, 2000; Di Salvo et al., 2001). Until recently, only two kHz QPO observations had indeed been thoroughly analyzed using spectral timing tools combining both sources of information (Vaughan et al., 1998; Kaaret et al., 1999). For a few years, these techniques have however met a growing success for the understanding of AGNs (see Chapter 1) and this triggered a renewed interest for applying those to high frequency variability in LMXBs.

Barret (2013) thus reported soft lags in the lower kHz QPO emission of 4U1608-522 varying with frequency and found a bump in the highest quality lag-energy spectrum suggestive of the presence of reverberation similarly to what is now routinely detected in AGNs. A simultaneous study confirmed the soft lags for the lower kHz QPO in another LMXB (4U1636-536) and also reported a possible hard lag for the upper kHz QPO in the same source and a lag consistent with zero in 4U1608-522 (de Avellar et al., 2013). Whereas the above mentioned studies used all or a significant part of the available PCA data for these sources, the RXTE archives still contain several hundreds of ks of kHz QPO data

from a large set of neutrons star LMXBs. As little was known about the spectral timing properties of the upper kHz QPO because of its poorer quality factor making its detection more difficult, in the following publication, we decided to study 4U1728-34 which is known for its high upper kHz QPO duty cycle but also to extend the range of spectral-timing techniques used for kHz QPOs.

2.4.2 Publication 2

The Astrophysical Journal, 811:109 (8pp), 2015 October 1 doi:10.1088/0004-637X/811/2/109

THE SPECTRAL-TIMING PROPERTIES OF UPPER AND LOWER kHz QPOs

Philippe Peille[1,2], Didier Barret[1,2], and Phil Uttley[3]
[1] Université de Toulouse; UPS-OMP; IRAP; Toulouse, France; philippe.peille@irap.omp.eu
[2] CNRS; Institut de Recherche en Astrophysique et Planétologie; 9 Av. colonel Roche, BP 44346, F-31028 Toulouse cedex 4, France
[3] Anton Pannekoek Institute, University of Amsterdam, Postbus 94249, 1090 GE Amsterdam, The Netherlands
Received 2015 February 9; accepted 2015 August 4; published 2015 September 28

ABSTRACT

Soft lags from the emission of the lower kilohertz quasi-periodic oscillations (kHz QPOs) of neutron star low-mass X-ray binaries have been reported from 4U1608-522 and 4U1636-536. Those lags hold prospects for constraining the origin of the QPO emission. In this paper, we investigate the spectral-timing properties of both the lower and upper kHz QPOs from the neutron star binary 4U1728-34, using the entire *Rossi X-Ray Timing Explorer* archive on this source. We show that the lag-energy spectra of the two QPOs are systematically different: while the lower kHz QPO shows soft lags, the upper kHz QPO shows either a flat lag-energy spectrum or hard variations lagging softer variations. This suggests two different QPO-generation mechanisms. We also performed the first spectral deconvolution of the covariance spectra of both kHz QPOs. The QPO spectra are consistent with Comptonized blackbody emission, similar to the one found in the time-averaged spectrum, but with a higher seed-photon temperature, suggesting that a more compact inner region of the Comptonization layer (boundary/spreading layer, corona) is responsible for the QPO emission. Considering our results together with other recent findings, this leads us to the hypothesis that the lower kHz QPO signal is generated by coherent oscillations of the compact boundary layer region itself. The upper kHz QPO signal may then be linked to less-coherent accretion-rate variations produced in the inner accretion disk, and is then detected when they reach the boundary layer.

Key words: accretion, accretion disks – stars: individual (4U1728-34) – stars: neutron – X-rays: binaries

1. INTRODUCTION

Since their first detection in neutron star low-mass X-ray binaries soon after the launch of the *Rossi X-Ray Timing Explorer* (*RXTE*; Bradt et al. 1993; Strohmayer et al. 1996; van der Klis et al. 1996), kilohertz quasi-periodic oscillations (kHz QPOs) have generated much interest. They are considered to be a potential probe of general relativity due to the commensurability of their frequencies with the orbital frequency of matter very close to the neutron star surface. Until now, no model could account for all of the properties of these oscillations (see van der Klis 2006, p. 39) and an application to testing strong field general relativity remains speculative. Until recently, most studies on kHz QPOs focused on their frequency, quality factor, and spectral and rms amplitude properties. However, Barret (2013) and de Avellar et al. (2013) recently reintroduced energy-dependent time lags long after the first detection of kHz QPO soft lags (variations in soft photons lagging those of hard photons) in the early years of *RXTE* (Vaughan et al. 1998). In active galactic nuclei (AGNs), high-frequency soft lags are now routinely detected (de Marco et al. 2011; Emmanoulopoulos et al. 2011; Tripathi et al. 2011; Zoghbi & Fabian 2011; Cackett et al. 2013). Broad Fe K lags have also been reported from several AGNs and interpreted as due to the light-travel time between the central hard irradiating sources and the reverberating disks (Zoghbi et al. 2012; Kara et al. 2013a, 2013b and see Uttley et al. 2014 for a review). Soft lags were also seen at frequencies above 1 Hz in the black hole X-ray binary GX 339-4 and were attributed to the reverberation of blackbody emission from the disk in response to driving Comptonized continuum variations (Uttley et al. 2011).

Soft lags for the lower kHz QPO were found in 4U1608-522, as well as hints for reverberation from the detection of a bump around the Fe line energy in the highest-quality lag-energy spectrum (Barret 2013). These soft lags were also reported in 4U1636-536 by de Avellar et al. (2013). Because the lower kHz QPOs are easier to detect, owing mostly to their higher quality factor compared to the upper kHz QPOs, very little is known about the lag properties of the latter. Nonetheless, de Avellar et al. (2013) reported a constant hard lag in the upper kHz QPOs from 4U1636-536 (but a lag consistent with zero from 4U1608-522). The *RXTE* data archives contain a wealth of observations with kHz QPOs from a large sample of neutron star systems. The detection of lags suggests that we should take a fresh look at these observations, using a wider range of spectral-timing techniques, because these data may enable us to understand where the kHz QPOs are produced. In this paper, we investigate the spectral-timing properties of the two kHz QPOs from 4U1728-34, for which the duty cycles of the lower and upper kHz QPO appearance in continuous data sets (ObsID in *RXTE* terminology) are comparable.

2. DATA ANALYSIS

We have retrieved all of the archival observations of 4U1728-34. In order to systematically detect the QPOs, the data in each event file is segmented in intervals of 1024 s, and mean Fourier power density spectra (PDSs) are computed as the average of 1024 PDSs integrated over 1 s (with $1/2^{12}$ s time resolution, in the 3–30 keV band). X-ray bursts, as well as count rate drops, were carefully removed from the data. QPOs are searched for as excess powers between 550 and 1300 Hz and fitted with the maximum likelihood method of Barret & Vaughan (2012). In each segment, zero, one, or two QPOs are thus detected and characterized. A QPO is considered significantly detected when the ratio between the Lorentzian normalization and its 1σ error is larger than 3 (Boutelier et al. 2010).

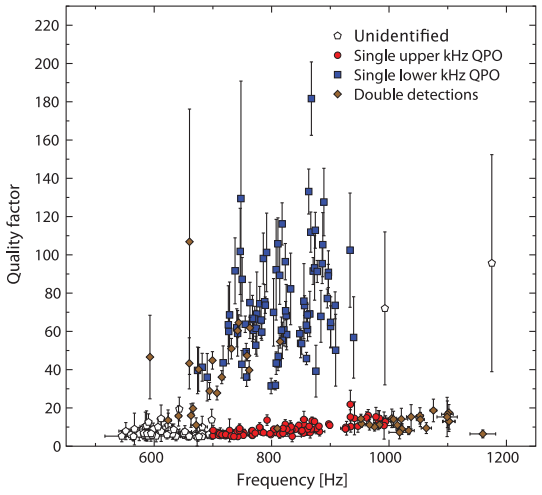

Figure 1. Quality factors of all of the kHz QPOs detected from 4U1728-34 on a timescale of 1024 s. Each point corresponds to one event file. In this diagram, lower and upper kHz QPOs follow two different branches and can thus be identified from their position. QPOs falling in between the two groups of QPOs are not considered (listed as unidentified).

2.1. QPO Identification

Among the properties of high-frequency QPOs, it is well known that the lower and upper kHz QPOs follow different tracks in a quality factor versus frequency diagram (Barret et al. 2006). In these diagrams, the lower kHz QPO shows larger quality factors rising with frequency (and dropping rapidly at the highest frequencies), while the upper kHz QPO shows smaller quality factors that follow a smooth rising trend with frequency. In this paper, we identify kHz QPOs based on their position in the quality factor-frequency diagram.

For this purpose, within each event file, all of the segments of data in which a QPO is significantly detected are shifted-and-added with respect to the mean QPO frequency. In case two QPOs were detected, the one with the highest duty cycle is chosen, by default the one of lower frequency. The event file averaged shifted-and-added PDS is then searched for excess powers, and one or two QPOs (the lower and/or the upper) are fitted and a quality factor (Q) is derived. This produces one or two values of Q per event file. The quality factors of all the QPOs detected from 4U1728-34 are shown in Figure 1. As can be seen, the lower and upper kHz QPO branches are easy to distinguish, allowing us to identify all event files as containing either a lower, or an upper or even twin kHz QPOs. Taking a conservative approach, we leave out segments of data containing QPOs with quality factors that are less than 5 and QPOs at the boundaries between the two branches. For event files in which a single QPO is detected, we define lower kHz QPOs as those with frequencies between 650 and 950 Hz, and quality factors larger than 30. Similarly, upper kHz QPOs are defined as those with frequencies between 700 and 1200 Hz and quality factors between 5 and 25. The identification of the lower and upper kHz QPOs is obvious in the 24 event files (corresponding to 17 ObsIDs) in which they are simultaneously detected (maroon diamonds in Figure 1). Detections with quality factors below 25 at frequencies smaller than 700 Hz were ignored, as they correspond to an overlap of the quality factor versus frequency correlations of both QPOs, hampering their identification in a reliable way.

2.2. Frequency Dependent Lags

For computing the lags, we follow Barret (2013). Namely, we compute the lags between the 3–8 keV and 8–30 keV emission, over continuous data segments of each event file. We average 1024 segments of 1 s duration and obtain the lags from the cross spectrum, averaged over the frequency range covered by the FWHM of the QPO Lorentzian profile, as derived from fitting the QPO profile averaged over the 1024 segment PDSs. To display trends otherwise not visible, the lags are also computed to a higher signal-to-noise (S/N) from the shifted-and-added cross spectra averaged over broader QPO frequency ranges. In order to correct for dead-time-induced cross talk, we subtracted from each cross spectrum the average Fourier amplitude in the 1350–1700 Hz band where Poisson fluctuations are the only source of variance, as suggested by van der Klis et al. (1987). The lags of both the lower and upper kHz QPOs are shown in Figure 2, together with the frequency-averaged values. From that figure, it is clear that the lower kHz QPO shows a soft lag, while for the upper kHz QPO, there is an indication of a hard lag at high frequencies. The soft lags for the lower kHz QPOs of 4U1728-34, which are reported for the first time here, are comparable to those of 4U1636-536 (de Avellar et al. 2013) and about twice as small as the lags of 4U1608-522 (Barret 2013; de Avellar et al. 2013).

One can also extend the frequency range for the lag measurements by shifting-and-adding the PDSs containing a lower kHz QPO to obtain a significant detection of the upper kHz QPO. This covers the upper frequency range spanned by the upper kHz QPO (above 1000 Hz). The lags obtained are shown in Figure 2, indicating a hard lag for the upper kHz QPO, although the error bars are quite large due to the weakness of the QPO signal (the rms amplitude of the upper kHz QPO keeps decreasing with frequency). A constant time lag fitted to the binned lags versus frequency distribution above 800 Hz yields -8.9 ± 2.3 μs.[4] A trend for the hard lag to increase with frequency is also suggested. The same procedure can be applied to segments containing upper kHz QPOs. This then extends the frequency range for the lags of the lower kHz QPO toward the lowest frequencies. Those lags are also reported in Figure 2, showing that the lags measured, although with large error bars, may be consistent with zero, possibly breaking the trend of the soft lags increasing when the frequency decreases. Higher quality data are required before firm conclusions can be drawn.

2.3. The Energy Spectrum of the Lags

We now wish to examine how the lags vary with energy. In each energy bin, using the same procedure as described above, the lag is computed between the light curve in that bin and the light curve in the reference energy band[5] (3–25 keV), where the S/N ratio of the QPO detection is the highest. The light curve in the energy bin considered is subtracted from the reference light curve to ensure that Poisson noise remains uncorrelated

[4] We note that in order to avoid using non-independent measurements we recomputed the time lags obtained from shifting-and-adding the lower kHz QPO without using the segments where both QPOs had already been detected.
[5] We cut our analysis at 25 keV in order to avoid the background-dominated part of the spectra.

The Astrophysical Journal, 811:109 (8pp), 2015 October 1

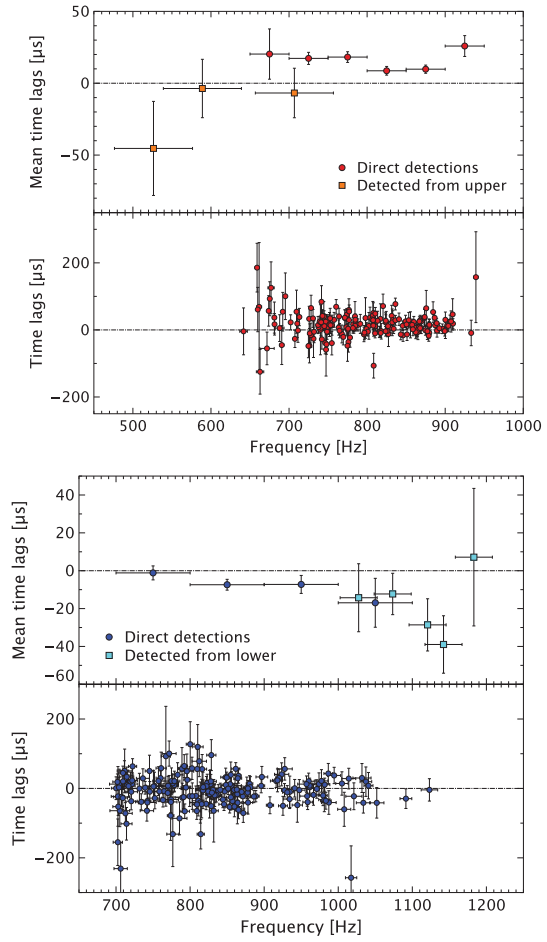

Figure 2. Time lags between the 3−8 keV and 8−30 keV time series as a function of frequency for the lower (top) and upper (bottom) kHz QPOs from 4U1728-34. A soft lag is positive. For each QPO, the upper part of the figure shows the distribution of the lags computed after shifting-and-adding all of the detected QPOs inside adjacent frequency bins (circles). To expand the frequency range, the PDSs containing an upper kHz QPO were shifted-and-added to obtain a significant detection of the lower kHz QPO, and vice-versa (squares). The bottom parts show the lags computed from the original individual detections on 1024 s segments. Clearly the lag behavior of the two QPOs is different. While the lower kHz QPO shows a soft lag, a hard lag is suggested for the upper kHz QPO.

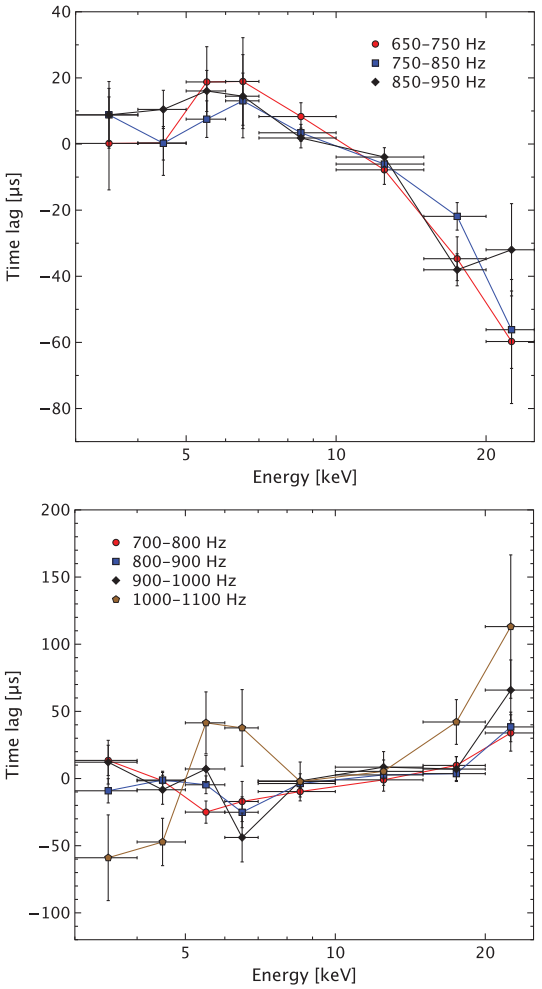

Figure 3. Lag-energy spectra of the lower (top) and upper (bottom) kHz QPOs of 4U1728-34, obtained by averaging cross-spectra within different frequency intervals. We note that these spectra should be looked at in relative units: a zero lag value only means that the given energy band is in phase with the reference band and its position in the spectra depends on the choice of the latter.

(Uttley et al. 2011, 2014). A mean lag-energy spectrum can be computed from the shifted-and-added cross spectrum over a given set of QPO segments. To improve the statistical errors on the lag-energy spectrum, we have used relatively large energy bins and grouped the data within adjacent frequency intervals. This way, minor changes in energy channel boundaries over the course of the observations considered in the average are small compared to the width of the energy bin. The lag-energy spectra of the lower and upper kHz QPOs of 4U1728-34 are shown in Figure 3. It is striking that the overall shapes of the lag-energy spectra of the two QPOs are very different (as illustrated by Figure 4). As for 4U1608-522 and 4U1636-536 the lag-energy spectra of the lower kHz QPO of 4U1728-34 show a smooth decrease with energy. At the lowest energy, the lag is positive, indicating that on average soft photons arrive after the broad continuum, while at the highest energy the lag is negative, indicating that hard X-ray photons on average reach the observer before the photons from the broad continuum. Although the energy resolution of the lag-energy spectrum is degraded as a result of the energy binning, there is no clear feature around 6–7 keV. Trying narrower binning degrades the statistics and prevents any features to be seen around these energies. As suggested by the flatness of the frequency dependency of the lower kHz QPO lags shown in Figure 2, the lag-energy spectrum does not show much dependence on frequency: the three frequency intervals considered in the analysis yield three lag-energy spectra consistent with one another within error bars. As for the

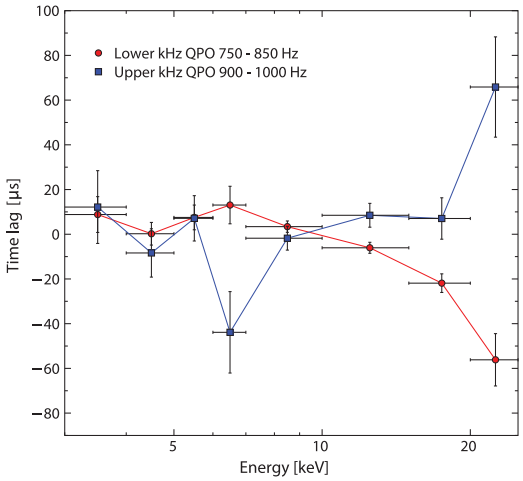

Figure 4. Comparison of the lag-energy spectra obtained for the lower kHz QPO between 750 and 850 Hz (red circles), and for the upper kHz QPO between 900 and 1000 Hz (blue squares). We note that these spectra should be looked at in relative units: a zero lag value only means that the given energy band is in phase with the reference band and its position in the spectra depends on the choice of the latter.

lag-energy spectrum of the upper kHz QPO, the shape is very different, in the sense that the lags show a plateau that is consistent with zero and then may rise with energy above ∼10 keV. The same trend was present in the lag-energy spectra of the upper kHz QPOs of 4U1608-522 and 4U1636-536, although with a larger scatter (de Avellar et al. 2013). One striking feature of Figure 3 is the last frequency interval (1000–1100 Hz) in which the lag-energy spectrum breaks the trend and shows a clear bump between 5 and 10 keV.

2.4. Covariance Spectra

As a by-product of the above analysis, one can also compute the frequency resolved covariance spectra of the two kHz QPOs, in the same frequency intervals and over the same energy bins. The covariance spectrum measures the amplitude of the variability in each energy bin, which is correlated with the variations in the reference band (see Wilkinson & Uttley 2009; Uttley et al. 2011, 2014 for details). In the case where the variability is spectrally coherent, i.e., variations are strongly correlated across all energies (which has been reported for the lower kHz QPO by de Avellar et al. 2013), the covariance spectrum is equivalent to the rms spectrum (e.g., Gilfanov et al. 2003), albeit with significantly better S/N (see Figure 6). The covariance spectra are shown in Figure 5, in which they are normalized by the mean spectra for the same data sets, i.e., to relative rms units. These are the first covariance spectra ever shown for kHz QPOs.

Gilfanov et al. (2003) found that the rms spectrum of the QPOs was consistent with the Comptonized blackbody emission assumed to originate from the boundary layer, with no obvious contribution from the accretion disk blackbody emission. Our covariance spectra are consistent with this overall behavior, with a drop in fractional covariance toward lower energies, and a flattening at higher energies, which could be due to the presence of a constant disk component diluting

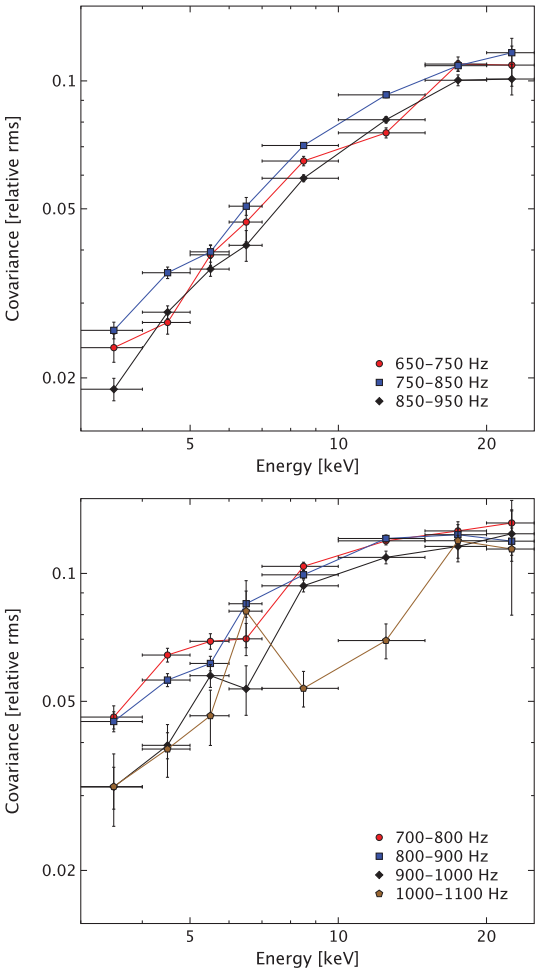

Figure 5. Fractional (relative rms) covariance spectra of the lower (top) and upper (bottom) kHz QPOs of 4U1728-34, obtained by averaging cross-spectra within different frequency intervals.

the harder variability (see Figure 5). To further confirm this, we performed a spectral deconvolution of all the covariance spectra obtained from the different ObsIDs. After grouping them by QPO type and frequency[6] to account for possible spectral changes, we fitted them simultaneously with a Comptonized emission model (`wabs*nthcomp` in `xspec 12.8`), i.e., in each bin as many covariance spectra as ObsID were simultaneously fitted.[7] The hydrogen column density was fixed to $N_H = 2.6 \times 10^{22}$ cm^{-2} (D'Aí et al. 2006) and only the normalization was allowed to vary between observations inside a frequency bin. We thus obtained good fits (reduced

[6] Only ObsIDs with at least two segments of 1024 s containing a QPO were kept in order to obtain covariance spectra with a sufficiently high S/N ratio.

[7] Some ObsIDs during which the response changes were split such that each spectrum has its correct response matrix. However, this is rather rare and we chose to keep the ObsID denomination in the rest of the paper to avoid confusion.

The Astrophysical Journal, 811:109 (8pp), 2015 October 1 Peille, Barret, & Uttley

Table 1
χ^2(dof) Values Obtained from the Joint Fits of the Mean and Covariance Spectra Corresponding to the Data Segments with kHz QPOs Using Different Methods

QPO Type	Frequency	All Linked	kT_e Free	Γ Free	kT_{seed} Free	All Free	#ObsID
Lower	650–750	1603(431)	1375(430)	1133(430)	1051(430)	1044(428)	7
	750–850	2974(857)	2680(856)	2279(856)	2116(856)	2099(854)	12
	850–950	1334(447)	1089(446)	770(446)	701(446)	692(444)	7
Upper	700–800	4025(915)	4025(914)	3991(914)	3933(914)	3920(912)	14
	800–900	3612(881)	3554(880)	3355(880)	3190(880)	3173(878)	13
	900–1000	1232(317)	1179(316)	1070(316)	1011(316)	998(314)	4
	1000–1100	194(95)	177(94)	178(94)	185(94)	172(92)	2

Note. The joint fits were conducted using the `xspec` model `wabs*(ntchomp+diskline+diskbb)`. For the covariance spectra, only the normalization of the `nthcomp` component was kept non-null. Depending on the cases, either the electron temperature (kT_e), the Γ shape parameter, the seed-photon temperature (kT_{seed}), none, or all of the parameters were allowed to differ between the covariance and the mean spectra. In all cases, the hydrogen column density was fixed to $N_H = 2.6 \times 10^{22}$ cm^{-2} (D'Aí et al. 2006). The last column indicates how many ObsIDs were combined in each frequency bin.

Table 2
Results of the Joint Fit of the Mean and Covariance Spectra Corresponding to the Data Segments with kHz QPOs

QPO Type	Frequency (Hz)	kT_{seed}(mean) (keV)	kT_{seed}(cov) (keV)	Γ	kT_e (keV)	E_{line} (keV)	kT_{in} (keV)	χ^2 (dof)
Lower	650–750	$1.25^{1.29}_{1.21}$	$2.17^{2.21}_{2.14}$	$2.20^{2.23}_{2.17}$	$3.51^{3.55}_{3.49}$	$6.58^{6.60}_{6.55}$	$0.83^{0.85}_{0.80}$	1051 (430)
	750–850	$1.12^{1.16}_{1.09}$	$2.08^{2.11}_{2.06}$	$2.12^{2.14}_{2.09}$	$3.28^{3.31}_{3.26}$	$6.56^{6.58}_{6.55}$	$0.73^{0.76}_{0.70}$	2116 (856)
	850–950	$1.12^{1.16}_{1.07}$	$2.17^{2.20}_{2.14}$	$2.01^{2.04}_{1.99}$	$3.07^{3.09}_{3.05}$	$6.65^{6.67}_{6.62}$	$0.74^{0.77}_{0.71}$	701 (446)
Upper	700–800	$1.43^{1.46}_{1.41}$	$1.80^{1.82}_{1.77}$	$2.37^{2.39}_{2.35}$	$9.56^{9.96}_{9.15}$	$6.60^{6.61}_{6.59}$	$1.05^{1.06}_{1.03}$	3933 (914)
	800–900	$1.28^{1.30}_{1.25}$	$1.84^{1.87}_{1.82}$	$2.35^{2.36}_{2.33}$	$6.00^{6.09}_{5.88}$	$6.58^{6.59}_{6.56}$	$0.87^{0.89}_{0.85}$	3190 (880)
	900–1000	$1.14^{1.16}_{1.11}$	$1.88^{1.93}_{1.83}$	$2.32^{2.34}_{2.30}$	$4.56^{4.66}_{4.49}$	$6.53^{6.56}_{6.51}$	$0.68^{0.70}_{0.66}$	1011 (316)
	1000–1100	$1.25^{1.33}_{1.21}$	$2.15^{2.47}_{1.84}$	$2.21^{2.30}_{2.13}$	$3.57^{3.62}_{3.52}$	$6.66^{6.71}_{6.59}$	$0.80^{0.83}_{0.74}$	185 (94)

Note. The joint fits were conducted using the `xspec` model `wabs*(ntchomp+diskline+diskbb)`. For the covariance spectra, only the normalization of the `nthcomp` component was kept non-null. Only the normalization and the seed-photon temperature were allowed to differ from mean spectra. kT_{seed} corresponds to the temperature of the seed photons of the `nthcomp` component, Γ to a shape parameter of this component, kT_e to the temperature of the Comptonizing electrons, E_{line} to the centroid energy of the iron line (only used during the fit of the mean spectrum), and kT_{in} to the inner temperature of the accretion disk (only used during the fit of the mean spectrum). The sub- and superscripts give the 1σ error *ranges* (i.e., best-fitting value plus lower and upper error bars respectively).

$\chi^2 \sim 1.0-1.3$). Interestingly enough, the models found for the lower kHz QPOs were all compatible within error bars, suggesting that the spectral shape of this emission is constant with frequency.

We now wish to see whether the spectral shape of the covariance spectra can be linked to a component in the total emission spectrum of the source (i.e., the mean, time-averaged, spectrum), which may also contain components that do not vary on the kHz QPO timescale (e.g., Gilfanov et al. 2003). The covariance spectra are therefore jointly fitted with their corresponding mean spectra. We use the common decomposition of the total emission into an accretion disk, a Comptonized component, and a relativistically broadened iron line (in `xspec`: `wabs*(diskbb+nthcomp+diskline)`) for the mean spectra (Barret 2013). Following the same idea as Gilfanov et al. (2003), who tried to identify the shape of the rms spectrum of the lower kHz QPO with the disk-subtracted spectrum of the source, only the Comptonized component is retained for the covariance spectra. The hydrogen column density is fixed, as well as the parameters of the iron line, using an inclination angle of $i = 50°$ (Shaposhnikov et al. 2003) and the default model parameters set otherwise (a disk emissivity dependence in R^{-2}, $R_{in} = 10\ r_g$, and $R_{out} = 1000\ r_g$). During the fits, the normalization of each component is left free between ObsIDs. We note that letting only the global normalization vary does not change the fitted parameters significantly, but only degrades the quality of the fits. Forcing all of the parameters of the Comptonization component to be the same for the mean and covariance spectra yields bad fits, but freeing the seed-photon temperature corrects them: once this is done, the fits are as good as those obtained with all of the parameters free, i.e., untying other parameters from the mean spectrum does not significantly change the fit statistic (see Table 1). Note that the seed-photon temperature is found to be systematically higher for the covariance spectra than for the mean spectra (see Table 2 and Figure 7 for an illustrative example of one ObsID).

The chosen decomposition for the continuum emission is one among the many others that work well with neutron star binaries (Lin et al. 2007). To test the robustness of our results against the choice of the continuum, we replaced the disk emission with a simple blackbody (`bbodyrad`) or replaced the Comptonization component with a broken power law (`bknpower`). Very similar results were found after the replacement of the thermal component: allowing a higher seed-photon temperature in the covariance spectra than in the continuum corrects the fits and yields similar final χ^2 values, as with `diskbb` (albeit slightly larger in six out of seven cases). However, when the Comptonization component is replaced by a broken power law, fits of comparable quality as before are only obtained when the continuum and covariance spectra are completely untied. We also note that the fits with the

parameters of the covariance tied to the continuum yield systematically worse χ^2 values in both cases. Our results were therefore found to be robust against the change of the thermal component, but in the absence of a significant change in all of the final χ^2 values of the fits, it is difficult to use this analysis as a way to disentangle the various spectral decompositions that can fit neutron star spectra.

It is important to mention that the fits using a single set of model parameters were made while combining the emission of the source from many observations grouped together using relatively large kHz QPO frequency ranges and therefore slightly different source spectra (Di Salvo et al. 2001). This explains the relatively poor χ^2 values obtained here.[8] Consistent with this explanation, we fitted the mean and covariance spectra by pairs, and found total reduced χ^2 for each frequency bin, typically around 1 for the different frequency/QPO combinations, when the seed-photon temperature of the two spectra were untied. As before, the seed-photon temperature was systematically found to be higher in the covariance spectra than in the mean spectrum, with values consistent with the previous analysis (simultaneous fits of all the spectra in one frequency bin).

In order to verify if the feature seen in 4U1728-34 is unique to this source or shared with others, we have carried out the same analysis on the first ObsID of 4U1608-522, namely 10072-05-01-00, which is known to contain QPO data of particularly high quality (see, e.g., Barret et al. 2005). A similar result was thus found (see Figure 6), with a decomposition of the continuum consistent within error bars with the one shown in Barret (2013). This supports the idea that this may be a common feature of the kHz QPOs and that their spectra are systematically harder than the Comptonization component of the continuum.

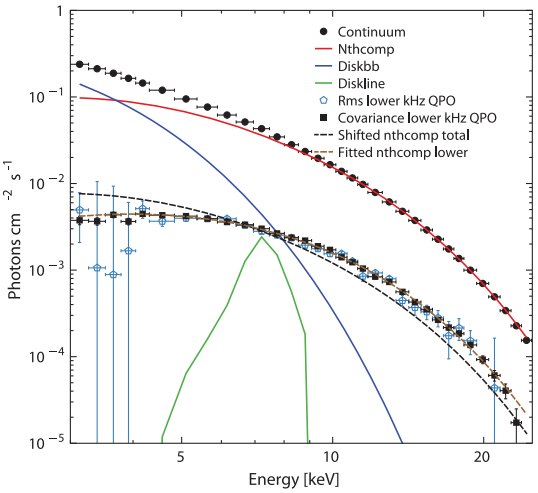

Figure 6. Comparison of the decomposition of the continuum spectrum (black circles) obtained from the first ObsID of 4U1608-522 (10072-05-01-00), with the covariance (black squares) and rms spectra (open points) of the lower kHz QPO detected in the same data segment. This decomposition was obtained from the joint fit of the covariance and continuum spectra ($\chi^2 = 94.89$ (56)). The continuum spectrum includes a Comptonization component (`nthcomp`, solid red line, $\Gamma = 1.96^{2.02}_{1.90}$, $kT_e = 2.61^{2.65}_{2.58}$ keV, $kT_{seed} = 1.10^{1.28}_{0.92}$ keV), a disk thermal emission (`diskbb`, solid blue line, $kT_{in} = 0.98^{1.07}_{0.88}$ keV), and a fluorescence iron line (`diskline`, solid green line, $E_{line} = 7.20^{7.31}_{7.10}$ keV). The dashed maroon line corresponds to the Comptonization component of the continuum spectrum fitted to the covariance spectrum, but allowing only the normalization and the seed-photon temperature to vary. The seed-photon temperature was thus found to be higher in the covariance spectrum than in the mean spectrum: $kT_{seed} = 1.84^{1.87}_{1.82}$ keV. The dashed black line corresponds to the same fit, but allowing only the normalization to vary. This figure also illustrates the better statistics of the covariance spectrum with respect to the rms spectrum.

3. DISCUSSION

The main observational results of our analysis can be summarized as follows:

1. The lag-energy spectra of the lower and upper kHz QPOs of 4U1728-34 are systematically different: the lower kHz QPO shows soft variations lagging hard variations, as seen in other sources, while the upper kHz QPO shows either a flat lag-energy spectrum or hard variations lagging softer variations.
2. The shapes of the lag-energy spectra depend only weakly on the QPO frequency.
3. The covariance spectra of both kHz QPOs are harder than the continuum Comptonization component fitted to the mean spectra of the persistent emission. Allowing the seed-photon temperature to be different in the kHz QPO covariance spectra than in the mean spectra improves the fit significantly, with a higher seed temperature seen in the kHz QPO spectra.

The simplest interpretation for the lag-energy spectra to be different is that despite their overall spectral similarity, the two QPOs are generated by different mechanisms. We now consider a number of possible mechanisms to explain the lags and spectral variability and comment on their viability considering our results.

As noted by Barret (2013), the soft lags seen in the lower kHz QPO might be produced by the light-travel delay associated with thermal reverberation (i.e., X-ray heating) of the accretion disk by the boundary layer continuum. However, this cannot be the whole story: the lag-energy spectrum continues to drop, well above energies where the disk blackbody emission should contribute, suggesting that at least some component of the lags is intrinsic to the primary Comptonized continuum that dominates at these energies. For the upper kHz QPO, reverberation of the variable boundary layer emission off the disk to produce a lagging reflection component, could be a viable mechanism to explain the lags, given the relative flatness, and then hardening of the lag-energy spectra. The observed lags are consistent with those expected from a disk extending close to the surface of a neutron star: the lags of order 100 μs correspond to light-travel distances of 30 km. Note that one would have to correct for the primary continuum source geometry as well as the dilution of the lag by the variable primary continuum to arrive at a reliable estimate for the disk inner radius (e.g., see Uttley et al. 2014).

Next, we consider variations linked to thermal Comptonization in the boundary layer, which seem to explain the energy-spectral shape of the QPOs quite well (see this paper and Gilfanov et al. 2003). Recently, Kumar & Misra (2014) considered different mechanisms linked to thermal Comptonization as causes of energy-dependent time-delays in kHz

[8] We also note that the exposure times in the spectra were not dead-time corrected and that this correction would lead to a reduction in the χ^2 values.

The Astrophysical Journal, 811:109 (8pp), 2015 October 1

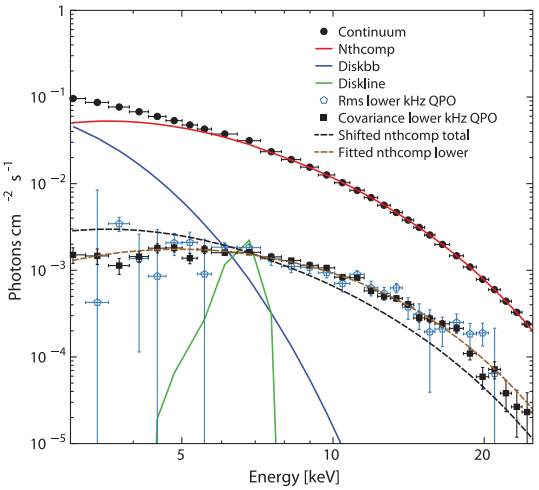

Figure 7. Comparison of the decomposition of the continuum spectrum (black circles) obtained from one ObsID of 4U1728-34 (20083-01-03-020), with the covariance (black squares) and rms spectra (open points) of the lower kHz QPO detected in the same data segment. This decomposition was obtained from the joint fit of the covariance and continuum spectra ($\chi^2 = 56.69$ (52)). The continuum spectrum includes a Comptonization component (`nthcomp`, solid red line, $\Gamma = 2.09^{2.16}_{2.01}$, $kT_e = 3.13^{3.19}_{3.05}$ keV, $kT_{seed} = 1.20^{1.29}_{1.08}$ keV), a disk thermal emission (`diskbb`, solid blue line, $kT_{in} = 0.75^{0.80}_{0.68}$ keV), and a fluorescence iron line (`diskline`, solid green line, $E_{line} = 6.60^{6.67}_{6.52}$ keV). The dashed maroon line corresponds to the Comptonization component of the continuum spectrum fitted to the covariance spectrum, but allowing only the normalization and the seed-photon temperature to vary. The seed-photon temperature was thus found to be higher than in the mean spectrum: $kT_{seed} = 2.24^{2.30}_{2.19}$ keV. The dashed black line corresponds to the same fit, but allowing only the normalization to vary.

QPOs, including predictions for the rms spectrum (equivalent in this case to the covariance) as well as the lags, which we can compare with our results. First, the case of pure seed-photon temperature oscillations seems to be ruled out, since it predicts a pivoting in the spectrum, leading to a deep minimum in the fractional rms at the pivot energy, between 10 and 20 keV, which is not seen in our data. In fact, we see no evidence for significant dips in fractional rms at energies where the Comptonized component dominates the mean and covariance spectra (see Figure 5). The covariance and mean spectra at these energies (above where the disk contributes to the mean) are well-fitted by the same spectral model, with the only difference being the seed temperature. The combination of different seed-photon temperatures with an additional constant disk component contributing to the mean spectrum can explain the observed energy dependence in fractional rms units of the covariance.

Kumar & Misra (2014) also investigated the case of oscillations in the heating rate of the Comptonizing region (see also Lee et al. 2001). Interestingly, such oscillations can produce either hard or soft lags, with soft lags being produced if a significant fraction of hard photons can impinge on and heat the seed-photon source. In this latter case, the oscillating region must also be rather compact ($\sim$1 km) in order to produce significant variability at the QPO frequencies (Kumar & Misra 2014). The existence of a compact oscillating region might be supported by our finding of a higher seed-photon temperature for the covariance spectra of both lower and upper kHz QPOs than for the mean spectrum, which suggests that the oscillating component of the Comptonizing region sees a hotter, more compact source of seed photons than the non-oscillating part. However, oscillations in the coronal heating rate also predict a fractional rms that continually increases with energy above 10 keV, whereas the data show that the fractional rms flattens above 10 keV. Kumar & Misra (2014) note similar rms spectral behavior in 4U1608-522 and suggest that an additional hard constant component may flatten the fractional rms at high energies. We find no evidence for such a component in our spectral fits: the mean spectrum, which will contain any constant components (such as the disk emission) can be simply explained by the same spectral model that produces the QPO covariance spectra, with the only difference being the seed-photon temperature and the presence of the disk at lower energies. No additional hard component is required to fit the mean spectrum.

None of the simple models that we have considered satisfactorily explain all of the spectral-timing features of both the lower and upper kHz QPOs. Therefore it may indeed be more likely that although the upper and lower kHz QPOs share some broad similarities (e.g., a thermal-Comptonized spectrum), the mechanisms producing each are fundamentally different in some way. For example, if the lag-energy spectrum in the upper kHz QPO is dominated by the reverberation signal, this would imply that there is little intrinsic spectral variation and corresponding lags from the primary continuum, with only the continuum normalization changing. This might then suggest that the upper kHz QPO corresponds to a simple variation in luminosity, perhaps driven by fluctuations in the accretion rate onto the neutron star boundary layer, generated in the innermost radii of the accretion disk. There is already evidence suggesting that accretion flow variability drives the broader noise components seen at lower frequencies (e.g., Uttley 2004; Uttley et al. 2011), and it seems more probable that the lower-coherence upper kHz QPO has such an origin than the much more coherent lower kHz QPO, which would be difficult to produce in a turbulent and shearing accretion flow (Barret et al. 2005).

In fact, recent work by Bult & van der Klis (2015) strongly links the upper kHz QPO to an oscillation in the inner disk by showing that the accretion-powered pulsations of the millisecond X-ray pulsar SAX J1808.4-3658 are suppressed when the upper kHz QPO frequency exceeds the spin-frequency (suggesting a centrifugal boundary). The signal is ultimately generated in the inner disk, which generates only a very small fraction of the observed disk emission, so the disk emission remains constant. The signal is thus only observed in the response of the boundary layer to the corresponding accretion variations.

In contrast, the lower kHz QPO might then be associated with a more coherent signal produced in a compact region of the boundary layer itself and is thus able to produce relatively coherent variations due to the small scale size. For instance, internal oscillations in the heating rate of the boundary layer could produce the observed soft lags as envisaged by Lee et al. (2001) and Kumar & Misra (2014), although more work is clearly needed to explain the shape of the rms spectrum. However, even if the lower and upper kHz QPOs are generated by different mechanisms, as seems likely, given their related frequencies, it is also likely that both QPOs track some underlying property of the flow, perhaps linked to the global accretion rate.

4. CONCLUSIONS

In this paper, we have presented the first exhaustive cross-spectral analysis of both kHz QPOs in 4U1728-34, which showed that the lower and upper kHz QPOs have distinct lag properties. Even if this could be an indication that the emission mechanisms and/or origins of each QPO are fundamentally different, a careful modeling of the light travel in neutron star low-mass X-ray binaries would be needed to unambiguously interpret the detailed shape of the lag spectra we measured. From the computation of high signal to noise covariance spectra of both kHz QPOs, we also found further evidence that the emission of both QPOs is compatible with that of a Comptonized component (Gilfanov et al. 2003). The fact that these spectra are better fitted with higher seed-photon temperatures than the same component in the mean spectra may also suggest that a particular compact region of the boundary layer is responsible for the X-ray emission at the two QPO frequencies.

Our results further illustrate the power of joint timing and spectral analysis of low-mass X-ray binaries, and we believe that these types of measurements should be extended to other sources in which kHz QPOs have been cleanly detected with the *RXTE* Proportional Counter Array. This may produce further information regarding the origin of the oscillators producing the kHz QPOs, and regarding the mechanisms by which the X-rays are ultimately modulated, which is a necessary step before we can use these signals to probe strong field general relativity. From this perspective, the need for better data is clear and a next-generation dedicated timing mission like *LOFT* (Feroci et al. 2012) would be decisive.

This research has made use of data obtained through the High Energy Astrophysics Science Archive Research Center On-line Service, provided by the NASA/Goddard Space Flight Center. We are grateful to the referee for very useful comments that helped to strengthen the claims made in this paper.

REFERENCES

Barret, D. 2013, ApJ, 770, 9
Barret, D., Kluźniak, W., Olive, J. F., Paltani, S., & Skinner, G. K. 2005, MNRAS, 357, 1288
Barret, D., Olive, J.-F., & Miller, M. C. 2006, MNRAS, 370, 1140
Barret, D., & Vaughan, S. 2012, ApJ, 746, 131
Boutelier, M., Barret, D., Lin, Y., & Török, G. 2010, MNRAS, 401, 1290
Bradt, H. V., Rothschild, R. E., & Swank, J. H. 1993, A&AS, 97, 355
Bult, P., & van der Klis, M. 2015, ApJL, 798, L29
Cackett, E. M., Fabian, A. C., Zogbhi, A., et al. 2013, ApJL, 764, L9
D'Aí, A., di Salvo, T., Iaria, R., et al. 2006, A&A, 448, 817
de Avellar, M. G. B., Méndez, M., Sanna, A., & Horvath, J. E. 2013, MNRAS, 433, 3453
de Marco, B., Ponti, G., Uttley, P., et al. 2011, MNRAS, 417, L98
Di Salvo, T., Méndez, M., van der Klis, M., Ford, E., & Robba, N. R. 2001, ApJ, 546, 1107
Emmanoulopoulos, D., McHardy, I. M., & Papadakis, I. E. 2011, MNRAS, 416, L94
Feroci, M., Stella, L., van der Klis, M., et al. 2012, ExA, 34, 415
Gilfanov, M., Revnivtsev, M., & Molkov, S. 2003, A&A, 410, 217
Kara, E., Fabian, A. C., Cackett, E. M., Miniutti, G., & Uttley, P. 2013a, MNRAS, 430, 1408
Kara, E., Fabian, A. C., Cackett, E. M., et al. 2013b, MNRAS, 428, 2795
Kumar, N., & Misra, R. 2014, MNRAS, 445, 2818
Lee, H. C., Misra, R., & Taam, R. E. 2001, ApJL, 549, L229
Lin, D., Remillard, R. A., & Homan, J. 2007, ApJ, 667, 1073
Shaposhnikov, N., Titarchuk, L., & Haberl, F. 2003, ApJL, 593, L35
Strohmayer, T. E., Zhang, W., Swank, J. H., et al. 1996, ApJL, 469, L9
Tripathi, S., Misra, R., Dewangan, G., & Rastogi, S. 2011, ApJL, 736, L37
Uttley, P. 2004, MNRAS, 347, L61
Uttley, P., Cackett, E. M., Fabian, A. C., Kara, E., & Wilkins, D. R. 2014, A&ARv, 22, 72
Uttley, P., Wilkinson, T., Cassatella, P., et al. 2011, MNRAS, 414, L60
van der Klis, M. 2006, in Compact Stellar X-Ray Sources, ed. W. Lewin & M. van der Klis (Cambridge Astrophysical Ser., No. 39; Cambridge: Cambridge Univ. Press), 39
van der Klis, M., Hasinger, G., Stella, L., et al. 1987, ApJL, 319, L13
van der Klis, M., Swank, J. H., Zhang, W., et al. 1996, ApJL, 469, L1
Vaughan, B. A., van der Klis, M., Méndez, M., et al. 1998, ApJL, 509, L145
Wilkinson, T., & Uttley, P. 2009, MNRAS, 397, 666
Zoghbi, A., & Fabian, A. C. 2011, MNRAS, 418, 2642
Zoghbi, A., Fabian, A. C., Reynolds, C. S., & Cackett, E. M. 2012, MNRAS, 422, 129

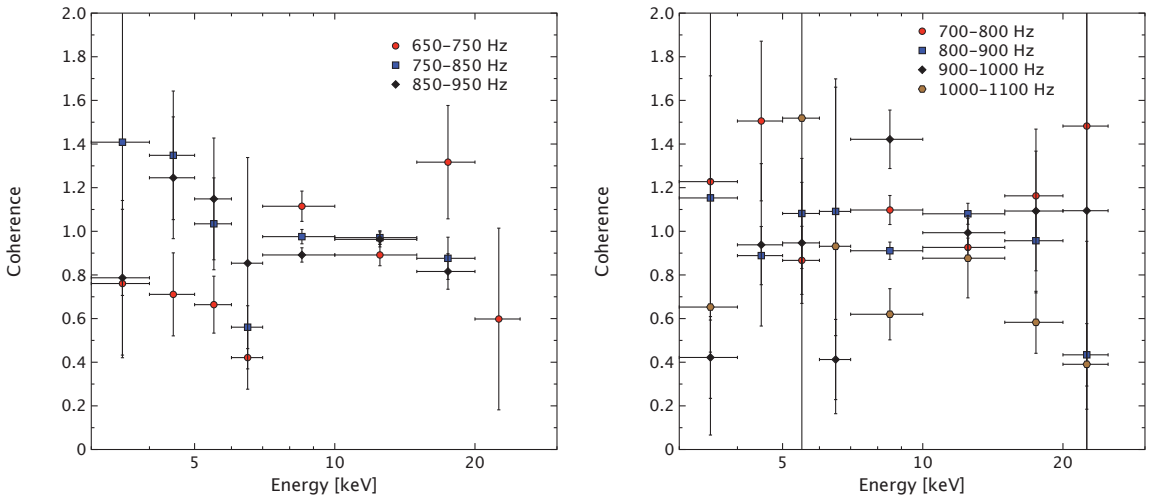

Figure 2.7: Intrinsic coherence of the lower (top) and upper (bottom) kHz QPOs of 4U1728-34, obtained by averaging all cross and power spectra within different frequency intervals. As can be seen, within the available statistics, the assumption of an intrinsic coherence close to unity is not rejected. We note that these spectra were obtained from combining a large number of observations inside relatively large QPO frequency bins and that slight variations of the cross-spectral properties inside these bins will affect the measured intrinsic coherence.

2.4.3 Supplements

The coherence of both kHz QPOs in 4U1728-34

One of the main assumptions for interpreting the results presented in this publication is the intrinsic coherence of both kHz QPOs across the studied energy range. Whereas de Avellar et al. (2013) already gave good indications that this may be the case for the lower kHz QPO, we decided to properly verify it in our own dataset. To do so, for each QPO type and studied frequency range, we used the power and cross spectra obtained from the presented covariance study and applied Equations 2.22 and 2.23 to derive average coherence spectra. Figure 2.7 shows the results of this analysis. Unfortunately, the intrinsic coherence estimates do not benefit from good statistics compared to other spectral timing products and it is difficult to derive a definitive proof of the coherence of the QPO signals with the currently available data. Nevertheless, we found no contraindication against making the assumption, at the least for the data set presented here.

Extension of the analysis to other kHz QPO sources

The above presented study provides a framework to analyze more kHz QPO sources and thus verify whether the results obtained for 4U1728-34 can be extended to the whole population of kHz QPO sources. In that prospect, we re-processed using exactly the same method the whole PCA archive from 4U1608-522 and 4U1636-536 which are known to be the most proficient kHz QPO sources.

Figure 2.8 and 2.9 show the results obtained on both sources for the lag versus frequency distributions as well as the average lag spectra. Because much more data was available for the lower kHz QPO of 4U1636-536, the lag and covariance spectra were averaged in 50 Hz large frequency bins. Our findings are consistent with previous studies (Barret, 2013; de Avellar et al., 2013). We notably find again the decreasing trend for the lower kHz QPO soft lags with frequency in both sources. An

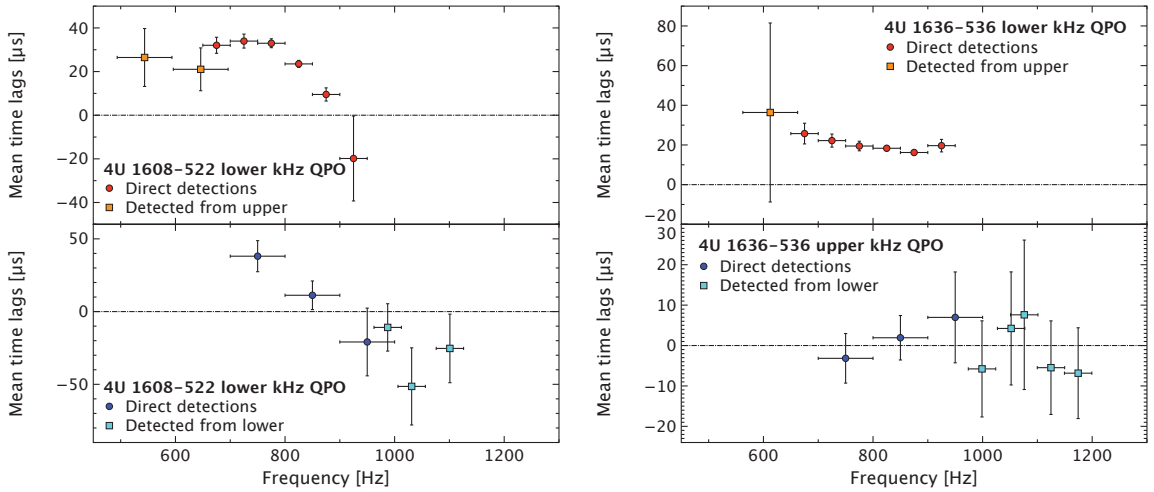

Figure 2.8: Time lag versus frequency distribution in 4U1608-522 (left) and 4U1636-536 (right). These results were obtained following the analysis method developed in Peille et al. (2015). As in previous studies, we find a soft lag for the lower kHz QPOs decreasing with frequency (Barret, 2013; de Avellar et al., 2013). The statistics however do not allow to draw any firm conclusions concerning the upper kHz QPO in theses sources.

interesting feature is also that we find indication of a bump around 5–7 keV in the first two lag spectra of 4U1636-536 similarly to what Barret (2013) observed in 4U1608-522 (not formally significant). As could be expected, limited by the available statistics, we however cannot draw any firm conclusion concerning the upper kHz QPO.

We therefore decided for these sources to only conduct the statistically more demanding covariance analysis for the lower kHz QPO. Figure 2.10 shows the average covariance spectra in RMS units whereas the results of the simultaneous fits with the continuum emission are shown in Tables 2.1 and 2.2. As in 4U1728-34, little variation with frequency is seen in the shape of the covariance spectra and at all frequencies, the covariance spectra of the lower kHz QPO are harder than the continuum Comptonization component fitted to the mean spectra of the persistent emission. In the two new sources, we also find that allowing the seed-photon temperature to be different in the kHz QPO covariance spectra than in the mean spectra improves the fit significantly, with a higher seed temperature seen in the kHz QPO spectra.

Overall, the extension of our analysis to the two most proficient kHz QPO sources confirmed our results for 4U1728-34, at least for the lower kHz QPO, and strongly indicates that these are common features to all kHz QPOs.

Other possible interpretation for the covariance spectrum fits

When directly fitting a covariance spectrum with a physical emission model like was done in the paper, implicitly, the assumption is made that the spectral shape of the oscillating component is constant and that the RMS amplitude at all energies comes from a varying normalization. In such a frame, the lags can only originate from intrinsic delays in the emission or geometric arguments. However, another possible interpretation of the covariance spectra is for them to be produced by a changing shape of the emission spectrum: depending on how the spectrum oscillates, this will create variations of different amplitudes across the measured energy range and could mimic a covariance spectrum fitable by a

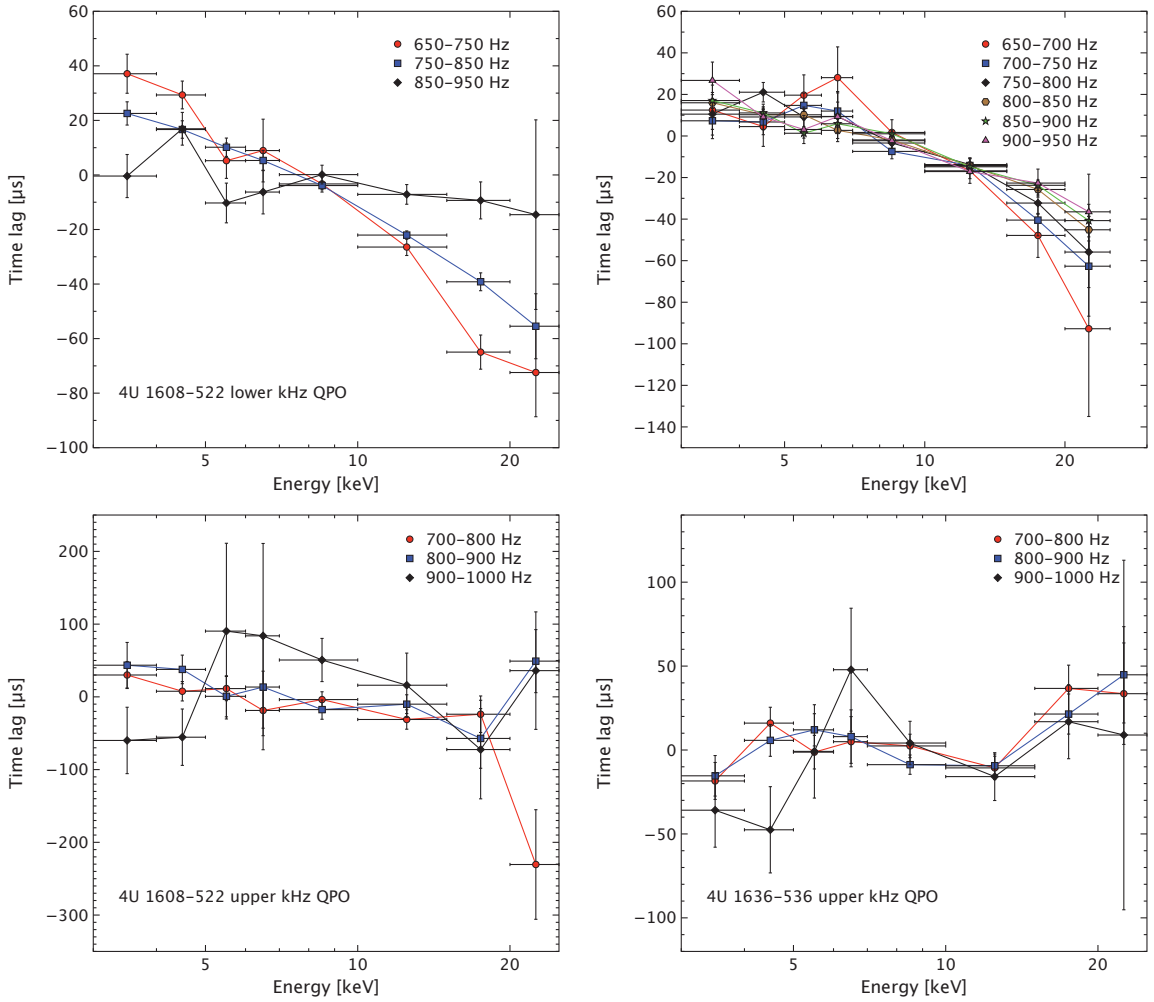

Figure 2.9: kHz QPO lag energy spectra in 4U1608-522 (left) and 4U1636-536 (right) for the lower (upper part) and upper (lower part) kHz QPOs. These results were obtained following the analysis method developed in Peille et al. (2015). There is a clear flattening of the lower kHz QPO spectra with frequency in both sources, coherent with the mean lag versus frequency measurements. The magnitude of the flattening is however bigger in 4U1608-522. Even though the overall shapes of the upper kHz QPO spectra seem different from the lower kHz QPO one, in theses sources, they cannot be formally distinguished.

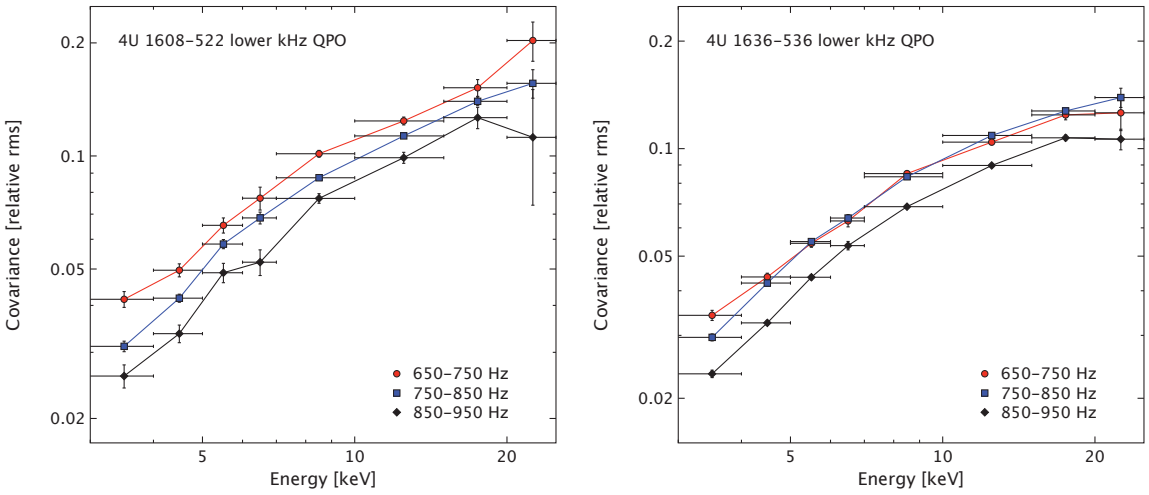

Figure 2.10: Average lower kHz QPO covariance spectra expressed in fractional RMS units in 4U1608-522 and 4U1636-536. These results were obtained following the analysis method developed in Peille et al. (2015) (see Table 1 in the article). We note, similarly to 4U1728-34, the relatively constant shape of the covariance spectra with a simple scaling with frequency suggestive of a constant emission source.

Table 2.1. χ^2(dof) values obtained from the joint fits of the mean and covariance spectra corresponding to data segments with lower kHz QPOs in 4U1608-522 and 4U1636-536 using different methods.

Source name	Frequency	all linked	kT_e free	Γ free	kT_{seed} free	all free	#ObsID
4U1608-522	650–750	2393(409)	2149(408)	1718(408)	1579(408)	1576(406)	7
	750–850	4235(489)	4167(488)	1572(488)	1556(488)	1553(486)	9
	850–950	1145(383)	1030(382)	920(382)	852(382)	839(380)	6
4U1636-536	650–700	1589(725)	1416(724)	1182(724)	1126(724)	1126(722)	9
	700–750	7425(1221)	7111(1220)	6884(1220)	6806(1220)	6805(1220)	20
	750–800	1978(839)	1649(838)	1293(838)	1162(838)	1158(836)	14
	800–850	5537(2067)	4724(2066)	3878(2066)	3572 (2066)	3569 (2064)	30
	850–900	5323(2215)	4729 (2214)	4101(2214)	3822 (2214)	3817 (2212)	36
	900–950	2188(1147)	2026(1146)	1899(1146)	1867(1146)	1866(1144)	18

Note. — As in Peille et al. (2015), the joint fits were conducted using the `xspec` model `wabs*(ntchomp+diskline+diskbb)`. For the covariance spectra, only the normalization of the `nthcomp` component was kept non-null. Depending on the cases, either the electron temperature (kT_e), the Γ shape parameter, the seed photon temperature (kT_{seed}), none, or all the parameters were allowed to differ between the covariance and the mean spectra. In all cases, the hydrogen column density was fixed to $N_H = 1.1 \times 10^{22}$ cm^{-2} (Pandel et al., 2008) and 0.36×10^{22} cm^{-2} (Güver et al., 2010) for 4U1608-522 and 4U1636-536 respectively. The last column indicates how many ObsIDs were combined in each frequency bin.

Table 2.2. Results of the joint fit of the mean and covariance spectra corresponding to the data segments with lower kHz QPOs in 4U1608-522 and 4U1636-536.

Source name	Frequency (Hz)	kT_{seed}(mean) (keV)	kT_{seed}(cov) (keV)	Γ	kT_e (keV)	E_{line} (keV)	kT_{in} (keV)	χ^2 (dof)
4U1608-522	650–750	$1.21^{1.22}_{1.19}$	$1.65^{1.66}_{1.63}$	$3.18^{3.25}_{3.11}$	$5.26^{5.57}_{4.99}$	$7.03^{7.07}_{6.99}$	$0.70^{0.71}_{0.69}$	1579 (408)
	750–850	$0.55^{0.56}_{0.55}$	$1.71^{1.72}_{1.70}$	$2.18^{2.18}_{2.17}$	$2.78^{2.79}_{2.77}$	$7.32^{7.35}_{7.29}$	$0.44^{0.46}_{0.43}$	1557 (488)
	850–950	$1.29^{1.33}_{1.26}$	$1.78^{1.80}_{1.76}$	$2.65^{2.72}_{2.58}$	$3.17^{3.24}_{3.11}$	$6.97^{7.03}_{6.92}$	$0.87^{0.88}_{0.86}$	852 (382)
4U1636-536	650–700	$1.16^{1.17}_{1.14}$	$1.82^{1.85}_{1.78}$	$2.64^{2.68}_{2.62}$	$4.31^{4.42}_{4.21}$	$6.98^{7.02}_{6.95}$	$0.66^{0.67}_{0.66}$	1126 (724)
	700–750	$1.16^{1.17}_{1.13}$	$1.71^{1.73}_{1.69}$	$2.49^{2.51}_{2.44}$	$3.65^{3.68}_{3.57}$	$7.21^{7.23}_{7.18}$	$0.70^{0.71}_{0.69}$	6806 (1220)
	750–800	$1.10^{1.13}_{1.08}$	$1.81^{1.83}_{1.79}$	$2.34^{2.38}_{2.31}$	$3.27^{3.31}_{3.24}$	$6.93^{6.97}_{6.90}$	$0.69^{0.71}_{0.68}$	1162 (838)
	800–850	$1.08^{1.10}_{1.07}$	$1.83^{1.84}_{1.82}$	$2.23^{2.26}_{2.22}$	$3.10^{3.11}_{3.08}$	$6.95^{6.97}_{6.92}$	$0.73^{0.74}_{0.73}$	3569 (2064)
	850–900	$1.13^{1.16}_{1.11}$	$1.86^{1.87}_{1.86}$	$2.18^{2.19}_{2.16}$	$3.01^{3.03}_{3.00}$	$6.74^{6.77}_{6.73}$	$0.84^{0.84}_{0.84}$	3822 (2214)
	900–950	$1.18^{1.20}_{1.13}$	$1.87^{1.90}_{1.84}$	$2.16^{2.18}_{2.14}$	$2.99^{3.01}_{2.97}$	$6.73^{6.75}_{6.69}$	$0.89^{0.90}_{0.87}$	1867 (1146)

Note. — The joint fits were conducted using the `xspec` model `wabs*(ntchomp+diskline+diskbb)`. For the covariance spectra, only the normalization of the `nthcomp` component was kept non-null. Only the normalization and the seed photon temperature were allowed to differ from mean spectra. kT_{seed} corresponds to the temperature of the seed photons of the `nthcomp` component, Γ to a shape parameter of this component, kT_e to the temperature of the Comptonizing electrons, E_{line} to the centroid energy of the iron line (only used during the fit of the mean spectrum), and kT_{in} to the inner temperature of the accretion disk (only used during the fit of the mean spectrum). The sub- and super-scripts give the 1σ error *ranges* (i.e. best-fitting value plus lower and upper error bars respectively). Equivalent to Table 2 in Peille et al. (2015).

physical model.

An easy way to test this hypothesis is to take an `Xspec` emission spectrum and vary one of its parameters by a small amount. In the small signal limit, the absolute difference with respect to the initial model will thus give an estimate of the shape of the covariance spectrum that would result from the sinusoidal oscillation of this physical parameter. In the case of kHz QPOs, the first candidate that comes to mind is the seed photon temperature of the Comptonization component. As an example, I therefore took the high signal to noise first ObsID of 4U1608-522 and applied this approach. When, fixing the shape parameter Γ and electron cloud temperature to the continuum values and allowing the seed photons temperature to oscillate around a different value than the continuum, an agreement of similar quality to the one reported in the paper (by a "varying norm" approach) can be found with the covariance spectrum if the seed photon temperature is increased to ~ 1.23 keV (see Fig. 2.11, left). One can also test varying other shape parameters such as the electron cloud temperature (cf. Fig. 2.11, right). In this particular case, this simple model features a pivoting around 4 keV that would create $\pm\pi$ energy lags. We further note that when using the `compTT` model for the Comptonized emission instead of `nthcomp`, a similar pivoting can be observed when varying this time again the seed photon temperature.

Whereas this simple approach illustrated how a variation of the seed photon temperature could reproduce the lower kHz QPO covariance spectrum in the frame of the `nthcomp` model, it also showed how particular care is necessary when interpreting covariance spectra produced by varying parameters of simple `Xspec` models. Overall, this further indicates that a self consistent modeling of the full spectral timing properties of the kHz QPOs is necessary before unambiguously interpreting these results.

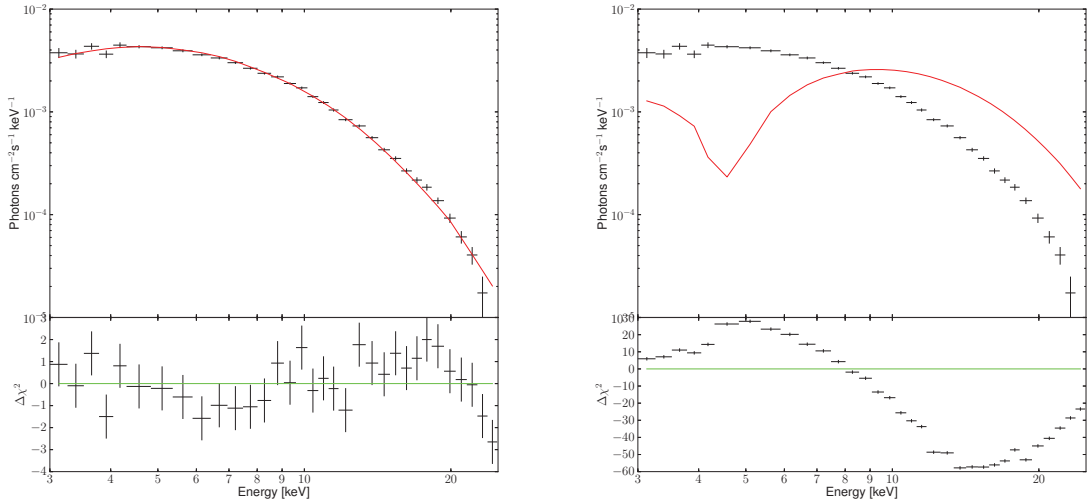

Figure 2.11: Left: The covariance spectrum of the lower kHz QPO measured form the first ObsID of 4U1608-522 is relatively well fitted by an absorbed `nthcomp` model whose Γ and kT_e parameters are the same as the continuum spectrum and whose seed photon temperature oscillates around 1.23 keV. **Right:** The naive model resulting from the oscillation of the electron cloud temperature around the continuum value features a pivoting around 4 keV.

2.4.4 Conclusions and perspectives

I have presented here a comprehensive cross-spectral analysis of both kHz QPOs in 4U1728-34, 4U1608-522 and 4U1636-536, the three most proficient known kHz QPO sources, using the whole archive of the RXTE PCA instrument. This revealed that the two QPOs have distinct lag properties and may well indicate that they have a distinct origin or emission mechanism. The application of a covariance spectral analysis to both QPOs brought further evidence that these oscillations might be emitted by a compact Comptonization region, possibly a part of the boundary layer between the accretion disk and the neutron star surface (Gilfanov et al., 2003).

In any case, the universality of our results in the three sources strongly indicates that the spectral timing properties we reported are common to all kHz QPO sources and that they are key to our understanding of kHz QPOs. One very promising Compton scattering model introduced by Lee et al. (2001) and further developed by Kumar & Misra (2014) and Kumar & Misra (2016) already tries to self-consistently explain the lag and rms/covariance spectra of the lower kHz QPO and may finally unveil the origin of this emission, even if it fails to simultaneously model the upper kHz QPO lag properties. Barret (2013) had also suggested reverberation as a viable mechanism to explain the shape of the lower kHz QPO lag-energy spectrum, but the first self-consistent modeling by Cackett (2016) seems to rule out this hypothesis. The obtained shape however resembles quite closely the one we measured for the upper kHz QPO in 4U1728-34.

Recent developments on the application of phase resolved spectroscopy to low frequency QPOs in BHB offer great perspectives for neutron star kHz QPOs (Ingram & van der Klis, 2015; Stevens et al., 2016). These techniques rely on a time domain interpretation of the cross spectra and may in principle be directly applicable to the data set presented here. If successful, this could offer another window to understand the origin of these oscillations.

In the prospect of breaking the degeneracy of possible emission mechanisms for the QPOs, whereas the available data may not be sufficient, the application of spectral timing tools like the ones presented here to observations by the next generation of timing missions like LOFT (Feroci et al., 2012) may well be decisive. In the nearer future, the LAXPC instrument on board the recently launched *ASTROSAT* satellite already offers promising perspectives with its effective area reaching harder X-rays than the PCA where the RMS amplitude of the QPOs is the largest (Agrawal, 2006).

Chapter 3: The X-ray Integral Field Unit of the ATHENA mission

3.1 The Advanced Telescope for High ENergy Astrophysics

Selected in June 2014 to implement the Hot and Energetic Universe science theme (Nandra et al., 2013), the Advanced Telescope for High ENergy Astrophysics (*Athena*) will be the second Large class mission of the European Space Agency (ESA) Cosmic Vision scientific space program. This next generation X-ray telescope will address a variety of key scientific questions ranging from the formation and evolution of groups and galaxy clusters, the chemical enrichment history of the universe and the missing baryons, to the formation of the first supermassive black holes, their role in the evolution of galaxies and the physics of accretion (Pointecouteau et al., 2013; Ettori et al., 2013; Croston et al., 2013; Kaastra et al., 2013; Aird et al., 2013; Georgakakis et al., 2013; Cappi et al., 2013; Dovciak et al., 2013). Conceived as an open and generic X-ray observatory, it will also offer breakthrough capabilities for a large panel of astrophysical topics. Some have been historically studied in the X-rays like compact objects, supernovae or massive stars, but others like exoplanets may benefit from a new window in their field (Branduardi-Raymont et al., 2013; Sciortino et al., 2013; Motch et al., 2013; Decourchelle et al., 2013; Jonker et al., 2013).

The *Athena* satellite is scheduled for launch on an Ariane VI in 2028 and will operate at either one of the two firsts Sun-Earth Lagrangian point (L1/L2) to have at the same time a very stable thermal environment as well as an optimal observing efficiency and good sky visibility. It will perform pointed observations ranging form 1 ks to 1 Ms but will also rapidly react (less than 4 hours) to external Target of Opportunity alerts (TOOs) in order to observe transient sources such as gamma ray burst (GRB) afterglows or supernovae. The first assessment studies projected a total mass of ~ 6 t for a twelve meter large telescope and an available power of ~ 5.5 kW to alternatively operate two payload instruments (Fig. 3.1, Barcons et al., 2015): the Wide Field Imager (WFI, Rau et al., 2013) and the X-ray Integral Field Unit (X-IFU, Barret et al., 2013; Ravera et al., 2014b).

After describing the *Athena* X-ray optics (Sect. 3.1.1), I will briefly present the WFI, its detection principle and main characteristics (Sect. 3.1.2). The X-IFU, central instrument of my thesis, will be described in more detail in Sect. 3.2.

3.1.1 The *Athena* X-ray optics

One of the key features of the *Athena* mission is its transformational effective area of $2\,m^2$ at 1 keV providing an order of magnitude increase compared to present time X-ray observatories such as *XMM-Newton*, *Chandra* or *Hitomi* (see Fig. 3.2, left). This collecting area will be realized by the gathering across a ~ 6–$7\,m^2$ open area of so-called Silicon Pore Optics (SPO) mirror modules currently being developed in ESA (Beijersbergen et al., 2004; Willingale et al., 2013). Each mirror module will consist

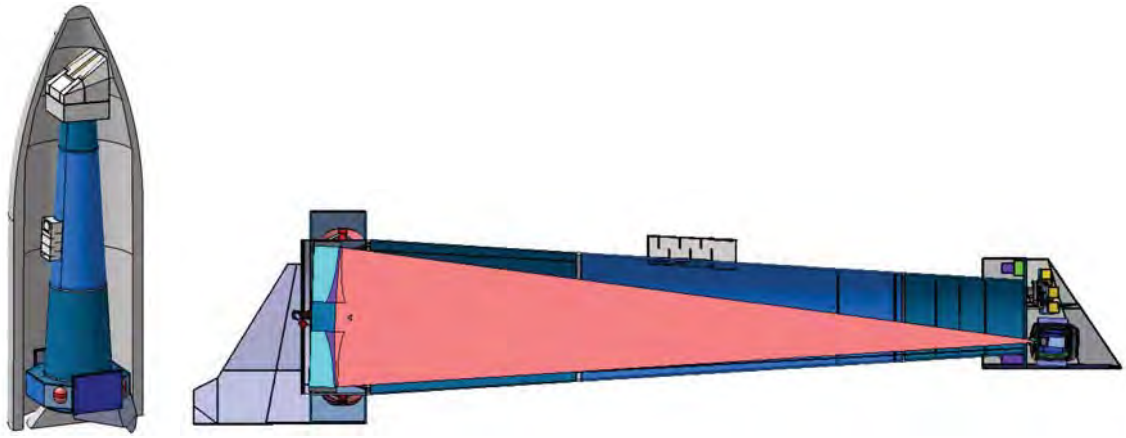

Figure 3.1: Preliminary design of the *Athena* X-ray observatory as presented during the ESA CDF study. **Left:** Overview of the satellite integrated in an Ariane V fairing. The two instruments are located inside the payload module at the top of the image while the Moveable Mirror Assembly (MMA) is integrated at the bottom of the satellite. **Right:** Detailed view of the MMA design allowing to switch between the two instruments. Here, the X-IFU is selected.

of the stacking of slightly curved and very smooth Si wafers creating thousands of little pores, each acting as a very small sector of a Wolter I telescope and focusing the X-rays to a single point through double grazing incidence reflection. The mirror modules will be assembled along several concentric circles and have an increasing length towards the center to maximize the collecting area (see Fig. 3.3). Following the first ESA study of the *Athena* satellite before the Phase A kick-off, two design points are are being considered: one with a large mirror area ($2\,\mathrm{m}^2$ at $1\,\mathrm{keV}$) and a second with a lower area ($1.4\,\mathrm{m}^2$ at $1\,\mathrm{keV}$).

The on-axis angular resolution of the *Athena* optics will be 5" half energy width (HEW) but will degrade to $\sim$ 7" at 20' at the edges of the WFI field of view. Similarly, the mirror effective area will decrease by a factor of a few at high off-axis angles (vignetting effect). We however note that the X-IFU with its smaller field of view will only see these effects at a few percents level.

From the first industrial studies, the *Athena* mirror is foreseen to be integrated on a hexapod structure called Mirror Moveable Assembly (see Fig. 3.1 right). This mechanism will allow easy switching between the two instruments. Benefiting from a full six degrees of freedom flexibility, it will also provide adjustable focus and allow to optimize the telescope angular resolution but could also offer the possibility to defocus on demand in order to increase the instrument count rate capabilities (see Sect. 4.5.2).

3.1.2 The Wide Field Imager

The *Athena* WFI, in conjunction with the *Athena* mirror effective area, will provide unprecedented imaging and deep field survey capability across a large field of view of 40'x40'. Its focal plane will be populated by four large 512x512 quadrants of Active Pixel Sensors (APS) based on DEpleted P-channel Field Effect Transistors (DEPFETs, see Fig. 3.4) to offer the required PSF oversampling and near Fano-limited energy resolution. It will also feature a 64x64 fast chip mounted out of focus and dedicated to the observation of high count rate point sources. Each DEPFET APS acts as a p-channel semiconductor transistor and detects X-rays through the photo-electrical effect: each impacting X-ray

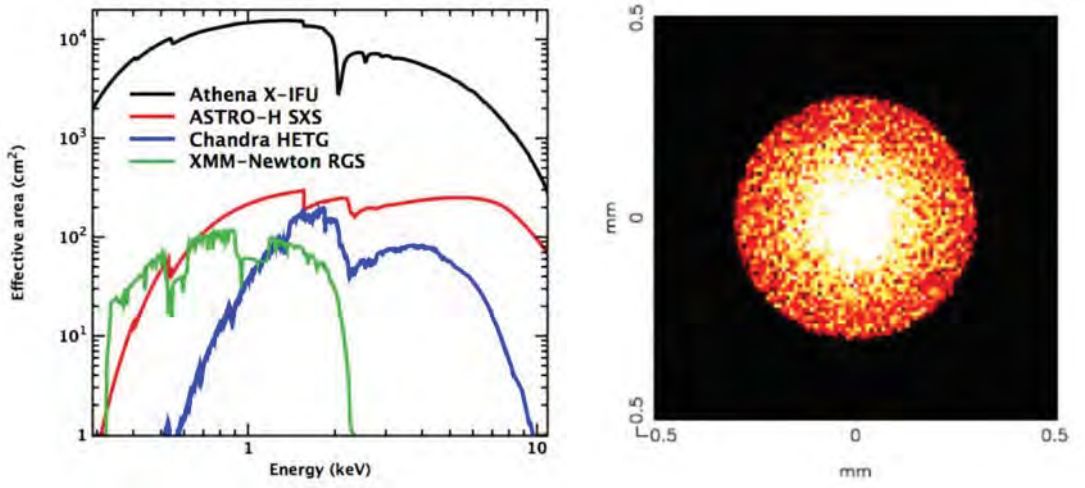

Figure 3.2: Left: Comparison of the projected *Athena* effective area with present day facilities. **Right:** On-axis PSF shape of the *Athena* optics providing 5" angular resolution.

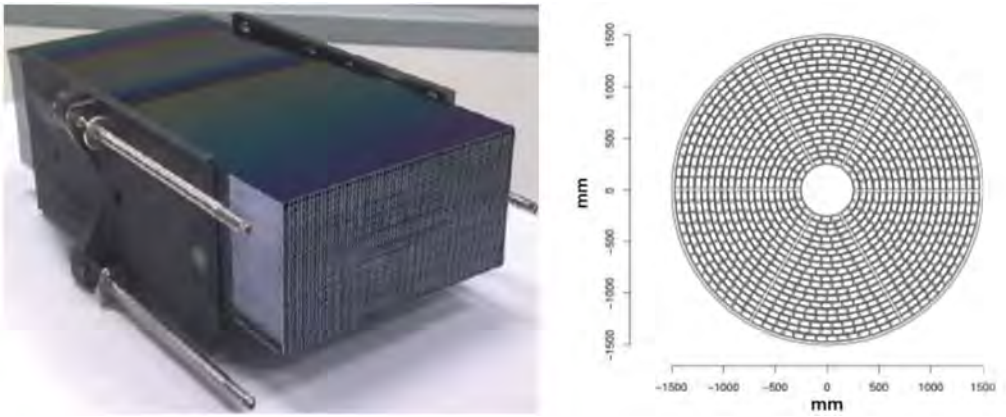

Figure 3.3: Left: Image of one SPO mirror module comprising two stacks of Si plates. The X-rays will be focused through the numerous pores. **Right:** Sketch of the mirror modules assembled along concentric circles. Figures taken from the *Athena* mission proposal.

will generate electrons by interacting with the bulk silicon wafer. These electrons will be collected at the FET gate and increase the transistor conductivity proportionally to the original energy of the photon.

As the gate persists regardless of the presence of transistor current, the DEPFET pixels only need to be turned on during readout and remain turned off for the rest of the time. The typical DEPFET read out process is described in Figure 3.4 (right): two conductivity measurements are performed before and after clearing of the accumulated charge. The difference between the two obtained values thus gives an estimate of the energy of the impacting photon. The energy resolution achieved by this process is expected to be $\lesssim 150\,\mathrm{eV}$ full width half maximum[1] at 6 keV.

In principle, the DEPFET pixels can be read out individually but due to readout power limitations,

[1]For a normal distribution of the energy measurement statistical error, this corresponds to $\sqrt{4\ln 2}\sigma \approx 2.355\,\sigma$ where σ is the natural Gaussian width.

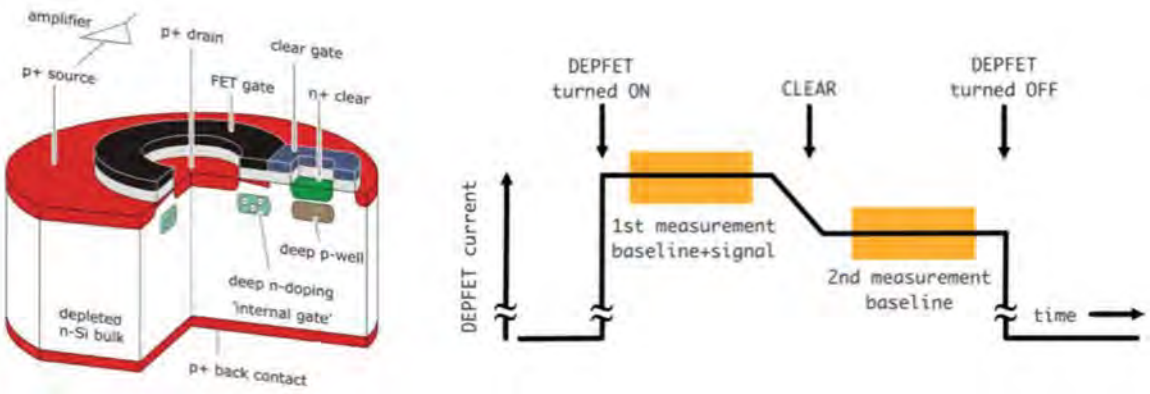

Figure 3.4: Left: Cutaway display of a WFI DEPFET APS. **Right:** Read out principle of the DEPFET pixels.

each quadrant row will be turned on and off successively. This process will be performed using Application-Specific Integrated Circuits (ASICs) set up in an architecture allowing the selection of different readout modes. For the moment two main modes are foreseen: the so-called fullframe mode during which the full quadrants are read out with ~ 1.2 ms time resolution, and a window mode allowing to address arbitrary sub parts of the detector with an improved time resolution of $\sim 40\,\mu$s. Dedicated read-out electronics are foreseen for the fast detector for which a time resolution of $\sim 80\mu$s could be achieved and an overall count rate capability of $\gtrsim 90\,\%$ throughput with $< 1\,\%$ pileup at 1 Crab (see Chapter 4 for more details on how to characterize an instrument's count rate capability).

In order to reach the required energy resolution, the detectors and readout electronics need to be thermally stabilized at temperatures below 60° C. This will be done through passive cooling by large radiators on the sides of the payload module (see Fig. 3.1).

3.2 The X-ray Integral Field Unit

The *Athena* X-IFU is an evolution of the previously studied XMS proposed at the time to be launched on the International X-ray Observatory (IXO) and later the L1 version of *Athena* (den Herder et al., 2012). It will operate ~ 3800 Transition Edge Sensors (TESs) providing spectro-imaging capability across a 5' field of view with 5" spatial resolution and an unprecedented 2.5 eV energy resolution. The X-IFU will thus be able to map gas velocity, turbulence, temperature and chemical abundances in distant clusters of galaxies and in nearby galaxies with high precision, but also allow the detection of the missing baryons in the Warm Hot Intergalactic Medium (WHIM). In general, this instrument will open the X-ray field to high resolution spatially resolved spectroscopy.

The top-level X-IFU requirements are summarized in Table 3.1 whereas Figure 3.5 gives the current block diagram representation of the X-IFU.

3.2.1 Detection principle and TES array

The X-IFU detector will consist of a large array of pixels comprised of X-ray absorbers deposited on top of TESs. Operated at very low temperatures ($\lesssim 100$ mK) in their transition between the superconducting and normal states, each TES is a very sensitive micro-calorimeter that will sense any temperature change in its absorber through a strong thermal link. After a photon thermalizes

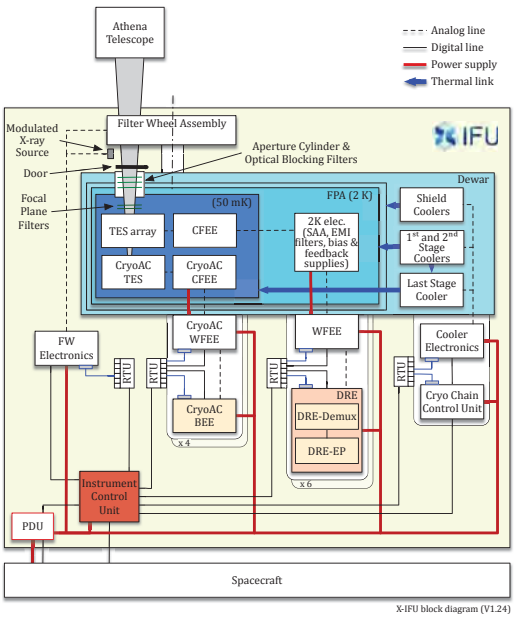

Figure 3.5: The X-IFU functional block diagram.

Parameters	Requirements
Energy range	0.2–12 keV
Energy resolution	2.5 eV @ E <7 keV
	$E/\Delta E = 2800$ above
	goal at 1.5 eV
Field of View	5' (diameter) (3840 TES)
Quantum efficiency	> 60 % @ 1 keV
	> 70 % @ 7 keV
Gain error (RMS)	0.4 eV
Count rate capability	1 mCrab (>80 % high-res events)
	goal at 10 mCrab
	1 Crab (>30 % low-res events)
Time resolution	10 µs
Non X-ray background	$< 5 \times 10^{-3}$ counts/s/cm^2/keV

Table 3.1: The X-IFU top level requirements.

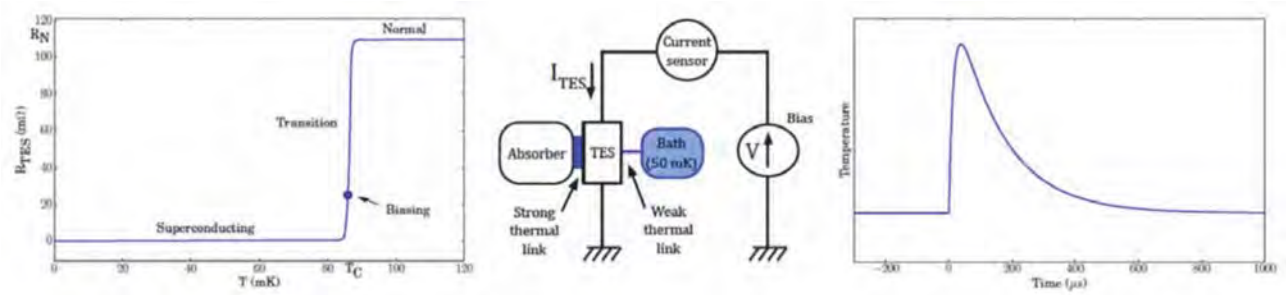

Figure 3.6: Left: The TES is set in its narrow transition between superconducting and normal state. **Middle:** The TES is voltage biased and shares a strong thermal link to its absorber in order to detect the photons thermalized in the absorber and a weak link to a cold thermal bath. **Right:** Temperature profile in the TES after a photon impact.

inside an absorber, the TES will see a very sharp temperature rise and move across its transition. The resulting resistance change will induce a change in the current going through the TES which will be measured to determine the energy of the photon. The operation of the TESs in their transition is ensured through a weak thermal link to a cold bath ($\sim$ 55 mK) and a voltage bias (see Fig. 3.6).

In the current baseline configuration, the focal plane of the X-IFU will be populated by 3840 pixels organized following a hexagonal pattern to cover a field of view of 5' equivalent diameter. The TESs are foreseen to be realized with $\sim$ 140 µm square Mo/Au bilayers deposited on a silicon-nitride wafer ensuring heat sinking to the cold thermal bath. The absorbers will be directly electro-plated onto the TESs in order to ensure a strong thermal link between both parts of the pixels and be made of a combination of gold and bismuth. Gold will provide the required heat capacity of $\sim$ 0.8 pJ/K allowing an appropriate temperature increase after each X-ray impact, while bismuth is suitable for reaching a high X-ray stopping power at a limited heat capacity cost. Currently, the foreseen composition is $\sim$ 2 µm of gold and $\sim$ 4 µm of bismuth.

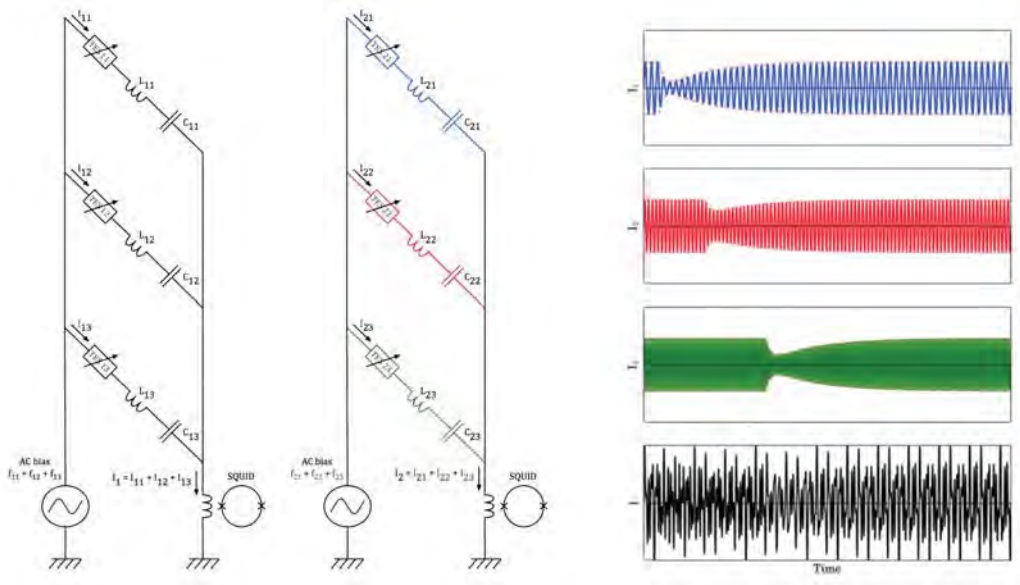

Figure 3.7: Principle of a TES FDM readout system. **Left:** Schematics of 2 channels of 3 pixels multiplexed in frequency. Each pixel is biased by a carrier matching the resonance frequency of its associated LC filter. **Right:** Each carrier gets modulated by the varying current going through the TESs following the arrival of an X-ray photon. The individual currents are then summed and read out by a single SQUID.

3.2.2 The X-IFU read-out system

The monitoring of the small current going through the TESs (a few tens of μA) will be realized at the focal plane level by a set of read-out coils and very sensitive Superconducting QUantum Interference Devices (SQUIDs) magnetometers. These magnetometers consist of two Josephson junctions mounted in parallel in a superconducting loop (Aviv, 2008) and will measure the varying magnetic field created in the read-out coils by the TES current. They provide a first pre-amplification of the signal with very low noise addition and dissipated power. In the baseline X-IFU configuration, two SQUID stages are considered, one at the coldest temperature ($\sim$ 50 mK) to amplify the signal with the smallest possible noise addition and a second stage at 300 mK where more power can be dissipated and an additional amplification performed (Gottardi et al., 2014). Once the signal reaches room temperature, a last analog amplification is realized by a semi-conductor Low Noise Amplifier in the Warm Front-End Electronics (WFEE) before transmission to the Digital Readout Electronics (DRE) (den Hartog et al., 2014).

In order to operate at cryogenic temperatures, very little power can be dissipated at the focal plane level. Large pixel arrays like the one foreseen for the X-IFU therefore cannot have a single read-out channel per pixel. The 3840 X-IFU pixels are thus grouped in 96 channels of 40 pixels and biased and read out using a Frequency Domain Multiplexing (FDM) scheme: all pixels of a given channel are simultaneously AC biased by a sum of sinusoidal signals at frequencies separated by $\sim$ 100 kHz between 1 and 5 MHz. By coupling each pixel to a narrow-band LC filter, only one carrier is then seen by each TES and provides the required bias level to set it in its transition. Similarly, all output TES currents are summed and routed to a single readout SQUID and subsequent amplifier chain. The signal coming from each pixel can then be reconstructed in the DRE by measuring envelops at the different frequencies (see Fig. 3.7 and Ravera et al., 2014a).

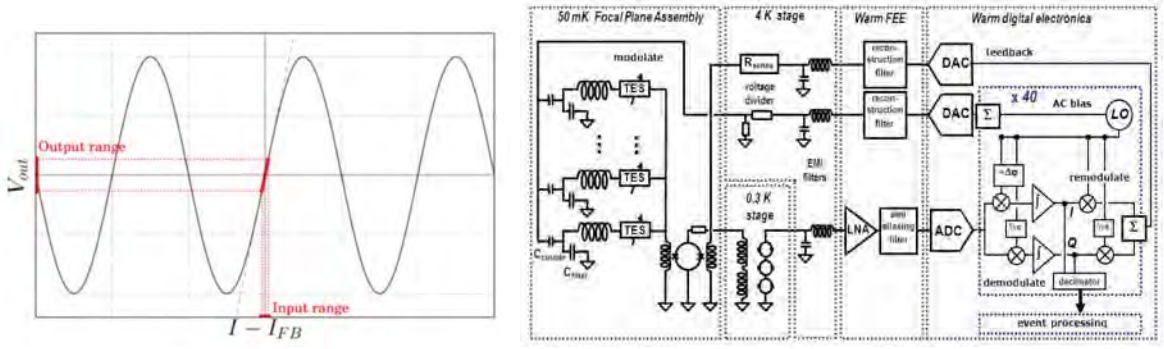

Figure 3.8: Left: Sinusoidal response of a SQUID. The application of a feedback signal is necessary to stay in the linear regime. **Right:** Close up view of the front-end and digital readout architecture of the X-IFU showing the TES biasing and the baseband feedback FDM readout system.

As the SQUID amplifiers are highly non-linear and have a sinusoidal response, they can only be operated in a limited dynamic range that would be exceeded when an X-ray photon impacts a pixel (see Fig. 3.8 left). The second role of the DRE is thus to provide feedback signal to the first stage SQUIDs via a so-called baseband feedback architecture (den Hartog et al., 2009, 2012). After estimating the current going through the SQUID at each relevant frequency with a first integration step, this process ensures that the feedback signal carriers are properly phased with the TES bias voltages, compensating for the propagation time through the analog harness and the digital processing time (see Fig. 3.8 right). Both MUX/DEMUX and feedback algorithms are planned to be implemented in dedicated Field-Programmable Gate Arrays (FPGAs, Ravera et al., 2014a). One of the most demanding aspects of this biasing and read-out method is that it requires a very fast digital to analog conversion (DAC) while covering the large dynamic range of the 2.5 eV resolution TES pixels.

As explained in Sect. 3.2.1, the energy of the impacting X-rays can be extracted from the resulting current pulses in each TES. The available telemetry being limited, this signal processing cannot be done on the ground and is performed in a second part of the DREs called Event Processor (EP, see Fig. 3.8). The EP is organized in two steps: A first stage of FPGA based electronics analyses the signal from each TES as demodulated by the DRE DEMUX and triggers on current pulses to only select useful parts of the signals coming from the 3840 pixels. In a second step, each triggered pulse is processed by a scientific software responsible for the precise extraction of the energy and arrival time of each photon (Ravera et al., 2014a). In the current baseline, the scientific software will be coded onto a space qualified processor and implement the now widely used optimal filtering technique (Szymkowiak et al., 1993).

3.2.3 The anti coincidence detector

The L1/L2 orbit at which the *Athena* satellite will operate suffers from a higher external charged particles flux (solar particles and cosmic rays) than the more common low Earth orbit where there is protection by the Earth magnetic field. The stringent non X-ray background requirement (see Table 3.1) can therefore only be met by the addition of an active anti-coincidence detector beneath the main TES pixel array (Cryo-AC, Lotti et al., 2014; Macculi et al., 2014, 2016). These particles will interact both directly with the X-IFU detector and through the production of secondary particles after the interaction with the surrounding material. Some of them will deposit an energy amount lying inside the energy range of the instrument and will not be distinguishable from normal X-rays.

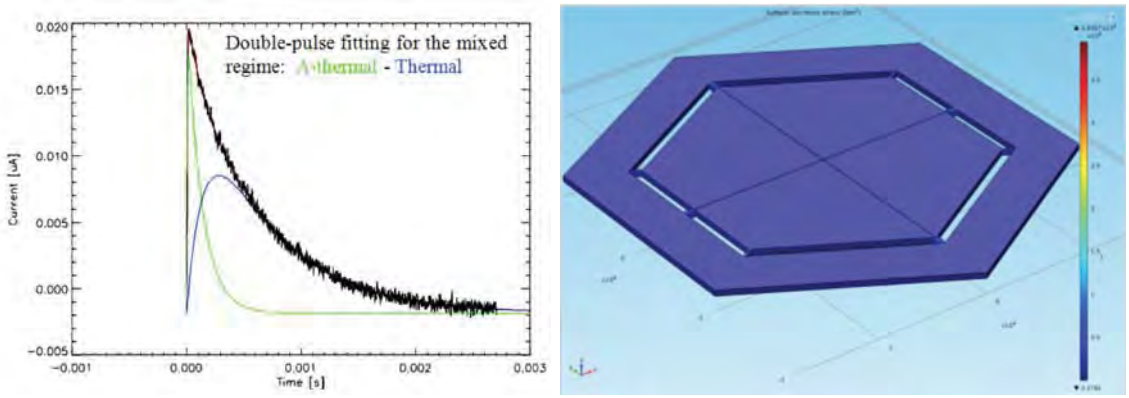

Figure 3.9: Left: Typical pulse generated by a charged particle in an anti-coincidence pixel showing the fast athermal rise. **Right:** Preliminary design of the anti-coincidence pixels. These will be integrated just beneath the main detector array.

The Cryo-AC, located very close to the main array ($\sim 1\,\mathrm{mm}$) will detect the charged particles that go through the main detector. It features 4 large Iridium TES operated in the so-called athermal regime allowing a very sharp rise time and thus a precise determination of the arrival time of the background events and an effective screening of the events in the main array (see Fig. 3.9 and Macculi et al., 2014). As the main detector, the anti-coincidence pixels are read out by a set of Cold Front-End Electronics (CryoAC CFEE), Warm Front-End Electronics (CryoAC WFEE), and BackEnd Electronics (CryoAC BEE). However, the charged particle flux is sufficiently small that the processing of the anti-coincidence data can be performed on the ground.

3.2.4 The X-IFU cooling chain and dewar system

In order to operate the TESs in their transition phase, it is necessary to cool the focal plane down to cryogenic temperatures below 100 mK (see Sect. 3.2.1). This cooling will be performed by an assembly of cryocoolers organized with several intermediate interface temperatures and shields forming a cryostat. The last stage cooler is baselined to be an ADR-Sorption cooler providing a heat lift of $\sim 1\,\mu\mathrm{K}$ at 50 mK (Duband et al., 2014). For the other coolers, a variety of options are still being considered but the cryo-chain may typically contain 2 K Joule Thomson coolers and 15 K pulse tubes. The shields cooling may be performed by an assembly of Stirling and Joule Thomson coolers (Charles et al., 2016). To maximize the mission lifetime, all the cryogenic engines are cryogen free and fully redundant except for the last stage which does not contain any movable part. Figure 3.10 (left) gives an overview of the design studied during the Mission Consolidation Review (MCR).

At the coldest temperatures, the dewar will incorporate a Focal Plane Assembly (FPA) providing thermal and mechanical support to the main and anti-coincidence detector arrays as well as the cold electronics (see Fig. 3.10 right). Special care will notably be made to insulate the sensor array from micro-vibrations produced by the cryocoolers. These vibrations might indeed dissipate a few nW which cannot be neglected in the noise budget of microcalorimeters (it indeed was the limiting factor to the resolution achieved by *Hitomi/SXS*, Mitsuda et al., 2014; Takei et al., 2016). The FPA is also responsible for the appropriate magnetic shielding to protect the electric and magnetic field sensitive TESs and SQUIDs. This will be realized by the combination of a superconducting Nb shield and a 2 K cryo-perm shield providing at least 10^5 attenuation, as well as an appropriate cooling sequence to

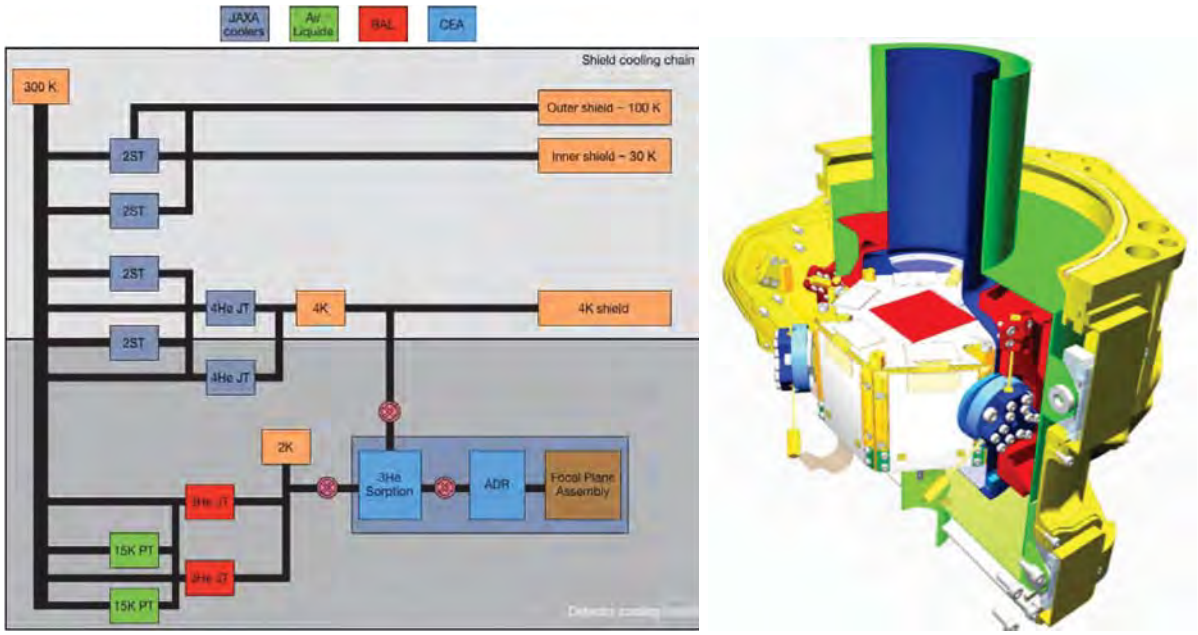

Figure 3.10: Left: Cryochain design studied during the Mission Consolidation Review, incorporating several intermediate temperature stages and shields. **Right:** Current design of the X-IFU focal plane assembly.

avoid field trapping.

The detector insulation with respect to outside thermal and IR load will be ensured by a set of five blocking filters (Barbera et al., 2014). These filters will consist of a fine layer of Aluminum deposited on a Polyimide substrate and be mounted onto the FPA as well as on an Aperture Cylinder providing the interface between the cryostat shields and the outside world. This will also allow appropriate radio frequency filtering from the satellite system. The filters will be protected from contamination, during ground operations and launch, by a door maintaining the cryostat under vacuum.

Outside the cryostat and above the Aperture Cylinder, a filter wheel will include additional Aluminum/polyimide filters for the observation of optically bright sources, as well as possibly neutral density filters to be used while observing bright X-ray sources and limit the energy resolution degradation happening at high count rates (see Chapter 4). The filter wheel will also incorporate a closed position realized with a thick Beryllium filter. It may also support the Modulated X-ray Source (MXS) and possibly a radioactive source. Similar to the one developed for *Hitomi/SXS* (Mitsuda et al., 2014), this source can emit X-ray flashes by the illumination of an iron target by an electronically controlled UV LED and allow the correction of energy scale drifts during an X-IFU observation.

3.2.5 Instrument power and control

The overall X-IFU control will be performed in the Instrument Control Unit (ICU). It notably includes the switching between instrument modes and operation with the desired settings. This unit will also be responsible for data collection and packeting as well as communication with the spacecraft. The raw power distribution will be ensured by a Power Distribution Unit (PDU) with the the power conversion being relocated to Remote Terminal Units (RTUs). Only the main array and Cryo-AC WFEE, as well as the DRE will operate their own power conversion due to tight electromagnetic compatibility requirements.

Chapter 4: The TES-array optimization exercise

4.1 Performance characterization of TES detectors and their first stage read-out

The discovery of superconductivity was made in 1911, when Heike Kamerlingh Onnes cooled a sample of mercury in a liquid helium bath and noticed the resistance of the material suddenly drop to zero around T_c =4.2 K (Kamerlingh Onnes, 1911). Since then, several materials were found to show similar phase transitions at various temperatures and were thus classified as "low-" and "high-T_c" superconductors. Whereas the origin of superconductivity in the latter remains unclear (see e.g. Leggett, 2006), Bardeen, Cooper, and Schrieffer explained this phenomenon in the former in 1957 through the formation of so-called Cooper pairs (Bardeen et al., 1957): when an electron goes through a superconducting material, positive ions in the lattice get attracted to it and form a positively charged cloud. A second electron gets in turn attracted to this cloud and form a Cooper pair with the first electron which acts as a single particle. The resulting binding energy prevents them from scattering and they flow through the material without resistance. At normal temperatures however, thermal excitation exceeds this binding energy and the Cooper pairs are broken: the material turns normal again.

Some of these "low-"T_c superconductors show a very sharp transition which makes them good candidates to be the base material for very sensitive thermometers. This idea was first put in practice in the 1940s by D.H. Andrews who applied a current to tantalum wires and then niobium nitride strips to measure respectively infrared fluxes and alpha particles (Andrews et al., 1942, 1949). This was the birth of the TESs. This technology however longly suffered from the difficulty of matching standard amplifiers to the TES noise, and it is only with the advent of cryogenic SQUID current amplifiers that they started to achieve the success we know today.

In this section, we will summarize the main elements necessary to understand the functioning and performance of TES based detectors and their first stage read-out circuit. This was largely inspired by the reference book by Irwin & Hilton (2005) but focuses on the most relevant aspects for the study of the X-IFU pixels.

4.1.1 The electro-thermal behavior of TES micro-calorimeters

To be able to detect input thermal power coming from X-rays, a TES is operated in its transition between zero and normal resistance. This setting point can typically be achieved through Joule heating coming from a current or a voltage bias. If the former solution was the first to be implemented (Andrews et al., 1942), the latter is now usually preferred as it provides better stability (see Sect. 4.1.1) and adequate cryogenic current amplification through SQUIDs. In this section, we will therefore concentrate on the behavior of TESs under voltage bias.

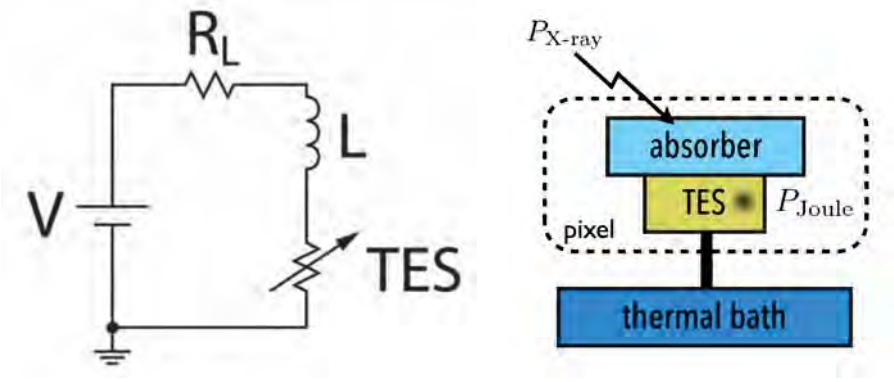

Figure 4.1: Schematics of the physics model coupling the thermal and electrical behavior of the TES/absorber pixel. **Left:** Thevenin equivalent of the first stage read-out circuit. **Right:** The thermal behavior is governed by the Joule dissipation in the TES, its link to the thermal bath and the incoming X-ray power.

Mathematical formulation and small signal solution

The response of a TES is essentially governed by two coupled differential equations: one describing the first stage read-out circuit and a second describing its thermal behavior. Whereas a variety of solutions can be implemented to operate TESs, without loss of generality, the TES electrical circuit can be replaced by its Thevenin equivalent featuring a voltage source V_0, a load resistor R_L, an inductance L, and the variable TES resistor R_{TES} (see Fig. 4.1, left). In the case of the X-IFU, operating its TESs under AC voltage bias (see Sect. 3.2.2), the inductance comes from the narrow-band filter defining the pixel carrier frequency, while the load resistor essentially consists of the parasitic resistance of the filter inductance. We can thus easily obtain the differential equation governing the evolution through time of the current I:

$$L\frac{dI}{dt} = V_0 - IR_{\mathrm{L}} - IR_{\mathrm{TES}} + \mathrm{Noise} \tag{4.1}$$

On the thermal side, the TES gets heated through both the Joule power ($R_{\mathrm{TES}}I^2$) and the absorption of sky X-rays ($P_{\mathrm{X\text{-}ray}}$) while being cooled by the cold heat bath (P_b). Usually, the TES and absorbers are strongly coupled such that they can be considered as a single thermal element of total heat capacity C. This is the case for the X-IFU pixels for which the absorbers will be directly electro-plated onto the TESs (see Sect. 3.2.1), but in some applications, a limited conductivity can be introduced between those elements to read out different absorbers with a single TES (see e.g. Smith et al., 2008). Under those conditions, the TES temperature T is governed by the following equation:

$$C\frac{dT}{dt} = -P_{\mathrm{b}} + R_{\mathrm{TES}}I^2 + P_{\mathrm{X\text{-}ray}} + \mathrm{Noise} \tag{4.2}$$

The heat flow to the thermal bath can then further be expanded to:

$$P_b = K(T^n - T^n_{\mathrm{bath}}) \tag{4.3}$$

As can be seen, these equations suffer from several non-linear terms, such that there does not exist a generic analytical solution to this system. Among the non-linearities, there are notably the

TES transition and the heat flow to the thermal bath. The first one is usually characterized by the resistance logarithmic derivatives at the set point with respect to temperature and current, α and β:

$$\alpha = \left.\frac{\partial \log R}{\partial \log T}\right|_{I_0} = \left.\frac{T_0}{R_0}\frac{\partial R}{\partial T}\right|_{I_0} \tag{4.4}$$

$$\beta = \left.\frac{\partial \log R}{\partial \log I}\right|_{T_0} = \left.\frac{I_0}{R_0}\frac{\partial R}{\partial I}\right|_{T_0} \tag{4.5}$$

These allow to define a simple two-dimensional linear model for the resistance:

$$R_{\mathrm{TES}} = R_0 + \left.\frac{\partial R}{\partial T}\right|_{I_0} \delta T + \left.\frac{\partial R}{\partial I}\right|_{T_0} \delta I \tag{4.6}$$

Apart from allowing the definition of a simple linear approximation of the TES transition, the α and β parameters are usually measured to characterize a newly obtained pixel. We note that generally, the TES resistance further depends on the neighboring magnetic field and that it can change throughout an event due to the read-out circuit generating its own magnetic field (Smith et al., 2013; Sadleir et al., 2014). This is however beyond the scope of this simple presentation of the TES behavior. Concerning the heat bath power flow, the usual approximation is to define a constant conductance G measured at the TES set point and assume a simple linear scaling with temperature:

$$P_b = P_{\mathrm{b},0} + G\delta T. \tag{4.7}$$

Using these two approximations and in the small signal limit around a set point (I_0, T_0), Lindeman (2000) showed that Equations 4.1 and 4.2 could be simplified to:

$$\frac{\mathrm{d}}{\mathrm{dt}}\begin{pmatrix}\delta I\\ \delta T\end{pmatrix} = \begin{pmatrix}\frac{1}{\tau_{\mathrm{el}}} & \frac{\mathcal{L}_I G}{I_0 L}\\ -\frac{I_0 R_0(2+\beta)}{C} & \frac{G(1-\mathcal{L}_I)}{C}\end{pmatrix}\begin{pmatrix}\delta I\\ \delta T\end{pmatrix} + \begin{pmatrix}0\\ \frac{P_{\text{X-ray}}}{C}\end{pmatrix} \tag{4.8}$$

where τ_{el} and $\mathcal{L}_I$ are respectively the electrical time constant and the low-frequency loop gain under constant current. They are defined by:

$$\tau_{\mathrm{el}} = \frac{L}{R_L + R_0(1+\beta)} \; ; \; \mathcal{L}_I = \frac{R_0 I_0^2 \alpha}{G T_0} \tag{4.9}$$

In the case of the response of a TES to an X-ray impact modeled by a delta function, the most illustrative way of solving these equations is to identify the coupling matrix eigenvalues to decouple the problem:

$$\frac{1}{\tau_\pm} = \frac{1}{2\tau_{\mathrm{el}}} + \frac{G(1-\mathcal{L}_I)}{2C} \pm \frac{1}{2}\sqrt{\left(\frac{1}{\tau_{\mathrm{el}}} - \frac{G(1-\mathcal{L}_I)}{C}\right)^2 - \frac{4R_0\mathcal{L}_I(2+\beta)G}{LC}} \tag{4.10}$$

It is then easily shown that the current response will follow a profile proportional to:

$$I(t) \propto (e^{-t/\tau_+} - e^{-t/\tau_-}) \tag{4.11}$$

The complete formula of the current response can be found in Lindeman (2000) and Irwin & Hilton (2005), but this already allows us to identify that the current will typically follow a profile close to an

exponential rise and decay characterized by a rise time τ_+ and a fall time τ_-. If we take the limit of low inductance $L \to 0$,

$$\tau_+ \to \tau_{\rm el} \tag{4.12}$$

$$\tau_- \to \frac{C}{G}\frac{1+\beta+R_L/R_0}{1+\beta+R_L/R_0+(1-R_L/R_0)\mathcal{L}_I} = \tau_{\rm eff} \tag{4.13}$$

This allows to see that the pulse rise time is essentially dominated by the electrical time constant, i.e. the inductance slowing the current, and the pulse fall time to another time constant $\tau_{\rm eff}$ which can be interpreted as an effective thermal time constant. Of course, in the real system where the inductance is not negligible (which is especially true for TESs under AC bias like those of the X-IFU), the poles of the system interact and both the rise and fall time are a mix of the two effects.

The stability of TES pixels and the electro thermal feedback

From the double exponential impulse response previously obtained for the TES, we see that the system is over-damped if τ_+ and τ_- are real and non-equal, whereas it is underdamped and shows oscillating patterns if τ_+ and τ_- are complex. In the particular case when both time constants are equal and real, we talk about critical damping. As has been shown by Irwin & Hilton (2005), the damping status of the system can be summarized to the choice of the circuit inductance. The system is over-damped if L is outside the $[L_{\rm crit-}; L_{\rm crit+}]$ interval defined by:

$$L_{\rm crit\pm} = \left\{ \mathcal{L}_I \left(3+\beta-\frac{R_L}{R_0}\right) + \left(1+\beta+\frac{R_L}{R_0}\right) \pm 2\sqrt{\mathcal{L}_I(2+\beta)\left(\mathcal{L}_I\left(1-\frac{R_L}{R_0}\right)+\left(1+\beta+\frac{R_L}{R_0}\right)\right)} \right\} \frac{R_0 C}{G(\mathcal{L}_I-1)^2} \tag{4.14}$$

When the inductance equals either of the two critical values, the system is critically damped. This situation is often adopted in a trade-off between energy resolution and the required slew rate of the read-out electronics. This is especially true for FDM systems like the X-IFU for which this slew rate needs to be followed by the demanding base-band feedback scheme. Usually, of the two critical damping solutions, the lower inductance solution is adopted in order to retain good responsivity of the TES current to the temperature rise (as we have seen, pulse rise time is dominated by the electrical time constant).

Looking back again at the shape of the impulse response, we see that the system is stable if the real part of both time constants are positive. In the case of an over-damped or critically damped system, this condition translates to:

$$\frac{1}{\tau_{\rm el}} + \frac{G(1-\mathcal{L}_I)}{C} > \sqrt{\left(\frac{1}{\tau_{\rm el}} - \frac{G(1-\mathcal{L}_I)}{C}\right)^2 - \frac{4R_0\mathcal{L}_I(2+\beta)G}{LC}} \tag{4.15}$$

$$\Leftrightarrow R_0 > \frac{\mathcal{L}_I - 1}{\mathcal{L}_I+\beta+1} R_L \tag{4.16}$$

We see that this condition is automatically verified in the case of voltage bias, for which $R_0 > R_L$. This is the main advantage of this biasing technique which rendered stability possible even for high loop gain values, i.e. high sensitivity, and is due to the so-called negative electro-thermal feedback: in

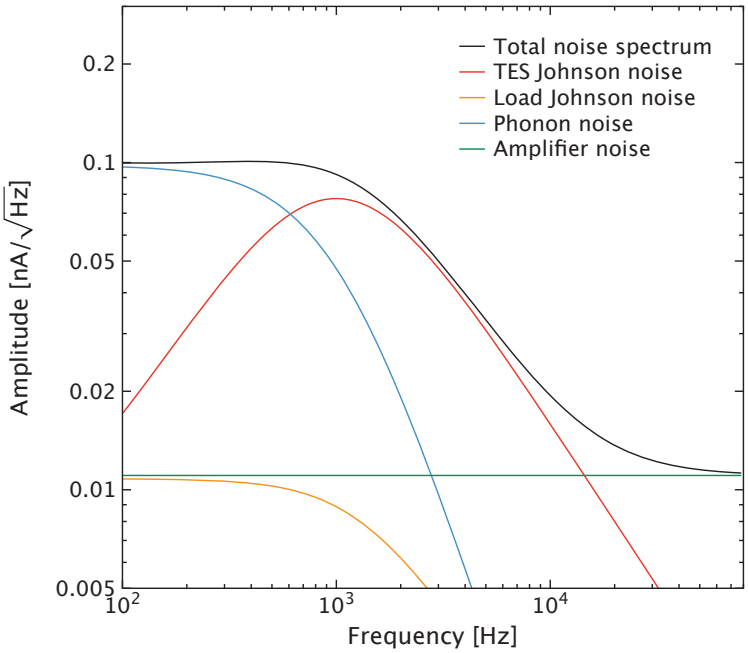

Figure 4.2: The different contributors to the TES current noise. All noise components were analytically computed in the small signal limit using Equations 4.18 to 4.22 with the baseline X-IFU pixel parameters.

the case of voltage bias, the Joule dissipation at the TES level equals V_0^2/R_{TES}. During an event, the resistance of the TES will rise, which will decrease the heat dissipation and thus the TES temperature and will oppose the resistance rise. On top of the direct consequence in terms of stability, the negative electro-thermal feedback will allow the automatic biasing of the TES inside its transition which has obvious practical advantages notably for large array applications like the X-IFU.

4.1.2 Noise contributors and energy resolution

In the frame of its application to high resolution spectroscopy like the X-IFU, one of the key elements of a TES is its low noise. This noise originates mostly originates from the thermodynamic fluctuations of the different elements of the TES. In this section, after reviewing the main contributors to the TES noise (an example of a TES noise decomposition for the X-IFU baseline pixels is given in Fig. 4.2), we will present how one can estimate the energy resolution of this type of detectors.

Johnson noise

Like all systems containing resistive elements, the TES system is subject to the so-called Johnson noise (Johnson, 1928; Nyquist, 1928). This noise arises from the thermal agitation of the electrons inside the resistive elements. For a linear resistance, like the load resistance, the spectral density of this component in the tension domain is:

$$S_{V,R_L}(\omega) = 4k_B T_L R_L \tag{4.17}$$

where k_B is the Boltzman constant and T_L the temperature of the load resistance. Translated to the current space in which the signal will actually be measured, this becomes (Irwin & Hilton, 2005):

$$S_{I,R_L}(\omega) = 4k_B T R_L I_0^2 \frac{(\mathcal{L}_I - 1)^2}{\mathcal{L}_I^2} \left(1 + \omega^2 \left(\frac{C}{G(1-\mathcal{L}_I)}\right)^2\right) |s_I(\omega)|^2 \tag{4.18}$$

where $s_I(\omega)$ is the power to current responsivity of the TES, which can also be seen as the Fourier Transform of a small signal pulse profile divided by the input energy (Doriese et al., 2009). It therefore has the same roll-offs frequencies as the signal, i.e. $1/\tau_-$ and $1/\tau_+$. A complete formulation of s_I is available in Irwin & Hilton (2005), but it is beyond the scope of the simple analysis presented here.

The formulation for the TES resistance itself is slightly more complicated as the resistance depends on the current going through the TES (Irwin & Hilton, 2005):

$$S_{I,\mathrm{TES}}(\omega) = 4k_B T R_0 I_0^2 \frac{1+2\beta}{\mathcal{L}_I^2} \left(1 + \omega^2 \left(\frac{C}{G}\right)^2\right) |s_I(\omega)|^2 \tag{4.19}$$

An important feature of the Johnson noise is that it severely decreases during a pulse: if the TES temperature rises as the same time as the resistance, the relative increase stays limited in comparison (the transition is sharp) and as the resistance rise is at the first order translated in a similar fall of the current, one see from Equation 4.19 that the overall noise level is diminished. On top of this direct effect, in the case of detectors with non-negligible β an additional diminution comes from the fact that it decreases inside the transition (if one considers for instance a fixed resistance versus current derivative, β is inversely proportional to the TES resistance – but see also e.g. Smith et al., 2012). This change is the main source of noise non-stationarity during an event.

Thermal fluctuation noise

The second main source of noise is the thermal fluctuation in the link between the TES and the thermal bath. When translated in the current domain, this contribution amounts to (Irwin & Hilton, 2005):

$$S_{I,TF}(\omega) = 4k_B T^2 G \gamma |s_I(\omega)|^2 \tag{4.20}$$

where γ is a correction factor between 0.5 and 1 which depends on the type of reflection of the phonons in the link and also on the TES temperature (Boyle & Rodgers, 1959; McCammon, 2005). Contrary to the Johnson noise, the thermal fluctuations increase during a pulse together with the TES temperature. This change however remains limited in comparison.

Unexplained electrical noise

On top of the previous noise contributions, some TESs have been known to require additional noise components to fully explain their observed noise spectra. These additional noise components can take a variety of forms and are generally referred to as excess noise (see Irwin & Hilton, 2005, for a general discussion). For the application we are interested in here the most distinctive type of excess noise is however the so-called unexplained electrical noise. This extra noise component features a spectrum with a shape very similar to that of Johnson noise and has classically been characterized by an empirical parameter M^2 (see e.g. Smith et al., 2013):

$$S_{I,\mathrm{unexp}}(\omega) = M^2 S_{I,\mathrm{TES}}(\omega) \tag{4.21}$$

Even though several explanations have been put forward to try to explain the origin of this component (Irwin & Hilton, 2005, and references therin), it remains unclear whether it is not just associated to higher orders of Johnson noise (Smith et al., 2013). Experimentally, this component has been seen to change significantly with pixel geometry and boundary conditions (Ullom et al., 2004) as well as within the TES transition (Ullom et al., 2004; Smith et al., 2013).

Amplifier noise

The last main contributor to the TES noise budget is the amplifier noise coming from the SQUID. This contribution is usually small compared to the previous components and can be considered to be constant with frequency in the current space:

$$S_{I,\mathrm{amp}}(\omega) = S_{I,\mathrm{amp}} \tag{4.22}$$

Energy resolution

Once all the noise components of the TES have been properly characterized, the energy resolution of the TES (FWHM) can be predicted by the following integral (Moseley et al., 1984):

$$\Delta E_{\mathrm{FWHM}} = \sqrt{8\ln 2}\left(\int_0^\infty \frac{4\mathrm{d}f}{\mathrm{NEP}^2(f)}\right)^{-1/2} \tag{4.23}$$

where $\mathrm{NEP}^2(f)$ is the noise equivalent power of the detector as a function of frequency. For an easier comprehension, this formula can be transposed to the TES readout current space:

$$\Delta E_{\mathrm{FWHM}} = \sqrt{8\ln 2}\left(\int_0^\infty \frac{4|s_I(f)|^2\mathrm{d}f}{S_{I,R_L}(f) + S_{I,\mathrm{TES}}(f) + S_{I,TF}(f) + S_{I,\mathrm{unexp}}(f) + S_{I,\mathrm{amp}}(f)}\right)^{-1/2} \tag{4.24}$$

$$= \sqrt{8\ln 2}\left(\int_0^\infty 4\,\mathrm{SNRD}^2(f)\right) \tag{4.25}$$

The energy resolution can thus be seen to be related to the integral of the squared signal to noise ratio density ($\mathrm{SNRD}^2(f)$), i.e. the ratio of the pulse power ($|s_I(f)|^2$) over the total noise power. In the small signal limit, when neglecting the amplifier noise, assuming strong electrothermal feedback and zero load resistance, Irwin & Hilton (2005) have shown that the energy resolution could be approximated by:

$$\Delta E_{\mathrm{FWHM}} \approx \sqrt{8\ln 2}\sqrt{\frac{4k_B T_0^2 C}{\alpha}\sqrt{\frac{n(1+2\beta)(1+M^2)\gamma}{1-(T_{\mathrm{bath}}/T_0)^n}}} \tag{4.26}$$

We see that to obtain a good energy resolution, one usually wants to construct a TES with a high α and a small heat capacity C. This can easily be understood by the fact that a low C means a higher temperature change for the same energy input and a higher α will produce in turn a bigger change of the TES resistance. The choice of the heat capacity is however limited by the energy range for which it needs to be operated as smaller heat capacity and higher α also mean that the TES will have a lower saturation energy.

In a space application where processing power is limited, one also has to take into account the fact that only a restricted amount of data will be used to reconstruct the energy of the individual events and will thus lead to a degradation of the achievable energy resolution. At the first order, this

degradation will mostly come from the rejection of the low frequency content of the signal to avoid contamination from external baseline fluctuations (see Chapter 5). Doriese et al. (2009) has shown that this effect would affect the energy resolution following:

$$\Delta E(t_{\rm rec}) = \frac{\lim\limits_{t_{\rm rec}\to\infty} \Delta E}{\sqrt{1 - 1/(2t_{\rm rec} f_{\rm eff})}} \tag{4.27}$$

where f_{eff} is the pixel effective roll-off frequency computed as:

$$f_{eff} = \frac{\int_0^\infty \mathrm{SNRD}^2(f)\mathrm{d}f}{\lim_{f\to} \mathrm{SNRD}^2(f)} \tag{4.28}$$

4.2 The TES-array optimization exercise: rationale and studied configurations

As illustrated in the previous section, the design of a TES depends on a very large set of parameters. A TES based micro-calorimeter pixel can therefore only be optimized for a particular application. One of the most important aspects to consider is notably the expected count rate: if one wants to accommodate higher count rates, faster pixels will indeed be required, at the expense of a higher load on the read-out system (higher slew rate and information bandwidth), or a penalty will be paid in terms of energy resolution due to the shortening of the available record length to process the pulses (see Eq. 4.27). Looking back at the X-IFU top level requirements (Table 3.1), we see that the count rate capability of the instrument is defined by a 80 % throughput requirement of nominal energy resolution events for 1 mCrab sources. This performance is actually driven by the observation of bright point sources (GRB afterglows to detect WHIM filaments Kaastra et al., 2013) only illuminating a few pixels at the same time and using this number to design all pixels would thus automatically result in an over-specification of the focal plane.

A logical approach is therefore to use two types of detectors, one to address the high point source count rate, and another for the coverage of the large X-IFU field of view. In this context, two alternative configurations to the baseline monolithic TES-array have been studied by the X-IFU consortium, both incorporating in their center a small pixel array (SPA) of ~ 400 detectors dedicated to the observation of bright sources (see Fig. 4.3). The main parameters of the considered pixels are summarized in Table 4.1. If the SPA pixels are slightly faster than the standard ones (see the lower thermal time constant C/G), the better count rate capability of the SPA pixels will actually be brought by a finer oversampling of the telescope PSF and thus in lower individual count rates seen by the pixels at a given flux. On top of the improved bright source performance and the possibility to reach towards the goal count rate capability, the SPA detectors can have a lower heat capacity (at equal stopping power a lower heat capacity is more easily achieved by smaller pixels) and thus a better energy resolution (see Eq. 4.26). Of course, the introduction of the pixels in the focal plane does not come without a certain penalty and to retain the required 5' field of view, the size of the large pixel array (LPA) detectors needs to be increased to $\sim 260\,\mu$m bringing a slight degradation of the instrument imaging capability (see Sect. 6.3). This is how the first alternative array configuration was defined (configuration (b)). The third studied solution (configuration (c)) corresponds to the maximum field of view that could be obtained by further increasing the LPA pitch to a maximum of $\sim 300\,\mu$m for which the required 2.5 eV resolution is still accessible. One can note that by relaxing the

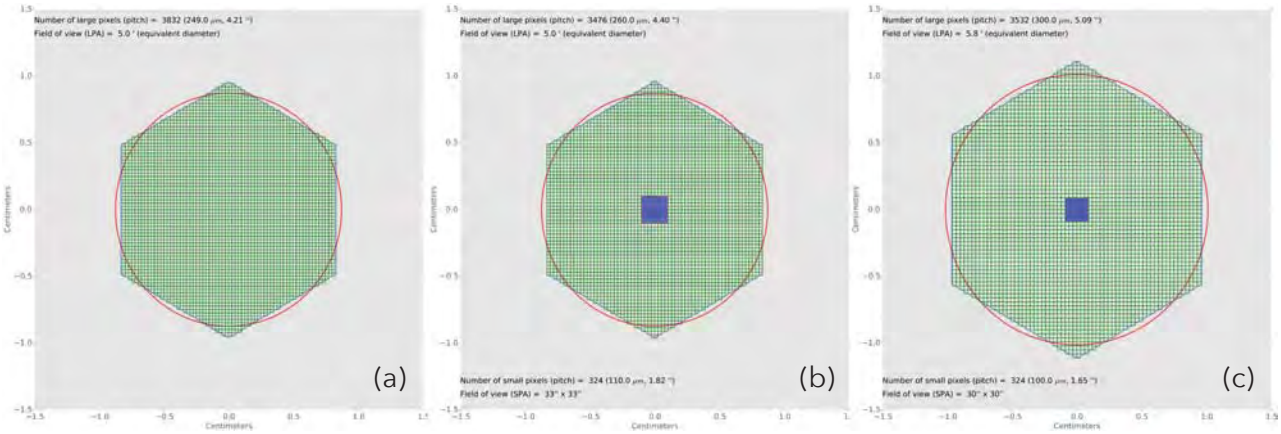

Figure 4.3: The three TES array configurations considered in the optimization exercise. (a) Baseline single pixel array with 249 µm pixel pitch. 5' FoV. (b) SPA: 324 small pixels with 110 µm pitch. LPA: 3476 large pixels with 260 µm pixel pitch. 5' FoV. (c) SPA: 324 small pixels with 100 µm pitch. LPA: 3532 large pixels with 300 µm pixel pitch. 5.8' FoV.

Table 4.1: Main parameters of the pixels considered in the TES-array optimization exercise.

Pixel parameter	LPA1	LPA2	LPA3	SPA
Pixel size	249 µm	260 µm	300 µm	100 µm
Heat capacity at bias C	0.8 pJ/K	0.8 pJ/K	0.8 pJ/K	0.26 pJ/K
Bath conductance at bias	200 pW/K	115 pW/K	57 pW/K	300 pW/K
Heat bath power flow exponent	3	3	3	4
α	75	75	75	100
β	1.25	1.25	1.25	10
Unexplained noise factor M	0	0	0	0.8
Bias resistance R_0	1 mΩ	1 mΩ	1 mΩ	1.1 mΩ
Bias temperature T_0	90 mK	90 mK	90 mK	90 mK
Bias current I_0	68 µA	52.5 µA	37.1 µA	73.5 µA
Effective load resistance R_L	49 µΩ	90 µΩ	207 µΩ	91 µΩ
Effective circuit inductance L	66 nH	120 nH	276 nH	122 nH
Small signal energy resolution	1.69 eV	1.70 eV	1.73 eV	1.54 eV
Slew rate	88 mA/s/keV	36 mA/s/keV	11 mA/s/keV	229 mA/s/keV

Notes – In the frame of the TES array optimization exercise, the pixel physical parameters (heat capacity, conductance, etc.) were linked to their size to limit the number of studied configuration. In practice, there is no restriction preventing for instance to design an LPA3 pixel on a 260 µm pitch.

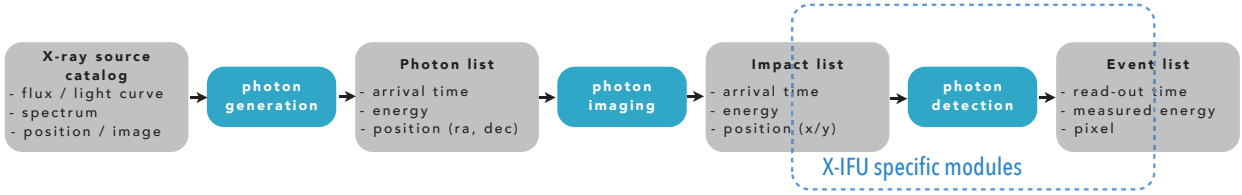

Figure 4.4: Overview of the SIXTE simulation process: From a source catalog containing a number of astrophysical X-ray sources, photons are randomly generated to create a perfect photon list with the energy and sky position information. The imaging process then projects the X-rays onto the focal plane to obtain an impact list. Finally the detection stage transforms those impacts onto detected events with pixel position and measured time and energy. This is at this step that the developed X-IFU specific modules come into play.

rapidity of the large pixels, a lower admissible slew rate will be required from the read-out electronics in these two configurations bringing potential margins to the design of the DRE.

In the following sections, we will investigate the energy resolution and count rate performance of the different TES array configurations using the X-IFU End-to-End simulator to which development I largely contributed in the frame of this thesis.

4.3 The X-IFU End-to-End simulator

4.3.1 SIXTE: a generic simulation software for X-ray observatories

The X-IFU End-to-End simulator was implemented in the frame of the "Simulation of X-ray Telescopes" software package (SIXTE, Schmid, 2012; Wilms et al., 2014), which has been developed as a generic simulation suite for the study of X-ray missions. It relies on the Monte Carlo simulation of individual photons from their emission by astrophysical sources to their detection and measurement by the instrument. Figure 4.4 shows the different steps of the simulation, namely photon generation, imaging and detection. These stages have been developed in a modular way such that the same processes can be used for the simulation of different instruments and a given physical process can be simulated using interchangeable methods. This allows the reuse of existing code for new missions (the X-IFU and WFI simulator for instance share the same imaging process), but also offers simulations with different levels of representativeness and computational speed depending on the required sophistication. As will be presented later, this is notably the case for the X-IFU for which two distinct approaches were developed.

In SIXTE, all instruments are defined using a specific XML format (see the SIXTE manual[1] for more details). This file notably contains the optical properties of the instrument (PSF, ARF, vignetting) but can also incorporate a description of the detection process through a large set of tags explaining how the instrument read-out process works. In the case of the X-IFU, the particularity of a calorimeter detection principle did not allow to use this standard format and another XML syntax was developed to describe it.

In this section, I will briefly describe the photon generation and imaging processes which are more or less common to all missions. I will present in greater detail in the subsequent sections the X-IFU specific modules to which development I largely participated during my thesis and that populate the

[1] http://www.sternwarte.uni-erlangen.de/research/sixte/data/simulator_manual_v1.1.pdf

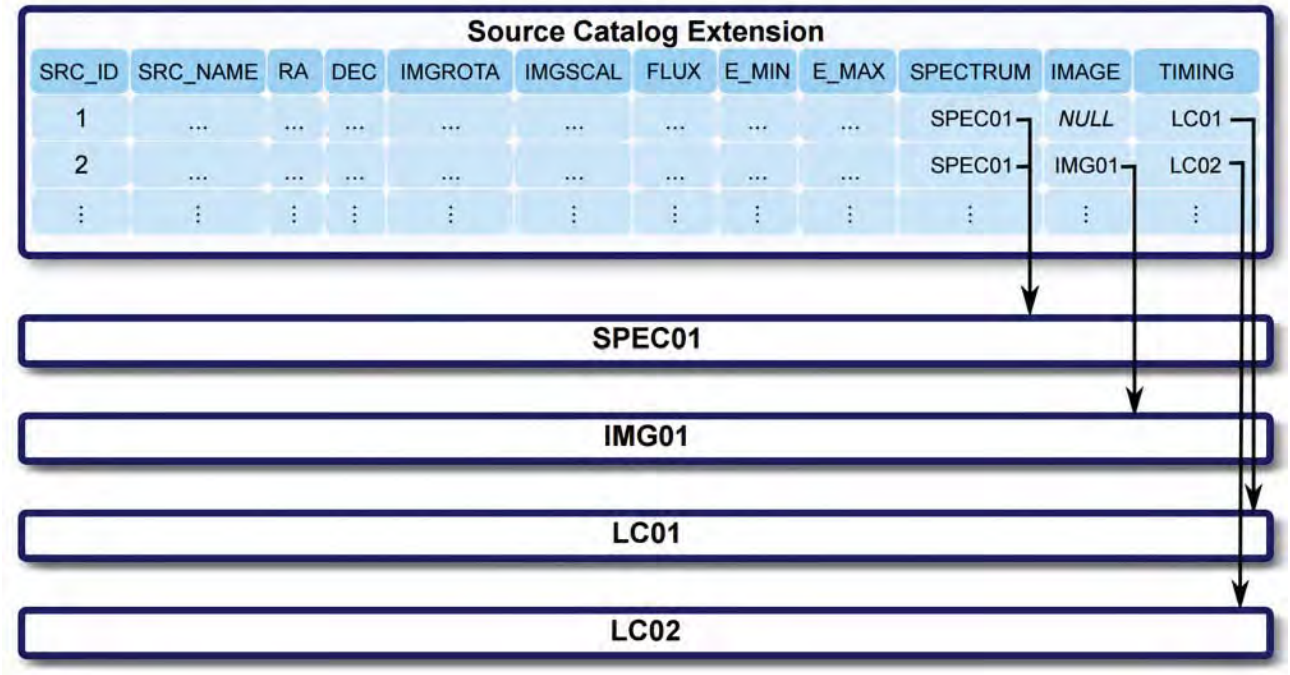

Figure 4.5: Schematic of the SIMPUT file format: The first extension is a source catalog containing basic information on the different sources as well as pointers to spectral, spatial and timing information. This information is saved in other extensions/files and can be shared by several sources. Figure taken from the SIMPUT manual.

photon detection step.

Photon generation

An End-to-End simulation starts with the definition of the astrophysical source(s) whose observation is going to be simulated. To do so, SIXTE relies on a FITS file format called SIMPUT[2] which provides a generic framework to define the input of several X-ray simulation tools (e.g. SIMX[3] or the *Chandra* simulator MARX[4]). A SIMPUT file is a source catalog which can in principle contain an arbitrary number of X-ray sources: the primary extension contains a binary table in which each source is defined by at least its ID, name, position on the sky and source flux in a given energy band, as well as a spectrum identification which points to another FITS extension of the SIMPUT file or another file all together using the extended FITS filename syntax (see Fig. 4.5). On top of this, the source can be affected a FITS image (scaled and rotated using the IMGROTA and IMGSCAL columns) to describe its spatial flux distribution (extended source), or timing properties in the form of a light curve or a power spectrum. The main advantage of the SIMPUT format is that it allows several sources to share the same spectral, spatial or timing properties (several sources can e.g. point to the same spectrum extension) such that the minimal necessary amount of information is saved in the file. This is particularly useful for large source catalogs in which several sources have similar spectral shapes (but can still have different fluxes) and for which the saving of a spectrum per source would be

[2] http://hea-www.harvard.edu/heasarc/formats/simput-1.1.0.pdf
[3] https://hea-www.harvard.edu/simx/
[4] http://space.mit.edu/CXC/MARX/

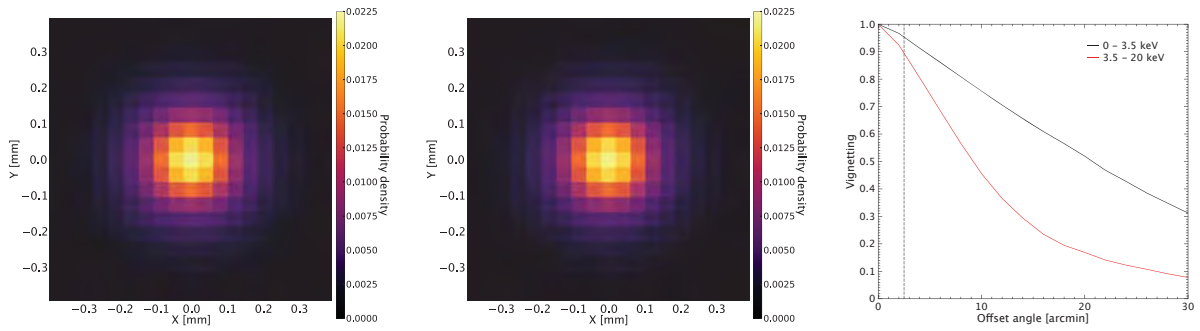

Figure 4.6: The on-axis *Athena* PSF at 0.5 (left) and 10 keV (middle) and vignetting functions (right) as used by SIXTE. If one looks closely, one will see that the PSF spread is slightly larger at high energy. In the vignetting plot, the vertical dotted line represents the extent of the X-IFU field of view highlighting that for this instrument, the vignetting effect stays limited.

prohibitive (see e.g. Sect. 6.3 or Sect. 6.2). The spectral, spatial and timing information can also be given through a photon list extension which directly contains a sufficient number of X-rays to describe the source emission. This is particularly useful when one wants to interface for instance an MHD or cosmological simulation (see Sect. 6.2).

Starting from a SIMPUT catalog, SIXTE will draw photons from all the sources present in the instrument field of view. In order to limit the number of simulated photons, the spectrum of each source is scaled by the source flux and convolved with the instrument effective area to compute the expected number of focal plane impacts generated by a given source. From there, a Poisson randomized number of photons are drawn from the source using a simple rejection technique on the spectral flux density and image to determine the energy and sky positions of the photons respectively. In the case of a photon list, the required number of X-rays are simply randomly selected from the list. As a rule of thumb, we note that a factor of at least five is advised between the photon list length and the expected number of events in the simulation for SIXTE to be able to provide a statistically accurate observation realization (otherwise, the same photon is quite likely to be selected 2 times).

Imaging

SIXTE does not incorporate yet any ray-tracing module such that the imaging process is the same for all X-ray missions. This process relies on the use of two different calibration files: the PSF and vignetting. We note that the ARF was used at the photon generation stage. The PSF gives the shape of the flux spread by the optics as a function of the photon energy and offset angle with respect to the line of sight, while the vignetting describes the telescope loss of effective area as a function of the photon offset angle for different energies (see Fig. 4.6). In SIXTE, for each source photon, a first uniformly distributed unit random variable is drawn to determine whether it is lost to the vignetting effect: if the random number is lower than the vignetting value corresponding to its energy and offset angle, the photon is kept, and it is rejected otherwise. If the photon is kept, it is projected onto the focal plane and its final impact position is determined through a 2D rejection method using the corresponding PSF as a 2D probability distribution.

4.3.2 XIFUPIPELINE: a tool for science simulations

As previously mentioned, the standard SIXTE approach for the detection stage, initially developed for silicon based detectors, is not applicable to micro-calorimeters such as the X-IFU in which the pixels are not organized following read-out lines. Two alternative simulation solutions were therefore implemented in SIXTE for this instrument. The first one (`xifupipeline`), which I first implemented and developed during the course of my thesis, will be presented here and is based on the parameterized randomization of the photon impact energies. The second (`tessim`, see Sect. 4.3.3) was mainly implemented by J. Wilms (with significant contributions from my part as the main user of this tool) and offers shorter term single pixel simulations of the actual physical evolution and read-out of the X-IFU TESs.

In order to be able to perform a representative simulation of the detection process, it is necessary to describe the geometry and properties of the X-FIU focal plane. For this purpose, a new Advanced Detector XML file was developed. It offers a great flexibility and each pixel position and properties can be defined individually such that virtually any detector geometry can be simulated. A set of loop tags were added to this format in order to ease the definition of an ensemble of similar pixels, but also offer a reasonable readability of the file. Among these notably figures a hexagon loop used for the building of the LPAs. The pixel properties can also be defined at the detector level in which case only a subset of special pixels can be specified. As a general rule, at the end of the focal plane geometry building, a check is made to remove potential overlapping pixels leaving only the later defined ones. This is particularly useful for the hybrid configurations considered here for which the SPA can simply be defined on top of the hexagonal LPA. An exhaustive description of the available XML tags is given in the SIXTE manual while the different XML files used for the TES-array optimization exercise are given in Appendix A.

In the X-IFU, the detection and measuring of X-rays goes through the on-board analysis of the current pulses created by the impacting photons. As mentioned in Sect. 4.1.2, this reconstruction typically has a degraded performance when pulses are close-by in time. To represent this property, each pixel gets affected a set of grades in the Advanced Detector XML which define the expected energy resolution (characterized by an RMF) as a function of the time separation between the events in the pixel timeline (see Sect. 4.4.2). The detection process in `xifupipeline` is thus simulated as follows: first, the imaged photons get affected to a pixel using the detector geometry (some impacts are lost at this stage due to the gaps between the pixels). Then, the software affects a grade to each remaining impact using the grading scheme and the time separation since the previous event and until the next one in the pixel timeline. Finally, the read-out energy of each event is randomly selected using the RMF matrix corresponding to its grade. On top of this time dependent energy randomization process, events separated by less than one readout sampling interval are considered to pileup and become a single event with the sum of the initial energies that is then treated as a normal event. At the end of the simulation, the `xifupipeline` tool writes an Event File containing the list of the detected and measured X-rays as well as their grade for later analysis by the standard X-ray tools.

The `xifupipeline` tool is a very efficient tool and the simulation of a typical 100 ks observation of an extended source usually takes a few minutes to run on laptop-like resources. Of course, it uses a relatively simple representation of the instrument performance and is not suited to the study of very fine instrumental effects, but it allows to test the global scientific performance of the instrument, as will be fully illustrated in Chapter 6. Moreover, the flexibility of its design, using standard calibration files (RMFs) to characterize the energy resolution performance as a function of energy and count

rate, makes it easy to update the simulation representativity with the most recent knowledge of the instrument. This knowledge can be characterized by more precise simulation tools such as the one presented in the next section.

4.3.3 TESSIM: a tool for realistic TES simulations

SIXTE also incorporates a slower, more representative device-level simulator for TES based instruments which is an ab initio representation of the physics of the detection process. Contrary to `xifupipeline` which creates X-ray Event Files, `tessim` directly simulates the read-out signal of a TES pixel following X-ray impacts. This data stream can then be analyzed by pulse processing methods, as will be shown later. In this section, after briefly describing the simulation procedure, I will perform a comparison of this simulator with real data streams obtained from TES pixels developed at the Goddard Space Flight Center.

Simulation method

In brief, `tessim` performs a numerical integration of the coupled differential equations governing the electro-thermal evolution of the TES. It uses the formulation by Irwin & Hilton (2005) described in Sect. 4.1.1, concretely Equations 4.1 and 4.1 and the same linear resistance transition as Equation 4.4. The input TES parameters for the different pixel types are summarized in Table 4.1. `tessim` simulates all the noise components presented in Sect. 4.1.2, i.e. the Johnson noise from both the load and TES resistors, including a potential unexplained noise contribution, the thermal fluctuations with the heat bath, and amplifier noise. The latter is fixed to $2\,\mathrm{pA}/\sqrt{\mathrm{Hz}}$ at the level of the input coil, which is close to the current state of the art for a 2-stage SQUID amplifier chain and consistent with the energy resolution budget of the instrument (Gottardi et al., 2014; den Hartog, 2015), while the others are directly computed using the TES parameters. In the software, the addition of the different noise components is done at the level of the physical parameter directly impacted (resistance voltage for the Johnson noise, TES temperature for the thermal fluctuations, read-out current for the amplifier chain), which allows to obtain a representative noise spectrum while using a time-domain integration. The noise levels are also updated throughout the simulation, such that the full non-stationary character is respected. As mentioned in Sect. 4.1.2, this notably means that the Johnson noise will decrease during an X-ray pulse.

In Figure 4.7 (left), we compare the simulated pulse shapes at different energies with the small signal profile predicted by Irwin & Hilton (2005) for the baseline LPA1 X-IFU pixels. As expected, `tessim` agrees with the analytical formulation at low energies, whereas we can see the non-linearity of the simulation at higher energies. In terms of noise spectrum (Fig. 4.7, right), the software fully agrees with the shape predicted by Equations 4.18 to 4.22 when measured from empty streams.

Main limitations

Even if `tessim` already constitutes a significant improvement in terms of representativity with respect to a small signal model, a certain number of approximations were made for this first implementation. These are listed below:

- *Pulse phase:* For simplicity reasons, pulses are currently simulated in phase with the sampling process, meaning that the pulse profile does not jitter around the time bins. In practice, this would induce a correlation between the filtered energy and the pulse arrival time that needs to be calibrated for to avoid a degradation of the energy resolution.

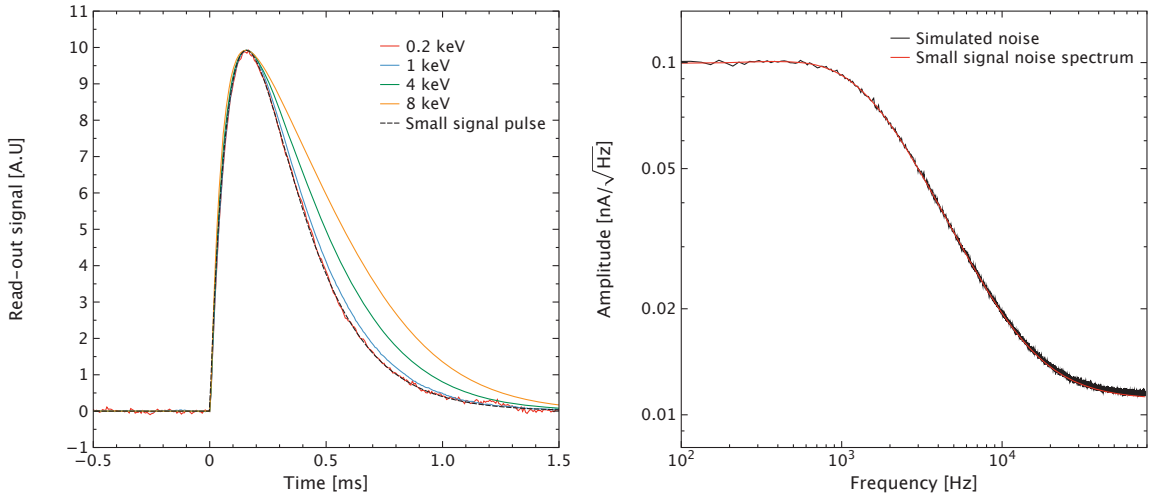

Figure 4.7: Comparison of simulated pulse shapes at different energies (left) and noise spectrum (right) with the small signal model described in Sect 4.1.1. The simulation corresponds to the baseline X-IFU pixels. The current pulses were flipped and scaled to have the same maximal value for better visual comparison.

- *Superconducting transition:* The TES transition used by `tessim` is for the moment a linear dependency of the TES resistance with temperature and current. In reality, it is known to be non-linear and to vary with magnetic field, and to sometimes feature kinks (Irwin & Hilton, 2005; Smith et al., 2013). The strongest approximation in the model is most probably the absence of any saturation at high temperature which will limit the representativity of the model at high energies close to the saturation value.

- *Noise non-stationarity:* Even if the model already takes into account most of the non-stationary character of the noise by recomputing its level throughout the course of an event, some second order changes like the diminution of M^2 during the transition (Smith et al., 2013) are not currently implemented.

4.4 Performance estimates of the different pixels and grading schemes

In order to investigate the performance of the different pixel designs proposed for the TES-array optimization exercise (see Sect. 4.2), a series of simulations was performed with the `tessim` TES device simulator. As mentioned before, this simulation tool provides realistic data streams. To draw any useful conclusion, the energy of the obtained synthetic pulses however needs to be reconstructed the same way as in the on-board processor. For this purpose, we decided to use the now standard optimal filtering technique (Moseley et al., 1988; Szymkowiak et al., 1993) which has been implemented in all the satellite micro-calorimeters flown until now (Boyce et al., 1999; Seta et al., 2012).

4.4.1 The optimal filter pulse processing technique

The so-called optimal filtering technique was introduced for the analysis of micro-calorimeter X-ray pulses by Moseley et al. (1988). It is in fact a particular case of Wiener filter in which the current signal is chi-square fitted in the Fourier space by a scaled version of a constant profile on top of a

baseline level ($d(t) = E \times s(t) + b$), weighting by the inverse of the noise power:

$$\chi^2 = \sum \frac{\left[D(f) - E \times S(f)\right]^2}{N^2(f)}, \tag{4.29}$$

where $D(f)$ and $S(f)$ are the Discrete Fourier Transforms of the signal and template, and $N^2(f)$ the noise power spectrum usually measured in empty streams. As can be understood from the χ^2 problem formulation, this reconstruction method automatically assumes that the noise during the pulses is stationary, which is not verified at high energies. As a linear optimization problem, Equation 4.29 provides a direct formulation for the best energy estimator $\hat{E}$ as a dot product:

$$\hat{E} = \frac{\left\langle D(f), S^*(f)/N^2(f) \right\rangle}{\sum |S(f)|^2/N^2(f)} \tag{4.30}$$

where * denotes the complex conjugation. In order to avoid the computational cost from the Fourier Transform of each data pulse, this estimator is usually computed in the time domain, using the property of equivalence of the dot product in the normal and Fourier spaces:

$$\hat{E} = \frac{\left\langle d(t), \mathcal{FFT}^{-1}\{S(f)/N^2(f)\} \right\rangle}{\sum |S(f)|^2/N^2(f)} \tag{4.31}$$

with the second member of the dot product being pre-calculated.

Typically, TES read-out data suffer from at least some $1/f$ noise. To limit its influence in the energy estimation, the 0 Hz bin is usually rejected from the analysis such that the final time domain filter has a null sum and the baseline level is efficiently suppressed. Figure 4.8 shows the frequency and time domain optimal filters obtained from 1 keV pulses simulated for the standard LPA1 X-IFU pixels. In this case, the X-ray impact is assumed to occur at $t = 0$.

If the TES detectors were fully linear and the assumption of a constant pulse shape verified, $\hat{E}$ would provide an unbiased energy estimator. This is unfortunately not the case and a gain scale must be applied to filtered energy value to compensate the non-linearities. This correction function is usually obtained through the filtering of pulse templates computed at different energies.

4.4.2 Performance characterization of the different TES pixels

Performance at high count rates and grading scheme

The main objective of the TES array optimization is to investigate the potential improvement in terms of count rate capability for the X-IFU through the introduction of an SPA. In this section, we will therefore first concentrate on the estimation of the energy resolution performance of the different pixels at high count rates. To do so, we simulated for each pixel type a series of monochromatic pulse triplets, which was then reconstructed using the optimal filtering technique. The energy resolution (FWHM) and measurement bias of the pulses sitting in the middle of the triplet was then determined as a function of the companion pulse separations and defined as:

$$\Delta E = 2\sqrt{2\log 2}\ \mathrm{STD}(E_i)\ ;\ E_{\mathrm{bias}} = \frac{\sum E_i - E}{N} \tag{4.32}$$

where E_i are the individual reconstructed energies.

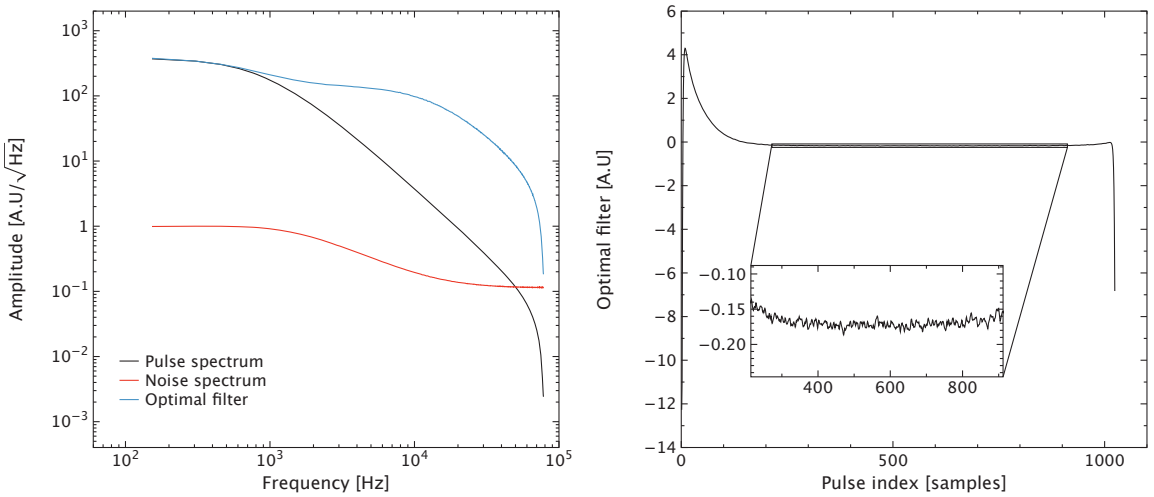

Figure 4.8: Left: Pulse, noise and resulting optimal filter spectra computed from the simulation of 1 keV current pulses for the baseline X-IFU pixels using the `tessim` tool. For better readability, the noise and pulse spectra were scaled to match 1 A.U./$\sqrt{\text{Hz}}$ for the noise spectrum at low frequencies. As can be seen the resulting optimal filter has the highest weights at frequencies with the highest signal to noise ratio. We note that the high frequency cut-off of the pulse spectrum is due to aliasing effects from the limited sampling frequency (~ 150 kHz) **Right:** Shape of the optimal filter in the time domain. The inset highlights the oscillations in the filter rejecting the frequencies where the noise dominates.

Figure 4.9 shows the energy resolution and measurement bias maps obtained for all pixels at 7 keV. This energy corresponds to the highest energy for which the nominal 2.5 eV resolution is required and thus the most constraining case. From these maps, we can identify two main effects: at small time separation, the pulse tail from the preceding pulse leaks signal into the pulse of interest and biases the energy estimation, while the subsequent pulse reduces the amount of data available for the reconstruction and thus degrades the energy resolution performance (see Eq. 4.27).

The former effect appears to be very sharp for all pixel types. The possibility of calibrating such an effect, which will depend on the energy of the preceding pulse, on the whole X-IFU energy range remains therefore questionable. It has however proven to be feasible for narrow-band studies (Lee et al., 2014). In order to be conservative, we will consider that such events, called secondaries, will need to be rejected from the science data (these events will be flagged during on-board processing): Not only would our knowledge of the energy of these pulses be poor, but keeping them would also degrade the average energy resolution, as they would not all have the same bias and would therefore broaden the energy redistribution. To study this effect more in detail, we performed noise-less simulations with a higher resolution around the boundary region. We thus took a threshold of 0.2 eV bias level at 7 keV to define the secondaries, in accordance with the 0.4 eV energy knowledge requirement (see Fig. 4.10, left, and Table 3.1) and with introducing a very limited degradation of the energy resolution at high count rates.

In terms of energy resolution degradation with pulse length, we observe a smoother variation, similar to the approximation proposed by Doriese et al. (2009). To characterize this effect, we then defined a set of three resolution grades (high, medium and low) following a similar approach as previous studies (see e.g. Seta et al., 2012). High resolution events were defined as those showing a degradation compatible with the current X-IFU noise budget for all detectors types (den Hartog, 2015;

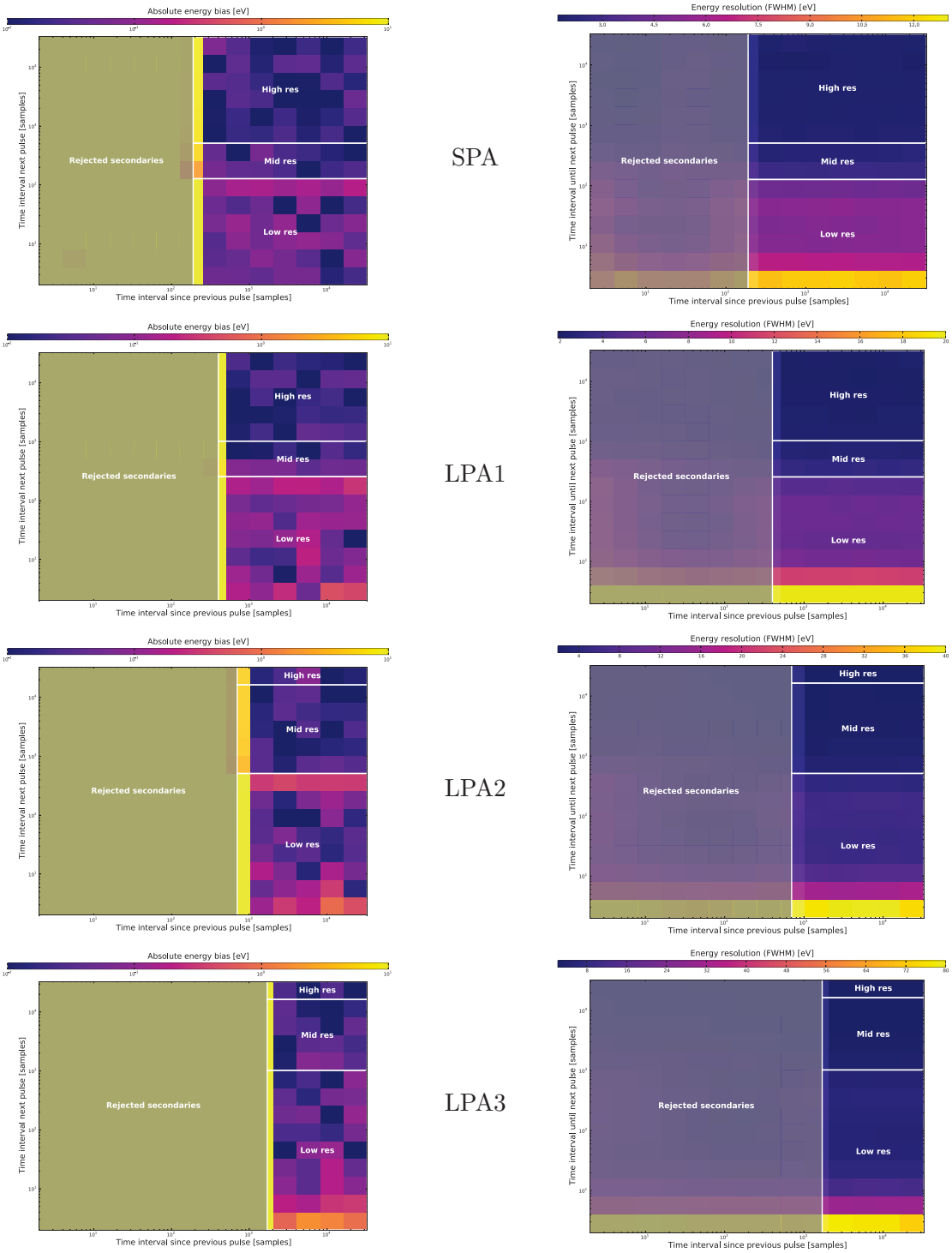

Figure 4.9: Reconstruction bias (left column) and energy resolution (right column) for all studied pixel types, as a function of time separation since the previous pulse and until the next one. Superimposed are the definition of the event grades: the vertical line delimits the area (to the left) where events should be rejected due to high bias values. The remaining events are then classified into three categories (high, medium, and low) according to their resolution values. Some relatively high absolute bias values can still be seen for valid events but these are only due to the limited statistics of the simulation and are formally compatible with zero. This effect is especially visible for low resolution points for which the precision on the average of the reconstructed energies is poorer.

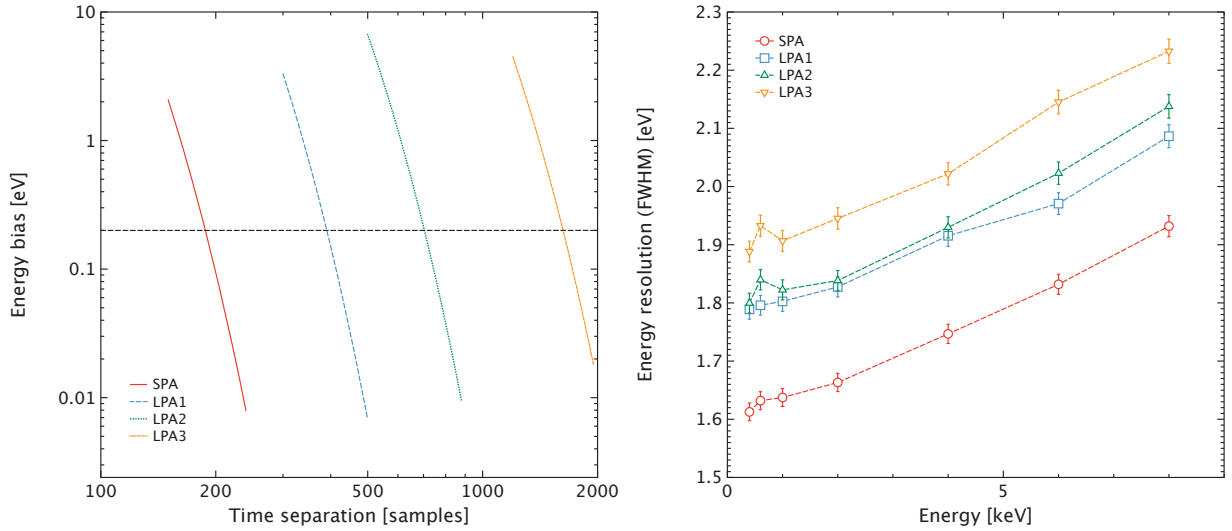

Figure 4.10: Left: Close-up study of the measurement bias limit for all pixel types. The horizontal stripped lined shows the 0.2 eV bias limit used to defined the secondary rejection. **Right:** Energy resolution as a function of energy for all pixel types obtained from `tessim` simulations. The error bars show the remaining statistical uncertainty from the simulation. The bumps visible at low energy for the LPA2 and LPA3 pixels are notably not significant. The pulses were reconstructed with the optimal filtering technique using a pulse template obtained at 1 keV and 16384 samples. All resolution values have been gain-scale corrected.

Smith, 2015), while medium resolution events were chosen to correspond to a final energy resolution of $\sim$ 3 eV, i.e. $\sim$2.5 eV before the other noise/environmental effects that are not yet included in the simulation. Low resolution events are the remaining valid events. Apart from these grades, we identify pile-up events where two photons cannot be separated from each other and which are therefore erroneously detected as single events with an energy corresponding roughly to the sum of the contributing photons[5].

The grading criteria and their corresponding energy resolution for the different pixel types are summarized in Table 4.2. We note that independently of the resolutions that were measured in the simulations for high resolution events, an external contribution was added to it in order for the final value to be equal to the X-IFU requirement of 2.5 eV. This contribution was then reported to the other grades. The intrinsic energy resolution differences between the pixels will be investigated in the next subsection. We also note that the quoted energy resolutions for the low resolution events correspond to the worst case value observed for these events (see Fig. 4.9)[6]. A trade-off may be ultimately made to choose to strengthen the criteria for these events in exchange of a better energy resolution.

Energy resolution as a function of energy

As mentioned above, on top of providing an increase in terms of count rate capability, the introduction of an SPA has the potential, with a specific design, to bring an improved energy resolution in a subpart

[5] As the actual impacts are known in the simulation, pile-up events can be identified here, but not in the real detector.

[6] The final low resolution values quoted in Table 4.2 correspond to those implemented in `xifupipeline` which were obtained at the time of the TES array optimization exercise with a different version of `tessim` and slightly different pixel parameters. We note that these resolutions, obtained from pulses with very few data points, strongly depend on the assumptions currently made by the simulator (see Sec. 4.3.3) and only constitute rough estimates at this stage.

Table 4.2: Definition of the event grades for the different pixels. Note that the given table is top-down exclusive, meaning that, e.g., "medium resolution" are all events which are not "high resolution" and fulfill the given criteria.

Grade	Time until next pulse	Time since previous pulse	Resolution
	SPA		
High resolution	$\geqslant$ 512 samples ($\sim$3.3 ms)	$\geqslant$ 190 samples ($\sim$1.2 ms)	2.5 eV
Medium resolution	$\geqslant$ 128 samples ($\sim$820 μs)	$\geqslant$ 190 samples ($\sim$1.2 ms)	3 eV
Low resolution	–	$\geqslant$ 190 samples ($\sim$1.2 ms)	$\sim$ 15 eV
Secondary	–	–	N/A
	LPA1		
High resolution	$\geqslant$ 1024 samples ($\sim$6.6 ms)	$\geqslant$ 400 samples ($\sim$2.6 ms)	2.5 eV
Medium resolution	$\geqslant$ 256 samples ($\sim$1.6 ms)	$\geqslant$ 400 samples ($\sim$2.6 ms)	3 eV
Low resolution	–	$\geqslant$ 400 samples ($\sim$2.6 ms)	$\sim$ 15 eV
Secondary	–	–	N/A
	LPA2		
High resolution	$\geqslant$ 16384 samples ($\sim$105 ms)	$\geqslant$ 700 samples ($\sim$4.5 ms)	2.5 eV
Medium resolution	$\geqslant$ 512 samples ($\sim$3.3 ms)	$\geqslant$ 700 samples ($\sim$4.5 ms)	3 eV
Low resolution	–	$\geqslant$ 700 samples ($\sim$4.5 ms)	$\sim$ 30 eV
Secondary	–	–	N/A
	LPA3		
High resolution	$\geqslant$ 16384 samples ($\sim$105 ms)	$\geqslant$ 1700 samples ($\sim$11 ms)	2.5 eV
Medium resolution	$\geqslant$ 1024 samples ($\sim$6.6 ms)	$\geqslant$ 1700 samples ($\sim$11 ms)	3 eV
Low resolution	–	$\geqslant$ 1700 samples ($\sim$11 ms)	$\sim$ 90 eV
Secondary	–	–	N/A

of the TES-array. The main interest for this would be to improve the weak line sensibility for point sources, notably for the detection of WHIM absorption lines in the afterglow of GRBs. In order to investigate this aspect thoroughly, I performed a series of `tessim` simulations of monochromatic pulses at different energies and reconstructed them with the optimal filtering technique. This allows to compare for each pixel type the energy resolution performance achieved as a function of energy. Because the energy resolution depends on the record length in a different manner for all pixels (see previous section), the reconstruction was performed with a large record length of 16384 samples ($\sim 105\,\mathrm{ms}$) so as to limit the influence of this effect.

Figure 4.10 (right) shows the results of this analysis. As can be seen, the SPA pixels do provide an improved resolution, especially at low energies where it reaches $\sim 1.6\,\mathrm{eV}$. Between the different LPAs however, only very limited differences can be observed, which was to be expected considering they were designed with the same heat capacity and transition parameters which are the main drivers of the energy resolution (see Table 4.1).

4.5 Overall count rate performance of the X-IFU

4.5.1 On focus performance

In the previous section, we have determined a set of grades characterizing the performance of each pixel type as a function of the time separation from other events. In order to translate these into the overall count rate capability of each configuration, we first need to compute the fraction of each grade as a function of the individual count rates in each pixel r_i. As the arrival time of X-ray events follow Poisson statistics, keeping in mind that the grades are top down exclusive in Table 4.2, these can be determined as:

$$\mathrm{HR}_i = P(\text{time separation} \geqslant \Delta T_{hr}) = e^{-r_i \Delta T_{hr}} \tag{4.33}$$

$$\mathrm{MR}_i = e^{-r_i \Delta T_{mr}} - e^{-r_i \Delta T_{hr}} \tag{4.34}$$

$$\mathrm{LR}_i = e^{-r_i \Delta T_{lr}} - e^{-r_i \Delta T_{mr}} \tag{4.35}$$

where ΔT_{hr}, ΔT_{mr}, and ΔT_{lr} are the sum of the grading criteria in both columns of Table 4.2 for the high, medium and low resolution events. If we consider that events separated by one sample corresponding to a time interval δt pile up, and that the other remaining events are rejected secondaries, the secondaries and pile-up fractions are:

$$\mathrm{S}_i = (1 - e^{-r_i \Delta T_{inv}}) e^{-r_i \delta t} \tag{4.36}$$

$$\mathrm{P}_i = 1 - e^{-r_i \delta t} \tag{4.37}$$

where ΔT_{inv} is the unbiased reconstruction criterium determined in the previous section.

Using these individual pixel ratios, we can propagate these ratios to the whole instrument. If we note f_i the flux repartition on the different pixels due to the PSF spread, the overall high resolution fraction can be computed as:

$$\mathrm{HR}_{\mathrm{total}} = \sum_{\text{pixels } i} f_i \mathrm{HR}_i \tag{4.38}$$

and the other ratios similarly. As a worst case situation, in the following, we will use the flux repartition obtained when a point source is centered on one pixel. This repartition can easily be obtained using the `xifupipeline` tool and the different TES array geometries (see Sect. 4.3.2 and Fig. 4.11).

Table 4.3: Definition of the Crab spectrum as X-ray standard candle: the Xspec model `tbabs*powerlaw` is used with the parameters below and assuming abundances of Wilms et al. (2000).

Parameter	Value	Unit
Γ	2.1	
norm	9.5	photons $\mathrm{keV}^{-1}\,\mathrm{cm}^{-2}\,\mathrm{s}^{-1}$ at 1 keV
N_{H}	0.4	$10^{22}\,\mathrm{cm}^{-2}$

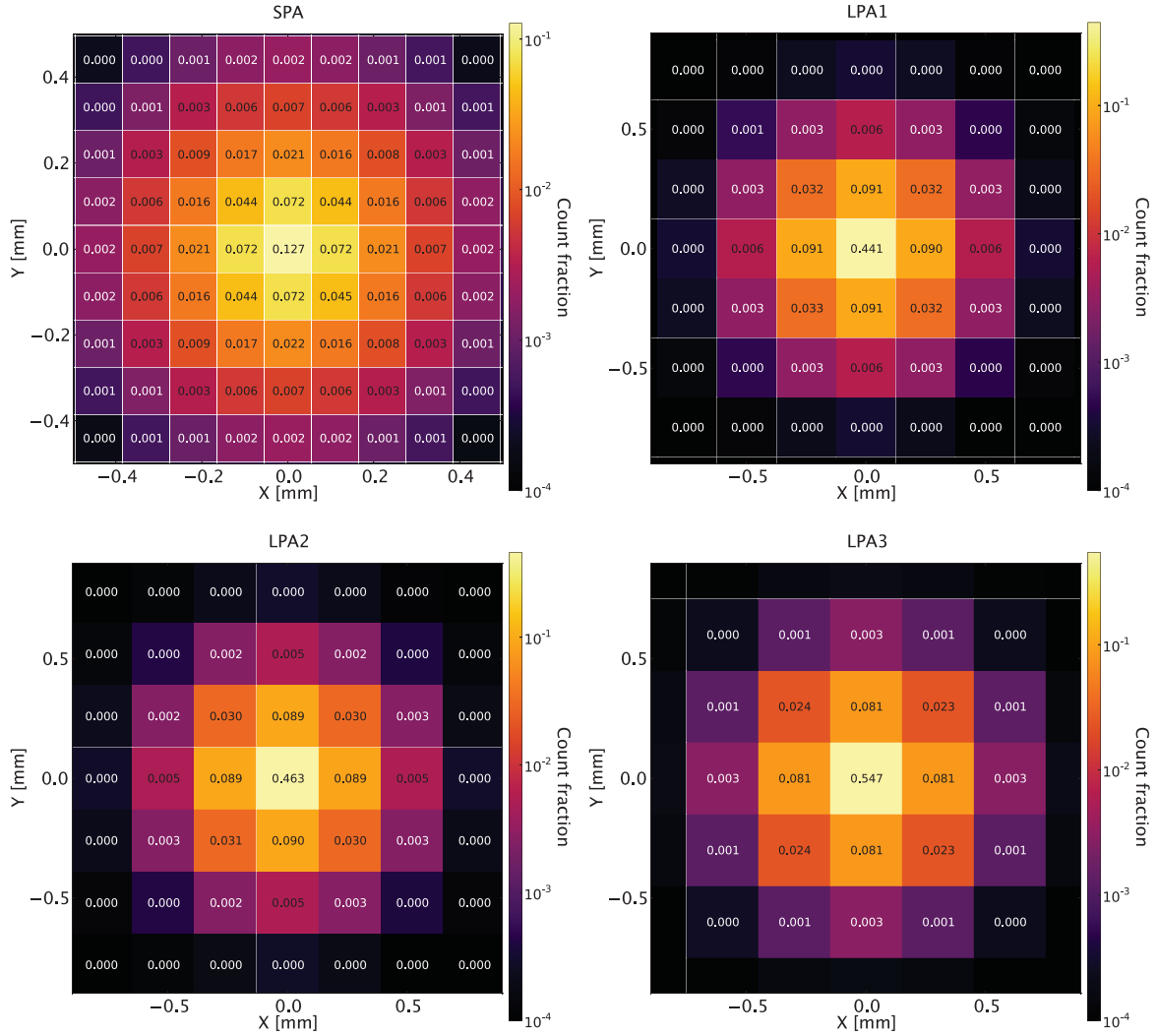

Figure 4.11: Baseline PSF spread on the different pixel types. These were obtained with the `xifupipeline` tool using the PSF provided by R. Willingale to the X-IFU End-to-End team (`athena_psf_onaxis_20150602.fits`).

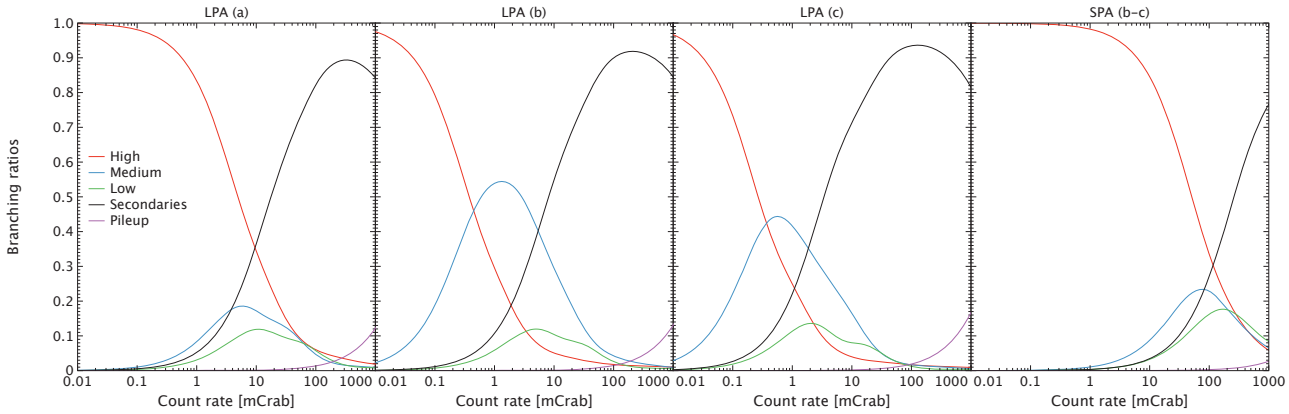

Figure 4.12: Branching ratios for the different TES array configurations. The introduction of an SPA provides an order of magnitude increase in the X-IFU count rate capability. In this figure, the ratios are normalized by the total of pixel impacts such that no filling factor effect is visible at low count rates. We note the this factor is already incorporated in the X-IFU quantum efficiency requirement.

In X-ray astronomy, the count rate capability of an instrument is usually defined for fluxes in units of Crabs, 1 Crab being the X-ray flux produced by the Crab nebula and pulsar as X-ray standard candle. Several models exist fitting the Crab emission spectrum and intensity. In this work, we used the Xspec model `tbabs*powerlaw` with the parameters given in Table 4.3. Using the baseline X-IFU ARF (`athena_xifu_sixte_1469_onaxis_v20150402.arf`), this model translates to ~ 94000 counts at the focal plane level. Combining this with the PSF pixel repartition for the different configuration and Equation 4.38 (with its equivalent for the other grades), we can obtain branched ratios showing as a function of count rate the fraction of each event grade. This result is shown in Figure 4.12.

As expected, the introduction of an SPA provides around an order of magnitude increase of the overall X-IFU capability with $\sim 80\%$ throughput at 10 mCrab where the standard LPA1 pixels have the same limit around 1 mCrab. Of course, this comes at the expense of a loss of count rate capability in the rest of the field of view, be it with LPA2 or LPA3 pixels. However, as was stressed before, this corresponds in principle to configurations much better adapted to the actual instrument needs.

4.5.2 Defocusing

All industrial studies of the *Athena* satellite have selected a Moveable Mirror Assembly based on a hexapod table as the instrument switching mechanism. If confirmed, such a mechanism could provide defocusing capability on top of the simple alternate illumination of the two payload instruments. Whereas there is no much interest in looking at extended sources with a defocused mirror, for point sources, a more widely spread PSF would reduce the individual pixel count rates at a given flux and thus improve the instrument count rate capability. To investigate this matter, R. Willingale simulated a set of PSFs for different defocus lengths going up to 40 mm. Figure 4.13 shows the resulting flux repartitions on the baseline TES-array in a few cases. One can notice that contrary to classical optical systems, the defocusing of these X-ray optics leads to a "hole" in the middle of the PSF.

Using these new PSF, the same exercise as done in the previous subsection can be performed again in order to see how much could be gained in terms of count rate capability. As the defocusing considered here can exceed the size of the SPA ($\sim 30''$), we will consider the three different array configurations instead of the four pixel types. Figure 4.14 gives for different defocus lengths the expected fractions

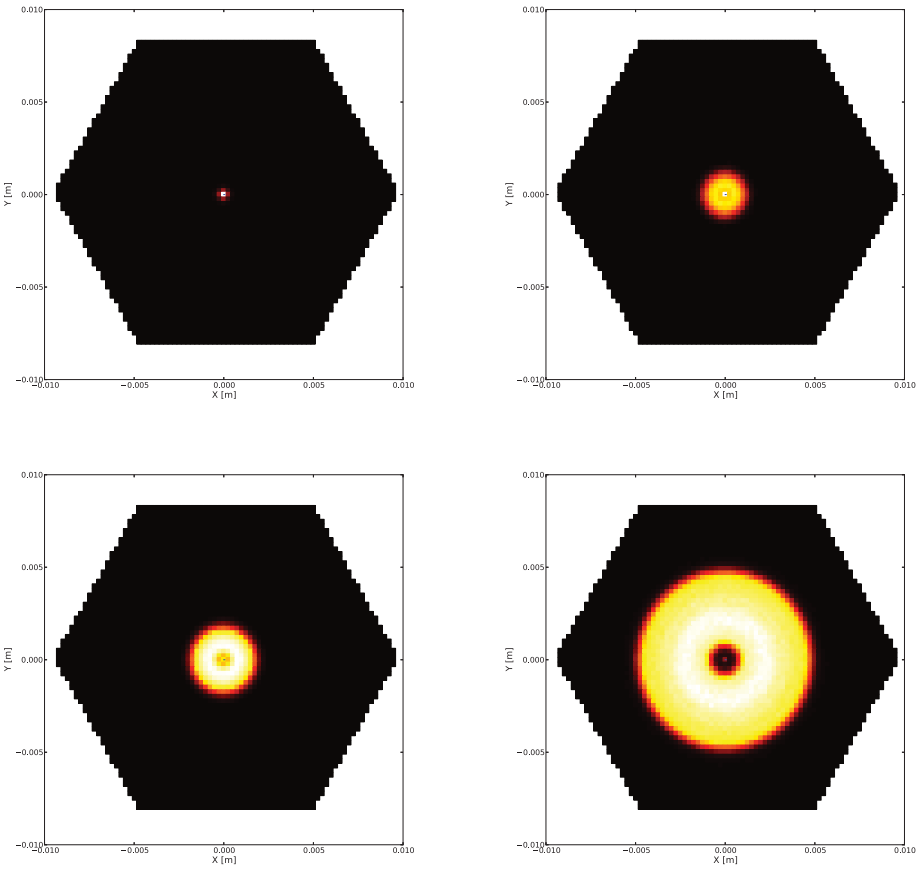

Figure 4.13: PSF spread on the baseline TES array for several defocus lengths. From left to right and top to bottom: on focus, 10, 15 and 40 mm.

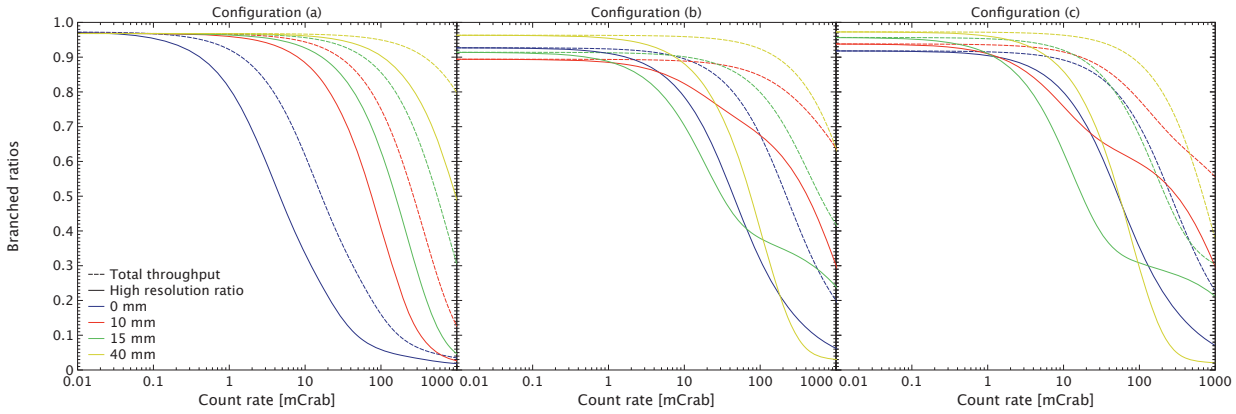

Figure 4.14: For all three studied configuration, the figure shows the faction of high resolution events and total throughput (fraction of valid events) as a function of count rate. In this figure, the ratios are normalized to the total number of imaged photons to highlight in the hybrid configurations effects at low count rates from the different SPA and LPA filling factors and the gap between the two subarrays in configuration (b).

of high resolution events and total throughput as a function count rate in all configurations. Contrary to what was presented on Figure 4.12, these ratios were normalized by the total number of imaged photons as filling factor effects can be observed in the hybrid configurations: as the SPA has a smaller filling factor than the LPAs, when defocusing the total throughput at low count rates increases because more and more events get spread to the LPA. We can also see in the figure the transition from the small defocus length situation where most of the photons fall onto the rapid SPA and at large defocus length where they mostly impact the LPA. Moreover, in configuration (b), due to an artificial large gap between the two subarrays, we can first see the realized filling factor decreasing because a significant part of the photons get lost in this insensitive region.

Overall, we see that a small 10 mm defocus already brings a higher than one order of magnitude improvement of the count rate capability of the baseline configuration. Very large defocus could even allow the instrument to observe in the Crab regime with very large throughput (taking all grades into account, the overall throughput at 1 Crab for the standard LPA and 40 mm defocus is $\sim 80\%$, see Fig. 4.14), if there was no limitation from the EP side[7]. In the hybrid configurations, the optimal position is actually at limited defocus as it maximizes the spread on the SPA while limiting the leakage onto the much slower LPAs. Again, defocusing could in this case allow observations at at least some hundreds of mCrab. We note that if LPA2 or LPA3 pixels were used to populate the whole field of view (not represented in Figure 4.14), $\sim 5 - 10$ mm defocus length would be required to recover the 80 % throughput requirement at 1 mCrab and ~ 20 mm to reach the 10 mCrab goal. In these cases, observations above a few tens of mCrabs would not be possible.

4.6 Conclusion

In this chapter, we have studied the performance impact of introducing an SPA at the center of the X-IFU field of view both in terms of count rate capability and energy resolution. Overall, such a choice would increase the instrument bright source performance by around an order of magnitude and offer better energy resolution at low energies amounting to ~ 0.2 eV difference compared to the standard pixels. An alternative solution to improve the X-IFU count rate capability would be to rely on a defocusing capability of the *Athena* mirror. If large defocus lengths up to ~ 40 mm prove to be feasible, this could even allow the observation of sources as bright as the Crab with the baseline configuration. We note that this does not completely replace the SPA which also offers better energy resolution. Moreover, in the case of hybrid configurations, Crab count rates would be accessible with only moderate defocus capability (~ 10 mm).

[7] 1 Crab means 94000 counts per second to process. That being said, the observation of very bright sources usually does not require the full instrument resolution and a quick energy estimation obtained at the triggering stage of the EP may be sufficient

Chapter 5: Advanced pulse reconstruction techniques

5.1 Context of the study

One of the most challenging requirements for the X-IFU is to reach the 2.5 eV energy resolution. As we have seen in the previous chapter, to properly take into account the TES detectors non-linearities and estimate the energy resolution achieved at 7 keV by different pixel types, it is necessary to properly take into account the whole processing and notably the last pulse reconstruction step. If, as of now, all the launched micro-calorimeters relied on optimal filtering for their on-board pulse processing (Boyce et al., 1999; Seta et al., 2012), the increasing success of less linear TESs has triggered in the recent years the development of several more advanced reconstruction techniques to try to compensate for the shortcomings of the standard method (see e.g. Bandler et al., 2006; Lee et al., 2015; Fixsen et al., 2002; Fixsen et al., 2004, 2014; Fowler et al., 2015). Some of these do not require in principle much more computational power than optimal filtering and could be considered for application in the X-IFU Event Processor. At this early stage of the development phase, it is important to look at all the possibilities in order to get the best achievable performance from the foreseen pixels.

In the following study, I present a comprehensive benchmark of various reconstruction techniques for the X-IFU pixels, taking into account the future major drivers of the reconstruction method choice: performance, computing power and required ground calibration. If this work is mainly centered on the X-IFU, the results presented here have the potential to be extended to a wider range of detectors.

5.2 Publication 3

Performance assessment of different pulse reconstruction algorithms for the Athena X-ray Integral Field Unit

Philippe Peille[a], Maria Teresa Ceballos[b], Beatriz Cobo[b], Joern Wilms[c], Simon Bandler[d], Stephen J. Smith[d], Thomas Dauser[c], Thorsten Brand[c], Roland den Hartog[e], Jelle de Plaa[e], Didier Barret[a], Jan-Willem den Herder[e], Luigi Piro[f], Xavier Barcons[b], and Etienne Pointecouteau[a]

[a]IRAP CNRS, 9 Av. colonel Roche, BP 44346, F-31028 Toulouse cedex 4, France and Université de Toulouse III Paul Sabatier / OMP, Toulouse, France
[b]Instituto de Física de Cantabria (CSIC-UC), Edificio Juan Jordá, Avenida de los Castros, s/n - E-39005 Santander, Cantabria
[c]ECAP, University of Erlangen-Nuremberg Sternwartstr. 7 96049 Bamberg, Germany
[d]NASA/Goddard Space Flight Center, 8800 Greenbelt Rd, Greenbelt, MD 20771, United States
[e]SRON, Netherlands Institute for Space Research, Sorbonnelaan 2, 3584 CA Utrecht
[f]Istituto di Astrofisica e Planetologia Spaziali, Via Fosso del Cavaliere 100, 00133, Roma, Italy

ABSTRACT

The X-ray Integral Field Unit (X-IFU) microcalorimeter, on-board Athena, with its focal plane comprising 3840 Transition Edge Sensors (TESs) operating at 90 mK, will provide unprecedented spectral-imaging capability in the 0.2-12 keV energy range. It will rely on the on-board digital processing of current pulses induced by the heat deposited in the TES absorber, as to recover the energy of each individual events. Assessing the capabilities of the pulse reconstruction is required to understand the overall scientific performance of the X-IFU, notably in terms of energy resolution degradation with both increasing energies and count rates. Using synthetic data streams generated by the X-IFU End-to-End simulator, we present here a comprehensive benchmark of various pulse reconstruction techniques, ranging from standard optimal filtering to more advanced algorithms based on noise covariance matrices. Beside deriving the spectral resolution achieved by the different algorithms, a first assessment of the computing power and ground calibration needs is presented. Overall, all methods show similar performances, with the reconstruction based on noise covariance matrices showing the best improvement with respect to the standard optimal filtering technique. Due to prohibitive calibration needs, this method might however not be applicable to the X-IFU and the best compromise currently appears to be the so-called resistance space analysis which also features very promising high count rate capabilities.

Keywords: Athena, X-IFU, X-rays, microcalorimeters, pulse reconstruction, performance analysis

1. INTRODUCTION

Scheduled for launch in 2028 on board the *Athena* X-ray observatory, the X-ray Integral Field Unit (X-IFU[1]) will provide spectral-imaging capability in the 0.2–12 keV with 5" spatial resolution and an unprecedented 2.5 eV energy resolution at 7 keV. It will address a variety of key scientific questions such as the dynamics and enrichment of clusters of galaxies, or the composition of the Warm Hot Intergalactic Medium.[2] The X-IFU is a cryogenic micro-calorimeter whose focal plane will be populated by 3840 X-ray absorbers organized following a hexagonal pattern across a 5' diameter field of view. Each absorber will be thermally linked to a Transition Edge Sensor (TES) voltage biased in its transition between the superconducting and normal states. The thermalization of an X-ray in the absorber will thus induce a sharp change of the TES resistance which will be measured as a

Further author information: (Send correspondence to Philippe Peille)
E-mail: philippe.peille@irap.omp.eu

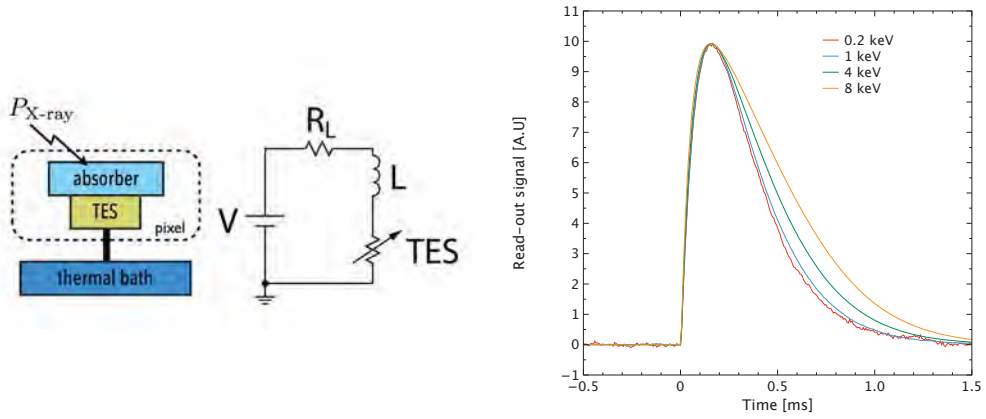

Figure 1. Left: Schematics of the physics model coupling the thermal and electrical behavior of the TES/absorber pixel used by `tessim`. For the thermal part, the link to the heat bath, the absorption of X-ray photons and the Joule dissipation are simulated. On the electrical side, an equivalent circuit with a constant voltage bias, a load resistor, an inductance and the variable TES resistant is used. Right: Example of simulated current pulses at different energies. The signals were flipped and scaled to have the same peak value to illustrate the simulation non-linearities.

pulse in the TES current. In order to limit the heat load on the cryogenic chain, the TESs will not be read out independently but pooled in 96 frequency multiplexed channels (FDM).[3] At the end of the readout chain, an on-board Event Processor (EP) will be responsible for the extraction of the time and energy information from the measured current pulses. Assessing the capabilities of the pulse reconstruction is therefore key to understand the overall performance of the instrument.

Over the past few years, several new pulse reconstruction techniques have been proposed to improve and replace the now widely used optimal filtering technique.[4–6] The main motivation for this is to reduce the energy resolution degradation with energy observed in non-linear detectors such as the TESs. In this paper, we will present a comprehensive benchmark of these analysis methods considered for the read out of the X-IFU pixels using a TES simulator (`tessim`[7]) newly developed in the frame of the X-IFU End-to-End simulator SIXTE.[8]

After presenting the physics model used by `tessim` (Sect. 2), we will review the different tested pulse processing algorithms (Sect. 3) and discuss their performance not only in terms of energy resolution degradation at high energy, but also in terms of count rate capability (Sect. 4). Finally, we will give a first comparative assessment of the computing power (Sect. 5) and ground calibration needs (Sect. 6) of theses techniques.

2. SIMULATING X-IFU PIXEL READOUT STREAMS WITH TESSIM

`tessim` is based on a generic model of the TES/absorber pixel considered as a single thermodynamical element interacting with a cold bath and an X-ray loading, together with its first stage read-out circuit including a voltage bias, a load resistor and an inductance (see e.g. Mather et al., 1982).[9] The overall setup of the model is presented in Figure 1 (left) and details on this software are available in Wilms et al. (2016).[7] In brief, the code performs a numerical solution of the differential equations for the time-dependent temperature, $T(t)$, and current, $I(t)$, in the TES, using the formulation of Irwin & Hilton (2005):[10]

$$C\frac{dT}{dt} = -P_{\text{b}} + R(T,I)I^2 + P_{\text{X-ray}} + \text{Noise}, \tag{1}$$

$$L\frac{dI}{dt} = V_0 - IR_{\text{L}} - IR(T,I) + \text{Noise}. \tag{2}$$

where C is the heat capacity of the pixel, P_b the power flow to the heat bath and $P_{\text{X-ray}}$ is the power deposited by X-rays thermalizing in the absorber. In the electrical equation, L is the effective inductance of the read-out

Table 1. Pixel parameters used to simulate the baseline X-IFU pixels.

Pixel parameter	Value
Heat capacity at bias C	0.8 pJ/K
Bath conductance at bias	200 pW/K
Heat bath power flow exponent	3
α	75
β	1.25
Bias resistance R_0	1 mΩ
Bias temperature T_0	90 mK
Bias current I_0	68 µA
Effective load resistance R_L	49 µΩ
Effective circuit inductance L	66 nH
Read-out sampling frequency	156.25 kHz

circuit, R_L the effective load resistor, and V_0 the constant voltage bias. To model the TES transition, `tessim` uses a simple temperature and current dependent resistance plane:

$$R(T,I) = R_0 + \left.\frac{\partial R}{\partial T}\right|_{I_0} (T - T_0) + \left.\frac{\partial R}{\partial I}\right|_{T_0} (I - I_0), \tag{3}$$

where the partial derivatives are defined at the TES bias point with the parameters

$$\alpha = \left.\frac{\partial \log R}{\partial \log T}\right|_{I_0} = \frac{T_0}{R_0} \left.\frac{\partial R}{\partial T}\right|_{I_0}, \tag{4}$$

$$\beta = \left.\frac{\partial \log R}{\partial \log I}\right|_{T_0} = \frac{I_0}{R_0} \left.\frac{\partial R}{\partial I}\right|_{T_0}. \tag{5}$$

The link to the thermal bath is modeled following the prescription of Irwin & Hilton (2005).[10] Currently, `tessim` simulates the following noise sources: thermal fluctuations between the TES and the heat bath, electrical Johnson noise in the TES and shunt resistor, as well as readout noise from the SQUID and amplifier chain. All noise levels are recomputed throughout the simulation such that their non-stationary character is respected. The Johnson noise notably significantly decreases during a pulse.

In order to simulate representative X-IFU pixels, we took pixel parameters adapted from the canonical pixels of the X-ray Microcalorimeter Spectrometer studied for the International X-ray Observatory,[11] which had similar energy resolution and count rate requirements to the X-IFU. The adopted values are summarized in Table 1 (see Smith et al., 2016[12] for more details). Figure 1 (right) shows sample pulses simulated with these pixels at different energies. One can notably notice how the pulse shape changes with energy due to the non-linearities of the detector and its read-out circuit. In order to simplify our analysis, all simulated pulses will be in phase with the read-out process such that no particular care will be needed for corrections of pulse arrival time effects.

3. PRESENTATION OF THE DIFFERENT PULSE RECONSTRUCTION TECHNIQUES

3.1 The standard optimal filtering technique

First introduced by Szymkowiak et al. (1993),[4] optimal filtering has rapidly become the standard technique for the analysis of X-ray micro-calorimeter pulses and has been used by all the currently flown instruments.[5,6] In brief, it consists of a χ^2 fit of the pulses in the frequency domain assuming that every pulse is an energy scaled

version of a single template ($d(t) = E \times s(t)$) and weighting by the measured noise spectrum of the system (assumed to be stationary):

$$\chi^2 = \sum \frac{\left[D(f) - E \times S(f)\right]^2}{N^2(f)}, \tag{6}$$

where $D(f)$ and $S(f)$ are the Discrete Fourier Transforms of the signal and template, and $N^2(f)$ the power spectrum of the noise measured from empty streams. As Equation 6 is a linear χ^2 problem, the optimal energy estimator $\hat{E}$ can be computed with a single dot product, whose time domain formula is given by:

$$\hat{E} = \frac{\left\langle d(t), \mathcal{FFT}^{-1}\left\{S(f)/N^2(f)\right\}\right\rangle}{\sum |S(f)|^2/N^2(f)}. \tag{7}$$

Usually, because of the presence of significant $1/f$ noise in the data stream due for instance to fluctuations of the TES thermal environment, the 0 Hz bin of the Fourier Transform is not used, such that the final filter is zero summed and the signal baseline is effectively rejected from the processing.

Of course, the assumption of a single pulse shape is not verified in non-linear detectors such as the X-IFU pixels. As a consequence, the raw energy estimation $\hat{E}$ has to be transformed to an unbiased final estimation $\hat{E}_{\text{final}}$ by the application of a gain scale typically obtained from the filtering of pulse templates measured at different energies. In the work presented here, we used 1 keV pulse shapes obtained from the averaging of many simulated streams, but our results were found to be mainly independent of this choice. It is important to note that even if the optimal filter is an unbiased estimate of the pulse energy when using a template computed at the exact same energy, any measure of the corresponding spectral resolution needs to take into account the associated gain scale in order to be in physical units.

3.2 "Resistance space" analysis

In order to treat the intrinsic non-linearities of the optimal filtering method, one can initially transform the input signal before the reconstruction such that it presents a more linear scaling with energy and a more stationary noise. Some authors notably proposed the so-called "resistance space" analysis which uses a proxy to the resistance signal instead of the current to perform the optimal filtering.[13,14] The idea is to suppress the main source of non-linearity of the detectors which comes from the first stage read-out circuit. For this transformation, the circuit inductance was neglected in previous works[14] and in the case of our model (see Fig. 1, left) this would translate to:

$$\tilde{R}(t) = \frac{V_0 - I(t)R_L}{I(t)}. \tag{8}$$

In Figure 2, we compare the transformed 7 keV pulse shape to the simulated resistance going through the TES as well as the resulting gain scale obtained by applying a 1 keV optimal filter to "resistance space" pulses at different energies. We notice that neither is the transformed pulse close to the actual TES resistance, nor is the obtained gain scale linear, which indicates that this simple transformation is not suitable for the X-IFU pixels. Although in previous examples of using this transformation the effect of the inductance was very small,[13,14] in the application considered here, relatively large inductors are used in order to critically damp the pixels and limit the load on the FDM readout scheme.[15] This however has the effect of producing a more non-linear response and slower current pulses. We further note that because the TES electro-thermal equations are not linear, there is also no reason for the TES resistance signal to be linear with energy in all cases.

The introduction of the inductance derivative term in Equation 8 would significantly increase the high frequency noise. Rather than looking for a more accurate resistance proxy, we therefore looked for a simple transformation, similar to Equation 8, that would produce the desired linear gain scale. Keeping in mind that the optimal filtering process is transparent to any linear modification of the signal, we used a series of simulated templates at different energies to fit the following generic transformation*:

$$\tilde{R}'(t) = \frac{V_0}{I_{fit} + I(t)}. \tag{9}$$

*Equation 8 corresponds to $I_{fit} = 0$ A, the subtraction by R_L being transparent to the optimal filtering process.

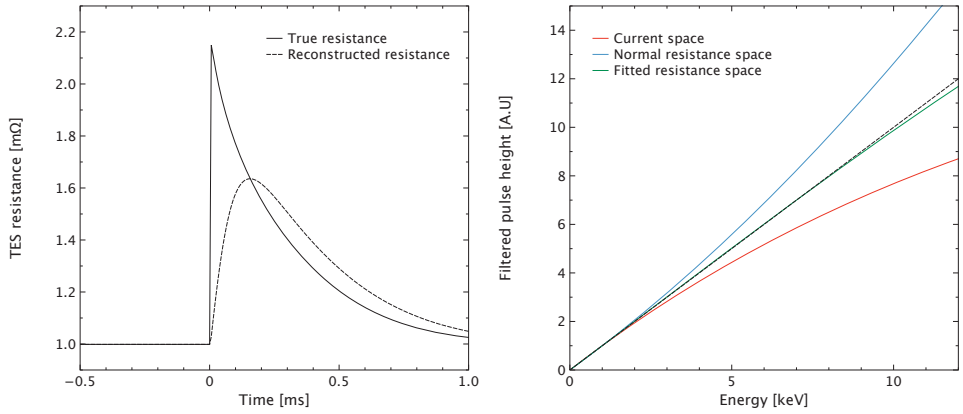

Figure 2. The "resistance space" analysis. Left: Comparison of the "resistance" pulse obtained from the transformation of the measured current pulse with Equation 8 (reconstructed resistance) with the actual simulated resistance at 7 keV (true resistance). Because of the circuit inductance, the current signal is slower than the resistance and this simple transformation does not give a reliable estimate of the TES resistance during the event. Right: Gain scales corresponding to "current space", "normal resistance space" (Equation 8) and "fitted resistance space" optimal filtering (Equation 9). The dotted line shows a perfectly linear scale.

The optimal I_{fit} was thus found to be 45.3 µA (the obtained quasi-linear gain scale is shown in Figure 2, right). In the following sections, for better readability, we refer to this final transformation as "fitted resistance space" and to Equation 8 as "normal resistance space".

3.3 Covariance based reconstruction

The aim of using an optimal filter is twofold: weight by the noise power in order to reject potential noise tones coming for instance from the cryo-chain, and use a template matched to the signal to maximize the signal-to-noise of the reconstruction. Because the constant shape assumption is not verified, the filter is not optimized for all energies. A first modification can thus be to use a locally linear assumption instead of a global one.

Let us consider a family of pulse templates $s_i(t)$ obtained at the energies E_i[†]. The signal of an event whose energy is straddled by E_α and E_β can be approximated as:

$$d(t) = b + s_\alpha(t) + \frac{E - E_\alpha}{E_\beta - E_\alpha}\big(s_\beta(t) - s_\alpha(t)\big), \tag{10}$$

where b is the baseline level that will be rejected by the processing.

On top of the linear assumption, by using a simple noise power spectrum to characterize the noise properties during the pulses, the optimal filtering further implicitly assumes that the noise is stationary. This is however known not to be true, the Johnson noise decreasing during the pulse as the resistance increases.[10,13,16] A more complete representation of the noise during the course of the pulse is the noise covariance matrix measured on top of the pulses (see Fig. 3) and its inverse can be used instead of the noise power to weight the optimization problem.[17–19] If we take the first order expansion of the pulse shape (see Eq. 10) as well as the constraint of rejecting the baseline level b, we can define a new χ^2 problem as:

$$\chi^2 = \left|\left|d(t) - \left[s_\alpha(t) - \frac{E_\alpha}{E_\beta - E_\alpha}\big(s_\beta(t) - s_\alpha(t)\big)\right] - E \times \frac{s_\beta(t) - s_\alpha(t)}{E_\beta - E_\alpha} - b\right|\right|^2_{C^{-1}}, \tag{11}$$

$$= (D' - E \times S' - b)^T C^{-1} (D' - E \times S' - b) \text{ using a matrix representation,} \tag{12}$$

[†]In the case of our simulations, this was obtained by averaging many signals simulated at the desired energy.

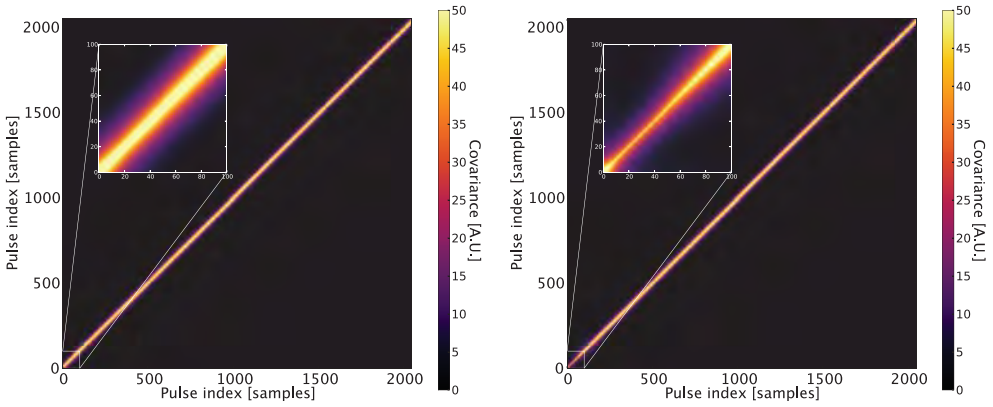

Figure 3. Covariance matrices measured from simulated X-IFU pulses at 1 (left) and 7 keV (right). The insets show the region corresponding to the top of the pulses. Because the pulses were simulated in phase with the readout process, the matrices are mostly diagonal and do not show the usual pattern near the pulse arrival time. One can notice the non-stationary character of the noise through the variable amplitude across the diagonal, notably in the inset at 7 keV.

with E and b being the fitted parameters, $d'(t) = d(t) - [s_\alpha(t) - E_\alpha(s_\beta(t) - s_\alpha(t))/(E_\beta - E_\alpha)]$ and $s'(t) = (s_\beta(t) - s_\alpha(t))/(E_\beta - E_\alpha)$. From there, we can build a new estimator $\hat{\theta} = [\hat{E}, \hat{b}]$:

$$\hat{\theta} = (R^T C^{-1} R)^{-1} R^T C^{-1} D' \text{ with } R = [S', \mathbb{1}]. \tag{13}$$

This simple formula can only be used if a constant covariance matrix is assumed in the α–β interval. In the work presented here, we took the average of the matrices measured at the two energies. It is also possible to linearly interpolate between the two calibration points and obtain a more precise estimation at the cost of a much more computationally intensive formulation, which was deemed to be prohibitive in the case of a future on-board implementation.[18] Contrary to the others, this reconstruction method also uses a known baseline and was therefore only kept as a reference of the achievable performance in terms of energy resolution degradation with energy and will be referred to as "interpolated covariance analysis". This derivation presented here is also only applicable under the assumption of the knowledge of the two calibration points straddling the pulse. This can however usually be achieved by using a very crude estimation of the energy, like e.g. the raw pulse height.

4. PERFORMANCE COMPARISON OF THE DIFFERENT TECHNIQUES

The performance of a pulse reconstruction technique can mainly be separated into two categories:

- its capacity to compensate for the detector's non-linearity and have a limited degradation of the energy resolution with energy,
- and its capacity to retain good energy resolution at high count rates.

4.1 Energy resolution degradation with energy

We simulated with `tessim` a large set of isolated pulses at different energies ranging from 0.2 to 8 keV and reconstructed it with the different techniques. The energy resolution as a function of energy is then simply estimated from the scatter of the measured values. In order to free the analysis from record length effects,[20] a large record length of ~ 13 ms (2048 samples) was used. Figure 4 shows the results of our analysis, comparing the performance of the different pulse processing methods. All values are after gain scale correction (see Sect. 3.1) and perfect knowledge was assumed by calibrating each method with a very large number of pulses (see Sect. 6 for the differential effect of calibration).

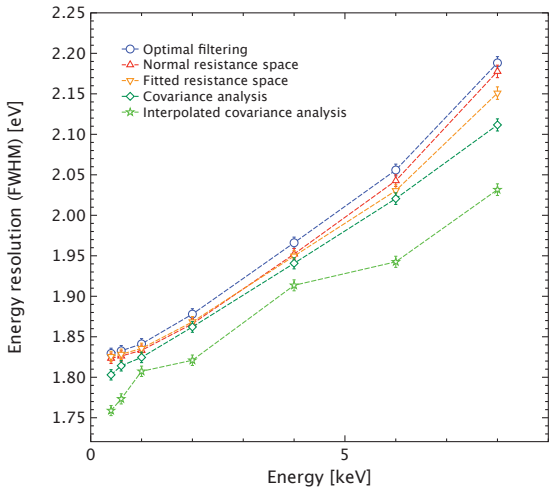

Figure 4. Comparison of the energy resolution performance of the different pulse reconstruction techniques as a function of energy for the baseline X-IFU pixels. The error bars give the $1\,\sigma$ uncertainty from the simulations.

Overall, all techniques show good linearity properties with an energy resolution of ~ 2.1 eV at 7 keV starting from a low-energy resolution of ~ 1.82 eV. The covariance analysis shows a systematic improvement of ~ 0.03–0.04 eV (~ 0.5 eV root mean squared) compared to the standard optimal filtering technique and appears in terms of performance as a promising candidate. The improvement from the resistance space analysis is more limited but nonetheless significant above 4–5 keV. We note that the modification of the transformation formula did further decrease the degradation at high energies. Comparing to the reference interpolated covariance analysis, we see that there remains some margin for improvement even though at least part of it is due to a known baseline in this case (see Sect. 3.3).

4.2 Energy resolution degradation with count rate

At high count rates, the current pulses created by the individual X-ray impacts will start to get closer and closer, leading to two distinct effects on the energy reconstruction of the events: firstly, the signal tail from preceding pulses will bias the energy estimation, and secondly, the presence of subsequent events will limit the amount of data useable for the pulse processing and lead to a degradation of the achievable energy resolution.[20]

To characterize these effects, we simulated multiple series of pulse doublets separated by different fixed pulse distances. The latter pulses were then used to estimate the varying bias of the energy estimation as a function of pulse separation, and the former to measure the energy resolution as a function of record length. As for the non-linearity study, the results presented in Figure 5 were gain scale corrected and perfect calibration knowledge was assumed. This study was performed with monochromatic 7 keV pulses which is the limiting energy for the 2.5 eV resolution requirement and therefore the most stringent situation.

All techniques show a sharp increase of the energy measurement bias below a few ms separation where no proper reconstruction can be performed anymore (see Fig. 5, left). In practice, these pulses would need to be flagged as secondaries and removed from the science data.[6] Some recent studies have tried to characterize and correct for this bias,[21] or simultaneously fit several pulses[22] to get the best throughput and energy resolution compromise at high count rates. However, as this bias depends on both the time separation and the energy, the applicability to such methods on the non-linear X-IFU pulses over the full instrument bandwidth remains unclear.

Concerning the energy resolution degradation with record length, as could be expected, the covariance based analysis provides an improvement to the standard optimal filtering based techniques. This method takes into

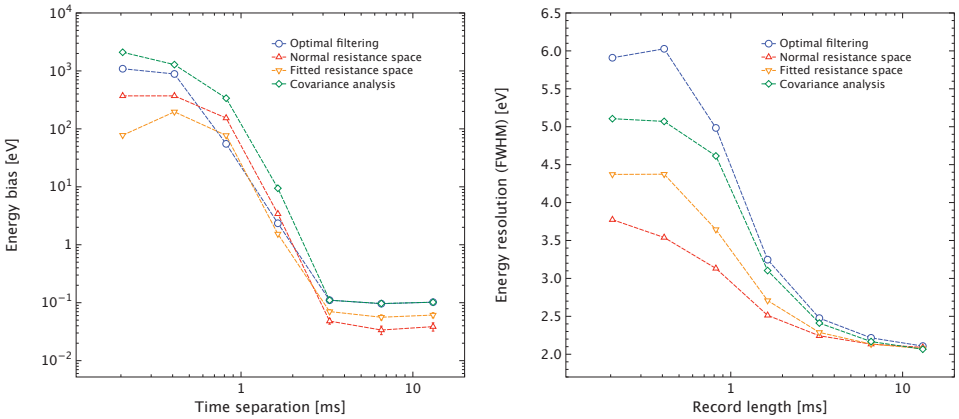

Figure 5. Comparative count rate performance of the different pulse reconstruction techniques for the baseline X-IFU pixels. Left: Energy bias as a function of time separation since the previous event. Right: Energy resolution (FWHM) as a function of record length.

account the non-stationarity character of the noise during the pulse and therefore makes the best out of the few available data points. More surprisingly, the resistance space techniques show even better performance. This is actually due to the ratios of the pulse and noise powers at different frequencies having been changed, resulting in a higher pixel effective roll-off frequency and therefore a slower degradation with record length.[13,20] If the covariance analysis shows the best performance for large record lengths, the resistance space methods could therefore be preferred for the treatment of pulses with limited record lengths. We note that this application would only concern the observation of bright point sources which are not the most privileged targets for the X-IFU and would mostly offer an improvement to the observatory capability of the instrument.

5. COMPUTATIONAL COST ESTIMATES OF THE DIFFERENT METHODS

Whereas, the overall performance of the reconstruction techniques should be one of the main drivers for the final choice of the algorithm, the fact that a limited computational power will be available on board cannot be overlooked. In this section we will therefore briefly discuss the computational cost of each pulse processing solution. The aim is not to present here accurate estimates of the maximum processable pulse rate for a realistic space qualified CPU and every reconstruction technique, which would be at best a wild guess in this early phase, but rather to highlight the differences/similarities in terms of complexity in our intention to propose an as complete as possible view of the problem. Table 2 gives, for the methods described in Section 3 the number of each type of operation required to process one high resolution pulse (due to the X-IFU count rate requirement of 80 % high resolution throughput at 1 mCrab, the high resolution record length is limited to 1024 samples) in pure algorithmic terms. We note that we do not consider here any triggering stage as it is independent of the reconstruction choice. In all cases, we considered that each pulse would need to be filtered 3 times (with ±1 sample offset) in order to correct for sub-sample arrival time jitter.

As previously mentioned, the optimal filtering can be summarized to a single dot product and is therefore the most efficient solution. For the covariance analysis, only an additional subtraction by a pre-computed template is actually necessary. We would like to emphasize the fact that even if Equation 13 shows multiple matrix products, all the first terms can actually be pre-multiplied and the energy estimation is again only a dot product[‡]. For

[‡]Equation 13 gives the formula to estimate both the energy and the baseline level at the same time. Even if this level could be required to correct for long term variations, it would also need to be computed for the other techniques or could be done by another process (e.g. baseline monitoring at the triggering stage). If this estimation is discarded, the energy estimation collapses to a single dot product.

Table 2. Computational cost of the different reconstruction techniques to process one high resolution event of 1024 samples.

Reconstruction method	Nb. of additions	Nb. of multiplications	Nb. of divisions
Optimal filtering	3072	3072	0
Normal resistance space	3072[b]	3072	1024
Fitted resistance space	4096[b]	3072	1024
Covariance analysis	4096 (+ 1024)[a]	3072 (+1024)[a]	0

Notes – [a] The covariance analysis method relies on the identification of the two calibration points straddling the analyzed pulse. The first rough estimation of the energy (whose cost was neglected here) might therefore not directly give the correct interval, in which case an additional filtering might be performed. This would however only happen for events of energy very close to the calibration points, i.e. very rarely. [b] As mentioned in Sect. 3.2, optimal filtering is transparent to any additional linear transformation of the signal. In Equation 8, the load resistance term can therefore be omitted and the transformation becomes a simple division. This can however not be done in the "fitted resistance space" case.

the resistance space analysis, the difference comes from the pre-transformation of the signal, which makes it the heaviest method. We note that all the methods presented here nonetheless require very limited computational power.

6. CALIBRATION ISSUES

The last aspect that should be looked at when comparing reconstruction techniques is calibration. Whereas this is usually not an issue when studying data coming from a few pixels for which a large number of sample pulses can be relatively quickly obtained, it could become a critical aspect for the X-IFU and its 3840 pixels, if they need to be independently characterized. To investigate the different needs of the pulse processing methods, we simulated calibration processes using a limited amount of pulses and compared the performance degradation observed at 7 keV. The covariance analysis was set up using 6, 7, and 8 keV monochromatic simulations, while all the optimal filtering methods used filters at 1 keV. For a more meaningful comparison, like for the covariance analysis, we also used the noise residuals on top of the pulses instead of empty streams to measure the noise power spectra needed by the optimal filters.

Figure 6 shows the results of our comparison. As can be seen, all optimal filtering techniques actually need only very few pulses (~ 1000) to reach the final energy resolution. We however need to keep in mind that with real non-monochromatic X-ray sources, more pulses will be needed to obtain stable pulse templates at each energy than what we observed here. The covariance analysis is much more demanding ($\sim 400\,000$ pulses, if not more) and if the X-IFU pixels turn out to require independent calibration, this could well disqualify this reconstruction method. This huge difference with the other methods is actually due to the estimation of the noise covariance matrices which suffer from much poorer statistics compared to simple power spectra computations.

7. CONCLUSION

We have presented here an extended benchmark of the different pulse reconstruction techniques that could be considered for implementation in the on-board X-IFU Event Processor. Overall, all techniques show very similar performances, with the covariance analysis[17–19] showing the most promising improvement of the energy resolution degradation with energy compared to standard optimal filtering (~ 0.04 eV or ~ 0.5 eV root mean squared at 7 keV). This method however requires a significantly more demanding calibration process than the others and this may prevent its implementation for the X-IFU. On the other hand, resistance space analysis could become a strong candidate. It indeed provides some performance improvement (~ 0.02 eV or ~ 0.2 root mean squared at 7 keV) at a very limited computational cost and no impact on the calibration process. It is also the most robust technique at high count rates.

We note that the simulations performed here were all done in a fixed environment for the TES and no low frequency variations of for instance the bath temperature or the voltage bias were considered. This will introduce degradations of the energy resolution which in principle might be different depending on the used reconstruction

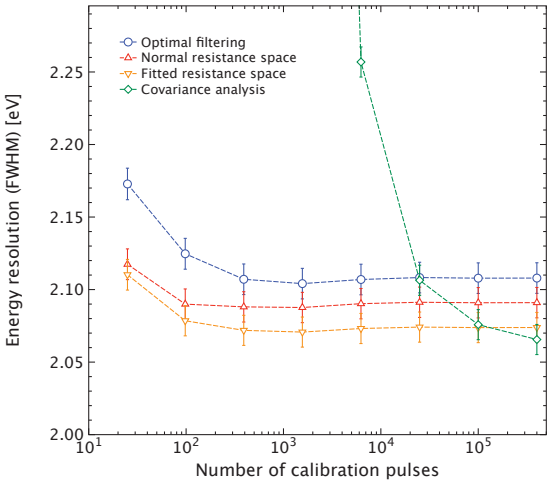

Figure 6. Comparison of the calibration needs for the different reconstruction methods with the baseline X-IFU pixels. The achieved energy resolution at 7 keV is given as a function of the number of pulses used for the calibration. The error bars give the $1\,\sigma$ uncertainty from the simulation statistics. As can be seen, the covariance analysis requires much more data than the optimal filtering techniques. The differences at high pulse calibration numbers is due to the energy dependent energy resolution (see Sect. 4) and is not related to the calibration process.

technique. To tackle this issue, a new processing technique based on Principal Component Analysis was also proposed which showed promising results for narrow band studies.[23,24] Its application to continuum spectra using an automated calibration process however needs to be investigated.

We further note that this study was conducted for particularly linear TESs which explains why only limited differences can be found between the different techniques. This proved to be also true for lower heat capacity TESs considered for implementation in a dedicated high count rate subarray of the X-IFU and for which very similar results were found (see Appendix A). Larger improvements could be observed in other types of detectors but we do not exclude that the ordering of the different reconstruction methods in terms of performance might also be different. The extension to severely non-linear detectors, including those operated up to their saturation level, would however need to be carefully investigated using notably a more realistic modeling of the superconducting transition.

The above results were obtained using the SIXTE simulation package, thus demonstrating its unique capabilities to assess the instrument performance under different configurations, as required in the early phases of the overall instrument optimization.

APPENDIX A. APPLICABILITY TO THE X-IFU SMALL PIXEL ARRAY

The baseline configuration for the X-IFU TES array consists of an assembly of 3840 identical pixels. Other sensor array configurations are however being considered with TESs of different properties in attempting to improve the X-IFU performance in terms of field of view, count rate performance, and potentially spectral resolution. These configurations notably include at their center a small pixel array (SPA) dedicated to the observation of bright point sources. To populate the SPA, smaller heat capacity pixels are considered, based on recent developments for Solar physics application.[25] In this appendix, we extended our analysis to this other pixel design whose parameters are given in Table 3. We note that in this case, an unexplained noise component was added in the simulations, parametrized by a scaling factor M with respect to the standard Johnson noise.

Table 3. Pixel parameters used to simulate the X-IFU SPA pixels.

Pixel parameter	Value
Heat capacity at bias C	0.26 pJ/K
Bath conductance at bias	300 pW/K
Heat bath power flow exponent	4
α	100
β	10
Unexplained noise factor M	0.8
Bias resistance R_0	1.1 mΩ
Bias temperature T_0	90 mK
Bias current I_0	72.6 µA
Effective load resistance R_L	91 µΩ
Effective circuit inductance L	122 nH
Read-out sampling frequency	156.25 kHz

Figure 7 shows the results of our simulations for the degradation of the energy resolution with energy. We find very similar results to those of the baseline pixels with the covariance analysis being the best reconstruction method. The "fitted resistance space" analysis again offers a smaller improvement but in this case, the "normal resistance space" reconstruction increases the energy uncertainty. This further indicates that this transformation is not directly applicable to high inductance cases. Overall, we however note that the differences between the methods are more limited than for the standard X-IFU pixels, including with the reference "interpolated covariance analysis".

In terms of performance at higher count rates (see Figure 8), as could be expected, these pixels, optimized for higher count rates, show slower performance degradation for all reconstruction techniques. The qualitative behavior nonetheless remains the same as before with a very sharp increase of the energy measurement bias when the previous pulse is too close, and the "normal resistance space" analysis showing the best performance for low record lengths.

Overall, the similarity of our results for both pixel types seems to indicate that the performance comparison presented here could be extended to a wider range of detectors.

ACKNOWLEDGMENTS

We thank Harvey Moseley and Dale Fixsen for helpful discussions on covariance reconstructions and principal component analysis. X. Barcons, M.T. Ceballos and B. Cobo acknowledge financial support from Spanish Ministry of Economy and Competitiveness (MINECO) under grant ESP2014-53672-C3-1-P, co-funded by FEDER funds.

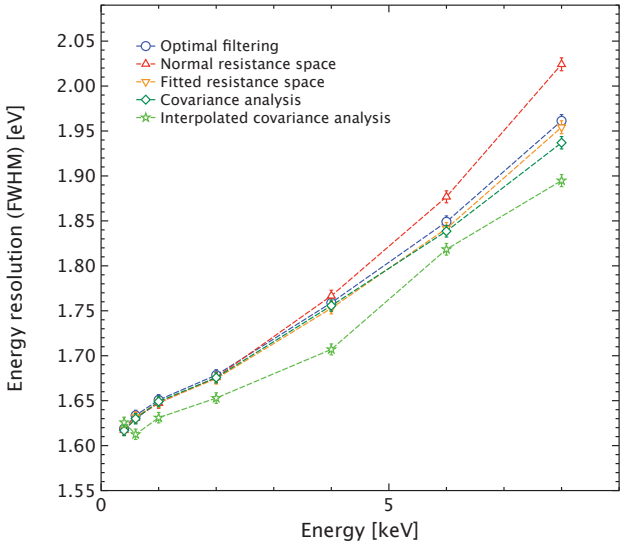

Figure 7. Comparison of the energy resolution performance of the different pulse reconstruction techniques as a function of energy for the X-IFU SPA pixels. The error bars give the $1\,\sigma$ uncertainty from the simulations.

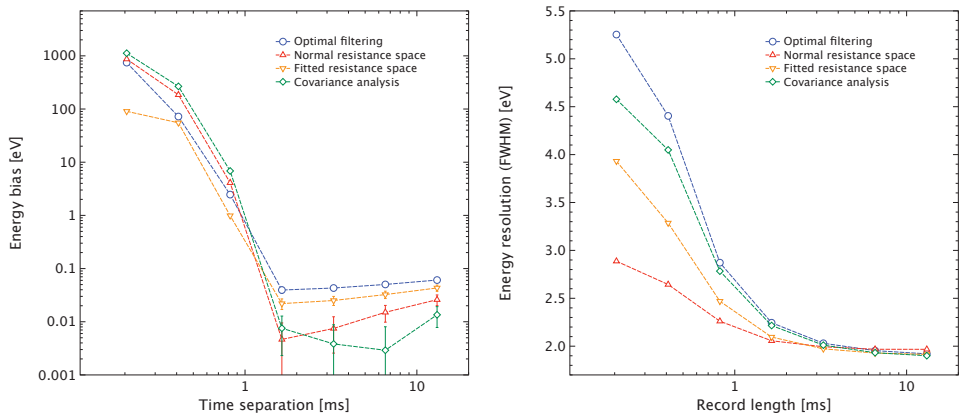

Figure 8. Comparative count rate performance of the different pulse reconstruction techniques for the X-IFU SPA pixels. Left: Energy bias as a function time separation since the previous event. Right: Energy resolution (FWHM) as a function of record length. The error bars give the $1\,\sigma$ uncertainty from the simulations.

REFERENCES

[1] Ravera, L., Barret, D., den Herder, J. W., Piro, L., Clédassou, R., Pointecouteau, E., Peille, P., Pajot, F., Arnaud, M., Pigot, C., Duband, L., Cara, C., den Hartog, R. H., Gottardi, L., Akamatsu, H., van der Kuur, J., van Weers, H. J., de Plaa, J., Macculi, C., Lotti, S., Torrioli, G., Gatti, F., Valenziano, L., Barbera, M., Barcons, X., Ceballos, M. T., Fàbrega, L., Mas-Hesse, J. M., Page, M. J., Guttridge, P. R., Willingale, R., Paltani, S., Genolet, L., Bozzo, E., Rauw, G., Renotte, E., Wilms, J., and Schmid, C., "The X-ray Integral Field Unit (X-IFU) for Athena," in [*Space Telescopes and Instrumentation 2014: Ultraviolet to Gamma Ray*], *Proc. SPIE* **9144**, 91442L (July 2014).

[2] Barret, D., den Herder, J. W., Piro, L., Ravera, L., Den Hartog, R., Macculi, C., Barcons, X., Page, M., Paltani, S., Rauw, G., Wilms, J., Ceballos, M., Duband, L., Gottardi, L., Lotti, S., de Plaa, J., Pointecouteau, E., Schmid, C., Akamatsu, H., Bagliani, D., Bandler, S., Barbera, M., Bastia, P., Biasotti, M., Branco, M., Camon, A., Cara, C., Cobo, B., Colasanti, L., Costa-Kramer, J. L., Corcione, L., Doriese, W., Duval, J. M., Fabrega, L., Gatti, F., de Gerone, M., Guttridge, P., Kelley, R., Kilbourne, C., van der Kuur, J., Mineo, T., Mitsuda, K., Natalucci, L., Ohashi, T., Peille, P., Perinati, E., Pigot, C., Pizzigoni, G., Pobes, C., Porter, F., Renotte, E., Sauvageot, J. L., Sciortino, S., Torrioli, G., Valenziano, L., Willingale, D., de Vries, C., and van Weers, H., "The Hot and Energetic Universe: The X-ray Integral Field Unit (X-IFU) for Athena+," *ArXiv e-prints* (Aug. 2013).

[3] Ravera, L., Cara, C., Ceballos, M. T., Barcons, X., Barret, D., Clédassou, R., Clénet, A., Cobo, B., Doumayrou, E., den Hartog, R. H., van Leeuwen, B.-J., van Loon, D., Mas-Hesse, J. M., Pigot, C., and Pointecouteau, E., "The DRE: the digital readout electronics for ATHENA X-IFU," in [*Space Telescopes and Instrumentation 2014: Ultraviolet to Gamma Ray*], *Proc. SPIE* **9144**, 91445T (July 2014).

[4] Szymkowiak, A. E., Kelley, R. L., Moseley, S. H., and Stahle, C. K., "Signal processing for microcalorimeters," *Journal of Low Temperature Physics* **93**(3), 281–285 (1993).

[5] Boyce, K. R., Audley, M. D., Baker, R. G., Dumonthier, J. J., Fujimoto, R., Gendreau, K. C., Ishisaki, Y., Kelley, R. L., Stahle, C. K., Szymkowiak, A. E., and Winkert, G. E., "Design and performance of the ASTRO-E/XRS signal processing system," in [*EUV, X-Ray, and Gamma-Ray Instrumentation for Astronomy X*], Siegmund, O. H. and Flanagan, K. A., eds., *Proc. SPIE* **3765**, 741–750 (Oct. 1999).

[6] Seta, H., Tashiro, M. S., Ishisaki, Y., Tsujimoto, M., Shimoda, Y., Abe, Y., Yasuda, T., Takeda, S., Asahina, M., Hiyama, Y., Yamaguchi, S., Terada, Y., Boyce, K. R., Porter, F. S., Kilbourne, C. A., Kelley, R. L., Fujimoto, R., Takei, Y., Mitsuda, K., Matsuda, K., and Masukawa, K., "The Digital Processing System for the Soft X-Ray Spectrometer Onboard ASTRO-H – The Design and the Performance –," *IEEE Transactions on Nuclear Science* **59**, 366–372 (Apr. 2012).

[7] Wilms, J., Smith, S. J., Peille, P., Ceballos, M. T., Cobo, B., Dauser, T., Brand, T., den Hartog, R., Bandler, S. R., de Plaa, J., and den Herder, J.-W., "TESSIM: a simulator for the ATHENA X-IFU," in [*Space Telescopes and Instrumentation 2016: Ultraviolet to Gamma Ray*], *Proc. SPIE* **9905**, 9905–192 (July 2016).

[8] Wilms, J., Brand, T., Barret, D., Beuchert, T., den Herder, J.-W., Kreykenbohm, I., Lotti, S., Meidinger, N., Nandra, K., Peille, P., Piro, L., Rau, A., Schmid, C., Smith, R. K., Tenzer, C., Wille, M., and Willingale, R., "ATHENA end-to-end simulations," in [*Space Telescopes and Instrumentation 2014: Ultraviolet to Gamma Ray*], *Proc. SPIE* **9144**, 91445X (July 2014).

[9] Mather, J. C., "Bolometer noise: nonequilibrium theory," *Appl. Opt.* **21**, 1125–1129 (Mar 1982).

[10] Irwin, K. D. and Hilton, G. C., [*Transition-Edge Sensors*], 63, Enss, C. (2005).

[11] Kilbourne, C. A., de Korte, P., Smith, S. J., Hoevers, H., van der Kuur, J., Ezoe, Y., and Ullom, J. N., "Ixo/xms detector trade-off study," tech. rep., NASA GSFC (2010).

[12] Smith, S. J., Adams, J. S., Bandler, S. R., Betancourt-Martinez, J. L., Chervenak, J. A., Chiao, M., Datesman, A. M., Eckart, M. E., Ewin, A. J., Finkbeiner, F. M., Kelley, R. L., Kilbourne, C. A., Porter, F. S., Sadleir, J. E., Wassel, E. J., Yoon, W., Bennett, D. A., Doriese, W. B., Hilton, G. C., Swetz, D. S., Ullom, J. N., Akamatsu, H., Gottardi, L., den Hartog, R. H., Jackson, B. D., van der Kuur, J., Barret, D., and Peille, P., "TES pixel parameter design of the microcalorimeter array for the x-ray integral field unit on ATHENA," in [*Space Telescopes and Instrumentation 2016: Ultraviolet to Gamma Ray*], *Proc. SPIE* **9905**, 9905–85 (July 2016).

[13] Bandler, S. R., Figueroa-Feliciano, E., Iyomoto, N., Kelley, R. L., Kilbourne, C. A., Murphy, K. D., Porter, F. S., Saab, T., and Sadleir, J., "Non-linear effects in transition edge sensors for X-ray detection," *Nuclear Instruments and Methods in Physics Research A* **559**, 817–819 (Apr. 2006).

[14] Lee, S. J., Adams, J. S., Bandler, S. R., Chervenak, J. A., Eckart, M. E., Finkbeiner, F. M., Kelley, R. L., Kilbourne, C. A., Porter, F. S., Sadleir, J. E., Smith, S. J., and Wassell, E. J., "Fine pitch transition-edge sensor x-ray microcalorimeters with sub-ev energy resolution at 1.5 kev," *Applied Physics Letters* **107**(22) (2015).

[15] den Hartog, R., Barret, D., Gottardi, L., den Herder, J.-W., Jackson, B., de Korte, P., van der Kuur, J., van Leeuwen, B.-J., van Loon, D., Nieuwenhuizen, A., and Ravera, L., "Requirements for the detectors and read-out of ATHENA X-IFU," in [*Space Telescopes and Instrumentation 2014: Ultraviolet to Gamma Ray*], *Proc. SPIE* **9144**, 91445Q (July 2014).

[16] Smith, S. J., Adams, J. S., Bandler, S. R., Busch, S. E., Chervenak, J. A., Eckart, M. E., Finkbeiner, F. M., Kelley, R. L., Kilbourne, C. A., Lee, S. J., Porst, J.-P., Porter, F. S., and Sadleir, J. E., "Characterization of Mo/Au Transition-Edge Sensors with Different Geometric Configurations," *Journal of Low Temperature Physics* **176**, 356–362 (Aug. 2014).

[17] Fixsen, D. J., Moseley, S. H., Cabrera, B., and Figueroa-Feliciano, E., "Optimal fitting of non-linear detector pulses with nonstationary noise," *Low Temperature Detectors* **605**, 339–342 (Feb. 2002).

[18] Fixsen, D., Moseley, S., Cabrera, B., and Figueroa-Feliciano, E., "Pulse estimation in nonlinear detectors with nonstationary noise," *Nuclear Instruments and Methods in Physics Research Section A: Accelerators, Spectrometers, Detectors and Associated Equipment* **520**(1-3), 555 – 558 (2004). Proceedings of the 10th International Workshop on Low Temperature Detectors.

[19] Fixsen, D. J., Moseley, S. H., Gerrits, T., Lita, A. E., and Nam, S. W., "Optimal energy measurement in nonlinear systems: An application of differential geometry," *Journal of Low Temperature Physics* **176**(1), 16–26 (2014).

[20] Doriese, W. B., Adams, J. S., Hilton, G. C., Irwin, K. D., Kilbourne, C. A., Schima, F. J., and Ullom, J. N., "Optimal filtering, record length, and count rate in transition-edge-sensor microcalorimeters," in [*American Institute of Physics Conference Series*], Young, B., Cabrera, B., and Miller, A., eds., *American Institute of Physics Conference Series* **1185**, 450–453 (Dec. 2009).

[21] Lee, S. J., Bandler, S. R., Busch, S. E., Adams, J. S., Chervenak, J. A., Eckart, M. E., Ewin, A. J., Finkbeiner, F. M., Kelley, R. L., Kilbourne, C. A., Porst, J.-P., Porter, F. S., Sadleir, J. E., Smith, S. J., and Wassel, E. J., "High Count-Rate Studies of Small-Pitch Transition-Edge Sensor X-ray Microcalorimeters," *Journal of Low Temperature Physics* **176**, 597–603 (Aug. 2014).

[22] Fowler, J. W., Alpert, B. K., Doriese, W. B., Fischer, D. A., Jaye, C., Joe, Y. I., O'Neil, G. C., Swetz, D. S., and Ullom, J. N., "Microcalorimeter Spectroscopy at High Pulse Rates: A Multi-pulse Fitting Technique," *ApJS* **219**, 35 (Aug. 2015).

[23] Busch, S. E., Adams, J. S., Bandler, S. R., Chervenak, J. A., Eckart, M. E., Finkbeiner, F. M., Fixsen, D. J., Kelley, R. L., Kilbourne, C. A., Lee, S.-J., Moseley, S. H., Porst, J.-P., Porter, F. S., Sadleir, J. E., and Smith, S. J., "Progress Towards Improved Analysis of TES X-ray Data Using Principal Component Analysis," *Journal of Low Temperature Physics* (Nov. 2015).

[24] Yan, D., Cecil, T., Gades, L., Jacobsen, C., Madden, T., and Miceli, A., "Processing of X-ray Microcalorimeter Data with Pulse Shape Variation using Principal Component Analysis," *Journal of Low Temperature Physics* (Jan. 2016).

[25] Smith, S. J., Adams, J. S., Bailey, C. N., Bandler, S. R., Chervenak, J. A., Eckart, M. E., Finkbeiner, F. M., Kelley, R. L., Kilbourne, C. A., Porter, F. S., and Sadleir, J. E., "Small pitch transition-edge sensors with broadband high spectral resolution for solar physics," *Journal of Low Temperature Physics* **167**(3), 168–175 (2012).

5.3 Supplements: study of other pixel types

This publication focused on the standard X-IFU pixels as well as the SPA as an example of a lower heat capacity detector. As this provided a framework to study a variety of pixel types, I extended this work to the LPA2 and LPA3 pixels. Figure 5.1 and 5.2 show the results obtained from these two pixel types. Unfortunately, because it is impossible to calibrate a covariance matrix bigger than 2048×2048 samples with reasonable resources, the comparison was made with records of 2048 samples, i.e. less than the high resolution definition. Both the degradation with energy and record length therefore get mixed. This is especially visible for the very slow LPA3 pixel for which we see a significant difference with the interpolated covariance analysis which assumes baseline knowledge and therefore has a much lower degradation with record length. In this case, the covariance analysis also ends up degrading above the other methods at high energies. We nonetheless find similar results with a limited difference between the reconstruction techniques (apart from the "interpolated covariance analysis"), the covariance analysis having the best performance in terms of energy resolution degradation with energy (if we could extend to higher record lengths) and the resistance space analysis in terms of high count rate capability. This study thus confirms the application of these results to a quite wide range of detectors, at least among those being fairly linear.

5.4 Conclusion

Overall, this study has highlighted that even if limited, some performance increase could be obtained by using more sophisticated reconstruction techniques such as covariance or "resistance space" analysis instead of the standard optimal filtering technique. This would even be possible at a very small onboard computational power cost. The applicability of the covariance method on the large X-IFU array however appears compromised due to the significant calibration effort it requires. The use of a first non-linear transformation before applying the optimal filter thus appears as the most promising candidate. In the present study, we limited ourselves to transformations close to the so-called "resistance space" method, but some additional improvement could be obtained from more complicated modifications.

Clearly, this analysis has shown the potential power of using realistic TES simulations to perform systematic performance studies. Of course, this does not replace actual lab measurements but still allows to explore more easily a wide range of setups using our current knowledge of the TES physics. In the near future, `tessim` could notably be modified to investigate for instance the sensibility of the reconstruction methods to low frequency drifts of for instance the bath temperature or voltage bias. It would also be interesting to see how much our results would be affected by the proper simulation of the pulse jitter with respect to the readout samples (for simplicity reasons, all pulses are currently simulated in phase with the readout process). On the longer term, the incorporation of a more realistic TES transition would allow the testing of less linear detectors with even lower heat capacity than the SPA (see e.g. Lee et al., 2015). These pixels have the potential of reaching a better energy resolution. If much of the energy resolution degradation with energy proves to be recoverable from the use of advance pulse processing techniques, considering them for implementation in an SPA could further improve the line sensitivity of the X-IFU for point sources which is at the core of some of the X-IFU science objectives. This would however imply increased differences between the LPA and SPA pixels and thus probably separated readout chains, which may be excluded because of feasibility/risk considerations.

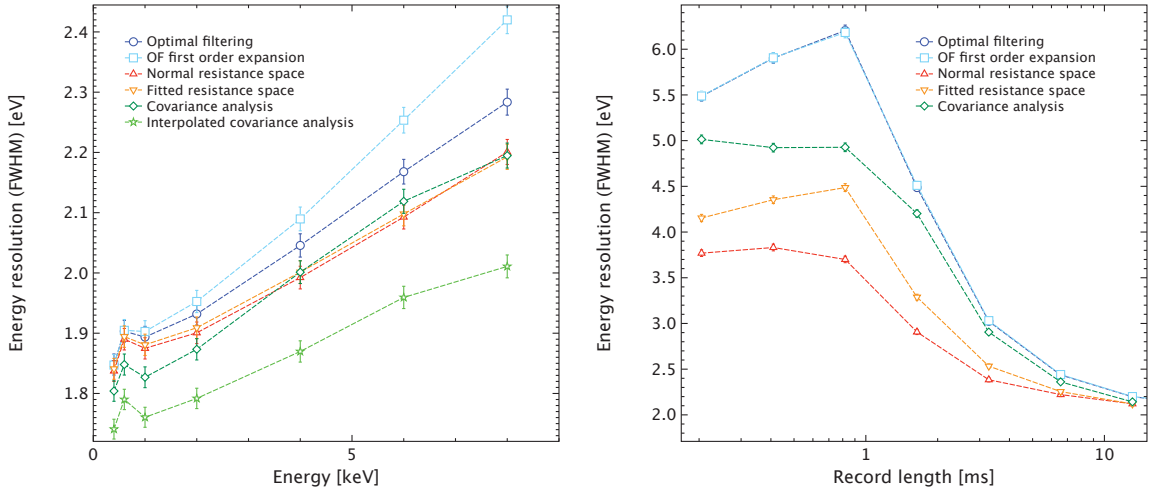

Figure 5.1: Comparison of different reconstruction techniques for the LPA2 pixels. **Left:** Energy resolution versus energy. We note that this figure was obtained with 2048 samples for all techniques, i.e. less than the high resolution definition. This is about the maximal covariance matrix size that can be calibrated with reasonable resources. **Right:** Energy resolution as a function of record length.

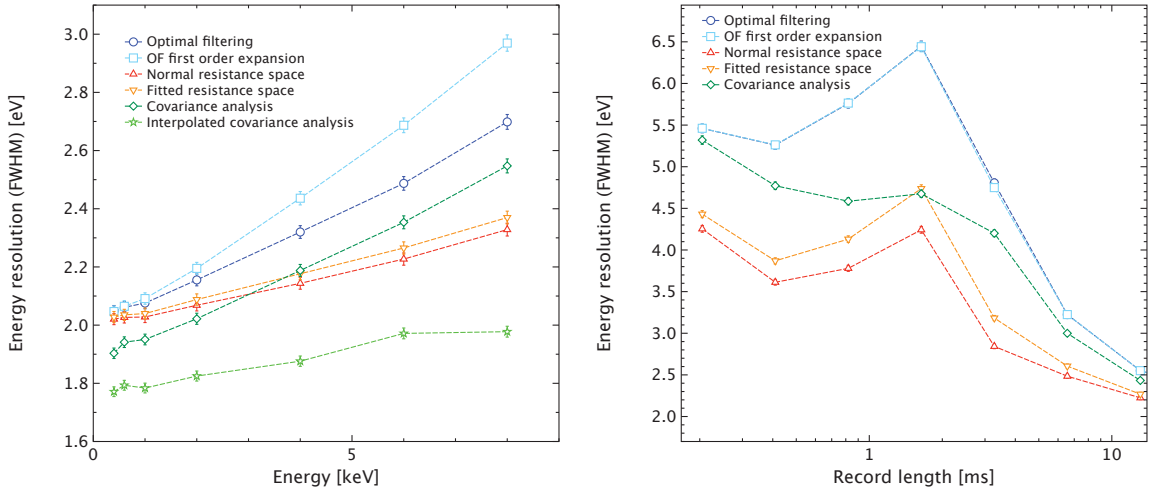

Figure 5.2: Comparison of different reconstruction techniques for the LPA3 pixels. **Left:** Energy resolution versus energy. We note that this figure was obtained with 2048 samples for all techniques, i.e. less than the high resolution definition. This is about the maximal covariance matrix size that can be calibrated with reasonable resources. **Right:** Energy resolution as a function of record length.

Chapter 6: Scientific simulations of the X-IFU

One of my major contributions to the X-IFU End-to-End simulations effort has been the implementation and development of the `xifupipeline` tool which uses the characterization of various pixel types conducted in Chapter 4 to perform realistic simulations of the X-IFU in its various configurations. In this chapter, I will present different studies of the overall X-IFU scientific performance I carried out, ranging from high count rate capabilities to spectral-imaging performance for complex observations. Beyond the intrinsic importance of these case studies, this will perfectly illustrate the potential of the `xifupipeline` tool to conduct advanced studies of the future scientific capability of the X-IFU.

6.1 Timing performance at high count rates: observing kHz QPOs with the X-IFU?

In Chapter 2, I studied kHz QPOs with the RXTE PCA. Now having available a representative simulator of the X-IFU even at high count rates (see Chapter 4), I now report on the potential of the X-IFU for the study of these high frequency phenomena, pushing the range of count rates to the limit of the instrument capabilities. Apart from the fundamental interest of this particular science theme, it is also a good test case for the overall timing performance of this instrument at high count rates.

6.1.1 Simulation setup and initial detectability

To perform this study, I decided to use the QPO and spectral parameters measured from the prototypical first ObsID of 4U1608-522 by the PCA. In this case, the lower kHz QPO had a quality factor of ~ 144 and was relatively stable in frequency at 849 Hz. Using the continuum and covariance spectra measured in Section 2.4 it is also possible to estimate with `Xspec` the QPO RMS level seen by the X-IFU in different energy bands. As shown by Equation 2.11, the detectability of the QPO scales linearly with the total count rate and quadratically with the RMS. With the QPO RMS increasing with energy and the X-IFU effective area dropping sharply above a few keV, the optimal detectability was thus found to be in the 3–12 keV energy range with $\sim 3.2\,\%$ RMS and an expected count rate of ~ 2100 counts per second (the total count rate amounts to ~ 7900 counts per second, i.e. ~ 80 mCrab). This RMS level can then be used to produce a suitable SIMPUT file and the simulation performed using the `xifupipeline`. This count rate would be very large for the baseline X-IFU concept (see Fig. 4.12) and I therefore chose to rather perform the simulation using the SPA (see Chapter 4).

As a first illustration of the overall QPO detectability with the X-IFU without any dead time, Figure 6.1 shows the PDS that is obtained from the pixel impact list (i.e. before the grading process, see Sect. 4.3.2) above 3 keV for an exposure time of 2048 s. This can also be seen as what could be obtained if large defocus lengths were available thus enabling 100 % throughput at the simulated count rate (see Fig. 4.14). It is important to note that because the QPO frequency is not stable in time,

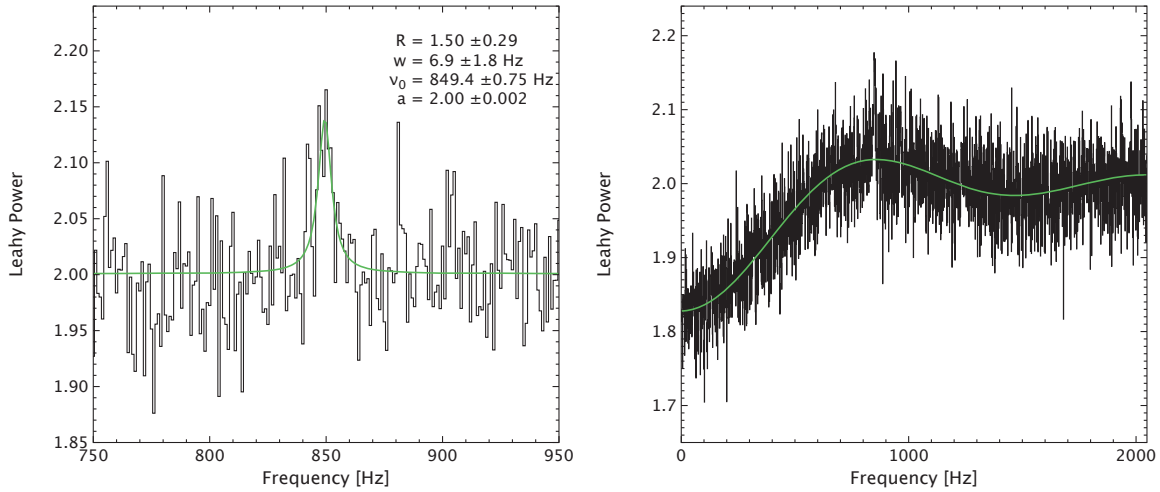

Figure 6.1: Left: Fit of the PDS obtained from the simulated QPO X-IFU observation before the grading process. The signal is hardly detected with a ratio of the Lorentzian normalization to its error just above 3. **Right:** Same PDS but after the rejection from the light curve of the misreconstructed secondaries (see Sect. 4.4.2). The effect of dead time is clearly visible. It can be modeled following the method proposed by Zhang et al. (1995) in the paralyzable dead time case using the known dead time value of 1.2 ms (green line, see Appendix C). The comparison of the model with the simulated PDS yields $\chi^2 = 2089$ (2047) with most of the deviation actually coming from the QPO.

the simulation of larger exposures would not be representative and that 2048 s of such a narrow QPO at a constant frequency is already a very optimistic case. As can be seen, even in this situation, the QPO is poorly detected in comparison to what could be achieved with the RXTE PCA (see Fig.2.2 for a comparison).

6.1.2 Dead time effects

If we now take into account the full detection process of the X-IFU, including the rejection of misreconstructed secondaries (see Chapter 4), the resulting PDS gets strongly distorted (see Fig. 6.1, right, for which only the valid events were used to construct the PDS). This distortion comes from so-called dead time effects: because no event can be properly measured closely after another, the statistics governing the final light curve deviates from the initial perfect Poisson regime. Zhang et al. (1995) proposed a very useful framework to model the average PDS expected in the presence of different dead time processes. In the case of the X-IFU, the secondaries rejection corresponds to "paralyzable dead time": even if the detector is dead (no photon can be reconstructed), the impact of a new event induces the prolongation of the dead time interval. In Appendix C, I extended this framework to take into account the fact that several independent pixels contribute to the light curve. Using this new formulation (Eq. C.6), the model nicely fits the distortion and if the dead time value is known (which is the case for the secondaries rejection process simulated here), a corrected PDS can be obtained by multiplying the measured PDS by $2/P_{\mathrm{model}}(f)$, thus enabling the recovery of the QPO (see Fig. 6.2, left). This particular scaling ensures that the usual property of the signal free Leahy normalized PDS (Leahy et al., 1983) having a standard deviation of $2/\sqrt{M}$ (M being the number of averaged powers) is conserved (see e.g. Bachetti et al., 2015).

In the frame of the *NuSTAR* mission, Bachetti et al. (2015) alternatively proposed to use the cross spectrum (see Sect. 2.3.1 for the definition of a cross spectrum) between two independent detectors

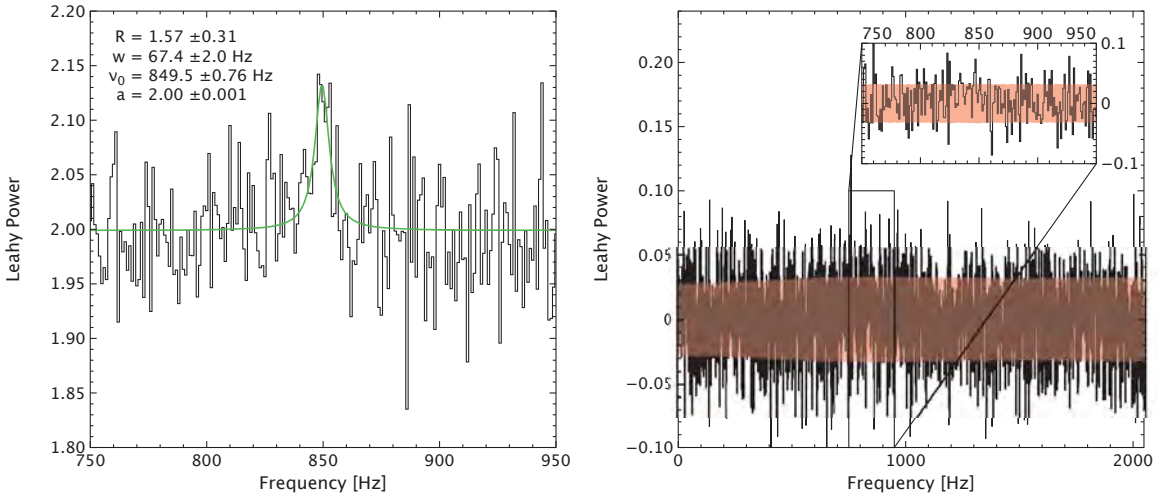

Figure 6.2: Two methods to correct dead time effects. **Left:** Corrected PDS using the analytical correction developed in Appendix C. In this case, the QPO parameters could be retrieved. **Right:** Ersatz PDS obtained from the real part of the cross spectrum between the light curves extracted from the brightest pixel and from the combination of all the others. No dead time induced systematic trend is visible anymore (see text). The red zone delimits the expected $1\,\sigma$ uncertainty as a function of frequency. In this case, as highlighted by the inset, the QPO cannot be detected.

(would be pixels in the case of the X-IFU) to compensate for the dead time effects. As the dead time processes in the two detectors are uncorrelated while the actual signal is, by taking the real part of the cross spectrum, only the relevant variability is kept. If the individual Fourier transforms are Leahy normalized, one thus obtains an ersatz of a PDS that is centered around zero instead of 2 (see Fig. 6.2). One just then just needs to assign corrected errors of $\overline{P}(f)/\sqrt{2M}$ to properly fit any detected signal, where $\overline{P}(f)$ is the harmonic mean of the powers measured from the two initial light curves (Bachetti et al., 2015). This method however decreases the sensibility to any variability by a factor $\sqrt{2}$ and in the case of this X-IFU simulation, the QPO became undetectable.

The main advantage of this second method is that it does not require any knowledge of the dead time process and works as long as it is uncorrelated in the two "detectors" used. It would for instance be robust to an energy-dependent secondary rejection process (like the one proposed by Lee et al. (2014) to accommodate very large count rates in TESs) whereas the analytical method would become spectral shape dependent, i.e. subject to uncontrolled systematic effects. We further note that if any event screening due to crosstalk between pixels needs to be incorporated for the X-IFU, this method will not be useable anymore as the initial assumption of uncorrelated dead time processes in different pixels would break down. Correcting this using an analytical method would not be impossible in principle but would require significant work compared to the simple extension proposed in Appendix C.

6.2 Spatially resolved spectroscopy with the X-IFU: galaxy clusters simulations

The X-IFU will enable for the first time spatially resolved high resolution spectroscopy. This capability is key to the scientific return of the X-IFU and will notably be used for the study of the structure and dynamics of nearby and distant galaxy clusters. As such observations and subsequent data analysis procedures have never been performed, simulating representative datasets would enable us to

demonstrate to the community the actual richness and complexity of the data that will be provided by the X-IFU. We would also properly test the actual capability of this instrument to reconstruct complex physical quantities such as the turbulent velocity, bulk motions, and the abundances of various chemical species within the intra-cluster gas, in order for instance, to optimize future observational strategies.

In this section, I will present two sets of simulations I conducted during my thesis: the first one (Sect. 6.2.1) interfaces with the result of a cosmological simulation in order to create representative samples of galaxy cluster observations with their full richness. The second one (Sect. 6.2.2) will use a physically justified toy model to try to estimate the capability of the X-IFU to differentiate different turbulence regimes.

6.2.1 Interfacing with cosmological simulations

Simulation inputs and SIMPUT interface

Existing X-ray observations from *XMM-Newton*, *Chandra*, or *Suzaku* instruments with spatially resolved spectroscopy capabilities do not carry the required spatial and spectral information to test the X-IFU full capabilities (e.g., spectral resolution to characterize line shifts and broadening). As a consequence, simulations of structure formation provide to date the best representation of the complex physics at play in clusters of galaxies (see e.g. Biffi et al., 2013; Rasia et al., 2015). With respect to a toy model, they provide an as-close-as possible representation of the reality and will give a view on the mixing of information along the line of sight and from the convolution with the X-IFU transfer function. In this study, we used a subset of the simulation results presented in Rasia et al. (2015).

Out of the different available clusters, we decided to look at a local one ($z \sim 0.1$), hot enough to allow the observation of the Iron K α line (for turbulence measurements) out to its outskirts, and presenting a dynamical structure traced by important velocity gradients. We choose to avoid working with an integrated cone generated from the whole numerical simulation in order to be able to simulate the emission of the cluster independently of any background and foreground emissions. We thereby only considered the particles/cells describing the cluster at the chosen redshift. In this simulated cluster, each particle is described by its position, velocity, density, total mass, temperature and by the mass of the following elements: Fe, Si, O, and H.

We first selected a line-of-sight and projected the coordinates of all particles in the chosen referential. Assuming a single X-IFU pointing towards the centre of the simulated cluster, we define a cone centered on the cluster and of angular diameter 5.1 arcmin (encompassing the whole X-IFU FoV). We selected all particles within this cone. From the initial inputs containing 4062889 particles we thus kept only 436337 particles as contributors in our X-IFU simulations. For the X-ray emission of the cluster, we decided to use the `Xspec vapec` model, an emission spectrum from collisionally-ionised diffuse plasma calculated using the `ATOMDB` code v2.0.2., the input parameters of this model being obtained from the particle properties, the abundances of the other elements being fixed to the default model values, i.e. $Z = Z_{\odot}$.

The volume associated to a particle is derived from the mass and density of the particle, whereas the density of hydrogen for a particle p is computed as:

$$M_H^p / M^p \times \rho^p / m_p, \tag{6.1}$$

where m_p is the proton mass. The abundances for each element X is then computed as:

$$Z_X = (M_X^p / M_H^p) / (Z_{\odot,X} \times \mathcal{M}_X), \tag{6.2}$$

Table 6.1: Distribution of the emission parameters in the simulated galaxy cluster

Parameter	Units	$X_{\min}$	$X_{\max}$	$\bar{X} \pm \sigma_X$	ΔX
kT	keV	0.086	151.2	9.34 ± 2.42	0.1
A_{Fe}	solar	0.0	8.3	0.29 ± 0.46	0.1
A_O	solar	0.0	4.23	0.23 ± 0.44	0.1
A_{Si}	solar	0.0	7.3	0.41 ± 0.77	0.1
z	–	0.0969	0.1128	0.1045 ± 0.0013	7×10^{-5} (a)

(a) Precision on z corresponding to a velocity of 20 km/s at the source redshift.

with $Z_{\odot,X}$ the solar abundance of element X and $\mathcal{M}_X$ its atomic weight. The solar abundances were fixed to these of Anders & Grevesse (1989). We assume the full ionization of the intra-cluster gas, and thus adopted $n_e = 1.2 \times n_p$. The effective redshift of each particle is computed as follows:

$$z = \left[\sqrt{\frac{c + v_z}{c - v_z}} - 1\right](1 + z') + z' \tag{6.3}$$

where v_z is the line of sight velocity and z' the redshift corresponding to the peculiar velocity of the cluster in the comobile referential with respect to the expansion of the Universe at the cluster redshift obtained from its angular distance using a ΛCDM model ($H = 72\,\mathrm{km/s/Mpc}$, $\Omega_M = 0.24$, $\Omega_L = 0.76$ Rasia et al., 2015).

Table 6.1 shows for each relevant emission model parameter its minimum and maximum value in the cluster, as well as its average and standard deviation, to be compared in the last column with the typical precision one would want to obtain from an X-IFU simulation. The cluster particles therefore sample a very wide range of emission spectral shapes and that it would not be possible to create a reasonably sized SIMPUT file (see Sect. 4.3.1) containing the spectra needed for generating photons from the full cluster, even if we were to bin particles together up to the X-IFU parameter accuracy[1]. We rather opted for an interface through a *perfect* photon list at the Earth. The SIMPUT format indeed allows to specify the spatial and spectral distribution of the emission with a set of photons just before the convolution with the instrumental transfer function. This solution presents the significant advantage of not saving to a file and loading during simulation a spectrum with ∼ 400000 channels per particle, that in most cases will only be used to generate a few hundreds of photons. Concretely, for each cluster particle, a sufficiently high number of photons were randomly drawn according to its spectrum to create a large photon list. The SIXTE simulator will then be able to randomly pick events from this list depending on the required integration time. We thus generated an event list at the Earth with 500 ks integration time and a flat $2\,\mathrm{m}^2$ mirror effective area. This allows us to have reliable statistics up to ∼50 ks observations without degrading the input information.

End-to-End simulation and data analysis

The X-IFU observation simulation was performed with the `xifupipeline` tool, pointing at the center of the cluster, for a 50 ks integration time, and using the baseline detector configuration. From the resulting event list, we grouped pixels together to extract spectra with at least 10 000 counts, using the `contbin` tool (Sanders, 2006) which chooses regions by following contours on a smoothed image of the

[1] In order to properly sample the line profiles to be detected by the X-IFU, spectra with more than 400000 channels (∼ 3 Mbytes) are needed.

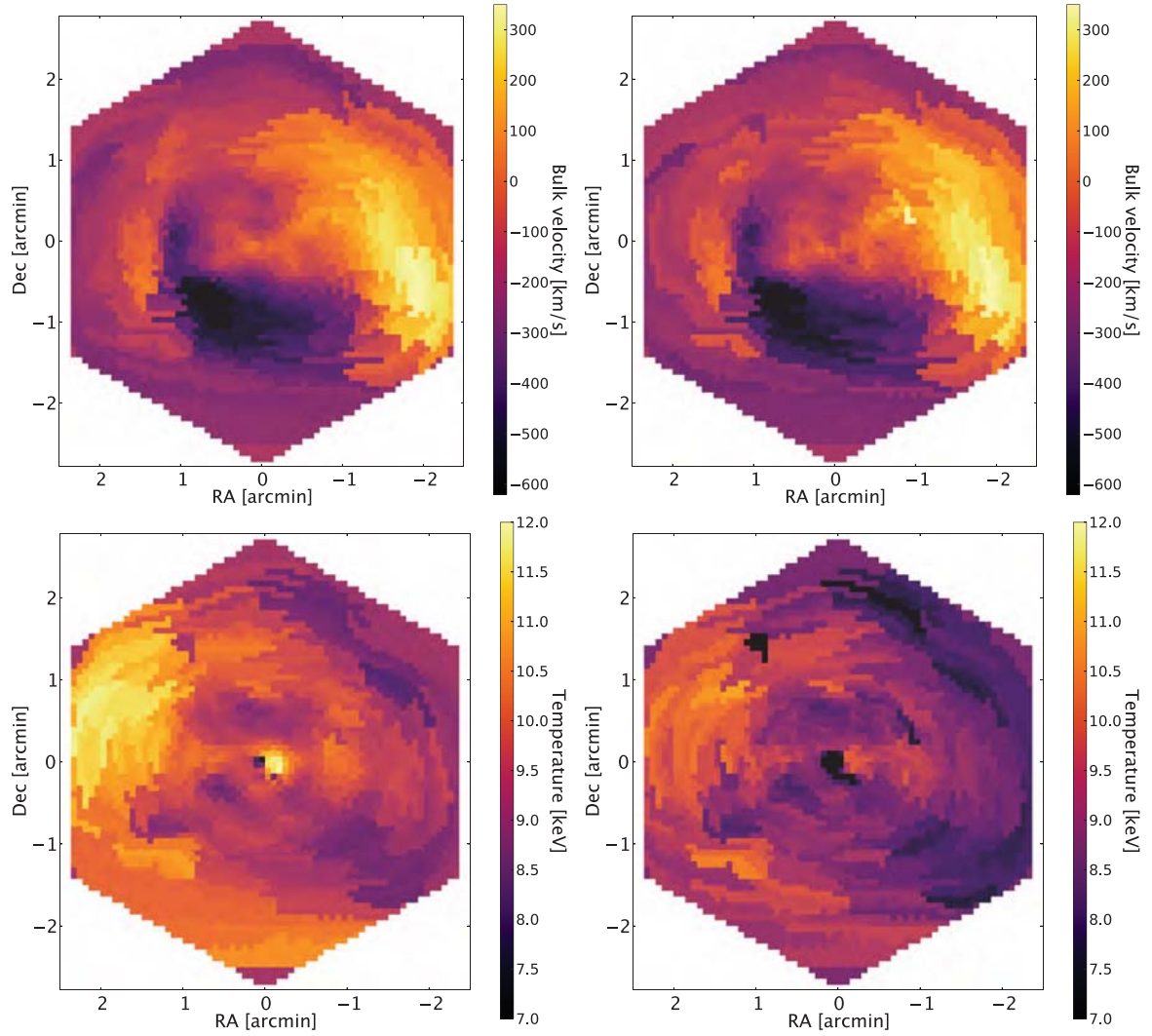

Figure 6.3: Comparison of input (left) and output (right) parameter maps (top: bulk velocity, bottom: temperature) for the simulated galaxy cluster. The input maps were obtained from the emission weighted projection of the particle parameters without any PSF nor vignetting effect.

object. The spectra were then rebinned in order to reach at least $5\,\sigma$ in each spectral bin and fitted in `Xspec` with the `vapec` model leaving free the following parameters: $Norm$, kT, A_{Fe}, A_O, A_{Si}, z. The redshift traces the cluster bulk motion whereas the `APECVELOCITY` keyword was used to fit the intra pixel turbulent velocity using an upper level χ^2 minimization[2]. Maps were thus obtained for all these parameters across the field of view, which can be compared with the emission weighted projection of the particle parameters (no PSF nor vignetting effect was taken into account, but these should be largely negligible). Figure 6.3 shows this comparison for the temperature and reconstructed bulk velocity which are the two most illustrative examples (the other maps can be found in Appendix B).

[2]In the `vapec` model, the turbulent velocity is not directly available as a fit parameter but through a fixed `Xspec` keyword. We thus run fits with different keyword values to determine its optimal level from the different χ^2 using the MIGRAD minimization algorithm (James & Roos, 1975).

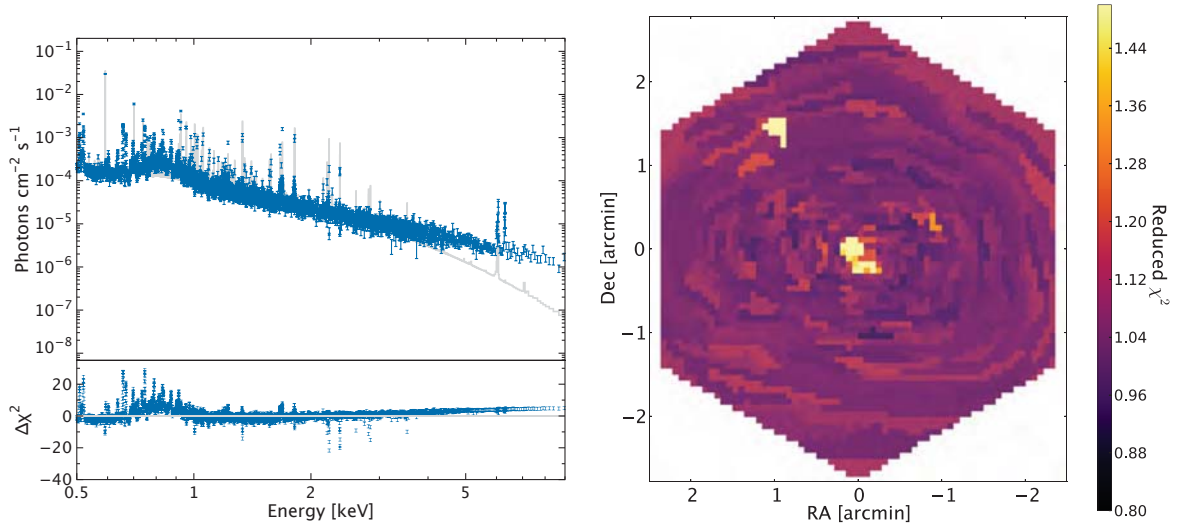

Figure 6.4: Left: Unfolded spectrum and $\Delta\chi^2$ residuals corresponding to the fit of the spectrum from the brightest pixel of the simulation. In this case, the modeling with a single temperature component (grey line) is not sufficient and we can clearly observe at the same time cold emission with proficient emission lines in the soft X-rays from the center of the cluster, as well as hot emission from its outskirts dominating at high energies. **Right:** Reduced χ^2 map. This large line of sight mixing effect is present around all the cold spots of the simulation.

Overall, these maps perfectly demonstrate the power of the X-IFU to reconstruct complex physical information on a large field of view, and of the `xifupipeline` tool to run advanced End-to-End simulations. Most of the different cluster structures were indeed properly recovered. We nonetheless identified two systematic effects in the simulation. Firstly, the reconstructed temperature is globally colder than its emission weighted projection. This is in fact a known effect originating from the mixing of several thermal components along the line of sight and it can be properly accounted for (Mazzotta et al., 2004; Vikhlinin, 2006) and is not a systematic error of our simulation process. Secondly, the input cosmological simulation contains a certain number of cold spots, the most pronounced one being at the center of the cluster, which are at the limit of the physical domain handled by the simulation (E. Rasia & V. Biffi, private communication). These can be easily identified in the temperature maps (see Fig. 6.3) and around them, the physical parameters could not be properly recovered (see also the abundance maps in Appendix B). Even if the effect is exaggerated compared to what would happen in a real observation, they serve as a good illustration of the consequences of the emission of multi-phase gas along the line of sight which is this time dominated by the cold emission of the dense spots. Figure 6.4 (left) shows the fit result obtained from the brightest pixel of the simulation. As can be seen, in this case, the adjustment with a single thermal component is not sufficient and this biases the measurement of the different physical quantities. This same effect is present around the other cold spots where wrong parameters were recovered as illustrated by the reduced χ^2 map (see Fig. 6.4, right).

Conclusion and perspectives

With these simulations, I have made the first steps towards properly testing the X-IFU galaxy cluster science cases in a fully representative setup. This work is of course a long term effort and will need to be developed in the coming years. This particular example has notably illustrated the intrinsic

complexity of an X-IFU dataset and the limitation of current data analysis methods, mainly based on the simple fitting of spectra extracted from various regions, to properly recover useful physical quantities in highly convolved situations, in the presence for instance of significant line of sight mixing effects. This has been identified in the X-IFU Science Advisory Team as a real hurdle and will be addressed in the form of a data challenge. Without addressing directly this issue, further studies could nonetheless be performed in the shorter term from this type of simulations which have also proven the potential of the `xifupipeline` tool to produce representative X-IFU observations of objects with very complex structure. This could notably include the simulation and measurement of a full set of clusters extracted from the same structure formation simulation to try to quantitatively estimate the ability of the X-IFU to test some of the large scale physics used as postulate in these simulations. On a smaller scale, the simulation of the outskirts of the same cluster could already help us to verify the capability of the X-IFU to perform the same types of measurements in a situation with a less advantageous signal to noise ratio, notably in the presence of a variable and not perfectly known instrumental background.

6.2.2 Measuring turbulence regimes with the X-IFU

In the previous section, I have developed an approach to simulate fully representative observations of galaxy clusters featuring complex structures using inputs from structure formation simulations. This method provided mixed datasets containing a wealth of information on different aspects of the dynamics of galaxy clusters, whose quantitative analysis is currently in progress. In order to further assess the X-IFU performances, I will take a different route, making use of less intricate inputs, focusing on a single science objective of the *Athena* mission which is the measurement of turbulence regimes in nearby galaxy clusters (Ettori et al., 2013).

Simulating turbulence in the Coma cluster

Recently, ZuHone et al. (2016) (hereafter Z16) studied the capacity of *Hitomi/SXS* to map gas turbulence in the Coma cluster and showed that this instrument would have been able to measure the Mach number and injection scale of the turbulent process in this cluster from a 15'×15' raster observation with sparse coverage. To do so, they relied on the simulation of emission-weighted line of sight velocity fields under different turbulence regimes using normally distributed velocity components to account for the measurement of systematic and statistical uncertainty. Here, I take this approach one step further and use the full capacity of the X-IFU End-to-End simulator to simulate the whole 3D X-ray emission of the cluster and perform actual velocity measurements emission lines detected by the X-IFU.

From the work presented in Sect. 6.2.1, we already have a framework to simulate the emission from clusters using a set of particles with known density, abundance and temperature[3]. We thus define a grid of particles with a central redshift of 0.023 matching the Coma cluster (i.e. an angular distance of $\sim$ 93 Mpc for, as in Sect. 6.2.1 $H = 72\,\mathrm{km/s/Mpc}$, $\Omega_M = 0.24$, $\Omega_L = 0.76$) spanning across a 15'×15' (i.e. $\sim$ 412 kpc in the cluster rest frame) field of view. The line of sight depth is taken five times bigger to correctly take into account the emission line of sight mixing, similarly to Z16, but with a spatial resolution matching one half of an X-IFU pixel to avoid aliasing effects ($\sim 2.14''$ or $\sim 0.97\,\mathrm{kpc}$). We note that this corresponds to more than 4×10^8 grid points and a tenth of this for a single X-IFU pointing. For simplicity reasons, we then adopt radial dependencies for the density,

[3]The only difference with the previous simulation method is that we did not distinguish between different element abundances and therefore used the simpler `apec` model for the X-ray spectra.

Table 6.2: Model parameters for the electron density, temperature and abundance profiles of the Coma cluster as provided by Planck Collaboration (2013) and Ettori et al. (2015)

Electron density		Temperature		Abundance	
n_0	$2.9\times10^{-3}\,\mathrm{cm}^{-3}$	T_0	6.9 keV	Z_0	0.7
r_c	400 kpc	r_t	260 kpc	R_{500}	1.31 Mpc
r_s	700 kpc	b	3.4	β_Z	0.56
β	0.57	c	0.6	γ	1.3
ϵ	1.3			z_{Coma}	0.023

abundance and temperature in the cluster. The electron density and gas temperature were assumed to follow the profiles adjusted by Planck Collaboration (2013) using the analytical functional proposed by Vikhlinin et al. (2006):

$$n_e(r) = n_0 \sqrt{\frac{1}{\left(1+(r/r_c)^2\right)^{3\beta}\left(1+(r/r_s)^3\right)^{\epsilon/3}}} \tag{6.4}$$

$$T(r) = T_0 \frac{1}{\left(1+(r/r_t)^b\right)^{c/b}} \tag{6.5}$$

We chose for the abundance the generic profile proposed by Ettori et al. (2015):

$$Z(r) = Z_0\left(1+\left(\frac{r}{0.15R_{500}}\right)^2\right)^{-\beta_Z}\left(1+z_{\mathrm{Coma}}\right)^{-\gamma} \tag{6.6}$$

All model parameters are given in Table 6.2. Again, we considered full gas ionization and thus $n_H = 1.2n_e$.

To generate an appropriate line of sight velocity field throughout the cluster $v_z(\boldsymbol{x} = (x;y;z))$[4], we follow the steps described in Z16. We first assume a standard Kolmogrov shape for the 3D velocity power spectrum as a function of the wave vector $\boldsymbol{k} = (k_x;k_y;k_z)$[5]:

$$P_{3\mathrm{D}}(\boldsymbol{k}) = C_n e^{-(k_1/k)^2} k^{\alpha} e^{-(k/k_0)^2} \tag{6.7}$$

with $k = |\boldsymbol{k}|$, k_0 and k_1 being the cutoffs of the Kolmogorov cascade at low and high wave numbers (small/dissipation and large/injection scales), α the spectral index of the spectrum, and C_n a normalization factor. A realization of the line of sight turbulent velocity field matching this power spectrum can thus be generated by drawing a random field in the Fourier domain $V_z(\boldsymbol{k}) = \nu e^{i\phi}$ using a Rayleigh distribution for the amplitude ν and a uniform distribution for the phase ϕ (see Z16 and references therein):

$$P(\nu,\phi)d\nu d\phi = \frac{\nu}{\Sigma_v^2} e^{-\frac{\nu^2}{2\Sigma_v^2}} d\nu \frac{d\phi}{2\pi} \tag{6.8}$$

with $\Sigma_v^2 = P_{3\mathrm{D}}(k)/2$. In this process, the normalization factor C_n is set by the choice of a given Mach number for the turbulent velocity M_z which scales from the speed of sound c_s (1460 km/s for the Coma

[4]Without loss of generality, the z axis will be used as the line of sight direction.
[5]With the $k = 1/r$ convention between scales and wave numbers.

cluster, Z16) the expected line of sight velocity dispersion at the center of the cluster: $< w_z >= M_z c_s$. These two quantities are related by (Zhuravleva et al., 2012):

$$< w_z^2 >= \int P_{3D}(\boldsymbol{k})\,(1 - P_\epsilon(k_z))\,d^3\boldsymbol{k} \tag{6.9}$$

In this equation, $P_\epsilon(k_z)$ is the power spectrum of the normalized X-ray emissivity along the line of sight. It is proportional to (Rybicki & Lightman, 1979):

$$\epsilon(\boldsymbol{x}) \propto Z(\boldsymbol{x})^2 n_e(\boldsymbol{x}) n_H(\boldsymbol{x}) \frac{e^{-E/kT(\boldsymbol{x})}}{\sqrt{T(\boldsymbol{x})}} \tag{6.10}$$

assuming that the variations in the cluster coming from the Gaunt factor are negligible. As for a hot cluster like Coma, the velocity determination is mostly dominated by the iron Kα line, we used the energy of this line at the cluster redshift $E = 6.26\,\mathrm{keV}$ to do this computation.

The inverse Fourier transform of $V_z(\boldsymbol{k})$ thus yields the velocity grid. It is important to note that this inverse Fourier transform, using conventional algorithms, can only be performed on the full grid at the same time. In the case of the X-IFU and its good spatial resolution, this quickly limits the maximal size of the field that can be generated with this method due to memory constraints. With the resources available on the IRAP cluster, this 15'×15' simulation with a half pixel resolution was on the edge of what was possible. If we now want to keep at least a factor 4 between the simulation grid size and the turbulence injection scale to avoid box effects, this limits us to the smallest value studied by Z16: 100 kpc. For the dissipation scale however, the small X-IFU pixels ($\sim 2\,\mathrm{kpc}$ for the Coma cluster) allow to test the full 10–50 kpc range put forward by Z16.

A sample X-IFU observation in the context of cosmic variance

For our first X-IFU simulation, we generated a turbulent velocity field with a dissipation scale of 20 kpc, a photon index $\alpha = -11/3$ for the power spectrum corresponding to the usual -5/3 index of the Kolmogrov cascade in the energy spectrum, an injection scale of 100 kpc, and a Mach number of 0.3. The X-ray emission and X-IFU simulations themselves were performed following the same steps as in Sect. 6.2.1 for an exposure time of 100 ks. In order to have spectra of sufficiently good quality to accurately measure velocities while keeping a regular geometry for the final map, the X-IFU pixels were this time binned together using a 3×3 pattern rather than the `contbin` tool. Figure 6.5 compares the reconstructed velocity field with the emissivity weighted projection of the simulated field. We see that the X-IFU was able to recover most of the field structure for scales as low as $\sim$ 20kpc, even if the average uncertainty on the velocity field was found to be $\sim 65\,\mathrm{km/s}$ by fitting a Gaussian to the distribution of the velocity measurement errors[6]. We note that we also measured across the field of view an averaged $452 \pm 100\,\mathrm{km/s}$ line broadening compatible with the expected 438 km/s from the Mach number choice.

To characterize the gas turbulence as a function of different scales, we use the second order structure function SF(r) defined as:

$$\mathrm{SF}(r) =< |v_z(\boldsymbol{x} + \boldsymbol{r}) - v_z(\boldsymbol{x})|^2 > \tag{6.11}$$

where <> denotes the averaging over the different pairs of sky points $\boldsymbol{x}$ and $\boldsymbol{x} + \boldsymbol{r}$ separated by a distance $r = |\boldsymbol{r}|$. As showed by Z16 (see also Zhuravleva et al., 2012), this function can be related to

[6] Histogram of the reconstructed map minus the emission weighted velocity field projection.

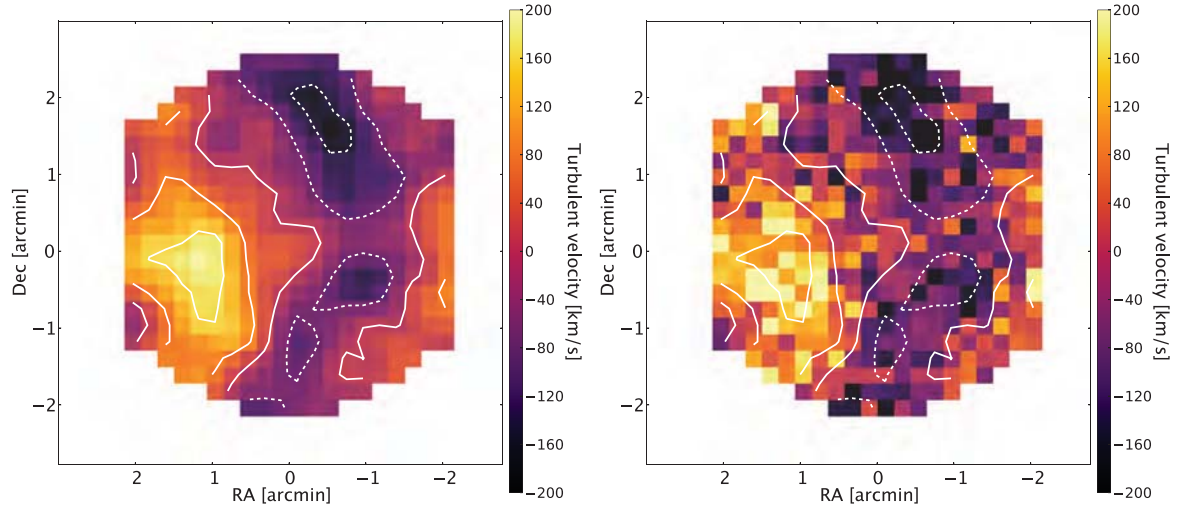

Figure 6.5: Comparison of the input projected velocity map (left) with the reconstructed field form the full End-to-End simulation (right). The coordinates are in relative units with respect to the center of the cluster. The represented contours were obtained from the input map and highlight how the main structures are recovered. The fluctuations in the reconstructed map arise from the statistical uncertainties from fitting the velocity in the spectra. Dashed contours correspond to negative values.

the 3D turbulent power spectrum through:

$$\mathrm{SF}(r) = 4\pi \int_0^\infty (1 - J_0(2\pi k r))\, P_{\mathrm{2D}}(k) dk \approx 4K\pi \int_0^\infty (1 - J_0(2\pi k r))\, P_{\mathrm{3D}}(k) dk \tag{6.12}$$

where K is a constant linking the 2D and 3D power spectra for large wave numbers[7]. It is important to note that contrary to the structure function, the line of sight velocity dispersion, obtained for instance from the broadening of emission lines, measures the total amount of turbulence and does not distinguish between different scales. The latter can also be contaminated by significant differential bulk motion across the z direction, whereas by definition, potential bulk flows can only affect the structure function at the largest scales.

By nature, the realization of a turbulent flow is random and a given turbulence regime, characterized by its 2D power spectrum, can give birth to different velocity fields and thus different measured structure functions if a limited field of view is observed. This principle is called cosmic variance. Concretely, even if we were to assume that all clusters were driven by exactly the same physics, their turbulent filed would still not be the same. To estimate the magnitude of this effect in the case of the studied X-IFU observation, we simulated 50 different velocity fields and projected them on the X-IFU field of view, weighting by the X-ray emissivity, and measured the scatter of the corresponding structure functions computed using the same pixel binning as the observation. On top of the cosmic variance, the uncertainty of the velocity measurements σ_{stat} will add to the scatter, but also bias the structure function following (Z16):

$$\mathrm{SF}'(r) = \mathrm{SF}(r) + 2\sigma^2_{\mathrm{stat}} \tag{6.13}$$

[7] $K = \int P_\epsilon(k_z, x, y) dk_z$ (Zhuravleva et al., 2012). We verified that this approximation was valid for our simulation by comparing the theoretical structure functions computed with the 2D and 3D power spectra.

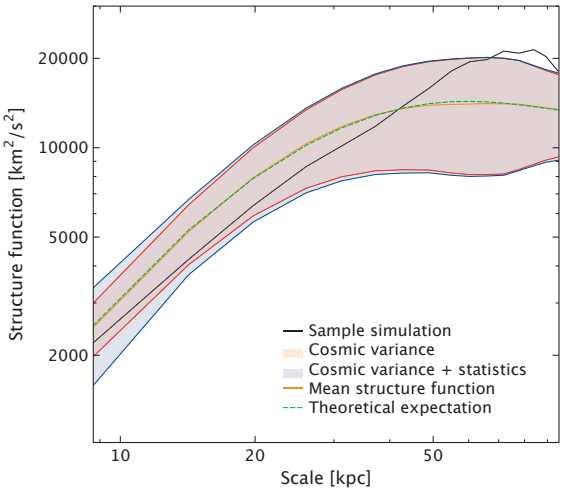

Figure 6.6: Comparison between the reconstructed structure and the expected scatter ($1\,\sigma$) from cosmic variance and statistical uncertainties. Also represented are the theoretical profile from Equation 6.12 as well as the average structure function of all the 1000 random maps used the estimate the variance. In the structure functions, the scales were linearly binned together with a 2 kpc step such that each point (16 in total) corresponds to similar numbers of line of sight velocity pairs (∼2000–5000).

Unfortunately, a single X-IFU simulation of the turbulent Coma cluster takes more than a day to run with the IRAP computing resources, such that we could not use the same approach as for the cosmic variance and simulate a large number of X-IFU observations to measure the resulting total scatter. It is nonetheless possible to obtain an estimate by replacing the velocity measurement uncertainties on different observations with a random Gaussian error whose width matches the 85 km/s uncertainty found in our sample simulation. This method is actually the one employed by Z16 in their analysis. From the 50 available velocity fields, we created 1000 maps by selecting each time one of the fields randomly and drawing a different Gaussian uncertainty field. As for the cosmic variance, the total scatter was measured form the resulting structure functions computed using the same pixel binning as for the observation. In Figure 6.6, we thus compare the structure function measured from our full simulation run with the obtained scatter as well as with the theoretical expression given by Equation 6.12. As expected, the average of the simulated projected velocity fields matches the theoretical expression[8] and our sample End-to-End simulation is found compatible with it within the statistical accuracy. It is interesting to note that the cosmic variance is a very large source of scatter, actually larger than the measurement statistics for most of the sampled scales, especially the large ones. This is actually due to the limited size of the X-IFU field of view: for scales larger or commensurable with the field of view, the structure function will strongly depend from the part of the velocity field that was sampled during the observation, whereas at small scales, this effect already averages out inside a single pointing.

With this first comparison, the setup put in place for this analysis has been validated and shows great promise for future analysis. This should notably include the full simulation and spectral reconstruction of a large number of velocity fields to estimate more accurately the final scatter of the structure function. This could then be used to refine the predictions presented in the next paragraph

[8]For the moment, we had to scale the theoretical profile to the average structure function with a normalization factor. The identification of this discrepancy is currently work in progress.

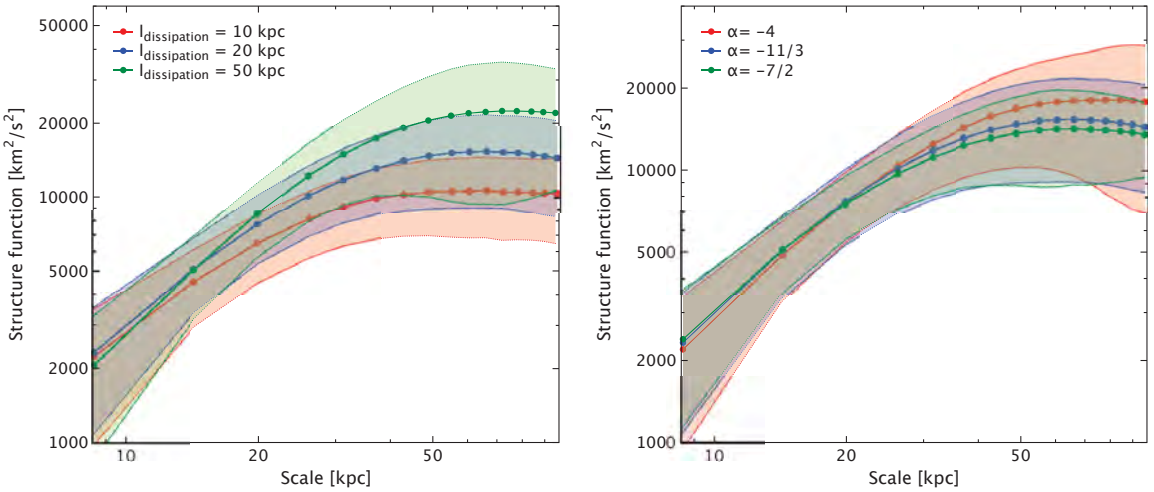

Figure 6.7: Structure functions for input power spectra with different dissipation scales (left) and spectral indices (right). When not affected, the power spectra parameters were kept to the values used for the sample full End-to-End simulation ($l_{\rm dissipation}$ =20 kpc, $l_{\rm injection}$ =100 kpc, $\alpha = -11/3$, $M_z = 0.3$). The envelopes give the 1 σ scatter due to both the cosmic variance and measurement uncertainties.

about the ability of the X-IFU to distinguish between different turbulence regimes.

Distinguishing different turbulence regimes with the X-IFU

Even if the full End-to-End study remains to be performed (see above), we can still give a first estimation of the capability of the X-IFU to measure different turbulence regimes following the method proposed Z16: for a number of dissipation scales (10, 20, and 50 kpc to sample the 10–50 kpc range proposed by Z16) and spectral indices ($\alpha = -11/3$, -7/2, -4 which correspond to different physically motivated values, as investigated by Z16 for *Hitomi/SXS*), we draw a set of 50 emission weighted velocity field projections. As for the previous paragraph, we then create 1000 reconstructed velocity maps and corresponding structure functions by randomly selecting one of the 50 fields and adding to them a random Gaussian field corresponding the the 65 km/s uncertainty level. Because the velocity uncertainty has only been properly estimated for a Mach number of 0.3, we did not test yet the possibility of varying this number. Similarly, as mentioned before, the maximal size of the velocity grid we can simulate with reasonable resources prevented us to explore larger injection scales than the adopted value of 100 kpc. Studying these larger scales would also require several X-IFU pointing, the same way as Z16 patched different observations for *Hitomi/SXS*, which is beyond the scope of this first study. These two changes will thus be tested in subsequent studies, but everything indicates that the X-IFU should be able to make decisive observations in this area way beyond what was already foreseen for *Hitomi/SXS* in terms of both the Mach number and the injection scale.

Figure 6.7 shows how various dissipation scales and turbulent spectral indices would result in different structure functions measured from a single X-IFU 100 ks pointing. Distinguishing between various spectral indices does not appear feasible whereas the identification of different dissipation scales will be challenging with only one field of view, even with the spatial resolution of the X-IFU. As the statistical uncertainty only dominates at low scales, it is important to note that increasing the exposure time will probably not be enough to obtain acceptable constraints. Properly sampling the full

cluster and not just its central part should however strongly decrease the cosmic variance especially at medium and large scales for which a limited number of structures were available per 5' field, and where we already have the tightest constraints. Patching together several X-IFU pointings as performed by Z16 should therefore be one of the next steps of this analysis. If this does not prove to be enough, the only alternative will then be to consider a sample of clusters. This would naturally offer better statistics but also introduce potential selection biases depending on the degree of representativity of such a sample with respect to the whole cluster population. Before drawing any firm conclusions from this first analysis, we however emphasize on the fact that there is intrinsically significant covariance between the different scales of a structure function (the values of a structure function at different scales are obtained from the same set of points). Taking this covariance into account, the realized functions under different input conditions might be more distinguishable that the simple visualization in Figure 6.7 would suggest. A more accurate manner to assess the capability of the X-IFU to distinguish different turbulence regimes would therefore be to fit the turbulence spectrum parameters in each realization while weighting by a covariance matrix calibrated from independent realizations. This would produce, for each regime, the expected scatter of the reconstructed parameters and one could then see whether these are distinguishable or not. As the X-IFU will be able to probe a large parameter space, it will also be crucial to take into account the degeneracy between the parameters, as Z16 did with the Mach number and injection scale. Finally, one could think of extending this study beyond the toy model approach and try to test it on cluster formation simulations, like the one used in Sect. 6.2.1, to see whether similar turbulent flows can be detected.

6.3 The magnitude of confusion in X-IFU data

On top of the standard particle background (see Sect. 3.2.3) which originates from Solar particles and cosmic rays and which will dominate at the highest energies, high galactic latitude observations with the X-IFU will suffer from contamination by the X-ray astrophysical background which comprises the emission from the Galactic local bubble and halo as well as the so-called *Cosmic X-ray Background* (CXB). This last component actually consists of X-ray emission formed by the summed contribution of high redshift AGNs covering the full sky. Thanks to the high resolving power of the X-IFU achieved by the combination of a large effective area and good spatial resolution, a large part of this background will be identified and will be masked out from the observations. The fact that not all the CXB sources will be detected is called *confusion*. In the frame of the TES array optimization exercise (see Sect. 4.2), pixels of larger size than the baseline design are being considered to either compensate for the introduction of an SPA or to reach for a larger field of view. Whereas no real scientific performance degradation is expected in terms of energy resolution or extended source count rate capability (if the bright point source science is covered by the SPA, only limited capability on the full field of view is actually required to perform the X-IFU science, see Table 3.1), the introduction of larger pixels will diminish the X-IFU resolving power and thus result in higher CXB levels. In this section, I will present the simulations I performed to investigate the magnitude of this effect.

6.3.1 Simulation setup

In order to properly quantify the impact of confusion for the different LPA pixel sizes (see Chapter 4.2), we decided to simulate N blank CXB fields for an exposure time matching expected typical X-IFU observation and to use them to estimate for each of the N fields:

- The fraction of resolved CXB

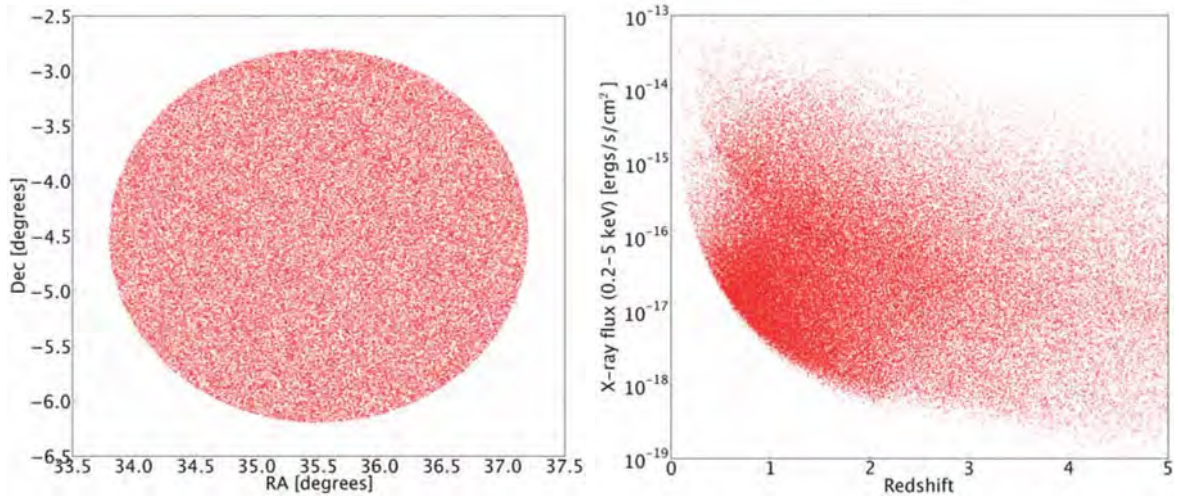

Figure 6.8: Distribution on the sky (left) and on the X-ray flux versus redshift plane (right) of the CXB sources used for the confusion simulation.

- The fraction of sources affected by confusion

The statistics over the N realizations should then provide a fair estimate of how confusion should affect X-IFU observations.

The X-IFU simulations were carried out with the `xifupipeline` tool taking a master SIMPUT file generated by N. Clerc (MPE), C. Schmidt (Bamberg) and T. Brand (Bamberg) originally created for eROSITA simulations[9]. This catalogue samples the population of AGN in the hyperspace of the X-ray luminosity, redshift, absorption, and photon index parameters while respecting the AGN spectro-photometric distribution put forward by Gilli et al. (2007) (see Fig. 6.8). Each source is modeled with a power law, disk reflexion and Iron K α line. No particular noise nor Galaxy contribution was added. From this input catalogue we simulated 675 independent X-IFU observations for an exposure time of 100 ksec each without addition of any instrumental background.

6.3.2 Source detection and results

Once the different blank fields simulated, we used the XMM SAS task ewavelet[10] to automatically detect the sources. It relies on a Mexican Hat Wavelet (MHW) filtering and we adopted a detection threshold of 5σ. The other main parameters of this task are the minimum and maximum scales for the wavelet decomposition which we respectively fixed to 1 and 3. The identification of the detected sources was then performed with respect to all sources from the input catalogue falling in the simulated fields. The search radius for identification was equal to each source extent (output by the detection task) with a minimum search radius equal to the X-IFU HEW (i.e., $\sim$ 1 pixel). Bright sources were identified first, i.e., they were associated to detection prior to less bright sources falling within the extent of the considered detection. Potential false detections were flagged and ignored in the subsequent analysis.

From these simulations, two main quantities were defined:

[9] N. Clerc, private communication.
[10] http://www.cosmos.esa.int/web/xmm-newton/sas

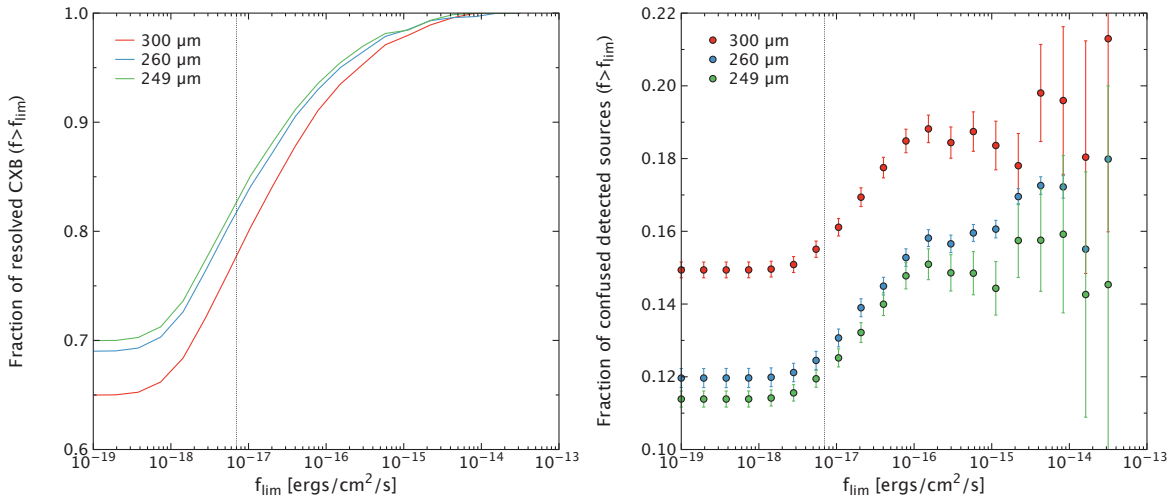

Figure 6.9: Fraction of resolved CXB (left) and fraction of sources affected by confusion (left) as a function of the source flux. Both fractions are computed for the pixel size of each three LPA configuration, ie. 249 µm (green), 260 µm (blue) and 300 µm (red). The dotted black lines mark the location of the flux above which the detection rate is 100%

- The fraction of resolved CXB is defined as the ratio of the number of sources detected to the number of sources in the field above a given flux threshold.

$$F_{\mathrm{CXB}}(f_{\mathrm{lim}}) = \frac{N(\mathrm{det} > 0, f > f_{\mathrm{lim}})}{N(\mathrm{all}, f_{\mathrm{lim}})} \tag{6.14}$$

- The fraction of confused sources is defined as the ratio of the number of sources detected and identified to more than one source in the FoV above a given flux threshold.

$$F_{\mathrm{conf}}(f_{\mathrm{lim}}) = \frac{N(\mathrm{det} > 1, f > f_{\mathrm{lim}})}{N(\mathrm{det} > 0, f_{\mathrm{lim}})} \tag{6.15}$$

Figure 6.9 shows these quantities as a function of the flux threshold. The statistical errors were estimated by a bootstrap process using 1000 realizations. As expected, at high fluxes, the CXB is fully resolved, but a higher fraction of the sources are affected by unresolved fainter sources.

Undetected sources will decrease the fraction of resolved CXB. These are of three types:

1. sources falling under the detection threshold
2. sources close to a bright source biasing the local background estimate in the MWH filtering.
3. sources on the edge of the FoV.

The third category was prevented by masking the edges of the FoV with bands 3 pixels wide. The other two are however part of the real detection and confusion process. In order to properly define the resolved CXB and confusion fractions, these thus need to be evaluated at the flux limit corresponding to the detection threshold above which all sources are detected by the X-IFU if there was no confusion issue (isolated sources). In this purpose, we simulated 9 sources spanning a flux interval

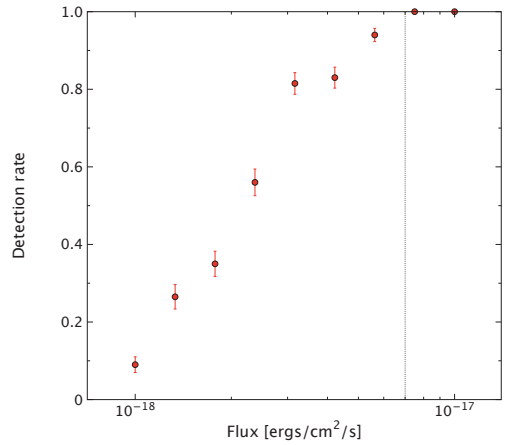

Figure 6.10: Detection rate of isolated point sources as a function of X-ray flux (0.2–5 keV). The black dotted line corresponds to the interpolated 100% detection threshold

Pixel size (µm/arcsec)	$F_{\rm CXB}(f_{\rm lim})$	$F_{\rm conf}(f_{\rm lim})$
249/4.21	83%	12%
260/4.40	82%	13%
300/5.09	77%	16%

Table 6.3: Resolved CXB and confusion fractions at the flux limit for completion.

of $[10^{-18}; 10^{-17}]$ ergs/s/cm^2, 200 times each. We ran the ewavelet source detection task and built the detection rate as a function of the source flux (see Fig 6.10). We interpolated a detection threshold of $f_{\rm lim} = 7 \times 10^{-18}$ ergs/s/cm^2.

Table 6.3 gathers for each pixel size/configuration of the TES array, the fraction of resolved CXB and the fraction of sources which detection is affected by confusion defined at the flux limit above which the detection is complete. Overall, the fractions of resolved CXB are consistent for the three pixel sizes with the prediction by Ettori & Molendi (2011). Numbers are almost identical for pixels of 249 and 260 µm. They tend to slightly degrade for 300 µm. This is linked to the ratio of the pixel size to the HEW (5"). The 249 and 260 µm configurations correspond to pixel angular size lower than the HEW (at 1 keV) where the 300 µm one is larger. Although a small effect, this slight degradation would argue for keeping the ratio of the pixel size to the HEW of the telescope below 1. It is to be noted that the chosen procedure, and more specifically the detection task (`ewavelet`) and its parametrization might introduce an unknown bias which may impact the detection rate as a function of flux (see Fig. 6.10).

Future work could imply adding signal from the Galaxy or from the particle background, or investigate different exposure times. This will certainly help to refine the predictions of the confusion issues for the X-IFU observations. However these additions are not expected to provide major inputs for discriminating between pixel sizes.

Chapter 7: Conclusion and perspectives

The objective of this thesis was dual: bring new constraints on the dynamics of the innermost parts of low mass X-ray binaries and study the high-level performance of the X-IFU by using a complete End-to-End simulator. To address the first part, I chose two probes, specific to the neutron star accreting systems: the X-ray bursts and kHz QPOs. I thus implemented dedicated data analysis tools to study these signals in detail from the archival data of the RXTE PCA instrument. They notably encompass the monitoring and characterization of QPOs on very short timescales, as well as a set of spectral timing products allowing to take into account simultaneously both the spectroscopic and timing information inherent to X-ray data.

In the second half of my thesis, benefitting from the knowledge of the signal and analysis techniques of X-ray astronomy acquired from these previous studies, I developed several aspects of the X-IFU End-to-End simulator. I notably implemented tools to thoroughly compare various TES arrays foreseen to populate the focal plane and then analyzed different reconstruction methods of the raw signal of the X-IFU pixels. Once the performance of these detectors characterized, I set up a fast simulation mode able to generate synthetic observations of complex astrophysical sources, representative of the level of detail the X-IFU will explore, to thus estimate the real End-to-End capability of this instrument on various science cases.

7.1 Main results

7.1.1 The interaction between X-ray bursts and kHz QPOs

From the analysis of 15 bursts from the two X-ray binaries 4U1636-536 and 4U1608-522, selected for their strong and coherent QPO, I could highlight for the first time an interaction between X-ray bursts and the lower kHz QPO. The observed variety of behaviors however proved difficult to reconcile with a single physical model and emphasized the complexity of the reaction of the accretion disk to a sudden strengthening of the neutron star luminosity. Moreover, by applying the spectral analysis proposed by Worpel et al. (2013), I demonstrated the incompatibility in most cases between the QPO recovery time and the idea of an increase of the accretion rate during bursts.

7.1.2 The spectral timing analysis of kHz QPOs

I presented in this thesis the first thorough spectral-timing analysis of both kHz QPOs in 4U1728-34 from the full archival data of the RXTE PCA. I could thus confirm with a large significance the incompatibility of the lag energy spectra obtained from these two oscillations. This would suggest that they actually have a different physical origin. From the analysis of the first kHz QPO covariance spectra, I then brought further evidence that these emissions have a spectrum compatible with the one of a Comptonization layer. After comparing them with the average source emission, it appears that a particularly hot part of this layer is at the center of the mechanism giving birth to these rapid oscillations. To give a final interpretation of these results, it however appears that a self-consistent model, explaining the full range of observed spectral-timing behavior is necessary.

7.1.3 The TES array optimization exercize

By using the `tessim` simulator, representative of the physics of TESs and of their first stage readout circuit, I could characterize the performance of different detector types which are foreseen to populate the X-IFU detection plane, in terms of energy resolution degradation with both energy and count rate. This study notably included the on-board pulse processing of the raw signal from the pixels, a key component of the readout chain. Overall, all pixels were found to feature a degradation of $\sim 0.2\,\mathrm{eV}$ of their resolution between 0 and 7 keV, with the SPA pixels bringing an $\sim 0.2\,\mathrm{eV}$ systematic improvement with respect to the baseline pixels. This would increase the X-IFU weak line sensitivity, a performance which is at the heart of many of its scientific objectives. In terms of count rate capability, whereas the baseline design is compliant with the required 80 % throughput of high resolution events at 1 mCrab, the introduction of a hybrid array could increase this limit by an order of magnitude. Of course, in this case, the rest of the detection plane would be limited to fainter extended sources. Another alternative to improve the X-IFU count rate capability would be to use a defocusing mechanism of the *Athena* mirror for bright point sources. Even with limited defocusing lengths, this would allow with the baseline configuration to observe sources up to 100 mCrab and reach for the Crab with a hybrid array. We note that alternatively, at equal scientific performance, this capacity enables the use of slower pixels which could be chosen to relax part of the complexity of the readout chain.

7.1.4 The study of different pulse reconstruction methods

By studying various techniques to reconstruct the pulses generated by the future X-IFU pixels, I demonstrated that a small but significative gain in energy resolution could be obtained from the use of more sophisticated methods than the standard optimal filtering. The most performant algorithm proved to be the covariance analysis which offers an improvement of 0.04 eV at 7 keV whereas the "resistance space" analysis differs from current space optimal filtering by 0.02 eV. However, due to the strong calibration needs of the former, the latter solution currently appears as the best trade-off, especially since it is the most robust method at high count rates. The extension of this study to other X-IFU pixels revealed very similar results, confirming that only moderated changes could be expected from relatively linear detectors.

7.1.5 Scientific simulations

I implemented a fast simulation model allowing, from the previously estimated performance of the different pixels, to generate in a limited computational time synthetic observations of complex astrophysical sources, while respecting the main properties of the photon detection process of this instrument.

The simulation of dead time effects for the study of kHz QPOs with the X-IFU have revealed the significant impact it had on the shape of any power spectrum, limiting the detectability of this signal. This effect could be corrected by either a precise modeling or the use of cross spectra between independent pixels instead of the usual power spectra. In any case, because the response of the X-IFU falls rapidly above a few keVs where the RMS amplitude of the QPOs is the highest, the observation of these signals with the X-IFU appears compromised.

With this same simulator, I also estimated the magnitude of confusion in the X-IFU data for the various potential pixel sizes. Only small differences were obtained and it seems that the limited increase of the pixel pitch in case of the introduction of an SPA are acceptable.

Finally, I conducted two types of galaxy cluster simulations, one based on the use of large scale structure formation simulations, and the other relying on a simpler model with density, abundance and temperature profiles to study the X-IFU capability to distinguish different turbulence regimes. With the first one, I could emphasize the richness of the X-IFU data as well as the inherent difficulty of spatially resolved spectroscopy in the presence of significant line of sight mixing. The second type of simulations has revealed that the distinction of various turbulence dissipation scales or spectral indices could prove difficult if a single X-IFU pointing is considered. These were in any case the very first steps towards the use of fully representative data to test the capability of the instrument for cluster science and they revealed the power of the End-to-End simulator to conduct such studies.

7.2 Perspectives

7.2.1 Rapid X-ray variability in low mass X-ray binaries

The two studies I conducted in the course of this thesis have strongly emphasized the potential of X-ray bursts and spectral timing tools to constrain the accretion flow in the innermost parts of LMXBs. The use of these latter techniques seems to be spreading in the community and could prove decisive for the understanding of the origin of kHz QPOs. They have notably triggered the arrival of the first emission models trying to take into account in a fully consistent manner the totality of these results.

The need for new data remains nonetheless pressing and the launch of *ASTROSAT* and its LAXPC instrument offers bright perspectives. With its effective area reaching higher energies than the PCA (see Fig. 7.1), where the RMS amplitude of the QPOs is the highest, it could notably allow a more efficient study of these signals during X-ray bursts saturating the softest X-ray band. The extension of spectral timing studies above 20–30 keV could also confirm the trend of the QPO lag energy spectra, revealing whether another hard component is at play in the emission of these oscillations. By comparing the cut-off of the continuum Comptonization layer with that of the covariance spectra, we would test as well the interpretation of this layer being at the origin of the QPOs. In the longer term, there is no doubt that dedicated next generation timing missions such as LOFT would trigger a revolution of this science area (see Fig. 7.1).

7.2.2 Pulse reconstruction techniques

The comparison proposed here of different pulse reconstruction techniques has clearly demonstrated the interest of using realistic TES simulations to conduct systematic performance studies. In the short term, this simulator could be modified to incorporate low frequency variations of the detectors environment which could have a different influence on the energy reconstruction, depending on the adopted filtering method. The implementation of a more realistic superconducting transition would also allow the extension of this type of analysis to less linear pixels, notably with a very low heat capacity. Such detectors could indeed offer a better resolution at low energies and if the high energy degradation can be compensated by the use of more advanced pulse processing techniques, they could become a very promising choice for implementation in an SPA. On the longer term, the addition in `tessim` of the full X-IFU readout chain, including the FDM and feedback process, might be needed to fully explore the main drivers of this instrument performance.

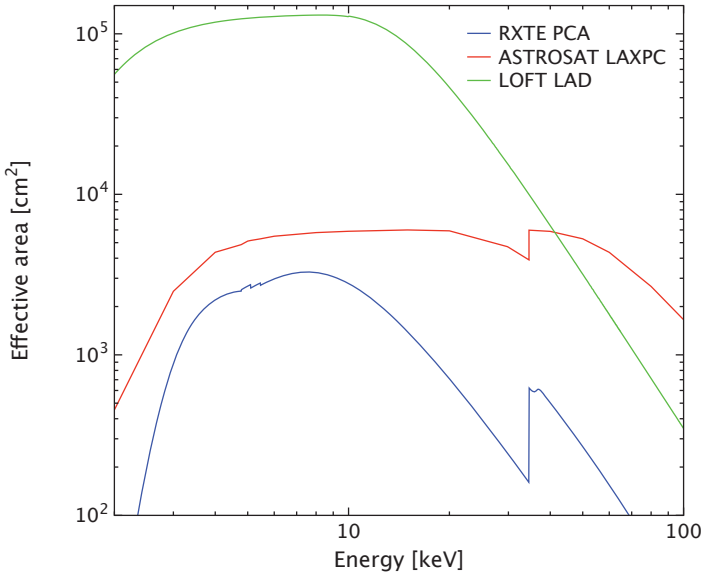

Figure 7.1: Comparison of the RXTE PCA effective area with the future ASTROSAT LAXPC and LOFT LAD timing instruments.

7.2.3 Crosstalk

During the last months of my thesis, I largely participated to the development of a crosstalk model in the End-to-End simulator (`xifupipeline` tool). This model takes into account both the thermal crosstalk arising from the common substract that the pixels share and the non linear effects from the FDM and feedback processes. These effects could prove to be decisive for a number of science cases, particularly at high count rates at which the probability of interaction between several events becomes large. The details of the implementation and our preliminary results are described in den Hartog et al. (2016). In short, the simulation setup relies on the use of coupling matrices for the thermal crosstalk with different weights depending on the pixel physical distance, and on lookup tables computed from the numerical simulation of pixel pairs with varying frequency separation, read out from a non-linear SQUID in the presence of the FDM and feedback processes. The effect of the optimal filtering process was also taken into account by measuring the influence of a small crosstalk event on the reconstructed energy as a function of its time separation with respect to the main event. Figure 7.2 shows the currently implemented readout scheme for the SPA as well as a preliminary quantification of the crosstalk influence for a point source of varying intensity. Overall, we find a predominance of thermal crosstalk as well as a global perturbation level of more than 0.1 eV influence for less than 5 % of the events for the SPA at 1 mCrab. If this level can appear as relatively low, efforts should be made in the near future to verify this in a full End-to-End process of a dimensioning science case such as the detection of weak WHIM absorption lines from GRB afterglows.

7.2.4 Studying galaxy clusters with the X-IFU

The first simulations I conducted have highlighted the potential of End-to-End models for the characterization of the future X-IFU performance during complex observations. The framework is now in place to conduct heavier simulations and try to really quantify the capability of the X-IFU to

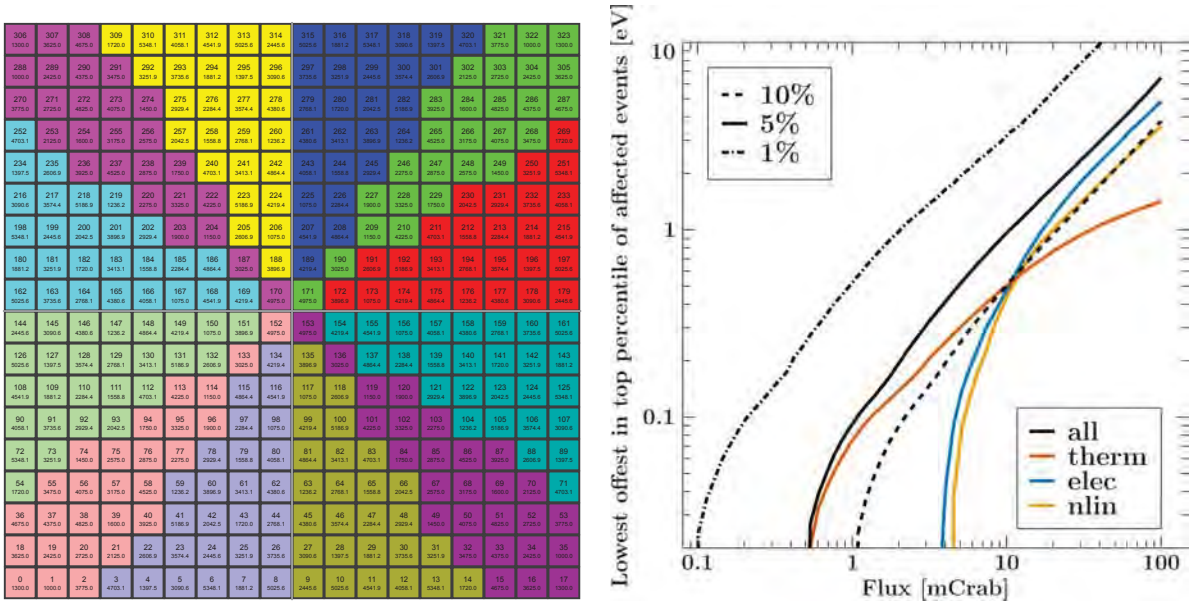

Figure 7.2: Left: SPA readout scheme implemented for the End-to-End crosstalk simulations. The routing was chosen in order to physically separate pixels close by in frequency and thus limit crosstalk for point source observations. **Right:** Preliminary results for a Crab-like point source simulation of varying intensity showing the lowest offset energy for different percentiles of the events as a function of count rate and for different crosstalk mechanisms (thermal crosstalk, electrical crosstalk, non-linear intermodulation crosstalk at the level of the SQUID, and the combination of all three). As can be seen, less than 5 % of the events are influenced at the 0.1 eV level. More details are available in den Hartog et al. (2016). Figure courtesy of T. Dauser.

constrain the physics of the hot plasma in galaxy clusters. The extension of the total field of view for the cluster extracted from cosmological simulations (see Sect. 6.2.1) by the addition of other pointings would notably allow to quantify what will be feasible in cluster outskirts (see Fig. 7.3 for preliminary results). With the study of other clusters from the same simulation, we could also test the aptitude of the X-IFU to recover some of the physical prescriptions contained in the simulation model, i.e. estimate how this instrument will probe the intrinsic cluster physics.

To go further in the study of turbulence in galaxy clusters as seen by the X-IFU, the extension of the field of view appears again as a promising short term improvement. It would indeed offer the possibility to probe this time different injection scales. In the longer term, the correct assessment of the convolved statistics of the obtention of a structure function from a projected velocity field will be needed to properly quantify the precision with which this instrument will measure turbulence mechanisms.

7.3 Concluding words

The recent outstanding *Hitomi/SXS* results have demonstrated the transformational power of spatially resolved X-ray spectroscopy and have offered us but a glimpse of what the X-IFU will unveil. Achieving the final performance of such a complex instrument will however be very challenging and, by following the hardware developments, the End-to-End simulator will continue to play a key role throughout the course of this project. Accounting for the results of instrumental effects onto a final

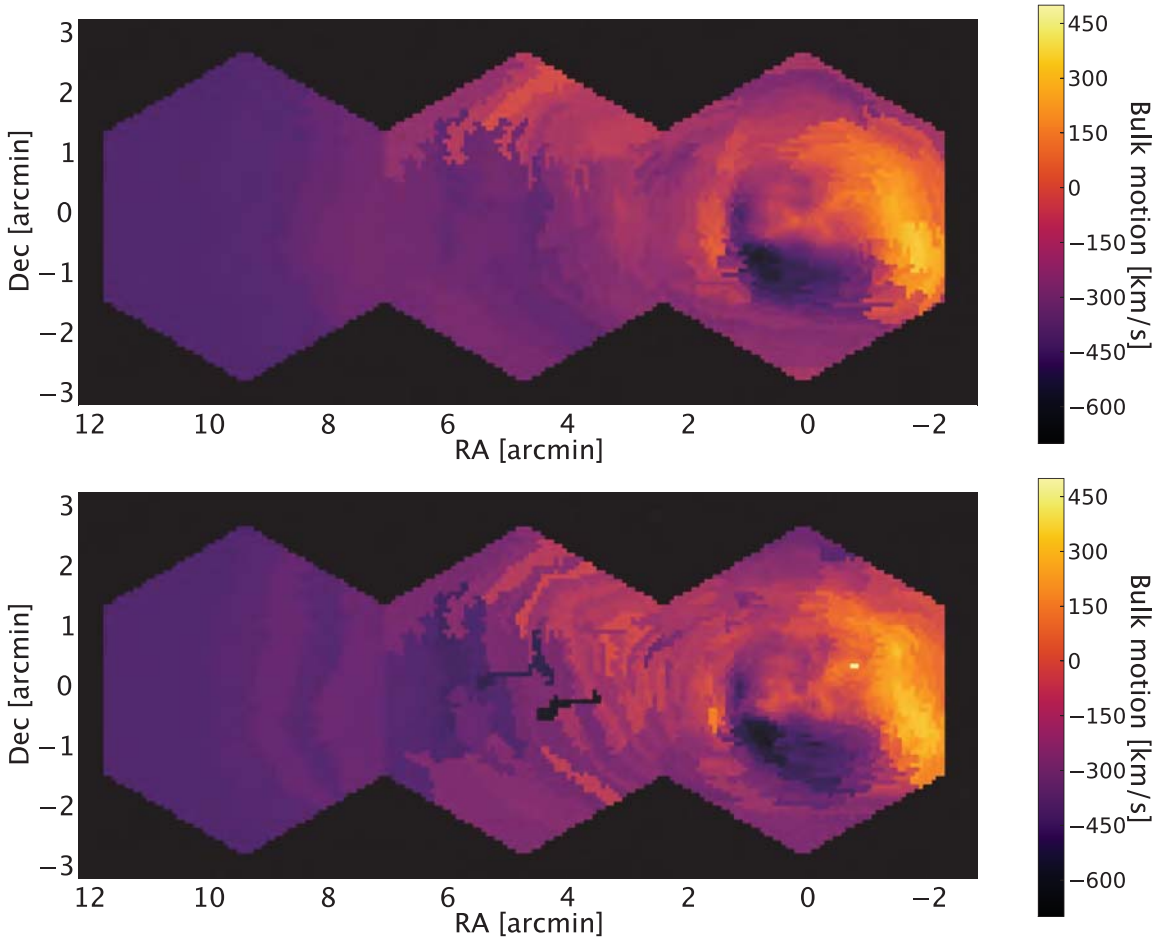

Figure 7.3: Preliminary results of the extension of the cluster simulation (see Sect. 6.2.1) to the outskirts. The input (top) and output (bottom) velocity maps are represented. In this case, a 100 ks exposure time was simulated and a continuum signal to noise ratio of 300 was adopted for the spatial binning.

scientific observation has indeed already proven to be extremely useful and this capability should not be forgotten. The foreseen richness of X-IFU dataset will without doubt require the development of innovative analysis tools and here also, by providing realistic synthetic observations, the End-to-End simulator could prove to be a key element to maximize the scientific return of this instrument from the first days of its operating phase.

Conclusion générale

L'objectif de cette thèse était double : apporter de nouvelles contraintes sur la dynamique des parties les plus internes des binaires X de faible masse et étudier les performances haut niveau du X-IFU à l'aide d'un simulateur End-to-End. Pour répondre à ce premier aspect, j'ai utilisé deux sondes particulières des systèmes accrétants à étoile à neutrons: les sursauts X et les kHz QPOs. J'ai donc mis en place des traitements de données dédiés pour étudier en détails ces signaux à partir des données d'archive de l'instrument PCA de la mission RXTE. Ils comprennent notamment le suivi et la caractérisation des QPOs sur des durées très courtes ainsi qu'un ensemble de produits spectro temporels permettant de prendre en compte simultanément les informations temporelles et spectrales contenues dans les données X. Dans la deuxième partie de ma thèse, j'ai pu développer plusieurs aspects du simulateur End-to-End du X-IFU. J'ai ainsi mis en place des outils permettant la comparaison de plusieurs matrices de détecteurs envisagées pour cet instrument, puis analysé différentes méthodes de reconstruction des signaux bruts générés par les futurs pixels X-IFU. Une fois les performances de ces détecteurs caractérisées, j'ai pu implémenter un mode de simulation rapide pour la génération d'observations synthétiques complexes, représentatives des futures données que pourra fournir le X-IFU et ainsi estimer la véritable capacité End-to-End de cet instrument pour différents cas scientifiques.

Synthèse des résultats

Interaction entre sursauts X et kHz QPOs

En analysant une quinzaine de sursauts des binaires 4U1636-536 et 4U1608-522 sélectionnées par la présence d'un QPO fort et très cohérent, j'ai pu mettre en évidence pour la première fois une interaction entre les sursauts X et le lower kHz QPO. La variété des comportements observés s'est malheureusement révélée difficile à réconcilier avec un unique modèle physique simple et a souligné la complexité de la réaction du disque d'accrétion à l'augmentation soudaine de la luminosité de l'étoile à neutrons. Par ailleurs, en appliquant l'analyse spectrale proposée par Worpel et al. (2013), j'ai pu montrer l'incompatibilité dans la plupart des cas entre la vitesse de rétablissement du QPO et l'interprétation selon laquelle une augmentation du taux d'accrétion peut être mesurée lors des sursauts.

Analyse spectro-temporelle des kHz QPOs

J'ai présenté dans cette thèse la première analyse spectro-temporelle exhaustive des deux kHz QPOs dans la source 4U1728-34 à partir de l'ensemble des données d'archive du satellite RXTE. J'ai ainsi pu confirmer avec une grande significativité la différence entre les spectres de retards de ces deux oscillations, ce qui laisse entendre qu'ils auraient une origine physique différente. Via l'analyse des premiers spectres de covariance des QPOs, j'ai ensuite amené des preuves supplémentaires que ces signaux avaient des spectres compatibles avec celui d'une couche de comptonisation et en les comparant à l'émission moyenne de cette source, il semblerait qu'une partie particulièrement chaude de cette couche puisse être au coeur du mécanisme donnant naissance à ces oscillations. Pour interpréter de

manière définitive ces résultats, que j'ai par ailleurs étendu à 4U1636-536 et 4U1608-522, il conviendra cependant de proposer un modèle complet expliquant de manière auto-consistante l'ensemble des propriétés spectro-temporelles mesurées.

L'exercise d'optimisation de la matrice de TES du X-IFU

A l'aide du simulateur `tessim` représentatif de la physique des TES et de leur premier étage de lecture, j'ai pu caractériser la performance de différents types de pixels envisagés pour peupler le plan de détection du X-IFU en termes de résolution en énergie en fonction de l'énergie et du taux de comptage. Cette étude incluait notamment une des étapes clés de la chaîne de lecture de cet instrument qui est la reconstruction à bord des pulses bruts issus des pixels. Dans l'ensemble, tous les pixels ont montré une dégradation d'environ 0.2 eV entre 0 et 7 keV, mais les pixels SPA offrent une amélioration globale d'environ 0.2 eV par rapport aux détecteurs de référence qui augmenterait la sensibilité du X-IFU à des raies faibles, une spécification requise pour nombre de ses objectifs scientifiques. En termes de capacité de taux de comptage, si les pixels standards vérifient la spécification de 80 % d'événements haute résolution à 1 mCrab, l'introduction d'une matrice de petits pixels pourrait repousser cette limite d'un ordre de grandeur, jusqu'à des flux de 10 mCrab. Evidemment, dans ce cas là, le reste du plan de détection serait limité à l'observation des sources étendues faibles. Une autre alternative pour améliorer la capacité de taux de comptage du X-IFU serait de faire usage d'une défocalisation du télescope d'*Athena* pour les sources ponctuelles brillantes. Même à des profondeurs de défocalisation limitées, cela permettrait d'observer avec la matrice de référence des sources au delà de la centaine de mCrab et avec une configuration hybride d'approcher le Crabe.

Etude de différentes méthodes de reconstruction de pulses

En étudiant différentes méthodes pour reconstruire les pulses issus des futurs pixels X-IFU, j'ai montré qu'un gain faible mais significatif pouvait être obtenu sur la résolution en énergie par l'application d'algorithmes plus avancés que la méthode standard du filtrage optimal. La méthode la plus performante s'est révélée être l'analyse à l'aide de matrices de covariance qui offre un gain d'environ 0.04 eV à 7 keV alors que la reconstruction dans l'"espace résistance" diffère du filtrage optimal à hauteur de 0.02 eV. Cependant, du fait des trop fortes contraintes en termes de calibration pour la première, cette deuxième solution apparaît aujourd'hui comme étant le meilleur compromis, d'autant plus qu'elle se révèle être la méthode la plus robuste aux hauts taux de comptage. L'application de cette étude aux autres pixels X-IFU a montré des résultats très similaires, confirmant que seuls des gains modérés peuvent être attendus pour des détecteurs relativement linéaires.

Simulations scientifiques

J'ai mis en place au sein du simulateur End-to-End du X-IFU une approche de modélisation rapide permettant, à l'aide de la mesure de la performance attendue des différents types de pixels, de générer en un temps raisonnable des observations synthétiques de sources astrophysiques complexes tout en respectant les principales propriétés de la mesure de photons par cet instrument.

L'étude par simulations des effets de temps mort sur la mesure de QPOs kHz par le X-IFU ont révélé un impact très fort sur la forme des spectres de puissance, limitant la détectabilité de ce signal. Cet effet peut cependant être corrigé à l'aide d'une modélisation précise ou par l'utilisation d'un spectre croisé entre pixels indépendants à la place du spectre de puissance. Dans tous les cas, du fait

de la réponse du X-IFU qui chute très rapidement au-delà de quelques keV, l'étude des QPOs avec cet instrument est peu prometteuse.

Ce même simulateur m'a également permis d'estimer pour les différentes tailles de pixels envisagées l'importance de la confusion dans les données X-IFU. Il en est ressorti uniquement des différences relativement limitées et il semblerait que les conséquences de la faible augmentation de la taille des pixels du grand champ suite à l'introduction d'un SPA soient acceptables.

J'ai enfin pu mener à bien deux types de simulations d'observations d'amas de galaxie, l'un se basant sur l'utilisation de résultats de simulations numériques de formation des grandes structures, et l'autre sur un modèle plus simple utilisant des profils radiaux en densité, abondance et température pour étudier la capacité du X-IFU à distinguer différents régimes de turbulence dans les amas. Avec le premier, j'ai pu mettre en évidence la richesse des données X-IFU ainsi que la difficulté inhérente à l'analyse spectrale résolue spatialement lorsque l'émission de la source se mélange le long de la ligne de visée. Le second type de simulations a quant à lui révélé qu'il pourrait s'avérer difficile de distinguer avec cet instrument différentes échelles de dissipation de la turbulence, ou différents indices spectraux de son spectre de puissance à l'aide d'un seul pointé. Il s'agit en tout cas ici des premiers pas vers l'utilisation de données véritablement représentatives pour tester la capacité du X-IFU pour la science des amas et ils ont démontré la puissance du simulateur End-to-End pour réaliser ce genre d'études.

Perspectives

Variabilité rapide dans les binaires X de faible masse

Les deux études que j'ai menées au cours de cette thèse ont largement mis en avant le potentiel des sursauts X et des outils d'analyse spectro-temporelle pour contraindre le flot d'accrétion dans les parties les plus internes des binaires X de faible masse. L'utilisation de ces derniers semble d'ailleurs se répandre dans la communauté et pourrait s'avérer décisive pour la compréhension de l'origine des kHz QPOs. Elle a d'ailleurs d'ores et déjà déclenché l'arrivée des premiers modèles d'émission essayant de prendre en compte de manière auto-consistante l'ensemble de ces résultats.

Le besoin de nouvelles données se fait malgré tout pressant et la mise en orbite du satellite ASTROSAT et de son instrument LAXPC offre de belles perspectives. Avec sa surface efficace se prolongeant à plus haute énergie que celle du PCA, là où la fraction RMS de ces oscillation est la plus forte, il pourrait notamment permettre d'étudier plus efficacement les QPOs lors de sursauts X qui saturent l'émission à basse énergie, mais également de confirmer la tendance à haute énergie des spectres de retards de ces oscillations. A plus long terme, il est indéniable que l'arrivée de missions de timing dédiées telles que LOFT sonnerait une véritable révolution du domaine.

Méthodes de reconstruction des pulses

La comparaison présentée ici de différentes méthodes de reconstruction de pulses a démontré l'intérêt de l'utilisation de simulations de TESs réalistes pour mener à bien des études de performances systématiques. Dans le futur proche, ce simulateur pourrait être modifié pour prendre en compte des variations basses fréquences de l'environnement des détecteurs (température du bain, tension de polarisation, etc.) qui pourraient se révéler avoir une influence différente selon le filtrage adopté pour extraire l'énergie des événements bruts issus des pixels X-IFU. L'implémentation d'une transition supraconductrice plus réaliste permettrait également d'étendre ce type d'analyse à des pixels moins linéaires, notamment avec une très faible capacité calorifique. De tels détecteurs pourraient en effet

offrir une meilleure résolution à basse énergie et si la dégradation à haute énergie peut être compensée par l'utilisation de méthodes de reconstruction plus avancées, ils deviendraient un choix très intéressant pour peupler un SPA.

Diaphonie

Au cours des derniers mois de ma thèse, j'ai participé à l'implémentation dans le simulateur End-to-End d'un modèle de diaphonie entre les pixels du plan de détection prenant en compte à la fois l'interaction thermique via le substrat commun à tous les pixels mais également les effets non linéaires du multiplexage fréquentiel. Ces effets pourraient se révéler être déterminants pour certains objectifs scientifiques du X-IFU, notamment à haut taux de comptage où la probabilité d'interaction entre plusieurs événements devient grande. Lors de l'écriture de ce manuscrit, une première implémentation de ces mécanismes venait d'être finalisée. Des résultats préliminaires semblent montrer une prédominance de la diaphonie thermique ainsi qu'un niveau de perturbation limitée à moins de 0.1 eV pour 95 % des événements pour une source ponctuelle de 1 mCrab observée par le SPA. Si à première vue, cela pourrait sembler acceptable, il convient maintenant de le vérifier lors d'une simulation End-to-End complète d'un cas scientifique dimensionnant tel que la détection de faibles raies d'absorption créées par le WHIM dans les spectres de sursauts gamma.

Etude des amas de galaxies avec le X-IFU

Les premières simulations que j'ai menées à bien ont mis en avant l'intérêt de modèles End-to-End pour caractériser la future performance scientifique du X-IFU lors d'observations complexes. Le cadre est maintenant en place pour mener des simulations plus poussées et essayer de véritablement quantifier la capacité du X-IFU à contraindre notre connaissance des amas de galaxies. L'extension du champ d'observation pour l'amas massif issu de simulations cosmologiques permettrait notamment d'estimer ce qu'il sera possible de faire dans la périphérie des amas, alors qu'au travers de la simulation d'autres amas prédits par le modèle de formation de grandes structures utilisé, nous pourrions tester l'aptitude de cet instrument à reconstruire certaines prescriptions physiques inhérentes à ce modèle.

Pour aller plus loin dans l'étude de la turbulence dans les amas vue par le X-IFU, augmenter là-aussi le champ d'observation en ajoutant des pointés supplémentaires offrirait la possibilité de mesurer sa capacité à distinguer cette fois-ci des échelles d'injection différentes. A plus long terme, la bonne prise en compte de la statistique convoluée liée au calcul de la fonction de structure d'un champs de vitesse projeté semble également indiquée afin de quantifier de manière certaine la précision avec laquelle cet instrument pourra mesurer la turbulence dans les amas de galaxie.

Remarques finales

Les résultats éblouissants obtenus récemment par *Hitomi/SXS* ont démontré le caractère transformationnel de la spectroscopie d'intégrale de champ en rayons X et nous ont donné un aperçu des possibilités que va offrir le X-IFU. L'atteinte des performances finales d'un instrument aussi complexe constituera malgré tout un défi majeur dans lequel le simulateur End-to-End continuera à jouer un rôle central en évoluant au cours des différents développements instrumentaux. La possibilité d'étudier les conséquences d'effets instrumentaux fins (pour l'instant modélisés mais qui seront à terme mesurés en laboratoire) sur le résultat final d'une observation scientifique s'est en effet déjà révélée très utile dans les premières phase de ce projet et il serait dommageable d'oublier cette capacité. La richesse attendue

des futures données X-IFU vont sans doute nécessiter le développement d'outils d'analyse dédiés et là aussi, la possibilité de fournir en avance de phase des observations synthétiques représentatives pourrait se révéler essentielle afin de maximiser le retour scientifique de cet instrument dès les premières phases de son exploitation.

Appendix A: XML files for the simulation of the different X-IFU configurations

In this appendix, we give the XML files newly implemented in SIXTE to describe the X-IFU focal plane in its various configurations (see Sect. 4.2). These files give a good view of the level of modularity available in this software to easily simulate a large number of designs.

- Configuration (a): Baseline single pixel array (LPA1 pixels) with 249 µm pitch and 5' field of view.

```
<?xml version="1.0"?>

<pixdetector type="x-ifu" npix="3832" xoff="0" yoff="0">
    <samplefreq value="156.25e+3"/>

    <grading num="1" name="high" pre="400" post="1024"
        rmf="athena_xifu_rmf_highres_v20150609.rmf"/>
    <grading num="2" name="mid" pre="400" post="256"
        rmf="athena_xifu_rmf_midres_v20150609.rmf"/>
    <grading num="3" name="low" pre="400" post="0"
        rmf="athena_xifu_rmf_lowres_v20150609.rmf"/>

    <hexagonloop radius="0.0095961370452" pixelpitch="249e-6" cross="1">
        <pixel>
            <shape posx="$x" delx="$p" posy="$y" dely="$p"
                width="245e-6" height="245e-6"/>
        </pixel>
    </hexagonloop>

</pixdetector>
```

- Configuration (b): Hybrid configuration comprising a small pixel array of 324 detectors (SPA) with 110 µm pitch and a large pixel array of 3476 LPA2 pixels with 260 µm pixel pitch. The total field of view reaches 5'.

```
<?xml version="1.0"?>

<pixdetector type="x-ifu" npix="3864" xoff="0" yoff="0">
    <samplefreq value="156.25e+3"/>

    <grading num="1" name="high" pre="700" post="16384"
        rmf="athena_xifu_rmf_highres_v20150609.rmf"/>
    <grading num="2" name="mid" pre="700" post="512"
        rmf="athena_xifu_rmf_midres_v20150609.rmf"/>
    <grading num="3" name="low" pre="700" post="0"
        rmf="athena_xifu_rmf_lowres_LPA2_01092015.rmf"/>


    <hexagonloop radius="0.0095961370452" pixelpitch="260e-6" cross="1">
        <pixel>
            <shape posx="$x" delx="$p" posy="$y" dely="$p" width="256e-6" height="256e-6"/>
        </pixel>
    </hexagonloop>

    <loop start="0" end="17" increment="1" variable="$l" offset="-8.5">
        <loop start="0" end="17" increment="1" variable="$c" offset="-8.5">
            <pixel>
                <shape posx="$c" delx="110e-6" posy="$l"
                    dely="110e-6" width="106e-6" height="106e-6"/>
                <grading num="1" name="high" pre="190" post="512"
                    rmf="athena_xifu_rmf_highres_v20150609.rmf"/>
                <grading num="2" name="mid" pre="190" post="128"
                    rmf="athena_xifu_rmf_midres_v20150609.rmf"/>
                <grading num="4" name="low" pre="190" post="0"
                    rmf="athena_xifu_rmf_lowres_v20150609.rmf"/>
            </pixel>
        </loop>
    </loop>

</pixdetector>
```

- Configuration (c): Hybrid configuration comprising a small pixel array of 324 detectors (SPA) with 100 µm pitch and a large pixel array of 3532 LPA3 pixels with 300 µm pixel pitch. The total field of view reaches 5.8'.

```
<?xml version="1.0"?>

<pixdetector type="x-ifu" npix="3892" xoff="0" yoff="0">
    <samplefreq value="156.25e+3"/>

    <grading num="1" name="high" pre="1700" post="16384"
        rmf="athena_xifu_rmf_highres_v20150609.rmf"/>
    <grading num="2" name="mid" pre="1700" post="1024"
        rmf="athena_xifu_rmf_midres_v20150609.rmf"/>
    <grading num="3" name="low" pre="1700" post="0"
        rmf="athena_xifu_rmf_lowres_LPA3_01092015.rmf"/>

    <hexagonloop radius="0.0111315196506" pixelpitch="300e-6" cross="1">
        <pixel>
            <shape posx="$x" delx="$p" posy="$y" dely="$p" width="296e-6" height="296e-6"/>
        </pixel>
    </hexagonloop>

    <loop start="0" end="17" increment="1" variable="$l" offset="-8.5">
        <loop start="0" end="17" increment="1" variable="$c" offset="-8.5">
            <pixel>
                <shape posx="$c" delx="100e-6" posy="$l"
                    dely="100e-6" width="96e-6" height="96e-6"/>
                <grading num="4" name="high" pre="190" post="512"
                    rmf="athena_xifu_rmf_highres_v20150609.rmf"/>
                <grading num="5" name="mid" pre="190" post="128"
                    rmf="athena_xifu_rmf_midres_v20150609.rmf"/>
                <grading num="6" name="low" pre="190" post="0"
                    rmf="athena_xifu_rmf_lowres_v20150609.rmf"/>
            </pixel>
        </loop>
    </loop>

</pixdetector>
```

Appendix B: Additional maps of the cluster simulation

We give here the remaining parameter maps of the cluster simulation presented in Section 6.2.1. The left column shows the input maps while the outputs are given on the right side. As in Figure 6.3, the input maps were obtained from the emission weighted projection of the particle parameters without any PSF nor vignetting effect. From top to bottom, the maps correspond to: the normalization of the `vapec` `Xspec` model used for the fits, the iron, oxygen and silicium abundances, and finally the velocity broadening. As can be seen, whereas for the redshift and temperature determination 10 000 counts per spectrum were sufficient, a more conservative spatial binning should probably be used for the abundance and line broadening maps. The relatively simple binning scheme used for the spectra (see Sect. 6.2.1) may also limit the quality of the results.

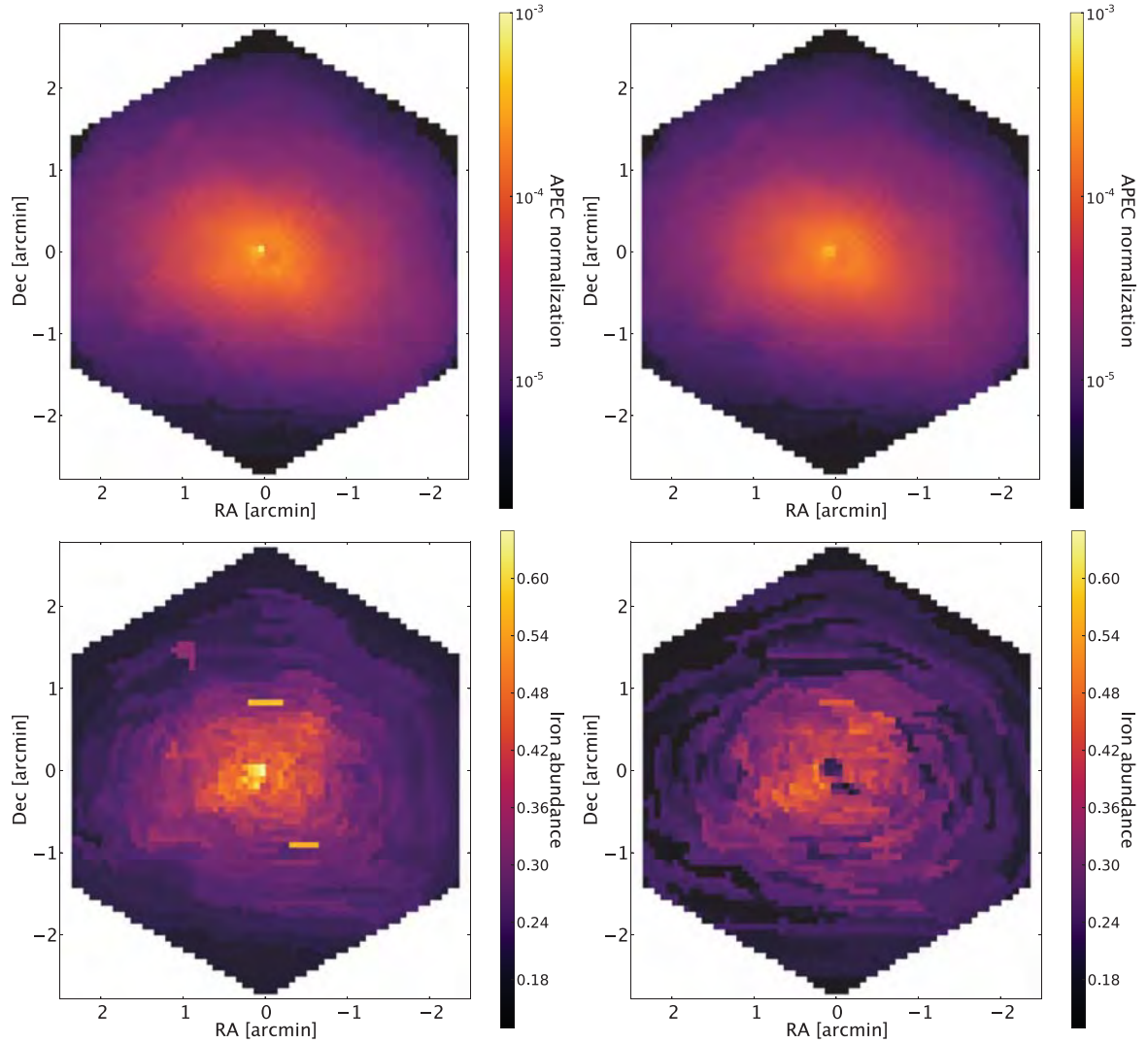

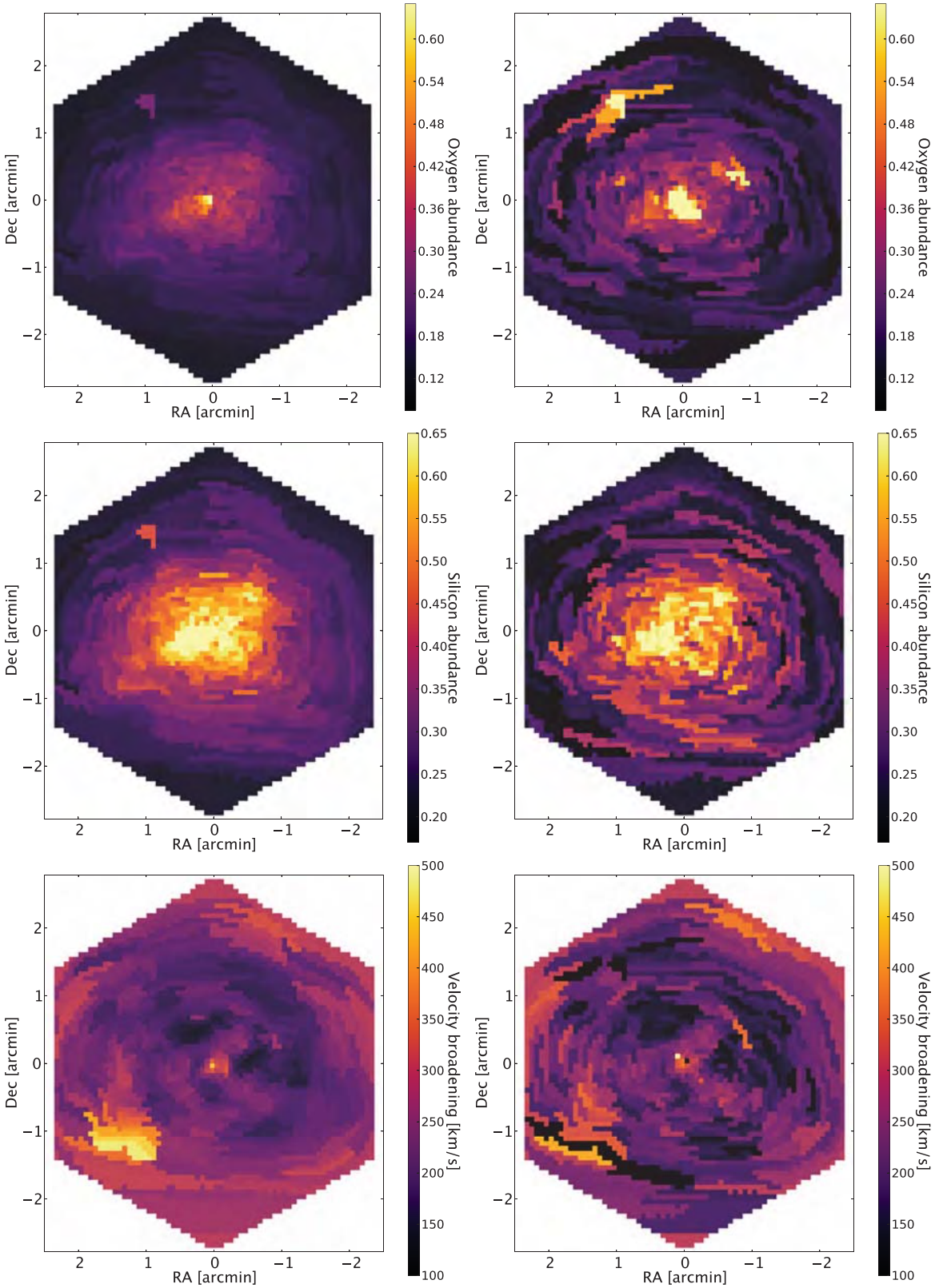
Dec [arcmin]
RA [arcmin]
Oxygen abundance
0.60
0.54
0.48
0.42
0.36
0.30
0.24
0.18
0.12
Silicon abundance
0.65
0.60
0.55
0.50
0.45
0.40
0.35
0.30
0.25
0.20
Velocity broadening [km/s]
500
450
400
350
300
250
200
150
100

Appendix C: Dead time correction for the X-IFU

Due to the non-linearity of the X-IFU detection process, the energy reconstruction of events occurring during the tail of a previous pulse will suffer from a significant bias and will need to be rejected from the scientific data (see Sect. 4.4.2). This will effectively result in a "paralyzable dead time" effect at the level of each individual pixel (each time there is a new photon impact on the TES, the dead time interval gets prolonged). Zhang et al. (1995) (hereafter Z95) developed a useful framework to describe the resulting shape modification of a power spectrum in the case of a single detector under Poisson statistics. For the X-IFU, as the counts will be extracted from a set of independent pixels, a slight modification of their formulation is required, which will be presented in this appendix.

Following the same notation as Z95, we define $x_i(t)$ $(i = 1...M)$ as the light curves obtained from the different pixels and $x(t)$ as the total time series:

$$x(t) = \sum_{i=0}^{M} x_i(t) \tag{C.1}$$

In reality, $x(t)$ is binned into a discrete series $x^k(k = 1...N)$ of number of X-ray counts per time bin of size t_b and we note $P_j(j = 1...N/2)$ its corresponding Leahy normalized discrete power spectrum (see Eq. 2.2 and 2.3).

The data extracted from the M detectors are statistically independent and as a consequence, their cross-correlation function $c_{ik}(\tau) = \int_{-\infty}^{\infty} x_i(t)x_k(t+\tau)dt$ is null. The autocorrelation function $a(\tau)$ of $x(t)$ is then simply given by:

$$\begin{aligned} a(\tau) &= \int_{-\infty}^{\infty} x(t)x(t+\tau)dt \\ &= \int_{-\infty}^{\infty} \sum_{i=0}^{M}\sum_{k=0}^{M} x_i(t)x_k(t+\tau)dt \\ &= \sum_{i=0}^{M} a_i(\tau) + \sum_{i=0}^{M}\sum_{\substack{k=0 \\ k\neq i}}^{M} c_{ik}(\tau) \\ &= \sum_{i=0}^{M} a_i(\tau) \end{aligned} \tag{C.2}$$

where $a_i(\tau)$ are the autocorrelation functions of the x_i light curves. Because the dead time process in the TESs is assimilable to paralyzable dead time, if we note t_d the duration of the secondaries rejection (i.e. the dead time interval, see Sect. 4.4.2), we have (Z95, Eq. 21):

$$a_i(t) = r_i\delta(t) + r_i^2\theta(t - t_d) \tag{C.3}$$

where $\theta(t)$ is the Heaviside function and r_i are the dead time affected count rates measured in each pixel. As demonstrated by Z95 (Eq. 8 and 9), the expectation for the Leahy normalized discrete

power spectrum P_j is given by:

$$< P_j >= \frac{2}{N_\phi}\left[\sum_{k=0}^{N-1}\xi(k)(N-k)\cos\left(\frac{2\pi jk}{N}\right)\int_0^{t_b}\int_{kt_b}^{(k+1)t_b} a(t_1-t_2)dt_1dt_2\right] \tag{C.4}$$

where $\xi(k) = 1$ if $k = 0$, 2 otherwise, and $N_\phi = N\sum_{i=0}^{M} r_i t_b$ is the total number of counts in the light curve. From there, the condensed form of P_j depends on the relation between t_b and t_d:

- If $t_b \geqslant t_d$, from Z95, Eq. 24:

$$< P_j >= \frac{2}{\sum_{i=0}^{M} r_i}\sum_{i=0}^{M}\left[r_i - 2r_i^2 t_d\left(1-\frac{t_d}{2t_b}\right) - \frac{N-1}{N}r_i^2 t_d\left(\frac{t_d}{t_b}\right)\cos\left(\frac{2\pi j}{N}\right)\right] \tag{C.5}$$

- If $t_b \geqslant t_d$, from Z95, Eq. 24:

$$\begin{aligned} < P_j >= \frac{2}{\sum_{i=0}^{M} r_i}\sum_{i=0}^{M}\Bigg[& r_i - 2r_i^2 t_b \\ & \times\Bigg\{1 - \frac{N-m}{N}\left(m+1-\frac{t_d}{t_b}\right)^2\cos\left(\frac{2m\pi j}{N}\right) \\ & + \frac{N-m-1}{N}\left(m-\frac{t_d}{t_b}\right)^2\cos\left(\frac{2\pi(m+1)j}{N}\right) \\ & + 2\cos\left(\frac{(m+1)\pi j}{N}\right)\sin\left(\frac{m\pi j}{N}\right)\Big/\sin\left(\frac{\pi j}{N}\right) \\ & - \frac{m+1}{N}\sin\left(\frac{(2m+1)\pi j}{N}\right)\Big/\sin\left(\frac{\pi j}{N}\right) \\ & + \frac{1}{N}\sin^2\left(\frac{(m+1)\pi j}{N}\right)\Big/\sin^2\left(\frac{\pi j}{N}\right)\Bigg\}\Bigg] \end{aligned} \tag{C.6}$$

where m is the integer part of t_d/t_b.

We note that because the energy distribution process (probability that a photon has a given energy) is independent of the counting statistics, the following formulas are also applicable when the power spectrum is computed from a restricted energy band as long as the dead time affected count rates are measured from the requested range.

List of Figures

List of Tables

Bibliography

Abbott, B. P., Abbott, R., Abbott, T. D., et al. 2016a, Physical Review Letters, 116, 241103

—. 2016b, Physical Review Letters, 116, 061102

Agrawal, P. C. 2006, Advances in Space Research, 38, 2989

Aird, J., Comastri, A., Brusa, M., et al. 2013, ArXiv e-prints, arXiv:1306.2325

Alston, W., Fabian, A., Markevičiutė, J., et al. 2016, Astronomische Nachrichten, 337, 417

Alston, W. N., Vaughan, S., & Uttley, P. 2013, MNRAS, 435, 1511

Altamirano, D., & Méndez, M. 2015, MNRAS, 449, 4027

Anders, E., & Grevesse, N. 1989, GCA, 53, 197

Andrews, D. H., Brucksch, Jr., W. F., Ziegler, W. T., & Blanchard, E. R. 1942, Review of Scientific Instruments, 13, 281

Andrews, D. H., Fowler, R. D., & Williams, M. C. 1949, Physical Review, 76, 154

Antoniadis, J., Freire, P. C. C., Wex, N., et al. 2013, Science, 340, 448

Artigue, R., Barret, D., Lamb, F. K., Lo, K. H., & Miller, M. C. 2013, MNRAS, 433, L64

Aviv, G. 2008, Department of Physics, Ben-Gurion University of the Negev, Experimental physics course

Bachetti, M., Harrison, F. A., Cook, R., et al. 2015, ApJ, 800, 109

Ballantyne, D. R., & Everett, J. E. 2005, ApJ, 626, 364

Ballantyne, D. R., & Strohmayer, T. E. 2004, ApJL, 602, L105

Balogh, M. L., Pearce, F. R., Bower, R. G., & Kay, S. T. 2001, MNRAS, 326, 1228

Bandler, S. R., Figueroa-Feliciano, E., Iyomoto, N., et al. 2006, Nuclear Instruments and Methods in Physics Research A, 559, 817

Barbera, M., Collura, A., Gatti, F., et al. 2014, in Proc. SPIE, Vol. 9144, Space Telescopes and Instrumentation 2014: Ultraviolet to Gamma Ray, 91445U

Barcons, X., Nandra, K., Barret, D., et al. 2015, Journal of Physics Conference Series, 610, 012008

Bardeen, J., Cooper, L. N., & Schrieffer, J. R. 1957, Physical Review, 108, 1175

Barger, A. J., Cowie, L. L., Mushotzky, R. F., et al. 2005, AJ, 129, 578

Barret, D. 2013, ApJ, 770, 9

Barret, D., Kluźniak, W., Olive, J. F., Paltani, S., & Skinner, G. K. 2005, MNRAS, 357, 1288

Barret, D., Olive, J.-F., & Miller, M. C. 2006, MNRAS, 370, 1140

—. 2007, MNRAS, 376, 1139

Barret, D., & Vaughan, S. 2012, ApJ, 746, 131

Barret, D., den Herder, J. W., Piro, L., et al. 2013, ArXiv e-prints, arXiv:1308.6784

Barret, D., Lam Trong, T., den Herder, J.-W., et al. 2016, in Proc. SPIE, Vol. 9905, Space Telescopes and Instrumentation 2016: Ultraviolet to Gamma Ray, 9905–83

Basko, M. M., & Sunyaev, R. A. 1976, MNRAS, 175, 395

Beijersbergen, M., Kraft, S., Gunther, R., et al. 2004, in Proc. SPIE, Vol. 5488, UV and Gamma-Ray Space Telescope Systems, ed. G. Hasinger & M. J. L. Turner, 868–874

Belloni, T., Méndez, M., & Homan, J. 2005, A&A, 437, 209

Bendat, J., & Piersol, A. 1986, Random Data: Analysis and Measurement Procedures, Wiley Series in Probability and Statistics (Wiley)

Berger, M., van der Klis, M., van Paradijs, J., et al. 1996, ApJL, 469, L13

Biffi, V., Dolag, K., & Böhringer, H. 2013, MNRAS, 428, 1395

Blandford, R. D., & Begelman, M. C. 1999, MNRAS, 303, L1

Blandford, R. D., & Znajek, R. L. 1977, MNRAS, 179, 433

Blustin, A. J., Page, M. J., Fuerst, S. V., Branduardi-Raymont, G., & Ashton, C. E. 2005, A&A, 431, 111

Bondi, H. 1952, MNRAS, 112, 195

Boyce, K. R., Audley, M. D., Baker, R. G., et al. 1999, in Proc. SPIE, Vol. 3765, EUV, X-Ray, and Gamma-Ray Instrumentation for Astronomy X, ed. O. H. Siegmund & K. A. Flanagan, 741–750

Boyle, W. S., & Rodgers, K. F. 1959, J. Opt. Soc. Am., 49, 66

Bradt, H. V., Rothschild, R. E., & Swank, J. H. 1993, A&A Supplement, 97, 355

Branduardi-Raymont, G., Sciortino, S., Dennerl, K., et al. 2013, ArXiv e-prints, arXiv:1306.2332

Cackett, E. M. 2016, ArXiv e-prints, arXiv:1601.07849

Cackett, E. M., Zoghbi, A., Reynolds, C., et al. 2014, MNRAS, 438, 2980

Cappi, M., Done, C., Behar, E., et al. 2013, ArXiv e-prints, arXiv:1306.2330

Cash, W. 1979, ApJ, 228, 939

Chainakun, P., & Young, A. J. 2015, MNRAS, 452, 333

Chakrabarty, D., Morgan, E. H., Muno, M. P., et al. 2003, Nature, 424, 42

Charles, I., Daniel, C., André, J., et al. 2016, in Proc. SPIE, Vol. 9905, Space Telescopes and Instrumentation 2016: Ultraviolet to Gamma Ray, 9905–87

Chen, Y.-P., Zhang, S., Torres, D. F., et al. 2011, A&A, 534, A101

Cooley, J. W., & Tukey, J. W. 1965, Mathematics of Computation, 19, 297, uRL: `http://cr.yp.to/bib/entries.html#1965/cooley`

Cornelisse, R., Heise, J., Kuulkers, E., Verbunt, F., & in't Zand, J. J. M. 2000, A&A, 357, L21

Corral-Santana, J. M., Casares, J., Muñoz-Darias, T., et al. 2016, A&A, 587, A61

Croston, J. H., Sanders, J. S., Heinz, S., et al. 2013, ArXiv e-prints, arXiv:1306.2323

Cumming, A., & Bildsten, L. 2001, ApJL, 559, L127

Dai, S., Smith, M. C., Lin, M. X., et al. 2015, ApJ, 802, 120

Dai, X., Kochanek, C. S., Chartas, G., et al. 2010, ApJ, 709, 278

Davis, S. W., Blaes, O. M., Hubeny, I., & Turner, N. J. 2005, ApJ, 621, 372

de Avellar, M. G. B., Méndez, M., Sanna, A., & Horvath, J. E. 2013, MNRAS, 433, 3453

Decourchelle, A., Costantini, E., Badenes, C., et al. 2013, ArXiv e-prints, arXiv:1306.2335

Degenaar, N., Miller, J. M., Wijnands, R., Altamirano, D., & Fabian, A. C. 2013, ApJL, 767, L37

Demorest, P. B., Pennucci, T., Ransom, S. M., Roberts, M. S. E., & Hessels, J. W. T. 2010, Nature, 467, 1081

den Hartog, R., Boersma, D., Bruijn, M., et al. 2009, in American Institute of Physics Conference Series, Vol. 1185, American Institute of Physics Conference Series, ed. B. Young, B. Cabrera, & A. Miller, 261–264

den Hartog, R., Audley, M. D., Beyer, J., et al. 2012, in Proc. SPIE, Vol. 8452, Millimeter, Submillimeter, and Far-Infrared Detectors and Instrumentation for Astronomy VI, 84520F

den Hartog, R., Barret, D., Gottardi, L., et al. 2014, in Proc. SPIE, Vol. 9144, Space Telescopes and Instrumentation 2014: Ultraviolet to Gamma Ray, 91445Q

den Hartog, R. H. 2015, SRON-XIFU-SP-2015-004 - Energy resolution budget - draft 0.3, Tech. rep., SRON

den Hartog, R. H., Peille, P., Dauser, T., et al. 2016, in Proc. SPIE, Vol. 9905, Space Telescopes and Instrumentation 2016: Ultraviolet to Gamma Ray, 9905–181

den Herder, J. W., Bagnali, D., Bandler, S., et al. 2012, in Proc. SPIE, Vol. 8443, Space Telescopes and Instrumentation 2012: Ultraviolet to Gamma Ray, 84432B

Di Salvo, T., Méndez, M., van der Klis, M., Ford, E., & Robba, N. R. 2001, ApJ, 546, 1107

Dieters, S. W., Vaughan, B. A., Kuulkers, E., Lamb, F. K., & van der Klis, M. 2000, A&A, 353, 203

Doriese, W. B., Adams, J. S., Hilton, G. C., et al. 2009, in American Institute of Physics Conference Series, Vol. 1185, American Institute of Physics Conference Series, ed. B. Young, B. Cabrera, & A. Miller, 450–453

Dovciak, M., Matt, G., Bianchi, S., et al. 2013, ArXiv e-prints, arXiv:1306.2331

Duband, L., Charles, I., & Duval, J.-M. 2014, in Proc. SPIE, Vol. 9144, Space Telescopes and Instrumentation 2014: Ultraviolet to Gamma Ray, 91445W

Emmanoulopoulos, D., Papadakis, I. E., Dovčiak, M., & McHardy, I. M. 2014, MNRAS, 439, 3931

Ettori, S., Baldi, A., Balestra, I., et al. 2015, A&A, 578, A46

Ettori, S., & Molendi, S. 2011, Memorie della Societa Astronomica Italiana Supplementi, 17, 47

Ettori, S., Pratt, G. W., de Plaa, J., et al. 2013, ArXiv e-prints, arXiv:1306.2322

Fabian, A. C. 2012, ARA&A, 50, 455

—. 2016, Astronomische Nachrichten, 337, 375

Fabian, A. C., Lohfink, A., Kara, E., et al. 2015, MNRAS, 451, 4375

Fabian, A. C., Reynolds, C. S., Taylor, G. B., & Dunn, R. J. H. 2005, MNRAS, 363, 891

Fabian, A. C., Sanders, J. S., Taylor, G. B., et al. 2006, MNRAS, 366, 417

Fabian, A. C., Zoghbi, A., Ross, R. R., et al. 2009, Nature, 459, 540

Fender, R. 2016, Astronomische Nachrichten, 337, 381

Feroci, M., Stella, L., van der Klis, M., et al. 2012, Experimental Astronomy, 34, 415

Fixsen, D., Moseley, S., Cabrera, B., & Figueroa-Feliciano, E. 2004, Nuclear Instruments and Methods in Physics Research Section A: Accelerators, Spectrometers, Detectors and Associated Equipment, 520, 555 , proceedings of the 10th International Workshop on Low Temperature Detectors

Fixsen, D. J., Moseley, S. H., Cabrera, B., & Figueroa-Feliciano, E. 2002, Low Temperature Detectors, 605, 339

Fixsen, D. J., Moseley, S. H., Gerrits, T., Lita, A. E., & Nam, S. W. 2014, Journal of Low Temperature Physics, 176, 16

Fowler, J. W., Alpert, B. K., Doriese, W. B., et al. 2015, ApJS, 219, 35

Frank, J., King, A., & Raine, D. J. 2002, Accretion Power in Astrophysics: Third Edition

Freire, P. C. C., Ransom, S. M., Bégin, S., et al. 2008a, ApJ, 675, 670

Freire, P. C. C., Wolszczan, A., van den Berg, M., & Hessels, J. W. T. 2008b, ApJ, 679, 1433

Fukumura, K., Kazanas, D., Contopoulos, I., & Behar, E. 2010, ApJ, 715, 636

Galloway, D. K., Muno, M. P., Hartman, J. M., Psaltis, D., & Chakrabarty, D. 2008, ApJS, 179, 360

García, J., Dauser, T., Reynolds, C. S., et al. 2013, ApJ, 768, 146

García, J., Kallman, T. R., & Mushotzky, R. F. 2011, ApJ, 731, 131

Georgakakis, A., Carrera, F., Lanzuisi, G., et al. 2013, ArXiv e-prints, arXiv:1306.2328

Gierliński, M., Middleton, M., Ward, M., & Done, C. 2008, Nature, 455, 369

Gilfanov, M., Revnivtsev, M., & Molkov, S. 2003, A&A, 410, 217

Gilli, R., Comastri, A., & Hasinger, G. 2007, A&A, 463, 79

Gottardi, L., Akamatsu, H., Barret, D., et al. 2014, in Proc. SPIE, Vol. 9144, Space Telescopes and Instrumentation 2014: Ultraviolet to Gamma Ray, 91442M

Gruber, D. E., Blanco, P. R., Heindl, W. A., et al. 1996, A&A Supplement, 120, C641

Gull, S. F., & Northover, K. J. E. 1973, Nature, 244, 80

Gültekin, K., Richstone, D. O., Gebhardt, K., et al. 2009, ApJ, 698, 198

Güver, T., Özel, F., Cabrera-Lavers, A., & Wroblewski, P. 2010, ApJ, 712, 964

Haardt, F., & Maraschi, L. 1991, ApJL, 380, L51

Hawley, J. F., & Krolik, J. H. 2006, ApJ, 641, 103

Hewish, A., Bell, S. J., Pilkington, J. D. H., Scott, P. F., & Collins, R. A. 1968, Nature, 217, 709

Hitomi Collaboration. 2016, Nature, 535, 117

Hulse, R. A., & Taylor, J. H. 1975, ApJL, 195, L51

Ingram, A., & van der Klis, M. 2015, MNRAS, 446, 3516

Inogamov, N. A., & Sunyaev, R. A. 2010, Astronomy Letters, 36, 848

in't Zand, J. J. M. 2011, ArXiv e-prints, arXiv:1102.3345

in't Zand, J. J. M., Galloway, D. K., & Ballantyne, D. R. 2011, A&A, 525, A111

in't Zand, J. J. M., Galloway, D. K., Marshall, H. L., et al. 2013, A&A, 553, A83

Irwin, K. D., & Hilton, G. C. 2005, Transition-Edge Sensors (Enss, C.), 63

Jahoda, K., Swank, J. H., Giles, A. B., et al. 1996, in Society of Photo-Optical Instrumentation Engineers (SPIE) Conference Series, Vol. 2808, Society of Photo-Optical Instrumentation Engineers (SPIE) Conference Series, ed. O. H. Siegmund & M. A. Gummin, 59–70

James, F., & Roos, M. 1975, Computer Physics Communications, 10, 343

Johnson, J. B. 1928, Phys. Rev., 32, 97

Jonker, P., O'Brien, P., Amati, L., et al. 2013, ArXiv e-prints, arXiv:1306.2336

Kaaret, P., Piraino, S., Ford, E. C., & Santangelo, A. 1999, ApJL, 514, L31

Kaastra, J., Finoguenov, A., Nicastro, F., et al. 2013, ArXiv e-prints, arXiv:1306.2324

Kamerlingh Onnes, H. 1911, Koninklijke Nederlandse Akademie van Wetenschappen Proceedings Series B Physical Sciences, 14, 113

Kauffmann, G., Heckman, T. M., Tremonti, C., et al. 2003, MNRAS, 346, 1055

Keek, L., Ballantyne, D. R., Kuulkers, E., & Strohmayer, T. E. 2014a, ApJ, 789, 121

—. 2014b, ApJL, 797, L23

Keek, L., Wolf, Z., & Ballantyne, D. R. 2016, ArXiv e-prints, arXiv:1605.06113

King, A. L., Miller, J. M., Raymond, J., et al. 2012, ApJL, 746, L20

King, A. R. 2010, MNRAS, 402, 1516

King, A. R., & Kolb, U. 1999, MNRAS, 305, 654

Kluźniak, W., & Abramowicz, M. A. 2005, Ap&SS, 300, 143

Kumar, N., & Misra, R. 2014, MNRAS, 445, 2818

—. 2016, ArXiv e-prints, arXiv:1602.08841

Kuulkers, E., den Hartog, P. R., in't Zand, J. J. M., et al. 2003, A&A, 399, 663

Laor, A. 1991, ApJ, 376, 90

Lattimer, J. M. 2012, Annual Review of Nuclear and Particle Science, 62, 485

Leahy, D. A., Darbro, W., Elsner, R. F., et al. 1983, ApJ, 266, 160

Lee, H. C., Misra, R., & Taam, R. E. 2001, ApJL, 549, L229

Lee, S. J., Bandler, S. R., Busch, S. E., et al. 2014, Journal of Low Temperature Physics, 176, 597

Lee, S. J., Adams, J. S., Bandler, S. R., et al. 2015, Applied Physics Letters, 107, doi:http://dx.doi.org/10.1063/1.4936793

Leggett, A. J. 2006, Nature Physics, 2, 134

Levine, A. M., Bradt, H., Cui, W., et al. 1996, ApJL, 469, L33

Lindeman, M. A. 2000, PhD thesis, University of California, Davis

Lo, K. H., Miller, M. C., Bhattacharyya, S., & Lamb, F. K. 2013, ApJ, 776, 19

Lotti, S., Cea, D., Macculi, C., et al. 2014, A&A, 569, A54

Lynden-Bell, D. 1969, Nature, 223, 690

Macculi, C., Piro, L., Cea, D., et al. 2014, in Proc. SPIE, Vol. 9144, Space Telescopes and Instrumentation 2014: Ultraviolet to Gamma Ray, 91445S

Macculi, C., Argan, A., D'Andrea, M., et al. 2016, Journal of Low Temperature Physics, doi:10.1007/s10909-015-1439-y

Marinucci, A., Matt, G., Kara, E., et al. 2014, MNRAS, 440, 2347

Mazzotta, P., Rasia, E., Moscardini, L., & Tormen, G. 2004, MNRAS, 354, 10

McCammon, D. 2005, Thermal Equilibrium Calorimeters - An Introduction, ed. C. Enss, 1

McKernan, B., Yaqoob, T., & Reynolds, C. S. 2007, MNRAS, 379, 1359

McNamara, B. R., Kazemzadeh, F., Rafferty, D. A., et al. 2009, The Astrophysical Journal, 698, 594

McNamara, B. R., & Nulsen, P. E. J. 2012, New Journal of Physics, 14, 055023

Méndez, M. 2006, MNRAS, 371, 1925

Méndez, M., Altamirano, D., Belloni, T., & Sanna, A. 2013, MNRAS, 435, 2132

Méndez, M., & Belloni, T. 2007, MNRAS, 381, 790

Méndez, M., & van der Klis, M. 1999, ApJL, 517, L51

Méndez, M., van der Klis, M., & Ford, E. C. 2001, ApJ, 561, 1016

Méndez, M., van der Klis, M., Ford, E. C., Wijnands, R., & van Paradijs, J. 1999, ApJL, 511, L49

Mendez, M., van der Klis, M., van Paradijs, J., et al. 1998, ApJL, 494, L65

Miller, J. M., Fabian, A. C., Kaastra, J., et al. 2015, ApJ, 814, 87

Miller, J. M., Raymond, J., Cackett, E., Grinberg, V., & Nowak, M. 2016, ApJL, 822, L18

Miller, J. M., Parker, M. L., Fuerst, F., et al. 2013, ApJL, 775, L45

Miller, M. C. 2013, ArXiv e-prints, arXiv:1312.0029

Miller, M. C., Lamb, F. K., & Psaltis, D. 1998, ApJ, 508, 791

Miller, M. C., & Miller, J. M. 2015, Phys. Rep., 548, 1

Mitsuda, K., Kelley, R. L., Akamatsu, H., et al. 2014, in Proc. SPIE, Vol. 9144, Space Telescopes and Instrumentation 2014: Ultraviolet to Gamma Ray, 91442A

Miyamoto, S., Kitamoto, S., Iga, S., Negoro, H., & Terada, K. 1992, ApJL, 391, L21

Morscher, M., Umbreit, S., Farr, W. M., & Rasio, F. A. 2013, ApJL, 763, L15

Moseley, S. H., Kelley, R. L., Schoelkopf, R. J., Szymkowiak, A. E., & McCammon, D. 1988, IEEE Transactions on Nuclear Science, 35, 59

Moseley, S. H., Mather, J. C., & McCammon, D. 1984, Journal of Applied Physics, 56, 1257

Motch, C., Wilms, J., Barret, D., et al. 2013, ArXiv e-prints, arXiv:1306.2334

Nandra, K., Barret, D., Fabian, A., et al. 2012, Experimental Astronomy, 34, 445

Nandra, K., Barret, D., Barcons, X., et al. 2013, ArXiv e-prints, arXiv:1306.2307

Narayan, R., & McClintock, J. E. 2008, NewAR, 51, 733

Narayan, R., & Yi, I. 1994, ApJL, 428, L13

Nowak, M. A., Vaughan, B. A., Wilms, J., Dove, J. B., & Begelman, M. C. 1999, ApJ, 510, 874

Nyquist, H. 1928, Phys. Rev., 32, 110

Pandel, D., Kaaret, P., & Corbel, S. 2008, ApJ, 688, 1288

Patruno, A., & Watts, A. L. 2012, ArXiv e-prints, arXiv:1206.2727

Peille, P., Barret, D., & Uttley, P. 2015, ApJ, 811, 109

Penna, R. F., McKinney, J. C., Narayan, R., et al. 2010, MNRAS, 408, 752

Planck Collaboration. 2013, A&A, 554, A140

Pointecouteau, E., Reiprich, T. H., Adami, C., et al. 2013, ArXiv e-prints, arXiv:1306.2319

Powell, M. J. D. 1964, The Computer Journal, 7, 155

Press, W. H., Teukolsky, S. A., Vetterling, W. T., & Flannery, B. P. 1992, Numerical recipes in FORTRAN. The art of scientific computing

Proga, D., & Kallman, T. R. 2004, ApJ, 616, 688

Psaltis, D. 2008, Living Reviews in Relativity, 11, arXiv:0806.1531

Rasia, E., Borgani, S., Murante, G., et al. 2015, ApJL, 813, L17

Rau, A., Meidinger, N., Nandra, K., et al. 2013, ArXiv e-prints, arXiv:1308.6785

Rauch, K. P., & Blandford, R. D. 1991, ApJL, 381, L39

Ravera, L., Cara, C., Ceballos, M. T., et al. 2014a, in Proc. SPIE, Vol. 9144, Space Telescopes and Instrumentation 2014: Ultraviolet to Gamma Ray, 91445T

Ravera, L., Barret, D., den Herder, J. W., et al. 2014b, in Proc. SPIE, Vol. 9144, Space Telescopes and Instrumentation 2014: Ultraviolet to Gamma Ray, 91442L

Reis, R. C., Reynolds, M. T., Miller, J. M., & Walton, D. J. 2014, Nature, 507, 207

Reynolds, C. S. 2016, Astronomische Nachrichten, 337, 404

Reynolds, C. S., & Begelman, M. C. 1997, ApJ, 488, 109

Reynolds, C. S., Young, A. J., Begelman, M. C., & Fabian, A. C. 1999, ApJ, 514, 164

Reynolds, M. T., & Miller, J. M. 2013, ApJ, 769, 16

Risaliti, G., Harrison, F. A., Madsen, K. K., et al. 2013, Nature, 494, 449

Russell, D. M., Fender, R. P., & Jonker, P. G. 2007, MNRAS, 379, 1108

Rybicki, G. B., & Lightman, A. P. 1979, Radiative processes in astrophysics

Rykoff, E. S., Miller, J. M., Steeghs, D., & Torres, M. A. P. 2007, ApJ, 666, 1129

Sadleir, J. E., Lee, S.-J., Smith, S. J., et al. 2014, Journal of Low Temperature Physics, 176, 392

Salpeter, E. E. 1964, ApJ, 140, 796

Sanders, J. S. 2006, MNRAS, 371, 829

Schmid, C. 2012, PhD thesis, Universität Erlangen-Nürnberg

Sciortino, S., Rauw, G., Audard, M., et al. 2013, ArXiv e-prints, arXiv:1306.2333

Serino, M., Mihara, T., Matsuoka, M., et al. 2012, PASJ, 64, 91

Seta, H., Tashiro, M. S., Ishisaki, Y., et al. 2012, IEEE Transactions on Nuclear Science, 59, 366

Shakura, N. I., & Sunyaev, R. A. 1973, A&A, 24, 337

Sim, S. A., Miller, L., Long, K. S., Turner, T. J., & Reeves, J. N. 2010, MNRAS, 404, 1369

Smith, S. J. 2015, parameters_revisited_v6.ppt, Tech. rep., NASA GSFC

Smith, S. J., Bandler, S. R., Brown, A.-D., et al. 2008, Journal of Low Temperature Physics, 151, 1009

Smith, S. J., Adams, J. S., Bailey, C. N., et al. 2012, Journal of Low Temperature Physics, 167, 168

Smith, S. J., Adams, J. S., Bailey, C. N., et al. 2013, Journal of Applied Physics, 114, 074513

Springel, V., Di Matteo, T., & Hernquist, L. 2005, MNRAS, 361, 776

Spruit, H., & Phinney, E. S. 1998, Nature, 393, 139

Steiner, J. F., McClintock, J. E., Remillard, R. A., et al. 2010, ApJL, 718, L117

Stella, L., & Vietri, M. 1998, ApJL, 492, L59

—. 1999, Physical Review Letters, 82, 17

Stevens, A. L., Uttley, P., & van der Klis, M. 2016, in AAS/High Energy Astrophysics Division, Vol. 15, AAS/High Energy Astrophysics Division, 105.01

Strohmayer, T. E., & Brown, E. F. 2002, ApJ, 566, 1045

Strohmayer, T. E., & Markwardt, C. B. 1999, ApJL, 516, L81

—. 2002, ApJ, 577, 337

Strohmayer, T. E., Markwardt, C. B., Swank, J. H., & in't Zand, J. 2003, ApJL, 596, L67

Strohmayer, T. E., Zhang, W., Swank, J. H., et al. 1996, ApJL, 469, L9

Sturm, E., González-Alfonso, E., Veilleux, S., et al. 2011, ApJL, 733, L16

Szymkowiak, A. E., Kelley, R. L., Moseley, S. H., & Stahle, C. K. 1993, Journal of Low Temperature Physics, 93, 281

Takei, Y., Yasuda, S., Ishimura, K., et al. 2016, in Proc. SPIE, Vol. 9905, Society of Photo-Optical Instrumentation Engineers (SPIE) Conference Series, 99050X

Thompson, C., & Duncan, R. C. 1993, ApJ, 408, 194

Thorne, K. S. 1974, ApJ, 191, 507

Timmer, J., & Koenig, M. 1995, A&A, 300, 707

Tombesi, F., Cappi, M., Reeves, J. N., et al. 2010, A&A, 521, A57

Ullom, J. N., Doriese, W. B., Hilton, G. C., et al. 2004, Applied Physics Letters, 84, 4206

Uttley, P., Cackett, E. M., Fabian, A. C., Kara, E., & Wilkins, D. R. 2014, AAPR, 22, 72

Uttley, P., Wilkinson, T., Cassatella, P., et al. 2011, MNRAS, 414, L60

van den Heuvel, E. P. J., Bhattacharya, D., Nomoto, K., & Rappaport, S. A. 1992, A&A, 262, 97

van der Klis, M. 2000, ARA&A, 38, 717

—. 2006, Rapid X-ray Variability, 39–112

van der Klis, M., Hasinger, G., Stella, L., et al. 1987, ApJL, 319, L13

van der Klis, M., Swank, J. H., Zhang, W., et al. 1996, ApJL, 469, L1

Vasudevan, R. V., Fabian, A. C., Reynolds, C. S., et al. 2016, MNRAS, 458, 2012

Vaughan, B. A., & Nowak, M. A. 1997, ApJL, 474, L43

Vaughan, B. A., van der Klis, M., Lewin, W. H. G., et al. 1999, A&A, 343, 197

Vaughan, B. A., van der Klis, M., Méndez, M., et al. 1998, ApJL, 509, L145

Vaughan, S. 2005, A&A, 431, 391

—. 2010, MNRAS, 402, 307

Vaughan, S., Uttley, P., Markowitz, A. G., et al. 2016, ArXiv e-prints, arXiv:1606.02620

Vikhlinin, A. 2006, ApJ, 640, 710

Vikhlinin, A., Kravtsov, A., Forman, W., et al. 2006, ApJ, 640, 691

Wijnands, R., Méndez, M., Miller, J. M., & Homan, J. 2001, MNRAS, 328, 451

Wijnands, R., & van der Klis, M. 2000, ApJL, 528, L93

Wilkins, D. R., & Fabian, A. C. 2013, MNRAS, 430, 247

Wilkinson, T., & Uttley, P. 2009, MNRAS, 397, 666

Will, C. M. 2014, Living Reviews in Relativity, 17, arXiv:1403.7377

Willingale, R., Pareschi, G., Christensen, F., & den Herder, J.-W. 2013, ArXiv e-prints, arXiv:1307.1709

Wilms, J., Allen, A., & McCray, R. 2000, ApJ, 542, 914

Wilms, J., Brand, T., Barret, D., et al. 2014, in Proc. SPIE, Vol. 9144, Space Telescopes and Instrumentation 2014: Ultraviolet to Gamma Ray, 91445X

Woosley, S. E., Heger, A., & Weaver, T. A. 2002, Reviews of Modern Physics, 74, 1015

Worpel, H., Galloway, D. K., & Price, D. J. 2013, ApJ, 772, 94

—. 2015, ApJ, 801, 60

Yu, W., Li, T. P., Zhang, W., & Zhang, S. N. 1999, ApJL, 512, L35

Zhang, W., Jahoda, K., Swank, J. H., Morgan, E. H., & Giles, A. B. 1995, ApJ, 449, 930

Zhuravleva, I., Churazov, E., Kravtsov, A., & Sunyaev, R. 2012, MNRAS, 422, 2712

Zhuravleva, I., Churazov, E., Sunyaev, R., et al. 2013, MNRAS, 435, 3111

Zoghbi, A., & Fabian, A. C. 2011, MNRAS, 418, 2642

ZuHone, J. A., Markevitch, M., & Zhuravleva, I. 2016, ApJ, 817, 110

Résumé

Cette thèse est consacrée au développement d'un modèle End-to-End pour le spectrocalorimètre X-IFU qui observera à partir de 2028 l'Univers en rayons X avec une précision jamais atteinte auparavant. Ce travail s'est essentiellement organisé en deux parties.

J'ai dans un premier temps étudié la dynamique des parties les plus internes des binaires X de faible masse à l'aide de deux sondes particulières que sont les sursauts X et les oscillations quasi-périodiques au kHz (kHz QPOs). En me basant sur les données d'archive du satellite Rossi X-ray Timing Explorer et sur des méthodes d'analyse spécifiquement développées dans ce but, j'ai notamment pu mettre en évidence pour la première fois une réaction du premier sur le second, confirmant le lien très étroit entre ces oscillations et les parties les plus internes du système. Le temps de rétablissement du système suite aux sursauts entre également en conflit dans la plupart des cas avec l'augmentation supposée du taux d'accrétion suite à ces explosions. Au travers d'une analyse spectro-temporelle complète des deux kHz QPOs de 4U 1728-34, j'ai également pu confirmer l'incompatibilité des spectres de retard des deux QPOs qui suggère une origine différente de ces deux oscillations. L'étude de leurs spectres de covariance, obtenus pour la première fois dans cette thèse, a quant à elle mis en évidence le rôle central de la couche de Comptonisation et potentiellement celui d'une zone particulièrement compacte de la couche limite pour l'émission des QPOs.

Dans le second volet de ma thèse, j'ai développé un simulateur End-to-End pour l'instrument X-IFU permettant de représenter l'ensemble du processus menant à une observation scientifique en rayons X, de l'émission des photons par une source jusqu'à leur mesure finale à bord du satellite. J'ai notamment mis en place des outils permettant la comparaison précise de plusieurs matrices de détecteurs en prenant en compte les effets de la reconstruction du signal brut issu des électroniques de lecture. Cette étude a mis en évidence l'intérêt de configurations hybrides, contenant une sous-matrice de petits pixels capables d'améliorer par un ordre de grandeur la capacité de comptage de l'instrument. Une solution alternative consisterait à défocaliser le miroir lors de l'observation de sources ponctuelles brillantes.

Situées au coeur de la performance du X-IFU, j'ai également comparé de manière exhaustive différentes méthodes de reconstruction des signaux bruts issus des détecteurs X-IFU. Ceci a permis de montrer qu'à faible coût en termes de puissance de calcul embarquée, une amélioration significative de la résolution en énergie finale de l'instrument pouvait être obtenue à l'aide d'algorithmes plus sophistiqués. En tenant compte des contraintes de calibration, le candidat le plus prometteur apparaît aujourd'hui être l'analyse dans l'espace de résistance.

En me servant de la caractérisation des performances des différents types de pixels, j'ai également mis en place une méthode de simulation rapide et modulable de l'ensemble de l'instrument permettant d'obtenir des observations synthétiques à long temps d'exposition de sources X très complexes, représentatives des futures capacités du X-IFU. Cet outil m'a notamment permis d'étudier la sensibilité de cet instrument aux effets de temps mort et de confusion, mais également d'estimer sa future capacité à distinguer différents régimes de turbulence dans les amas de galaxies et de mesurer leur profil d'abondance et de température. A plus long terme ce simulateur pourra servir à l'étude d'autres cas scientifiques, ainsi qu'à l'analyse d'effets à l'échelle de l'ensemble du plan de détection tels que la diaphonie entre pixels.

Mots-clés: Astrophysique, Rayons X, Athena/X-IFU, Instrumentation spatiale, Détecteurs basse température, Simulations de performance, Accrétion, Oscillations Quasi-Périodiques, Analyse spectro-temporelle.

Abstract

This thesis is dedicated to the development of an End-to-End model for the X-IFU spectrocalorimeter scheduled for launch in 2028 on board the *Athena* mission and which will observe the X-ray universe with unprecedented precision. This work has been mainly organized in two parts.

I studied first the dynamics of the innermost parts of low mass X-ray binaries using two specific probes of the accretion flow: type I X-ray bursts and kHz quasi-periodic oscillations (kHz QPOs). Starting from the archival data of the *Rossi X-ray Timing Explorer* mission and using specific data analysis techniques, I notably highlighted for the first time a reaction of the latter to the former, confirming the tight link between this oscillation and the inner parts of the system. The measured recovery time was also found in conflict with recent claims of an enhancement of the accretion rate following these thermonuclear explosions. From the exhaustive spectral timing analysis of both kHz QPOs in 4U 1728-34, I further confirmed the inconsistancy of their lag energy spectra, pointing towards a different origin for these two oscillations. The study of their covariance spectra, obtained here for the first time, has revealed the key role of the Comptonization layer, and potentially of a more compact part of it, in the emission of the QPOs.

In the second part of my thesis, I focused on the development of an End-to-End simulator for the X-IFU capable of depicting the full process leading to an X-ray observation, from the photon emission by the astrophysical source to their on-board detection. I notably implemented tools allowing the precise comparison of different potential pixel array configurations taking into account the effects of the event reconstruction from the raw data coming from the readout electronics. This study highlighted the advantage of using hybrid arrays containing a small pixel sub-array capable of improving by an order of magnitude the count rate capability of the instrument. An alternative solution would consist in defocusing the mirror during the observation of bright point sources.

Being a key component of the overall X-IFU performance, I also thoroughly compared different reconstruction methods of the pixel raw signal. This showed that with a minimal impact on the required on-board processing power, a significant improvement of the final energy resolution could be obtained from more sophisticated reconstruction methods. Taking into account the calibration constraints, the most promising candidate currently appears to be the so-called "resistance space analysis".

Taking advantage of the obtained performance characterization of the different foreseen pixel types, I also developed a fast and modular simulation method of the complete instrument providing representative synthetic observations with long exposure times of complex astrophysical sources sufficiently detailed for evaluating the future capabilities of the X-IFU. I notably used this tool to study the X-IFU sensitivity to dead time and confusion effects, but also to estimate its capability to distinguish different turbulence regimes in galaxy clusters and to measure abundance and temperature profiles. In the longer run, this simulator will be useful for the study of other scientific cases as well as the analysis of instrumental effects at the full detection plane level such as pixel crosstalk.

Keywords: Astrophysics, X-rays, Athena/X-IFU, Space instrumentation, Low temperature detectors, Performance simulations, Accretion physics, Quasiperiodic oscillations, Spectral timing analysis.